MANCHESTER 1824
The University of Manchester

Non-Standard Mechanisms for Cosmic Microwave Background B-mode Production

A thesis submitted to the University of Manchester for the degree of
Doctor of Philosophy
in the Faculty of Science and Engineering

2021

Christopher Joel Williams
Department of Physics and Astronomy

Contents

Word Count: 38680

List of figures

List of tables

List of publications

- The Simons Observatory Collaboration, Peter Ade, *et al.*, "The Simons Observatory: Science goals and forecasts," *Journal of Cosmology and Astroparticle Physics,* vol. 2019, no. 02, p. 056, Feb. 2019.
- The Simons Observatory Collaboration, Peter Ade, *et al.*, "The Simons Observatory: Astro2020 Decadal Project Whitepaper,", 2019. arXiv: 1908.08284.
- J. Williams, A. Rotti, R. Battye, "Constraining cosmic polarization rotation and implications for primordial b-modes," *Journal of Cosmology and Astroparticle Physics*, vol. 2020, no. 09, p. 006, Sep. 2020.
- J. Williams, N. McCallum, A. Rotti, D. B. Thomas, R. Battye, and M. L. Brown, "Blind map level systematics cleaning: A quadratic estimator approach," *Journal of Cosmology and Astroparticle Physics*, vol. 2021, no. 07, p. 016, Jul. 2021.

Abstract

The search for the primordial B-mode polarization signal in the cosmic microwave background (CMB), sourced by gravitational waves in the early universe, is a primary science goal of many contemporary and future experiments. However, a number of cosmological effects and imperfections in instrument design may also source B-modes that may contaminate the primordial signal. In this thesis we study these systematic instrument imperfections, and a cosmological effect, that may source B-modes, known as cosmological birefringence (CB). The CB effect involves a beyond standard model coupling between a pseudo-scalar field (such as the axion) and the photon that can generate either a uniform, or a direction dependent rotation of the linear polarization angle of CMB photons.

We begin this study by examining constraints on what is known as the uniform CB effect, which involves a direction independent rotation of CMB polarization, α_0. This study focuses on the constraints that the future Simons Observatory and CMB-S4 experiments may place on uniform CB. We forecast 1σ constraints of $\alpha_0 \leq 6.06 \times 10^{-3}$ degrees for Simons Observatory and $\alpha_0 \leq 1.8 \times 10^{-3}$ degrees for CMB-S4.

We follow this by investigating two techniques which may be used to place constraints on the power spectrum for anisotropic CB effect. The first technique is a quadratic estimator (QE) method and the second utilizes observations of the B-mode power spectrum (BB). We find that the QE technique outperforms the BB method. However, for some experimental configurations we find the difference is marginal and the more efficient BB method should be used to place constraints. We also find that experiments with a larger sky coverage may be able to place stronger constraints than equivalent experiments with access to less of the sky.

We then turn our attention to B-modes sourced by instrument systematics. For the first time we apply QEs to reconstruct systematics present in realistically simulated maps. We carry out a case study where we use QEs to reconstruct maps of a temperature to polarization leakage sourced by a differential detector gain. We are able to reconstruct and, using an iterative process, remove this leakage, recovering the primordial B-mode signal and reducing the bias on the tensor to scalar ratio, r, by a factor of ~ 100.

Finally, we apply a QE approach to the *Planck* 2018 data to reconstruct the CB map and power spectrum. We apply a likelihood to the reconstructed spectra in order to place constraints the amplitude of the CB spectrum, A_{CB}. We find constraints of $A_{CB} \leq 1.97 \times 10^{-5}$ $\left[\text{rad}^2\right]$, within 95% confidence limits (C.L.), corresponding to a photon-axion coupling strength of $g_{\phi\gamma\gamma} \leq 5.58 \times 10^{-2}$ $\left[H_I^{-1}\right]$. Our constraints offer a factor of ~ 1.3 improvement over the best existing A_{CB} constraints from *Planck* data.

Declaration of originality

I hereby confirm that no portion of the work referred to in the thesis has been submitted in support of an application for another degree or qualification of this or any other university or other institute of learning.

Copyright statement

i The author of this thesis (including any appendices and/or schedules to this thesis) owns certain copyright or related rights in it (the "Copyright") and s/he has given The University of Manchester certain rights to use such Copyright, including for administrative purposes.

ii Copies of this thesis, either in full or in extracts and whether in hard or electronic copy, may be made *only* in accordance with the Copyright, Designs and Patents Act 1988 (as amended) and regulations issued under it or, where appropriate, in accordance with licensing agreements which the University has from time to time. This page must form part of any such copies made.

iii The ownership of certain Copyright, patents, designs, trademarks and other intellectual property (the "Intellectual Property") and any reproductions of copyright works in the thesis, for example graphs and tables ("Reproductions"), which may be described in this thesis, may not be owned by the author and may be owned by third parties. Such Intellectual Property and Reproductions cannot and must not be made available for use without the prior written permission of the owner(s) of the relevant Intellectual Property and/or Reproductions.

iv Further information on the conditions under which disclosure, publication and commercialisation of this thesis, the Copyright and any Intellectual Property and/or Reproductions described in it may take place is available in the University IP Policy (see `http://documents.manchester.ac.uk/DocuInfo.aspx?DocID=24420`), in any relevant Thesis restriction declarations deposited in the University Library, The University Library's regulations (see `http://www.library.manchester.ac.uk/about/regulations/`) and in The University's policy on Presentation of Theses.

Acknowledgements

I would like to begin by thanking my supervisor Richard Battye. He always gave honest and clear feedback, and challenged me to be self-critical, and to think more deeply. I would especially like to thank him for being understanding during the times when elements of my personal life became challenging, insisting that sometimes there were more important things in life than science. Many thanks also go to Aditya Rotti, my unofficial co-supervisor. Aditya held me to a very high standard, and taught me to hold myself and my work to a higher standard. He has my gratitude for all the advice, support and feedback he gave. My sincere thanks go out those who collaborated on my second paper Nialh McCallum, Dan Thomas, and Michael Brown who worked tirelessly along Richard, Aditya and me. It was a joy working with all of them.

I would like to thank Luke Hart for his friendship, for checking up on me during the Covid lockdown, for the countless coffees we've had together, for keeping me enthusiastic about my work and showing genuine interest in it, and for teaching me how to program in C++. My thanks also go out to the rest of those I shared the 3.135 office with, Dom Viatic, Sankarshana Srinivasan, Eunseong Lee, Andy May, Josh Hayes, Danelius Banys, Francesca Pearce, and Edoardo Altamura. In addition I would like Alastair Savin with whom I shared my home office. I would like to thank all of them them for the fun, laughter, encouragement, coffee and beer they have provided. They have all taught me so much, and been so kind to me. I could not ask for better office mates, work colleagues, and friends.

I would like to thank my parents Chis and Sarah Williams for always encouraging me to work hard and to to never stop learning, and for always being there for me when I needed help and advice. I also want to think my siblings, Michael, Hannah, Rebeccah, and AT. I am so grateful to my whole family for the love and support they have provided, and continue to provide.

Finally, there are two people I would like to give special thanks to. The first is the most important person in my life, my long suffering fiancée Katie Whitehouse. I am so grateful for her love, her endless patience, her tireless encouragement and her overwhelming support. Without her I would not have made it to the end of my Ph.D. program. The second is my best friend Adam Van Cleef. Adam was a dear friend; we could chat for hours about anything and everything, and I have countless amazing memories of time we spent together. Adam sadly passed away during the course of my studies. He is unforgettable and irreplaceable, and is deeply missed. It is to both Katie Whitehouse and Adam Van Cleef that I would like to dedicate this thesis.

Chapter 1

Introduction

1.1 The Expanding Universe

1.1.1 From expansion to the Big Bang

In the early 20^{th} century the prevailing consensus was that the Universe was static, the cosmos was infinite, with astrophysical bodies set at a fixed distance from one another, and space and time were rigid and fixed. This consensus was ended by Einstein's theory of General Relativity [1] and work by Friedmann, Lemaitre, and the observations made by Hubble. Einstein's theory was one of a space-time that was not rigid, but was curved by the presence of matter and energy. This relationship between the curvature of space-time and the distribution of matter and energy are elegantly presented in Einstein's field equations [2],

$$G_{\mu\nu} = \frac{8\pi G}{c^4} T_{\mu\nu} + \Lambda g_{\mu\nu} \ . \tag{1.1}$$

Both Friedmann, and Lemaîtra independently derived dynamic solutions to Einstein's equations for a Universe which was expanding at a calculable rate [3], [4]. Indeed Lemaîtra even estimated what would later become known as the Hubble constant. The theoretical work of Friedmann, and Lemaîtra was verified by observations made by Hubble, that galaxies appeared to be moving at away from the observer rate proportional to their distance from the observer. From the work of Friedmann, Lemaitre, and Hubble the Big Bang theory emerged.

The consensus among the majority of cosmologists today is that the Universe began in an state of extreme temperature and density, and expanded from this state to the state in which it now exists [5]. What is known today as the Big Bang theory describes a number of key epochs that occur during the expansion of the Universe, with a number of measurable predictions for a number of these epochs. One of the most exciting of these epochs is recombination. Before recombination the temperature and density of the of the Universe is high enough that the background photon plasma was larger than 13.6eV. Therefore, the energy of photons was higher than the binding energy of hydrogen keeping the Universe ionized and preventing neutral toms from forming [5], [6]. Recombination occurred when the temperature and density of the Universe reduced enough that the photons decoupled from electrons and free streamed,

allowing neutral atoms to form [7]. This epoch is exciting because it provides important observable evidence for the Big Bang today. The decoupled free streaming photons from the epoch of recombination are observed today as the cosmic microwave background (CMB).

1.1.2 The cosmic microwave background

The CMB, formed when photons decoupled from electrons in the Early Universe during the epoch of recombination, is one of the most important cosmological observables in modern cosmology. It is the oldest observable source of electromagnetic radiation in the cosmos and giving key information about the structure and composition of the Universe providing measurements that include measurements of the density of different species in the Universe including the dark matter, dark energy, and baryon density, measurements the curvature of the Universe, and measurements the expansion rate of the Universe [5], [7].

Discovered in 1964 by Penzias and Wilson, the CMB is the closest example to a perfect black body that exists in our Universe. While appearing to be isotropic in Penzias and Wilson's original observations, local anisotropies in the structure of the CMB were first observed by the *COBE* satellite [8]. The particular measurements made of the properties, composition, and structure of the Universe come from analysis of the statistical structure of these CMB anisotropies. Often these statistical properties are summarized using the CMB temperature and polarization power spectra.

The temperature anisotropies are defined as

$$T(\hat{\mathbf{n}}) \equiv \frac{\bar{T}(\hat{\mathbf{n}}) - T_0}{T_0} \ , \tag{1.2}$$

where $\bar{T}(\hat{\mathbf{n}})$ is the temperature of the CMB measured today in direction $\hat{\mathbf{n}}$ and T_0 is the average temperature across the sky [5]. The temperature anisotropies can be decomposed into modes with different scale dependence using spherical harmonic decomposition so that

$$T(\hat{\mathbf{n}}) = \sum_{lm} T_{lm} Y_{lm}(\hat{\mathbf{n}}) \ , \tag{1.3}$$

The T_{lm} is the spherical harmonic decomposition coefficient[1] and is a Gaussian random variable. Here, $Y_{lm}(\hat{\mathbf{n}})$ are the spherical harmonic functions [9]. The advantage of this approach is that all the geometric behavior is captured in the spherical harmonic functions, and all of the statistical behavior of the CMB is captured in the coefficients. The temperature power spectrum, C_l^{TT} is then defined as the ensemble average of the 2-point correlation of the CMB temperature anisotropies so that,

$$\langle T_{lm} T^*_{l'm'} \rangle = C_l^{TT} \delta_{ll'} \delta_{mm'} \ . \tag{1.4}$$

[1] Often T_{lm} is denoted a_{lm} or a^T_{lm} in the literature.

Often the ensemble average, $\langle T_{lm} T^*_{l'm'} \rangle$, is referred to as the CMB covariance. Note that the ensemble average is over the different possible realizations of the process by which the CMB is formed [10]. In reality we only measure one realization of the CMB, so we instead use an estimator of the true CMB temperature power spectrum which has the form [9]

$$\widehat{C}_l^{TT} = \frac{1}{2l+1} \sum_m |T_{lm}|^2 \ . \tag{1.5}$$

As the Thompson scattering process that produces the CMB generates linearly polarized photons another key observable from the CMB are the maps of the direction dependent Q and U Stokes polarization parameters, $Q(\hat{\mathbf{n}})$ and $U(\hat{\mathbf{n}})$. The Stokes parameters are defined in terms of the complex amplitude of the x and y components of the electromagnetic field, a_x and a_y, such that

$$\begin{aligned} I &\equiv \langle a_x^2 \rangle + \langle a_y^2 \rangle \ , \\ Q &\equiv \langle a_x^2 \rangle - \langle a_y^2 \rangle \ , \\ U &\equiv \langle 2 a_x a_y \cos(\theta_x - \theta_y) \rangle \ , \\ V &\equiv \langle 2 a_x a_y \sin(\theta_x - \theta_y) \rangle \ , \end{aligned} \tag{1.6}$$

where θ_x and θ_y are phase terms for the x and y components of the electromagnetic fields. Here, the intensity is equivalent to the temperature. The Q and U stokes parameters represent the linear polarization components of the electromagnetic field, and V represents the circular polarization component. The $Q(\hat{\mathbf{n}})$ and $U(\hat{\mathbf{n}})$ fields represent the stokes parameters at a given direction $\hat{\mathbf{n}}$ on the sky. The specific details of this projection of coordinate dependent fields onto the sky are discussed in Chapter 2.4.

If the stokes fields are transformed under a rotation by an angle ϑ they are transformed so that

$$\begin{aligned} Q'(\hat{\mathbf{n}}) &= Q(\hat{\mathbf{n}}) \cos 2\vartheta + U(\hat{\mathbf{n}}) \sin 2\vartheta \ , \\ U'(\hat{\mathbf{n}}) &= -Q(\hat{\mathbf{n}}) \sin 2\vartheta + U(\hat{\mathbf{n}}) \cos 2\vartheta \ . \end{aligned} \tag{1.7}$$

The $Q(\hat{\mathbf{n}})$ and $U(\hat{\mathbf{n}})$ fields transform as components spin-2 symmetric trace free tensor. Therefore, they can be decomposed using a spin-weighted spherical harmonic decomposition into what are known as E- and B-modes, so that [11],

$$Q(\hat{\mathbf{n}}) \pm i U(\hat{\mathbf{n}}) = -\sum_{lm} (E_{lm} \pm i B_{lm})_{\pm 2} Y_{lm}(\hat{\mathbf{n}}) \ . \tag{1.8}$$

The ${}_{\pm 2}Y_{lm}(\hat{\mathbf{n}})$ are the spin ± 2 spherical harmonic functions. If the spin-weighted spherical harmonics are rewritten in terms of the non-weighted spherical harmonics then the E_{lm} and B_{lm} coefficients have basis the basis functions $Y^E_{lm}(\hat{\mathbf{n}})$ and $Y^B_{lm}(\hat{\mathbf{n}})$ respectively. These basis functions are composed of covariant derivatives of the spherical harmonic functions Y_{lm} in such a way that $Y^E_{lm}(\hat{\mathbf{n}})$ is gradient containing, and $Y^B_{lm}(\hat{\mathbf{n}})$ is curl containing [9]. In this way the decomposition of the polarization fields into E_{lm} and B_{lm} is analogous to the Helmholtz

decomposition of the electric and magnetic fields with the E_{lm} and B_{lm} notation chosen accordingly[2].

The E- and $B-$modes have their own power spectra

$$\langle E_{lm} E^*_{l'm'} \rangle = C_l^{EE} \delta_{ll'} \delta_{mm'} \ , \tag{1.9a}$$

$$\langle B_{lm} B^*_{l'm'} \rangle = C_l^{BB} \delta_{ll'} \delta_{mm'} \ . \tag{1.9b}$$

with estimators equivalent to $\widehat{C}_l^{TT}$ in (1.5) such that [9],

$$\widehat{C}_l^{EE} = \frac{1}{2l+1} \sum_m |E_{lm}|^2 \ , \tag{1.10a}$$

$$\widehat{C}_l^{BB} = \frac{1}{2l+1} \sum_m |B_{lm}|^2 \ . \tag{1.10b}$$

As only the observed CMB constitutes a single realization only there is an inherent uncertainty in the observed power spectrum known as cosmic variance. This is in addition to any uncertainty due to instrumental noise on the spectra due to the measurement process, or any systematic errors in the measurement and takes the value

$$\sigma_l^2 = \frac{2}{2l+1} (C_l^A)^2 \tag{1.11}$$

where $A \in [TT, EE, BB]$ [10].

In order to use the power spectra to establish values physical parameters, Markov-Chain Monte-Carlo (MCMC) simulations of the power spectra for values are fit to observed spectra. The fit is found by varying six parameters that are used to define the ΛCDM cosmological model. This is the minimum number of parameters required in order to completely specify the model [12]. There is some flexibility as to which six parameters are chosen but some examples are the physical baryon density parameters, $\Omega_b h^2$, the physical dark matter density parameter, $\Omega_c h^2$, the current Hubble expansion rate, H_0, the ionization optical depth τ, the amplitude of primordial curvature perturbations, A_s, and the scalar spectral index, n_s [13]. An example of the data fit to measured estimates of the CMB spectra is shown in Figure 1.1.

While the temperature and E-mode power spectra have been measured to an extremely high precision by a number of CMB experiments, only the B-modes sourced by weak lensing of the CMB [15] have been measured to date. The primordial B-modes from the surface of last scattering (LSS) have yet to be observed. The observation of primordial B-modes is an important science goal of many contemporary CMB experiments [14], [16] as the presence of primordial B-modes is a key prediction of the theory of inflation.

[2]In the literature E_{lm} and B_{lm} are often denoted as a^E_{lm} and a^B_{lm}. Historically, they were denoted a^G_{lm} and a^C_{lm} corresponding to the gradient and curl containing parts of the decomposition.

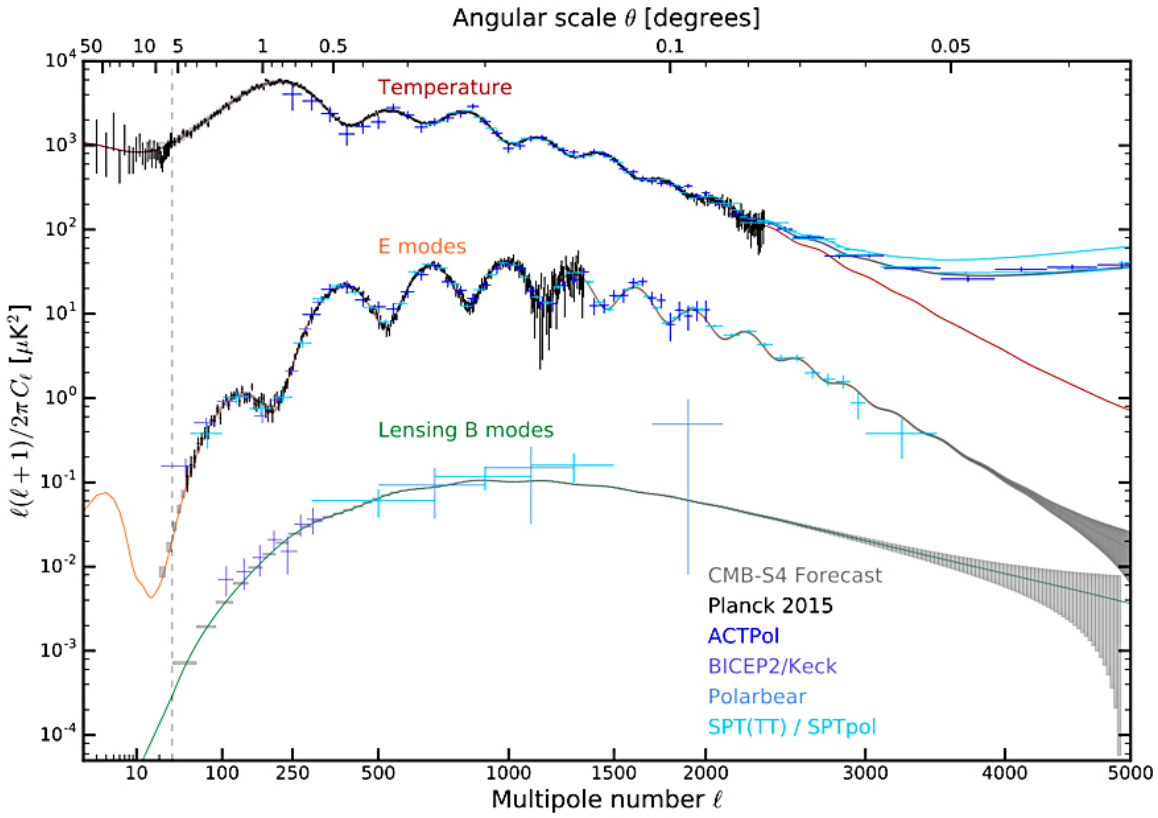

Figure 1.1: The ΛCDM best fit C_l^{TT}, C_l^{EE}, and C_l^{BB} spectra compared to measurements from a range of CMB instruments including *Planck*, ACTpol, BICEP2/Keck, Polarbear and SPT/SPTpol. This figure is taken from the CMB-S4 science book [14].

1.1.3 Inflation

The theory of inflation came about as a solution to three important problems with the Big Bang theory. While there is strong evidence for the Big Bang in the form of the CMB a number of problems arose which could not be resolved in within the framework of the Big Bang and subsequent expansion alone. These problems all arose as a result of observations that did not match what was expected for the Big Bang theory. They are as follows [5]:

- *The flatness problem*: The Universe as we measure it today has an nearly perfectly flat geometry. The measured value of the total density parameter is $\Omega_{\text{tot}} - 1 = 0.0007 \pm 0.0037$ [13], where $\Omega_{\text{tot}} = 1$ is the requirement for a perfectly geometrically flat universe. This level of flatness today requires the initial conditions of the Universe to be such that at matter radiation equality $\Omega_{\text{tot}} < 10^{-20}$ and at the Planck scale $\Omega_{\text{tot}} < 10^{-60}$. This requires a large amount of fine tuning if no mechanism is present to drive the flatness to current observed value.

- *The horizon problem*: When *COBE* made its observations of the CMB anisotropy it was noted that the CMB was in thermal equilibrium across the full sky [8]. This is unexpected as the length of the mean free path of photons before the CMB was formed was too short

for the photons across the entire horizon distance to have enough time to come into causal contact with one another. In fact, accounting for the expansion of the Universe, a region in causal contact before photon free streaming would cover less than 2° of the sky.

- *The relic abundance problem*: A number of particle theories predict the presence of relics formed in the Early Universe such as monopoles, cosmic strings, and domain walls. However, these relics and their effects on the evolution of the Universe are not observed today. This is a problem as normal expansion does not account for the reduction of the density of these species to levels where they are not observed and do not dominate the evolution of the Universe.

Fortunately a solution to these issues was proposed by Starobinsky [17], Guth [18], and Linde [19] in the form of inflation. Inflation refers to an epoch during which the Universe undergoes a period of exponential expansion where the scale factor, $a(t)$ which relates physical distance to comoving evolves as [5]

$$a(t) \propto e^{Ht} \, , \tag{1.12}$$

where H is the Hubble constant and t is time. This period of exponential expansion can be shown to drive the Universe towards a flat geometry so that,

$$\Omega_{\text{tot}} - 1 \propto \exp(-2Ht) \, . \tag{1.13}$$

This mechanism avoids the fine tuning flatness problem, as initial conditions where the Universe is near perfectly flat are no longer required for the Universe to be close to flat after inflation. Inflation also provides a solution to the horizon problem. During inflation, volumes that are in causal contact with one another can expand rapidly during inflation without changes to the characteristic length scale of the Universe, allowing the area in thermal equilibrium to be larger than the horizon. The dilution of relic particle density at the levels required to prevent them from dominating is also provided by inflation. During inflation the relic particle density decreases quicker than the overall energy density to negligible levels, preventing relics from becoming the dominant factor in determining the dynamics of the Universe's evolution. Indeed, inflation itself also allows for the Gaussian fluctuations that form the structure in the CMB [5].

A key prediction of inflation is that, as well as the scalar perturbations that seed the structure in the CMB temperature and E-mode polarization, there should also be primordial tensor perturbations, primordial gravitational waves. As only tensor perturbations source primordial B-modes[3] [9], [20], the B-mode signal constitutes an important observable signature of the gravitational waves in the Early Universe sourced by inflation. Indeed it may be possible to use B-modes to constrain the energy scale and different models for inflation [11]. The level

[3]Scalar perturbations cannot contribute to the B-mode signal due to the difference in parity between the scalar perturbations and the basis functions for B-modes [9].

of tensor perturbations is often parameterized as the ratio between tensor and scalar modes, r.

However, primordial tensor perturbations are not the only potential source of CMB B-modes. As previously mentioned, B-modes sourced by weak lensing of the CMB radiation have already been observed [21]–[24]. However, weak lensing is not the only non-inflationary source of B-modes. Parity violating mechanisms may exist in the Early Universe that result in a mixing between E- and B-modes, generating a B-mode signal that is additional to the primordial signal. These mechanisms may be primordial magnetic fields waves [25], [26], or parity violating extensions to the standard model Lagrangian [25], [27]. Both these mechanisms result in the rotation of the linear polarization angle of light. The phenomenon of this rotation is referred to as either Cosmic Polarization Rotation (CPR) or Cosmological Birefringence (CB), although in some literature only the standard model extension is referred to as CB. Additionally, a contaminant B-mode signal may also be generated by systematic effects from imperfections in CMB instruments such as a differential gain between detectors, or an ellipticity in the observation beam [28].

Both systematic and cosmological effects that source these B-modes provide a large challenge to the robustness of future claims of primordial B-modes. To circumvent this issue, both cosmological and systematic effects must either be detected in a way that allows the removal of non-primordial B-modes from the observed CMB polarization or be constrained to levels where the spurious B-modes are subdominant to the primordial signal. Additional motivation to search for cosmological effects that source B-modes is that a detection of CPR would be of large scientific significance, providing an exciting signature of new and exotic physics. The search for CPR, and the attempts to detect, constrain, and remove systematic sources of non-primordial B-modes is the primary focus of this thesis.

1.2 Thesis Structure

This thesis consists of seven chapters including this introductory chapter. Four of these chapters contain original scientific content, with the remaining consisting of this introduction, a literature review, and a concluding chapter. Here the structure of this thesis is summarized and a description of the content of each chapter is provided.

In Chapter 2 literature surrounding alternative mechanisms of producing B-mode polarization in the CMB. In this chapter literature on extensions to the electrodynamics that lead to CPR or CB are discussed, as well as the way these modifications manifest CMB. Literature surrounding methods for detecting monopole CB is discussed. Moreover, literature on the quadratic estimator (QE) approaches that can be used to detect both anisotropic CB and systematic effects is discussed.

Chapter 3 constitutes the first scientific content chapter. This chapter focuses on work

that was carried out for Simons-Observatory (SO), forecasting the constraints that SO and CMB-S4 could place on monopole birefringence. This work summarized in this chapter was submitted as a logbook entry on the SO wiki. In the thesis chapter a fisher forecast of the monopole CB effect.

The content in Chapter 4 is an adapted version of a paper published in JCAP [29] that I wrote with Aditya Rotti and Richard Battye. The scientific content that went into this work is largely my own work, carried out with guidance from my coauthors. This chapter focuses on a comparison between two different methods that can be used to constrain CPR, a direct likelihood approach using measurements of the B-mode power spectrum and a QE approach. This chapter also includes forecast of the expected CPR constraints from the SO and *LiteBIRD* experiments, as well as the levels of B-mode contamination from CPR that correspond to these constraints.

The content in Chapter 5 is an adapted version of a paper published in JCAP [30] that I wrote in collaboration with Nialh McCallum, Aditya Rotti, Dan Thomas, Richard Battye and Michael Brown. The chapter, and the paper it is based upon, provides the first example of a QE based blind systematic cleaning approach applied to a set of realistic time ordered simulations. In this chapter we describe the QE approach that we use to not only diagnose a differential gain systematic in realistic simulated maps, but remove the systematic effect from these maps. In addition to this, we illustrate that this cleaning is capable of significantly reducing the bias on the tensor-to-scaler ratio r. For this body of work I developed the QE, associated QE code and cleaning pipeline used throughout the work, as well as applying the QE to simulations provided by Nialh McCallum and Dan Thomas. My contribution also includes the likelihood work carried out in the paper, and the introduction of a novel filtering scheme used in the cleaning pipeline. The majority of the writing in [30] was carried out by me, with descriptions of the simulations provided by Nialh McCallum and Dan Thomas.

The final scientific content chapter is Chapter 6. The work that is shown in this chapter has been carried out in preparation for submission to a scholarly journal. In this chapter a QE approach is used to place CB constraints using the *Planck* 2018 polarization data. In this chapter we reconstruct the CB power spectrum, and map as well as placing model dependent constraints on the CB power spectrum by applying likelihood approach.

Finally in Chapter 7 a general summary of this thesis is provided. This summary includes discussing the key results presented in each chapter as well as their significance in the context of the thesis as a whole. This is followed by a discussion of future avenues of research that could follow on form this work.

Chapter 2

A review of alternative sources of CMB B-mode Polarization

2.1 Introduction

2.1.1 Electrodynamics

The physical behavior of light has been described by many theories, from Newtons Corpuscular theory of light to the modern theory of electrodynamics. Since the latter theory was introduced by James Clerk Maxwell in his original paper in 1865 [31] there have been many experiments that have confirmed the predictions made by Maxwell, as well as further theoretical work that has advanced the understanding of electrodynamics. Electrodynamics stands today as one of the best tested and most well understood theories of modern physics.

However, an important question that is often asked about many well understood theories of physics is at what point do they fail? That is, is there some energy scale or length scale at which the theory fails to describe the observed physics? If the answer to this question is 'yes' then it is necessary to modify the original theory in some way to capture this new behavior. This question can be asked of Maxwell's laws. Is there an energy or a length scale at which they fail to describe the behavior of light? It so happens that electrodynamics seems to match observations on all of the energy scales that have been tested so far. However, there are a number of theoretical modifications to electrodynamics that predict behavior that could be seen on cosmological length scales. This predicted behavior is known as cosmological birefringence and refers to a rotation of the linear polarisation angle of photons as they propagate through a vacuum. This is analogous to the birefringence of light as it passes through optically active media.

Among the theories that predict cosmological birefringence are potential candidates for theories of inflation. These theories involve an interaction between the photon gauge field and an axion field [32][33][34][35]. Inflation is necessary to solve both the horizons and the flatness problem in cosmology. As it plays a key role in the understanding of the evolution of the Early Universe it is important to determine the mechanism for inflation. Observations of a

cosmological birefringence angle of the orders of magnitude predicted by the axion inflation theories could provide supporting evidence for these theories. Alternatively, failure to observe the predicted birefringence effect would provide a strong test for these theories, potentially ruling them out.

In addition to testing theories of inflation the cosmological birefringence effect is parity violating, and can be Lorentz violating. Therefore, an observation of birefringence could be a valuable tests of these important fundamental symmetries in nature [36]. Moreover, as models predicting cosmological birefringence involve a coupling between axion-like particles and the photon, constraints on the birefringence effect may provide constraints on the coupling between axion-like particles and the gauge field.

2.1.2 The cosmological laboratory

While cosmological birefringence would act as a good test for a number of important theories of inflation as well as a test for Lorentz and parity symmetry the effect is predicted to be very small. It would be impossible to detect such a rotation in terrestrial laboratory experiments. It could be, as mentioned previously, possible to detect a cosmological birefringence effect on light propagating on cosmological scales. In this sense the Universe can be used as a laboratory to test fundamental physics.

The two primary sources of polarised photons that are at a large enough distance to make a detection of cosmological birefringence possible are distant radio galaxies and the cosmic microwave background (CMB). The cosmic microwave background is favoured for observations of birefringence as it provides observations of the propagation of linearly polarised photons on the largest length scales. Moreover, as there are many experiments and much effort focused on measuring the CMB polarisation it is likely that if the birefringence angle is measured it will be measured through observations of the CMB.

A primary science goal of CMB polarization experiments is the search for primordial tensor perturbations through the measurement of primordial B-modes of polarization [9], [16], [37]. However, cosmological birefringence (in particular anisotropic birefringence) can act as a non-standard mechanism of B-mode production, providing potential contamination in primordial B-mode searches. So, while detecting cosmological birefringence may be an important science goal, constraining the effect is also important in order to claim a robust detection of primordial tensor perturbations.

In addition to beyond standard model physics, B-mode contamination can also be sourced by systematic effects due to imperfections in the instrument. These systematics, like the birefringence effect, must be well characterised before claims of B-mode detection can be made.

One of the primary mathematical tools used in the detection of anisotropic birefringence

is the quadratic estimator (QE) [38], [39]. This technique is commonly deployed in studies of weak gravitational lensing of the CMB [15], [40], [41]. Both birefringence and weak lensing distort the CMB maps and generate off diagonal correlations in the CMB covariance matrix. The QE technique makes use of these off diagonal correlations in order to reconstruct maps of the fields that source these distortions. In the case of birefringence this field is the polarization rotation-angle field. As many systematic effects distort the CMB in a similar way to both birefringence and lensing, generating diagonal CMB correlations, it may also be possible to to employ quadratic estimators in order to diagnose such effects [28].

In this literature review the theoretical aspects of the cosmological birefringence effect and the methods for detecting such an effect are discussed. Section 2.2 describes the methods of modifying electrodynamics that lead to a rotation of the polarisation angle in linearly polarised electromagnetic waves. This description begins with a focus on a general modification of electromagnetism that was introduced by Carroll, Field and Jackiw. Then an equivalent modification, in which a pseudo-scalar field is coupled to electromagnetism, is described. This equivalent modification is found in inflationary models which couple an axion field to the gauge field in the electrodynamic Lagrangian. Section 2.3 describes an alternative picture of the axion-gauge field coupling that involves a mixing between the axion field and linearly polarised photons, introduced by George Raffelt. Section 2.4 describes how cosmological birefringence can be measured through CMB polarisation observations. This section begins with a description of methods used to estimate the birefringence angle from the cross correlations of the temperature, E mode and B mode CMB anisotropies. Section 2.5 discusses the effect of anisotropic birefringence on the CMB and how QEs can be applied to reconstruct the anisotropic birefringence field. Finally, in section 2.6 the impact of systematics on CMB polarization experiments is discussed, along with the relationship between instrument imperfections and distortions in the CMB maps that it may be possible to reconstruct using QEs.

2.2 Modifying Electrodynamics

2.2.1 Coupling electrodynamics to a general Chern-Simons term

In their work in 1990 - seen in [25] - Carroll, Field and Jackiw examined a Lorentz violating modification to electrodynamics that predicted a rotation of the polarisation angle of linearly polarised photons. This modification begins by coupling the gauge field to an arbitrary four-vector p^μ in the following Chern-Simons-like term,

$$\mathcal{L}_{CS} = -p_\mu A_\nu \tilde{F}^{\mu\nu} \ , \tag{2.1}$$

where $\tilde{F}^{\mu\nu}$ is the dual of the electromagnetic field strength tensor and has the form $\tilde{F}^{\mu\nu} = \epsilon^{\mu\nu\rho\sigma} F_{\rho\sigma}/2$, and A_ν is the gauge field. This term is combined with the usual Lagrangian for

electrodynamics to give a total Lagrangian,

$$\mathcal{L} = \mathcal{L}_{EM} + \mathcal{L}_{CS} = -\frac{1}{4}F_{\mu\nu}F^{\mu\nu} - 4\pi A_\nu J^\nu - p_\mu A_\nu \tilde{F}^{\mu\nu} \ , \tag{2.2}$$

where a source term has been included. The Euler-Lagrange equations are used to arrive at an equation of motion,

$$-\partial_\mu F^{\mu\nu} + 4\pi J^\nu + p_\mu \tilde{F}^{\mu\nu} = 0 \ . \tag{2.3}$$

This modification does not change the identity $\partial_a \tilde{F}^{ab} = 0$. Using this identity and equation (2.3) it is possible to write down a set of modified Maxwell's equations,

$$\begin{aligned} \boldsymbol{\nabla} \cdot \mathbf{B} &= 0 \ , \\ \partial_t \mathbf{B} + \boldsymbol{\nabla} \times \mathbf{E} &= 0 \ , \\ -\partial_t \mathbf{E} + \boldsymbol{\nabla} \times \mathbf{B} &= 4\pi \mathbf{J} - p_0 \mathbf{B} + \mathbf{p} \times \mathbf{E} \ , \\ \boldsymbol{\nabla} \cdot \mathbf{E} &= 4\pi\rho \ - \mathbf{p} \cdot \mathbf{B} \ . \end{aligned} \tag{2.4}$$

Then a plane wave ansatz is used. For the source-free case, the third line of equation (2.4) becomes,

$$-i\omega \mathbf{E_0} - i\mathbf{k} \times \mathbf{B_0} = -p_0 \mathbf{B_0} + \mathbf{p} \times \mathbf{E_0} \ . \tag{2.5}$$

The second line of (2.4) is used to replace $\mathbf{B_0}$ with $\frac{1}{\omega}\mathbf{k} \times \mathbf{E_0}$. Next, Lagrange's formula is used to rewrite (2.5) as,

$$(\omega^2 - k^2)\mathbf{E_0} + \mathbf{k}(\mathbf{k} \cdot \mathbf{E_0}) - i(-p_0 \mathbf{k} + \omega \mathbf{p}) \times \mathbf{E} = 0 \ . \tag{2.6}$$

This can be written as a matrix equation, $M_{ij}E_j = 0$, where,

$$M_{ij} = (\omega^2 - k^2)\delta_{ij} + k^2 \hat{k}_i \hat{k}_j - i\epsilon_{ijk}(\omega p \hat{p}_l - p_0 k \hat{k}_l) \ . \tag{2.7}$$

Note that for a photon traveling along the z-direction it is possible to write

$$\mathbf{k} = k \begin{pmatrix} 0 \\ 0 \\ 1 \end{pmatrix} \ , \mathbf{p} = p \begin{pmatrix} \sin(\theta)\cos(\phi) \\ \sin(\theta)\sin(\phi) \\ \cos(\theta) \end{pmatrix} \ , \tag{2.8}$$

where θ is the angle between $\mathbf{k}$ and $\mathbf{p}$. The final matrix is then,

$$M_{ij} = \begin{pmatrix} \omega^2 - k^2 & -i(\omega p \cos(\theta) - p_0 k) & i\omega p \sin(\theta)\sin(\phi) \\ i(\omega p \cos(\theta) - p_0 k) & \omega^2 - k^2 & -i\omega p \sin(\theta)\cos(\phi) \\ -i\omega p \sin(\theta)\sin(\phi) & i\omega p \sin(\theta)\cos(\phi) & \omega^2 \end{pmatrix} \tag{2.9}$$

The determinant of this matrix should be equal to zero. It is possible to use a symbolic algebra package like Mathematica to compute the determinant and to simplify the resulting equation,

$$k^4 + \omega^4 - k^2(p_0^2 + 2\omega^2) + p\omega\cos(\theta)(2kp_0 - p\omega\cos(\theta)) + p^2(k^2 - \omega^2)\sin^2(\theta) = 0 \ . \quad (2.10)$$

This can be expanded,

$$k^4 + \omega^4 - 2\omega^2k^2 + p^2k^2\sin^2(\theta) - p^2\omega^2\sin^2(\theta) \quad (2.11)$$
$$= p_0^2k^2 - 2p_0kp\omega\cos(\theta) + p^2\omega^2\cos^2(\theta) \ . \quad (2.12)$$

Simplifying (2.11) gives,

$$(\omega^2 - k^2)^2 - (\omega^2 - k^2)p^2\sin^2(\theta) = (p_0k - p\omega\cos(\theta))^2 \ . \quad (2.13)$$

Rearranging (2.13) gives a dispersion relation of the form [25],

$$\omega^2 - k^2 = \pm(p_0k - p\omega\cos(\theta))\left[1 - \frac{p^2\sin^2(\theta)}{\omega^2 - k^2}\right]^{-\frac{1}{2}} \ . \quad (2.14)$$

This dispersion relation is noticeably different to the usual dispersion relation for electrodynamics in a vacuum. This can be expanded in terms of p_α. The expansion has the form,

$$k = \omega + p_0a + pb + O(p^2) \ . \quad (2.15)$$

squaring this gives,

$$k^2 = \omega^2 + 2\omega(p_0a + pb) + O(p^2) \ . \quad (2.16)$$

It is possible to infer from (2.14) and (2.16) that

$$2\omega(p_0a + pb) + O(p^2) = \mp(p_0k - p\omega\cos(\theta))(1 + O(p)) \ . \quad (2.17)$$

Substituting the expression in (2.15) in for k gives,

$$2\omega(p_0a + pb) + O(p^2) = \mp(p_0\omega - p\omega\cos(\theta) + O(p^2))(1 + O(p)) \ . \quad (2.18)$$

If higher order terms are neglected then $a = \mp\frac{1}{2}$ and $b = \pm\frac{1}{2}\cos(\theta)$. The expanded dispersion relation is therefore,

$$k = \omega \mp \frac{1}{2}(p_0 - p\cos(\theta)) \ , \quad (2.19)$$

which can be written as $k = n\omega$ where the refractive index is,

$$n = 1 \mp \frac{1}{2\omega}(p_0 - p\cos(\theta)) \ . \quad (2.20)$$

We can define a set of basis functions for linearly polarized light ϵ_x and ϵ_y. These basis functions represented in terms of normalized Jones vectors are

$$\epsilon_x = \begin{pmatrix} 1 \\ 0 \\ 0 \end{pmatrix} , \qquad \epsilon_y = \begin{pmatrix} 0 \\ 1 \\ 0 \end{pmatrix} . \tag{2.21}$$

This basis represents the horizontal and vertical components of the linear polarization. We can introduce circular polarization basis functions ϵ_L and ϵ_R. The normalized Jones vector representation of these basis functions is

$$\epsilon_L = \frac{1}{\sqrt{2}} \begin{pmatrix} 1 \\ +i \\ 0 \end{pmatrix} , \qquad \epsilon_R = \frac{1}{\sqrt{2}} \begin{pmatrix} 1 \\ -i \\ 0 \end{pmatrix} . \tag{2.22}$$

These two sets of basis functions are easily related so that,

$$\epsilon_{L/R} = \frac{1}{\sqrt{2}} \left(\epsilon_x \pm i\epsilon_y)\right) \tag{2.23}$$

As the linear polarization basis can be expressed as linear combinations of the circular polarization basis, any linearly polarised photon state can be written as a linear combination of right-handed and left-handed circularly polarised photon states. The linearly polarised photon undergoes a birefringent rotation if there is a change in phase between the two circularly polarised photon states. The rotation angle α is given as $\alpha = \frac{1}{2}(\xi_L - \xi_R)$, where ξ_L and ξ_R are the phases of the left-handed and right-handed states respectively. It is also worth noting that the $-$ and the $+$ in (2.19) correspond respectively to the right-handed, and left-handed polarisation states. The phase change of a photon traveling a path length L is kL. The rotation angle of the photon is therefore,

$$\alpha = \frac{1}{2}(p_0 - p\cos(\theta))L \, , \tag{2.24}$$

as predicted in [25].

In order to see how this modification is Lorentz-violating note that under the gauge transformation $\Delta A_\mu = \partial_\mu \chi$ the Chern-Simons Lagrangian becomes $\Delta \mathcal{L}_{CS} = \frac{1}{4}\chi \tilde{F}^{\mu\nu} (\partial_\mu p_\nu - \partial_\nu p_\mu)$. For the Lagrangian to be gauge invariant $\partial_\mu p_\nu - \partial_\nu p_\mu$ must vanish. This will occur in all frames in flat spacetime if there is a frame in which $\partial_\mu p_\nu = 0$. This requires p^μ to be a constant four-vector. This is where the Lorentz violation occurs as the prescence of a constant four-vector coupled to observable fields picks out a prefered direction in spacetime. The Lorentz symmetry is also violated in curved spacetime. The p_μ vector picks out a prefered coordinate frame. In this frame $\partial_\mu p_\nu = 0$. So, in any frame $\partial_\mu p_\nu - \partial_\nu p_\mu = \nabla_\mu p_\nu - \nabla_\nu p_\mu = 0$. However, the four-vector p^μ is still an arbitrary four-vector with no physical meaning. This modification must be treated slightly differently in order to

see how such rotations might arise in real physical settings.

2.2.2 Coupling of pseudo-scalar fields to electrodynamics

An equivalent way to formulate a Lorentz violating modification to modify electrodynamics is by writing the Chern-Simons Lagrangian term is in terms of a pseudo scalar field ϕ. It is possible to interpret this pseudo scalar field as being some theoretically predicted physical field that couples to the gauge field such as quintessence field or the field for an axion like particle. The Chern-Simons like term in this case is

$$\mathcal{L}_{CS} = -\frac{\beta\phi}{2M} F^{\mu\nu}\tilde{F}_{\mu\nu} \ . \tag{2.25}$$

Here, M has dimensions of mass and represents the energy scales that were integrated out in order to work in this low energy regime, and β is a dimensionless coupling term [27]. The Euler-Lagrange equations for the modified Lagrangian are,

$$0 = \frac{\partial\mathcal{L}_{EM}}{\partial A^b} + \frac{\partial\mathcal{L}_{CS}}{\partial A^b} - \partial^a\left(\frac{\partial\mathcal{L}_{EM}}{\partial(\partial^a A^b)}\right) - \partial^a\left(\frac{\partial\mathcal{L}_{CS}}{\partial(\partial^a A^b)}\right) \ . \tag{2.26}$$

The first and second terms are zero. The third and fourth term are more interesting, with the third term taking the form,

$$-\frac{1}{4}\partial^a\left(\frac{\partial(F^{\mu\nu}\eta_{\mu\sigma}\eta_{\nu\rho}F^{\sigma\rho})}{\partial(\partial^a A^b)}\right) = \partial^a F_{ba} \ , \tag{2.27}$$

and the fourth term taking the form,

$$-\frac{\beta}{4M}\partial^a\left(\frac{\partial(\phi F^{\mu\nu}\epsilon_{\mu\nu\sigma\rho}F^{\sigma\rho})}{\partial(\partial^a A^b)}\right) = -\frac{\beta\phi}{M}\epsilon_{ab\sigma\rho}\partial^a F^{\sigma\rho} - \frac{\beta}{M}\epsilon_{ab\sigma\rho}F^{\sigma\rho}\partial^a\phi \ . \tag{2.28}$$

However, $\epsilon_{ab\sigma\rho}\partial^a F^{\sigma\rho}$ can be written as $\partial^{[b}F^{\sigma\rho]}$ which is zero. Therefore, the resulting equations are

$$\partial^a F_{ba} + \frac{\beta}{M}\epsilon_{b\sigma\rho a}F^{\sigma\rho}\partial^a\phi = 0 \ . \tag{2.29}$$

The vanishing anti-symmetric term $\epsilon_{ab\sigma\rho}\partial^a F^{\sigma\rho}$, representing the homogeneous part of the relativistic Maxwell's equations, can be conveniently expressed as the derivative of the dual of the electromagnetic tensor so that,

$$\partial^a\tilde{F}_{ab} = 0 \ . \tag{2.30}$$

As $E^i = -F^{0i}$ and $B^i = -\epsilon^{ijk}F_{jk}$, equations (2.29) and (2.30) become

$$\begin{aligned} \boldsymbol{\nabla}\cdot\mathbf{B} &= 0\ , \\ \partial_t\mathbf{B} + \boldsymbol{\nabla}\times\mathbf{E} &= 0\ , \\ \boldsymbol{\nabla}\cdot\mathbf{E} - \frac{\beta}{M}\mathbf{B}\cdot\boldsymbol{\nabla}\phi &= 0\ , \\ \boldsymbol{\nabla}\times\mathbf{B} - \partial_t\mathbf{E} + \frac{\beta}{M}\left(\mathbf{E}\times\boldsymbol{\nabla}\phi - \mathbf{B}\,\partial_t\phi\right) &= 0\ . \end{aligned} \tag{2.31}$$

If ϕ is uniform in space and we choose plane wave solutions for **B** and **E** then the final equation in (2.31) becomes

$$i\mathbf{k}\times\mathbf{B_0} + i\omega\mathbf{E_0} = \frac{\beta}{M}\mathbf{B_0}\,\partial_t\phi\ . \tag{2.32}$$

It is possible to infer from this that the presence of the changing pseudo-scalar is inducing a change in the electric field in the direction of the magnetic field [42]. It is, however, possible to go further, and calculate a modified dispersion relation. First, the cross product of **k** and equation 2.32 is taken. By using the identity for the vector triple product, and using the first and second equation in (2.31) this cross product can be written as

$$(\omega^2 - k^2)\mathbf{B_0} + i\frac{\beta}{M}\mathbf{k}\times\mathbf{B_0}\,\partial_t\phi = 0\ . \tag{2.33}$$

This derivation is similar to that presented in the previous subsection. However, here we choose to approach this in an alternative way in order to more clearly demonstrate the effect of this interaction with the left and right handed circular polarization states. Note that linearly polarized light is composed of a superposition of the two circular polarization states. These polarisation states can be represented explicitly by the normalised Jones vectors. For the right handed circular polarisation,

$$\mathbf{B_0} = \frac{B_0}{\sqrt{2}}\begin{pmatrix} 1 \\ -i \\ 0 \end{pmatrix}\ . \tag{2.34}$$

To consider what will happen to right hand circular polarized modes in this modified regime we insert this Jones vector into equation (2.33),

$$\left(\omega^2 - k^2\right)B_0\begin{pmatrix} 1 \\ -i \\ 0 \end{pmatrix} = \frac{\beta}{M}k\,\partial_t\phi B_0\begin{pmatrix} 1 \\ -i \\ 0 \end{pmatrix}\ . \tag{2.35}$$

The Jones vector for the left handed circular polarisation is the same, except there is a positive i. Inserting, this into equation (2.33) gives,

$$\left(\omega^2 - k^2\right)B_0\begin{pmatrix} 1 \\ i \\ 0 \end{pmatrix} = -\frac{\beta}{M}k\,\partial_t\phi B_0\begin{pmatrix} 1 \\ i \\ 0 \end{pmatrix}\ . \tag{2.36}$$

From (2.34) and (2.36) it is possible to infer that,

$$\omega^2 - k^2 = \pm\frac{\beta}{M} k\, \partial_t\phi \ , \tag{2.37}$$

where now it is more clear that the + and - respectively refer to the right and left handed circular polarisation states. Here, $k = |\mathbf{k}|$. A more intuitive picture is found when the dispersion relationship is expanded in terms of $\partial_t\phi$,

$$\omega - k = \pm\frac{\beta}{M} a\, \partial_t\phi + O((\partial_t\phi)^2) \ , \tag{2.38}$$

where a is an unknown expansion coefficient. Rearranging (2.38) and squaring the expression gives

$$\omega^2 = k^2 \pm 2k\left(\frac{\beta}{M} a\, \partial_t\phi\right) + O((\partial_t\phi)^2) \ . \tag{2.39}$$

Neglecting higher order terms it is possible to infer from (2.37) and (2.39) that $2k\left(\frac{\beta}{M} a\, \partial_t\phi\right) = \frac{\beta}{M} k\partial_t\phi$. Therefore, given that $a = \frac{1}{2}$, the expansion of the dispersion relation to first order is,

$$k = \omega \mp \frac{\beta}{2M}\partial_t\phi \ . \tag{2.40}$$

This can be rewritten in the more familiar $k = n\omega$ form of the dispersion relation. Here, the refractive index n has the form,

$$n = 1 \mp \frac{\beta}{2\omega M}\partial_t\phi \ . \tag{2.41}$$

As before, the linearly polarised photon state can be treated as a superposition of right handed and left handed circularly polarised photon states. Therefore, the rotation angle of the linearly polarised photon in terms of the changing scalar field is [43],

$$\alpha = \frac{\beta}{M}\int \frac{\partial\phi}{\partial\eta} d\eta \ , \tag{2.42}$$

where the numerical factor of $\frac{1}{2}$ is absorbed into the arbitrary coupling β and the path length for the photon is $L = \int a d\eta$. Here η represents conformal time, and a is the cosmological scale factor. This rotation would effect the light from the CMB uniformly across the whole sky. The linear polarisation modes of the CMB would be rotated completely isotropically by angle α. It is entirely possible that the scalar field may not be spacially uniform. If that is the case then equation (2.42) instead becomes [44]

$$\alpha(\hat{\mathbf{n}}) = \frac{\beta}{M}\int d\eta \left(\frac{\partial}{\partial\eta} + \hat{\mathbf{n}}\cdot\boldsymbol{\nabla}\right)\phi \ . \tag{2.43}$$

In this case the rotation angle would not be uniform across the sky; there would be an anisotropy in the rotation angle of linearly polarised light traveling cosmological distances.

2.3 Axion-Photon Mixing

2.3.1 Axions and photons in strong magnetic fields

It is possible for photon-axion mixing to occur for photons traveling in the presence of a strong magnetic field $\mathbf{B}_e$ as shown in [45]. The equations of motion for axion-photon interactions are needed in order to understand how this mixing takes place. The Lagrangian that will be useful in deriving the equations of motion is as follows:

$$\mathcal{L} = -\frac{1}{4}F_{\mu\nu}F^{\mu\nu} + \frac{1}{2}\left(\partial_\mu a \partial^\mu a - m_a^2 a^2\right) + \frac{1}{4M}F_{\mu\nu}\tilde{F}^{\mu\nu}a + \frac{\alpha^2}{90m_e^4}\left[\left(F_{\mu\nu}F^{\mu\nu}\right)^2 + \frac{7}{4}\left(F_{\mu\nu}\tilde{F}^{\mu\nu}\right)^2\right] , \tag{2.44}$$

where the first two terms are the normal Lagrangians for electromagnetism and scalar fields respectively, the third term is an interaction term between the axions and the photons, and the fourth term is a photon self-interaction term. Here, a is used to represent the pseudo-scalar axion field and m_a represents the mass of this field. The fourth term only holds in the limit where photon frequencies are much smaller than the electron mass m_e. Perturbing the Lagrangian leads to an equation of motion for the axion,

$$-\partial_\mu\partial^\mu a - m_a^2 + \frac{1}{4M}F_{\mu\nu}\tilde{F}^{\mu\nu} = 0 , \tag{2.45}$$

and for a propagating photon,

$$-\partial^\alpha F_{\alpha\beta} + \frac{1}{2M}\epsilon^{\alpha\beta\rho\sigma}F_{\rho\sigma}\partial_\alpha a + \frac{4\alpha^2}{45m_e^4}\partial^\alpha\left(F_{\alpha\beta}F_{\mu\nu}F^{\mu\nu}\right) + \frac{7\alpha^2}{45m_e^4}\partial_\alpha\left(\tilde{F}_{\alpha\beta}F_{\mu\nu}\tilde{F}^{\mu\nu}\right) = 0 . \tag{2.46}$$

The photon can be taken to be propagating in the z direction with two linear photon polarisation states, A_x and A_y. The chosen convention is that the polarisation vectors point in the direction of the electric field. The y axis can be chosen such that the projection of the strong, constant magnetic field $\mathbf{B}_e$ that is perpendicular to the z axis points along the y axis. if this is the case then $B_x = 0$ and $B_y = |\mathbf{B}_t| = B_e \sin\theta$. So, $A_y = A_\parallel$ and $A_x = A_\perp$, where the notation $\parallel$ and $\perp$ represent polarisations parallel and perpendicular to the external field respectively [46]. A new term ξ is defined as follows:

$$\xi = \frac{\alpha}{45\pi}\left(\frac{B_e}{B_{crit}}\right)^2 , \tag{2.47}$$

where $B_{crit} = \frac{m_e^2}{e} = 4.41 \times 10^{13}$G [45]. Note the units used are natural, rationalized electromagnetic units (or Lorentz-Heaviside units). In these units $h = c = 1$ and $\alpha = \frac{e^2}{4\pi} \approx \frac{1}{137}$.

The $\perp$ photon state is even under CP transformations, whereas the $\parallel$ photon state is odd under CP transformation. Morevover, B_e is invariant under CP interactions so the equations of motion should be CP-conserving. As the axion plane wave states are odd it only mixes with the $A_\parallel$ photon state. If the equation of motion for the axion in (2.45) is restricted using the mixing conditions, and the choice that the magnetic field must point along the y-axis then the equation of motion becomes

$$\omega^2 a + \partial_z^2 a - m_a^2 a + \frac{B_y \omega}{M} A_\parallel = 0 \, . \tag{2.48}$$

In a similar way constraints can be applied to equation (2.3.1). It is required that the external magnetic field acts along the y-axis, moreover the perpendicular photon polarisation mode $A_\perp$ does not mix with the axion field. With these constraints in place the equations of motion for the perpendicular photon modes reduce to

$$\left(\omega^2 + \partial_z^2\right) A_\perp + \frac{4\alpha e^2 \omega^2}{45\pi m_e^4} B_y^2 A_\perp = 0 \, . \tag{2.49}$$

Similarly, given that the axion and parallel photon modes do mix, it is found that

$$\left(\omega^2 + \partial_z^2\right) A_\parallel + \frac{7\alpha e^2 \omega^2}{45\pi m_e^4} B_y^2 A_\parallel + \frac{B_y \omega}{M} a = 0 \, . \tag{2.50}$$

The wave equation is

$$\left[\omega^2 + \partial_z^2 + \begin{pmatrix} Q_\perp & 0 & 0 \\ 0 & Q_\parallel & \frac{B_y\omega}{M} \\ 0 & \frac{B_y\omega}{M} & -m_a^2 \end{pmatrix}\right] \begin{pmatrix} A_\perp \\ A_\parallel \\ a \end{pmatrix} = 0 \, , \tag{2.51}$$

where using the expression for ξ in (2.47)

$$Q_\perp = 4\omega^2 \xi \sin^2\theta, \quad Q_\parallel = 7\omega^2 \xi \sin^2\theta \, . \tag{2.52}$$

A useful approximation can be made using the dispersion relation for propagating light. A dispersion relation has the form $k = n\omega$. However, in this case $n \approx 1$, leading to the approximation $k = \omega$. Moreover, as $\omega^2 + \partial_z^2 = (\omega + i\partial_z)(\omega - i\partial_z) = (\omega + k)(\omega - i\partial_z)$, the approximation can be applied so that $\omega^2 + \partial_z^2 = 2\omega(\omega - i\partial_z)$. Equation (2.51) can be rewritten using this approximation, and both sides of the equation can be divided by 2ω leading to the following new equations of motion

$$\left[\omega - i\partial_z + \begin{pmatrix} \Delta_\perp & 0 & 0 \\ 0 & \Delta_\parallel & \Delta_M \\ 0 & \Delta_M & \Delta_a \end{pmatrix}\right] \begin{pmatrix} A_\perp \\ A_\parallel \\ a \end{pmatrix} = 0 \, . \tag{2.53}$$

The new Δ_i components have been defined as

$$\begin{aligned}
\Delta_M &= \frac{B_e}{2M}\sin\theta \ , \\
\Delta_\perp &= 2\omega\xi\sin^2\theta \ , \\
\Delta_\parallel &= \frac{7}{2}\omega\xi\sin^2\theta \ , \\
\Delta_a &= -\frac{m_a^2}{2\omega} \ ,
\end{aligned}$$

where the diagonal components represent the difference in momentum between the different modes, and the counterparts to those modes if no magnetic field was present. The refractive indices, as given by the dispersion relation $k_i = n_i\omega$, are $n_i = 1 + \frac{\Delta_i}{\omega}$.

To see how this equation of motion leads to mixing between the parallel photon modes and the axion the lower right hand quadrant of (2.53) must be diagonolised. This is done through a rotation R which, when applied to the $A_\parallel$ and a fields, leads to mixed $A'_\parallel$ and a' fields,

$$\begin{pmatrix} A'_\parallel \\ a' \end{pmatrix} = \begin{pmatrix} \cos\vartheta & \sin\vartheta \\ -\sin\vartheta & \cos\vartheta \end{pmatrix} \begin{pmatrix} A_\parallel \\ a \end{pmatrix} \ . \tag{2.54}$$

Considering the lower quadrant the equation of motion is

$$\left[\omega - i\partial_z + M\right] \begin{pmatrix} A_\parallel \\ a \end{pmatrix} = 0 \ , \tag{2.55}$$

where

$$M = \begin{pmatrix} \Delta_\parallel & \Delta_M \\ \Delta_M & \Delta_a \end{pmatrix} \ . \tag{2.56}$$

The rotation R is applied to the equations of motion,

$$R\left[\omega - i\partial_z + M\right] \begin{pmatrix} A_\parallel \\ a \end{pmatrix} = 0 \ , \tag{2.57}$$

which can be written as

$$R\left[\omega - i\partial_z + M\right] R^T R \begin{pmatrix} A_\parallel \\ a \end{pmatrix} = 0 \ . \tag{2.58}$$

This is allowed because the rotation matrix is an orthogonal matrix so $R^T R = R R^T = I$. The rotation matrix on the right hand side rotates $A_\parallel$ and a into the primed fields, giving the

following equations of motion for the primed fields

$$R\left[\omega - i\partial_z + M\right] R^T \begin{pmatrix} A'_\parallel \\ a' \end{pmatrix} = 0 \ . \tag{2.59}$$

The rotation matrix and its transpose have no effect on the first two terms, however they act to diagonalise the matrix M. Explicitly calculating RMR^T gives

$$\begin{pmatrix} \cos\vartheta & \sin\vartheta \\ -\sin\vartheta & \cos\vartheta \end{pmatrix} \begin{pmatrix} \Delta_\parallel & \Delta_M \\ \Delta_M & \Delta_a \end{pmatrix} \begin{pmatrix} \cos\vartheta & -\sin\vartheta \\ \sin\vartheta & \cos\vartheta \end{pmatrix} =$$
$$\begin{pmatrix} \Delta_\parallel \cos^2\vartheta + \Delta_a \sin^2\vartheta + \Delta_M \sin 2\vartheta & \frac{1}{2}\Delta_a \sin 2\vartheta - \frac{1}{2}\Delta_\parallel \sin 2\vartheta + \Delta_M \cos 2\vartheta \\ \frac{1}{2}\Delta_a \sin 2\vartheta - \frac{1}{2}\Delta_\parallel \sin 2\vartheta + \Delta_M \cos 2\vartheta & \Delta_\parallel \sin^2\vartheta + \Delta_a \cos^2\vartheta - \Delta_M \sin 2\vartheta \end{pmatrix} . \tag{2.60}$$

As this operation must diagonalise M it is necessary to set the off diagonal components to zero to find the mixing angle,

$$-\frac{1}{2}\Delta_\parallel \sin 2\vartheta + \frac{1}{2}\Delta_a \sin 2\vartheta + \Delta_M \cos 2\vartheta = 0 \ . \tag{2.61}$$

Rearanging this expression leads to

$$\frac{1}{2}\tan 2\vartheta = \frac{\Delta_M}{\Delta_\parallel - \Delta_a} \ , \tag{2.62}$$

which characterizes the strength of the mixing. Now, it is necessary to simplify the diagonal terms, writing them entirely in terms of $\Delta_\parallel$, Δ_a, and ϑ. The upper left hand term in the diagonalised matrix in (2.3.1) will be labeled $\Delta'_\parallel$, as it is the matrix element that acts on $A'_\parallel$. Equation (2.62) is used to substitute for Δ_M in $\Delta'_\parallel$,

$$\Delta'_\parallel = \Delta_\parallel \cos^2\vartheta + \Delta_a \sin^2\vartheta + \frac{1}{2}\tan 2\vartheta(\Delta_\parallel - \Delta_a)\sin 2\vartheta \ . \tag{2.63}$$

This is rewritten as

$$\Delta'_\parallel = \Delta_\parallel \cos^2\vartheta + \Delta_a \sin^2\vartheta + (\Delta_\parallel - \Delta_a)\frac{1 - cos^2 2\vartheta}{2\cos 2\vartheta} \ , \tag{2.64}$$

which is the same as

$$\Delta'_\parallel = \Delta_\parallel \cos^2\vartheta + \Delta_a \sin^2\vartheta + \frac{(\Delta_\parallel - \Delta_a)}{2\cos 2\vartheta} - \frac{1}{2}(\Delta_\parallel - \Delta_a)\cos 2\vartheta \ . \tag{2.65}$$

Now, using the trigonometric identity for $\cos 2\vartheta$, (2.65) can be expanded to give

$$\Delta'_\parallel = \Delta_\parallel \cos^2\vartheta + \Delta_a \sin^2\vartheta + \frac{(\Delta_\parallel - \Delta_a)}{2\cos 2\vartheta} + \frac{\Delta_\parallel}{2} - \Delta_\parallel \cos^2\vartheta + \frac{\Delta_a}{2} - \Delta_a \sin^2\vartheta \ . \tag{2.66}$$

Therefore, $\Delta'_{\parallel}$ simplifies to the following expression,

$$\Delta'_{\parallel} = \frac{(\Delta_{\parallel} + \Delta_a)}{2} + \frac{(\Delta_{\parallel} - \Delta_a)}{2\cos 2\vartheta} \,. \tag{2.67}$$

In a similar way, the bottom right expression from the diagonalised matrix can be relabled as Δ'_a and simplified giving

$$\Delta'_a = \frac{(\Delta_{\parallel} + \Delta_a)}{2} - \frac{(\Delta_{\parallel} - \Delta_a)}{2\cos 2\vartheta} \,. \tag{2.68}$$

The equation of motion for the mixed states is then

$$\left[\omega - i\partial_z + \begin{pmatrix} \Delta'_{\parallel} & 0 \\ 0 & \Delta'_a \end{pmatrix}\right] \begin{pmatrix} A'_{\parallel} \\ a' \end{pmatrix} = 0 \,. \tag{2.69}$$

Consider the beam of photons propagating in the z direction. It is possible to simplify the description by taking all modes to be measured with respect to the phase of the unmixed $A_{\parallel}$ mode. If this is the case then the perpendicular mode propagates as follows:

$$A_{\perp}(z) = e^{-i(\Delta_{\perp} - \Delta_{\parallel})z} A_{\perp}(0) \,. \tag{2.70}$$

The parallel and axion mixing modes must be treated slightly differently. They propagate as

$$\begin{pmatrix} A_{\parallel}(z) \\ a(z) \end{pmatrix} = \mathcal{M}(z) \begin{pmatrix} A_{\parallel}(0) \\ a(0) \end{pmatrix} \,. \tag{2.71}$$

Here $\mathcal{M}(z)$ is

$$\mathcal{M}(z) = \begin{pmatrix} \cos\vartheta & -\sin\vartheta \\ \sin\vartheta & \cos\vartheta \end{pmatrix} \begin{pmatrix} e^{-i\left(\Delta'_{\parallel} - \Delta_{\parallel}\right)z} & 0 \\ 0 & e^{-i(\Delta'_a - \Delta_{\parallel})z} \end{pmatrix} \begin{pmatrix} \cos\vartheta & \sin\vartheta \\ -\sin\vartheta & \cos\vartheta \end{pmatrix} \,. \tag{2.72}$$

It is easy to see why this is the case when the mixing matrix $\mathcal{M}(z)$ is applied explicitly in equation (2.71),

$$\begin{pmatrix} A_{\parallel}(z) \\ a(z) \end{pmatrix} = \begin{pmatrix} \cos\vartheta & -\sin\vartheta \\ \sin\vartheta & \cos\vartheta \end{pmatrix} \begin{pmatrix} A'_{\parallel}(0) e^{-i\left(\Delta'_{\parallel} - \Delta_{\parallel}\right)z} \\ a'(0) e^{-i(\Delta'_a - \Delta_{\parallel})z} \,. \end{pmatrix} \tag{2.73}$$

From this it follows that

$$\begin{pmatrix} A_{\parallel}(z) \\ a(z) \end{pmatrix} = \begin{pmatrix} A_{\parallel}(0) e^{-i\left(\Delta'_{\parallel} - \Delta_{\parallel}\right)z} \\ a(0) e^{-i(\Delta'_a - \Delta_{\parallel})z} \end{pmatrix} \tag{2.74}$$

2.3.2 Weak mixing and birefringence

In the case of a weak mixing, that is $\vartheta \ll 1$ the mixing matrix can be expanded to second order

$$\mathcal{M}(z) = \mathcal{M}_0(z) + \vartheta\mathcal{M}_1(z) + \vartheta^2\mathcal{M}_2(z) \; . \tag{2.75}$$

It is easier if Δ_{osc} is defined as $\Delta_{\text{osc}} = \Delta_{\parallel} - \Delta_a$ and the term $\zeta = \Delta_{\text{osc}} z$ is defined. By performing the expansion explicitly an expression for $\mathcal{M}(z)$ is found

$$\begin{aligned} \mathcal{M}_0(\zeta) = \begin{pmatrix} 1 & 0 \\ 0 & e^{i\zeta} \end{pmatrix}, \qquad \mathcal{M}_1(\zeta) = \left(1 - e^{i\zeta}\right) \begin{pmatrix} 0 & 1 \\ 1 & 0 \end{pmatrix}, \\ \mathcal{M}_2(\zeta) = \begin{pmatrix} -i\zeta - \left(1 - e^{i\zeta}\right) & 0 \\ 0 & \left(1 - e^{i\zeta}\right) + i\zeta e^{i\zeta} \end{pmatrix} . \end{aligned} \tag{2.76}$$

In this case the birefringence effect arises due to the magnetic field if the photons are propagating along the direction of the field lines and no axions are present. This is the Faraday effect and is due to a phase shift between the $\parallel$ and $\perp$ polarisation modes. This phase shift is given as $\varphi(z) = (\Delta_{\parallel} - \Delta_{\perp})z$. However, in the presence of the axion field there is an extra contribution to the rotation of the angle of plane polarisation for the photons. This extra contribution is given by the imaginary part of the upper left hand term in the mixing matrix $\mathcal{M}_{(11)}(z)$ and is

$$\varphi_a(z) = \text{Im}\mathcal{M}_{(11)}(z) = \vartheta^2(\Delta_{\text{osc}} z - \sin \Delta_{\text{osc}} z) \; . \tag{2.77}$$

Moreover, there is a reduction in the magnitude of $A_{\parallel}$ due to the conversion of photons in to axions. Assuming no axions are present to begin with this reduction is by a factor of $1 - \epsilon(z)$ where

$$\epsilon(z) = 1 - \text{Re}\mathcal{M}_{(11)}(z) = 2\vartheta^2 \sin^2\left(\frac{\Delta_{\text{osc}} z}{2}\right) \; . \tag{2.78}$$

The rotation of the angle of plane polarisation is then $\epsilon(z)/2$ if it is assumed the angle of plane polarisation is initially at an angle of 45° to the external field $\mathbf{B}_e$. Therefore, there is a birefringence effect due to the magnetic field and the conversion of photons into axions.

2.4 Observing Birefringence in Cross Correlations in the CMB

If these modifications of electrodynamics are correct and there is an induced uniform rotation of linearly polarised light then it will have an effect on the linearly polarised light of the CMB. Such an effect would produce a non zero signal in the C_l^{TB} and C_l^{EB} cross correlation power spectra. These cross correlation moments are, as will be shown below, zero if no birefringence effect is present. So, in order to measure the birefringence angle the cross correlation should be measured.

2.4.1 E and B modes

In order to understand how to measure the cross correlations between temperature and B modes, and between E and B modes it is first important to understand where the cross correlations come from. It is also important to understand why C_l^{EB} and C_l^{TB} are zero when there is no birefringence, and what the E and B mode signals are. Understanding the latter two points provides insight into why a rotation of the linear polarised light from the CMB leads to a non-zero cross correlation signal. The origin of the E and B modes and the null value of C_l^{EB} and C_l^{TB} is explained in detail by Kamionkowski, Kosowsky, and Stebbins in [9]. Here, we summarize their work and review some of the concepts discussed in Chapter 1.

The polarisation of light can be described by the set of Stokes parameters,

$$\begin{aligned} I &\equiv \langle a_x^2 \rangle + \langle a_y^2 \rangle \ , \\ Q &\equiv \langle a_x^2 \rangle - \langle a_y^2 \rangle \ , \\ U &\equiv \langle 2a_x a_y \cos\left(\theta_x - \theta_y\right) \rangle \ , \\ V &\equiv \langle 2a_x a_y \sin\left(\theta_x - \theta_y\right) \rangle \ , \end{aligned} \tag{2.79}$$

where a_x and a_y are the x and y components of the amplitude of the electric field of an electromagnetic wave that propagates in the z direction. The I Stokes parameter indicates the radiation intensity, the Q and U parameters describe linear polarisation modes, and the V parameter describes circular polarisation modes. As the Compton scattering process that produces the polarisation in the CMB does not produce circular polarisation the V parameter is not important. The Q and U parameters refer to modes that are orthogonal, however they are dependent on the choice of coordinate system. From the Q and U modes it is possible to construct coordinate independent E and B modes. First, it must be noted that Q and U transform as independent components of a symmetric, trace free tensor. This can be seen by noting that under a rotation of angle ϑ the transformation is given as

$$\begin{aligned} Q' &= Q\cos 2\vartheta + U\sin 2\vartheta \ , \\ U' &= -Q\sin 2\vartheta + U\cos 2\vartheta \ . \end{aligned} \tag{2.80}$$

It is possible to write down this symmetric trace free polarisation tensor $\mathcal{P}_{ab}(\hat{\mathbf{n}})$, which fully describes the linear polarisation states. For a full sky map of the CMB polarisation the polarisation tensor in spherical coordinates is

$$\mathcal{P}_{ab}(\hat{\mathbf{n}}) = \frac{1}{2}\begin{pmatrix} Q(\hat{\mathbf{n}}) & -U(\hat{\mathbf{n}})\sin\theta \\ -U(\hat{\mathbf{n}})\sin\theta & -Q(\hat{\mathbf{n}})\sin^2\theta \end{pmatrix} \ , \tag{2.81}$$

and the metric for a 2-sphere S^2 is

$$g_{ab} = \begin{pmatrix} 1 & 0 \\ 0 & \sin^2\theta \end{pmatrix} . \tag{2.82}$$

In analogy to the expansion of the temperature contrast into a set of orthonormal spherical harmonics, the polarisation tensor can be expanded into a complete set of orthonormal basis functions. The expansion that is appropriate for a tensor that is symmetric, trace free and on a 2-sphere is

$$\frac{\mathcal{P}_{ab}(\hat{\mathbf{n}})}{T_0} = \sum_{l=2}^{\infty} \sum_{m=-l}^{l} \left[a^E_{(lm)} Y^E_{(lm)ab}(\hat{\mathbf{n}}) + a^B_{(lm)} Y^B_{(lm)ab}(\hat{\mathbf{n}}) \right] , \tag{2.83}$$

where T_0 is the statistical mean of the CMB temperature map.

The reason that there are two sets of basis functions, as opposed to the one set for the temperature contrast, is that any symmetric trace free tensor in two dimensions can be decomposed into a curl free part, $A_{;ab} - \frac{1}{2} g_{ab} A_{;c}{}^{c}$, and a curl containing part, $B_{;ac}\epsilon^{c}{}_{b} + B_{;bc}\epsilon^{c}{}_{a}$. Here A and B are scalar functions. Note that here semicolons, ";", are used in order to denote derivatives on S^2 rather than the covariant derivative in four dimensions [9]. As the spherical harmonics, Y_{lm}, form a complete basis of scalar functions on a 2-sphere it is possible to write the basis functions for the curl free part of the polarisation tensor as

$$Y^E_{(lm)ab} = N_l \left(Y_{(lm);ab} - \frac{1}{2} g_{ab} Y_{(lm);c}{}^{c} \right) , \tag{2.84}$$

and the curl containing part as

$$Y^B_{(lm)ab} = \frac{N_l}{2} \left(Y_{(lm);ac}\epsilon^{c}{}_{b} + Y_{(lm);bc}\epsilon^{c}{}_{a} \right) . \tag{2.85}$$

N_l is merely a normalization factor and is defined as

$$N_l \equiv \sqrt{\frac{2(l-2)!}{(l+2)!}} . \tag{2.86}$$

The parts of the decomposition of $\mathcal{P}_{ab}$ are labeled E and B in analogy to the electric and magnetic fields which are curl free and curl containing respectively. Now, the expansion coefficients are given as

$$\begin{aligned} a^E_{(lm)} &= \frac{1}{T_0} \int d\hat{\mathbf{n}} \mathcal{P}_{ab}(\hat{\mathbf{n}}) Y^{E\,ab\,*}_{(lm)}(\hat{\mathbf{n}}) , \\ a^B_{(lm)} &= \frac{1}{T_0} \int d\hat{\mathbf{n}} \mathcal{P}_{ab}(\hat{\mathbf{n}}) Y^{B\,ab\,*}_{(lm)}(\hat{\mathbf{n}}) . \end{aligned} \tag{2.87}$$

Using the explicit definition of the E and B basis functions, and differentiating by parts gives

the expansion coefficients as

$$\begin{aligned} a^E_{(lm)} &= \frac{N_l}{T_0}\int d\hat{\mathbf{n}} Y^*_{(lm)}(\hat{\mathbf{n}})\mathcal{P}_{ab}{}^{;ab}(\hat{\mathbf{n}}), \\ a^B_{(lm)} &= \frac{N_l}{T_0}\int d\hat{\mathbf{n}} Y^*_{(lm)}(\hat{\mathbf{n}})\mathcal{P}_{ab}{}^{;ac}(\hat{\mathbf{n}})\epsilon_c{}^b \ . \end{aligned} \tag{2.88}$$

Therefore, given the origin of the E and B mode decomposition it is possible to go on to calculate the value of the $C_l^{EB} = \left\langle a^E_{(lm)} a^{B*}_{(l'm')} \right\rangle$ and $C_l^{TB} = \left\langle a^T_{(lm)} a^{B*}_{(l'm')} \right\rangle$ cross correlations, and ultimately see that they are zero.

2.4.2 Calculating the cross correlations

In order to demonstrate that the C_l^{TB} and C_l^{EB} vanish they must be calculated for both scalar metric perturbations, and tensor perturbations separately. Starting with the scalar perturbations the Stokes parameters are expanded in terms of Legendre polynomials,

$$\begin{aligned} \left(\frac{Q(\mathbf{k},\hat{\mathbf{n}})}{T_0}\right)^2 &= \frac{1}{4}\sum_{j=0}^{\infty}(2j+1)P_j(\hat{\mathbf{k}}\cdot\hat{\mathbf{n}})\Delta^s_{Qj}(k)\cos 2\xi' \ , \\ \left(\frac{U(\mathbf{k},\hat{\mathbf{n}})}{T_0}\right)^2 &= \frac{1}{4}\sum_{j=0}^{\infty}(2j+1)P_j(\hat{\mathbf{k}}\cdot\hat{\mathbf{n}})\Delta^s_{Qj}(k)\sin 2\xi' \ , \end{aligned} \tag{2.89}$$

where Δ^s_{Qj} are the Legendre coefficients that correspond to the perturbation of the photon polarisation brightness distribution due to scalar metric perturbations. For a more detailed picture of this expansion see Kosowsky's work in [20]. Here, ξ' is the angle required to rotate the coordinate system for each k mode so that the k modes can be summed in a consistent way, as Q and U are coordinate dependent. The orientation of the coordinate system in the $\hat{\mathbf{n}}$ direction is different for each k mode. Therefore, ξ' is the angle required to rotate the coordinate system of the k modes so that they coincide with those for $\hat{\mathbf{n}}$, in order to ensure that they are consistent for the summation. The terms $Q(\mathbf{k},\hat{\mathbf{n}})$ and $U(\mathbf{k},\hat{\mathbf{n}})$ are just the Stokes parameters induced in the direction $\hat{\mathbf{n}}$ by a single $\mathbf{k}$ mode. The $\mathbf{k}$ mode is taken to be pointing in the $\hat{\mathbf{z}}$ direction, in which case ξ' can be chosen to be zero. Therefore,

$$\left(\frac{Q(\mathbf{k},\hat{\mathbf{n}})}{T_0}\right)^2 = \frac{1}{4}\sum_{j=0}^{\infty}(2j+1)P_j(\hat{\mathbf{k}}\cdot\hat{\mathbf{n}})\Delta^s_{Qj}(k) \ , \quad \frac{U(\mathbf{k},\hat{\mathbf{n}})}{T_0} = 0 \ . \tag{2.90}$$

By substituting (2.90) into the definition of the polarisation tensor in (2.81) $\mathcal{P}_{ab}(\mathbf{k},\hat{\mathbf{n}})$ can

be written as

$$\begin{aligned}\frac{\mathcal{P}_{ab}(\mathbf{k},\hat{\mathbf{n}})}{T_0} &= \frac{1}{8}\sum_{j=0}^{\infty}(2j+1)P_j(\hat{\mathbf{k}}\cdot\hat{\mathbf{n}})\Delta^s_{Qj}(k)\begin{pmatrix}1 & 0\\ 0 & -\sin^2\theta\end{pmatrix}\,,\\ &= \frac{1}{8}\sum_{j=0}^{\infty}(2j+1)\Delta^s_{Qj}(k)M_{(j)ab}(\hat{\mathbf{k}},\hat{\mathbf{n}})\,,\end{aligned} \tag{2.91}$$

where M_{ab} is defined such that

$$M^{ab}(\hat{\mathbf{k}}=\hat{\mathbf{z}},\hat{\mathbf{n}}) = P_j(\cos\theta)\begin{pmatrix}1 & 0\\ 0 & -\csc^2\theta\end{pmatrix}\,. \tag{2.92}$$

This expression for the polarisation tensor can be substituted into the expression for $a^B_{(lm)}$ in (2.88). This gives

$$a^{B,s}_{lm}(\mathbf{k}) = \frac{N_l}{8}\sum_{j=0}^{\infty}(2j+1)\Delta^s_{Qj}(k)\int d\hat{\mathbf{n}}Y^*_{(lm)}(\hat{\mathbf{n}})M^{ab}_{(j);ac}(\hat{\mathbf{n}})\epsilon^c{}_b\,. \tag{2.93}$$

Then $M^{ab}_{(j);ac}(\hat{\mathbf{n}})\epsilon^c{}_b$ can be calculated explicitly,

$$\begin{aligned}M^{ab}{}_{;ac}\epsilon^c{}_b &= \sin\theta\left(M^{\theta\phi}{}_{,\theta\theta}+M^{\phi\phi}{}_{,\phi\theta}\right)-\csc\theta\left(M^{\theta\theta}{}_{,\theta\phi}+M^{\phi\theta}{}_{,\phi\phi}\right)-\cot\theta\csc\theta M^{\theta\theta}{}_{,\phi}\\ &\quad+5\cos\theta M^{\theta\phi}{}_{,\theta}+3\cos\theta M^{\phi\phi}{}_{,\phi}+3(\cos\theta\cot\theta-\sin\theta)M^{\theta\phi}\,.\end{aligned} \tag{2.94}$$

Given the explicit form of $M^{ab}(\hat{\mathbf{k}}=\hat{\mathbf{z}},\hat{\mathbf{n}})$ in (2.92) it is clear that $M^{ab}{}_{;ac}\epsilon^c{}_b = 0$. Therefore $a^B_{(lm)} = 0$. So,

$$C^{XB}_l = \left\langle a^{X*}_{(lm)}a^B_{(lm)}\right\rangle = 0\,, \tag{2.95}$$

where $X\in\{T,E\}$.

Now, the cross correlation must be shown to be zero for the tensor modes. This is less trivial and involves calculating the expansion coefficients for the temperature and the E and B modes for both the $+$ and $\times$ tensor perturbation polarisation states. Starting with temperature and remembering that

$$a^T_{(lm)} = \frac{1}{T_0}\int d\hat{\mathbf{n}}\,T(\hat{\mathbf{n}})\,Y^*_{(lm)}(\hat{\mathbf{n}})\,. \tag{2.96}$$

For a $\mathbf{k}$ mode that points along the $\hat{\mathbf{z}}$ direction that is generated by the $+$ polarisation of the tensor metric perturbations, the contribution to the temperature anisotropy expanded in Legendre polynomials is

$$\frac{T(\mathbf{k},\hat{\mathbf{n}})}{T_0} = \frac{1}{4}\sum_j(2j+1)P_j(\hat{\mathbf{k}}\cdot\hat{\mathbf{n}})\sin^2\theta\cos2\phi\tilde{\Delta}^+_{Ij}(k)\,, \tag{2.97}$$

where $\tilde{\Delta}^+_{Ij}(k)$ are the Legendre coefficients corresponding to the perturbation of the photon brightness that is induced by the tensor mode $\mathbf{k}$. This is substituted into the definition of $a^T_{(lm)}$

to give

$$a^{T,+}_{(lm)}(\mathbf{k}) = \frac{1}{4}\sum_j (2j+1)\tilde{\Delta}^+_{Ij}(k)\int d\hat{\mathbf{n}}\, P_j(\hat{\mathbf{k}}\cdot\hat{\mathbf{n}})Y^*_{(lm)}(\hat{\mathbf{n}})\sin^2\theta\cos 2\phi\ . \tag{2.98}$$

It's possible to use the relation $P(\cos\theta) = \sqrt{\frac{4\pi}{2j+1}}Y_{j0}$ in (2.98) giving

$$a^{T,+}_{(lm)}(\mathbf{k}) = \frac{1}{4}\sum_j (2j+1)\tilde{\Delta}^+_{Ij}(k)\int d\hat{\mathbf{n}}\sqrt{\frac{4\pi}{2j+1}}Y_{(j0)}(\hat{\mathbf{n}})\sin^2\theta\cos 2\phi Y^*_{(lm)}(\hat{\mathbf{n}})\ . \tag{2.99}$$

Angular momentum raising and lowering operators can be employed in order to rewrite $\sin^2\theta\cos 2\phi Y_{(j0)}$ as

$$\begin{aligned}\sin^2\theta\cos 2\phi Y_{(j0)} = \frac{1}{2}\Bigg\{ &\left[\frac{(j+1)(j+2)(j+3)(j+4)}{(2j+1)(2j+3)^2(2j+5)}\right]^{\frac{1}{2}}\left(Y_{(j+2,2)}+Y_{(j+2,-2)}\right)\\ &-2\frac{\sqrt{j(j-1)(j+1)(j+2)}}{(2j-1)(2j+3)}\left(Y_{(j,2)}+Y_{(j,-2)}\right)\\ &+\left[\frac{j(j-1)(j-2)(j-3)}{(2j-3)(2j-1)^2(2j+1)}\right]^{\frac{1}{2}}\left(Y_{(j-2,2)}+Y_{(j-2,-2)}\right)\Bigg\}\ .\end{aligned} \tag{2.100}$$

Now, this can be substituted into (2.99) giving

$$\begin{aligned}a^{T,+}_{(lm)}(\mathbf{k}) = \frac{1}{8}\left(\delta_{m,2}+\delta_{m,-2}\right)\sum_j (2j+1)\sqrt{\frac{4\pi}{2j+1}}\tilde{\Delta}^+_{Ij}(k)\\ \times\Bigg\{\left[\frac{(j+1)(j+2)(j+3)(j+4)}{(2j+1)(2j+3)^2(2j+5)}\right]^{\frac{1}{2}}\delta_{l,j+2} - 2\frac{\sqrt{j(j-1)(j+1)(j+2)}}{(2j-1)(2j+3)}\delta_{l,j}\\ +\left[\frac{j(j-1)(j-2)(j-3)}{(2j-3)(2j-1)^2(2j+1)}\right]^{\frac{1}{2}}\delta_{l,j-2}\Bigg\}\ .\end{aligned} \tag{2.101}$$

Applying the Kronecker deltas to rewrite (2.4.2) in terms of l and simplifying gives a useful expression for $a^T_{(lm)}(\mathbf{k})$,

$$\begin{aligned}a^{T,+}_{(lm)}(\mathbf{k}) = \frac{1}{8}\left(\delta_{m,2}+\delta_{m,-2}\right)\sqrt{\frac{(l+2)!}{(l-2)!}}\\ \times\left[\frac{\Delta^+_{I,l-2}(k)}{(2l-1)(2l+1)} - \frac{2\Delta^+_{I,l}(k)}{(2l+3)(2l-1)} + \frac{\Delta^+_{I,l+2}(k)}{(2l+3)(2l+1)}\right]\ .\end{aligned} \tag{2.102}$$

For the $\times$ polarisation the expression is exactly the same except that $\Delta^+_{I,l}(k) \to \Delta^\times_{I,l}(k)$, and $(\delta_{m,2}+\delta_{m,-2}) \to -i\left(\delta_{m,2}-\delta_{m,-2}\right)$.

Now, moving on to the polarisation, the Stokes parameters induced by a tensor mode $\mathbf{k}$, in

the case of the + polarisation are given as

$$\begin{aligned}\frac{Q(\mathbf{k},\hat{\mathbf{n}})}{T_0} &= \frac{1}{4}\sum_j (2j+1)P_j(\cos\theta)(1+\cos^2\theta)\cos 2\phi\tilde{\Delta}^+_{Qj}(k)\ ,\\ \frac{U(\mathbf{k},\hat{\mathbf{n}})}{T_0} &= \frac{1}{4}\sum_j (2j+1)P_j(\cos\theta)2\cos\theta\sin 2\phi\tilde{\Delta}^+_{Qj}(k)\ .\end{aligned} \tag{2.103}$$

Once again, making the substitution of (2.103) into the definition of the polarisation tensor in equation (2.81) gives

$$\frac{\mathcal{P}^{ab}_+(\mathbf{k},\hat{\mathbf{n}})}{T_0} = \frac{1}{8}\sum_j (2j+1)\tilde{\Delta}^+_{Qj}(k)\, M^{ab}_j(\hat{\mathbf{n}})\ , \tag{2.104}$$

where

$$M^{ab}_{(j)}(\hat{\mathbf{n}}) = P_j(\cos\theta)\begin{pmatrix} (1+\cos^2\theta)\cos 2\phi & -2\cot\theta\sin 2\phi \\ -2\cot\theta\sin 2\phi & -(1+\cos^2\theta)\csc^2\theta\cos 2\phi\end{pmatrix}\ . \tag{2.105}$$

This is substituted into the definition of the expansion coefficients for the E modes found in (2.88) to give

$$a^{E,+}_{(lm)}(\mathbf{k}) = \frac{N_l}{8}\sum_j (2j+1)\tilde{\Delta}_{Qj}(k)\int d\hat{\mathbf{n}}\, Y^*_{(lm)}(\hat{\mathbf{n}})\, M^{ab}_{(j);ab}(\hat{\mathbf{n}})\ . \tag{2.106}$$

Explicitly performing the covariant derivative as follows,

$$\begin{aligned}M^{ab}_{(j);ab} = {} & M^{\theta\theta}{}_{,\theta\theta} + 2M^{\theta\phi}{}_{,\theta\phi} + M^{\phi\phi}{}_{,\phi\phi} - \sin\theta\cos\theta M^{\phi\phi}{}_{,\theta} + 2\cot\theta M^{\theta\theta}{}_{,\theta}\\ & +4\cot\theta M^{\theta\phi}{}_{,\phi} + (1-3\cos^2\theta)M^{\phi\phi} - M^{\theta\theta}\ ,\end{aligned} \tag{2.107}$$

leads to the expression

$$\begin{aligned}M^{ab}_{(j);ab} = \cos 2\phi[& 12(1-\cos^2\theta)P_j(\cos\theta) + 8\cos\theta(1-\cos^2\theta)P'_j(\cos\theta)\\ & +(1-\cos^4\theta)P''_j(\cos\theta)]\ .\end{aligned} \tag{2.108}$$

For the $\times$ tensor mode polarisation, $\cos 2\phi \to \sin 2\phi$. Now, the identities,

$$P^m_l(x) = (-1)^m(1-x^2)^{\frac{m}{2}}\frac{d^m}{dx^m}[P_l(x)]\ , \tag{2.109}$$

$$(2l+1)\sqrt{1-x^2}\,P^{m-1}_l(x) = P^m_{l-1}(x) + P^m_{l-1}(x)\ , \tag{2.110}$$

$$(1+x^2)P_j(x) = \frac{P^2_{j+2}(x)}{(2j+1)(2j+3)} - \frac{2P^2_j(x)}{(2j-1)(2j+3)} + \frac{P^2_{j-2}(x)}{(2j+1)(2J-1)}\ , \tag{2.111}$$

are used to rewrite (2.4.2). The identity (2.111) is used to rewrite the first term in (2.4.2), the identity (2.109) is used to rewrite the final term, and a combination of (2.109) and (2.110) are used to rewrite the second term. After rewriting entirely in terms of P_l^2 it is found that

$$M^{ab}_{(j);ab} = \cos 2\phi \Bigg[\frac{(j+3)(j+4)P^2_{j+2}(\cos\theta)}{(2j+1)(2j+3)} + \frac{6j(j+1)P^2 j(\cos\theta)}{(2j+3)(2j-1)} + \frac{(j-2)(j-3)P^2_{j-2}(\cos\theta)}{(2j+1)(2j-1)} \Bigg] . \tag{2.112}$$

Now, the following identity is employed,

$$Y_{(lm)}(\theta,\phi) = \sqrt{\frac{(2l+1)}{4\pi}\frac{(l-|m|)!}{(l+|m|)!}}\, P_l^{|m|}(\cos\theta) e^{im\phi} . \tag{2.113}$$

This is used by noting that

$$\cos 2\phi\, P_l^2(cos\theta) = \frac{1}{2}\left(e^{i2\phi}P_l^2(\cos\theta) + e^{-i2\phi}P_l^2(cos\theta)\right) = \frac{1}{2}\sqrt{\frac{4\pi}{(2l+1)}\frac{(l+2)!}{(l-2)!}}\,(Y_{l,2}+Y_{l,-2}) . \tag{2.114}$$

This expression is used to rewrite the Legendre polynomials in (2.4.2) in terms of spherical harmonics. Then the new expression for $M^{ab}_{(j);ab}(\hat{\mathbf{n}})$ is substituted into the integral in (2.106) giving

$$\int d\hat{\mathbf{n}} Y^*_{(lm)}(\hat{\mathbf{n}}) = (\delta_{m,2}+\delta_{m,-2})\sqrt{\frac{\pi}{(2l+1)}\frac{(l+2)!}{(l-2)!}}\left[\frac{(j+3)(j+4)}{(2j+1)(2j+3)}\delta_{l,j+2} + \frac{6j(j+1)}{(2j+3)(2j-1)}\delta_{l,j} + \frac{(j-2)(j-3)}{(2j+1)(2j-1)}\delta_{l,j-2}\right] . \tag{2.115}$$

Then, (2.4.2) is substituted into (2.106) giving

$$a^{E,+}_{(lm)}(\mathbf{k}) = \frac{1}{8}\sum_j (\delta_{m,2}+\delta_{m,-2})\tilde{\Delta}^+_{Q,j}(k)\sqrt{\frac{2(l-2)!}{(l+2)!}}\sqrt{\frac{\pi}{(2l+1)}\frac{(l+2)!}{(l-2)!}} \times\left[\frac{(j+3)(j+4)(2j+1)}{(2j+1)(2j+3)}\delta_{l,j+2} + \frac{6j(j+1)(2j+1)}{(2j+3)(2j-1)}\delta_{l,j} + \frac{(j-2)(j-3)(2j+1)}{(2j+1)(2j-1)}\delta_{l,j-2}\right] . \tag{2.116}$$

The Kronecker deltas that contain j and l are applied, the first and third term in square brackets are multiplied by $\frac{2l+1}{2l+1}$, and the expression is simplified,

$$a^{E,+}_{(lm)}(\mathbf{k}) = \frac{1}{8}(\delta_{m,2}+\delta_{m,-2})\sqrt{2\pi(2l+1)}\left[\frac{(l+1)(l+2)}{(2l-1)(2l+1)}\Delta^+_{Q,l-2}(k)\right.$$

$$+\frac{6l(l+1)}{(2l+3)(2l-1)}\Delta^{+}_{Q,l}(k)+\frac{l(l-1)}{(2l+1)(2l+3)}\Delta^{+}_{Q,l+2}(k)\Bigg]\,. \tag{2.117}$$

For the $\times$ polarisation the equation is the same, however as $\cos 2\phi \rightarrow \sin 2\phi$ then $(\delta_{m,2}+\delta_{m,-2}) \rightarrow -i(\delta_{m,2}-\delta_{m,-2})$.

A similar calculation is used to obtain the expansion coefficients for the B modes. The result of the calculation is

$$a^{B,+}_{(lm)}(\mathbf{k}) = -\frac{i}{4}(\delta_{m,2}-\delta_{m,2})\sqrt{\frac{2\pi}{2l+l}}\left[(l+2)\Delta^{+}_{Q,l-1}(k)+(l-1)\Delta^{+}_{Q,l+1}(k)\right]\,. \tag{2.118}$$

Again, for the $\times$ polarisations $-i(\delta_{m,2}-\delta_{m,-2}) \rightarrow -(\delta_{m,2}+\delta_{m,-2})$.

Now, it is important to notice that for $C_l^{XB,+} = \left\langle a^{X*,+}_{(lm)} a^{B,+}_{(lm)} \right\rangle$ there will be a product of the remaining Kronecker delta terms, $(\delta_{m,2}+\delta_{m,-2})(\delta_{m,2}-\delta_{m,-2})$, which, after summing over over m, is equal to zero. The product of the Kronecker deltas is the same for the $\times$ tensor mode polarisations, however the minus sign swaps places. So, the EB and TB cross correlations vanish for both the tensor modes and the scalar modes. That is,

$$C_l^{XB} = 0\,, \tag{2.119}$$

where $X \in \{T, E\}$. For the original calculation see [9] and [20].

2.4.3 The cross correlations under the birefringence effect

It is worth noting that the vanishing of the EB and TB cross correlations occurs in the primordial power spectra, C_l^{XB}. However, in the presence of a uniform birefringence the linearly polarised light is rotated and mixing of the E and B modes occurs in the observed spectra, $C_l^{XB,\mathrm{obs}}$ [47].

The effect of the rotation on the cross correlations is seen by applying a uniform rotation of birefringence angle α to the E and B mode expansion coefficients to find the observed value of the expansion coefficients,

$$\begin{aligned} a^{B,obs}_{(lm)} &= a^{B}_{(lm)}\cos 2\alpha + a^{E}_{(lm)}\sin 2\alpha\,, \\ a^{E,obs}_{(lm)} &= -a^{B}_{(lm)}\sin 2\alpha + a^{E}_{(lm)}\cos 2\alpha\,. \end{aligned} \tag{2.120}$$

Therefore, the observed spectra for the self and cross correlations become

$$\begin{aligned} C_l^{TE,obs} &= C_l^{TE}\cos 2\alpha \ , \\ C_l^{TB,obs} &= C_l^{TE}\sin 2\alpha \ , \\ C_l^{EB,obs} &= \frac{1}{2}(C_l^{EE} - C_l^{BB})\sin 4\alpha; \ , \\ C_l^{BB,obs} &= C_l^{BB}\cos^2 2\alpha + C_l^{EE}\sin^2 2\alpha \ , \\ C_l^{EE,obs} &= C_l^{BB}\sin^2 2\alpha + C_l^{EE}\cos^2 2\alpha \ . \end{aligned} \tag{2.121}$$

Measuring the deviation from zero of the EB and TB cross correlations is the best way to measure the uniform rotation angle induced by the cosmological birefringence effect [47][48][49].

2.4.4 Estimating errors in CMB experiments

In order to successfully forecast the CMB spectra in the presence of birefringence effects the potential errors and noise must be taken into account. Kamionkowski, Kosowsky, and Stebbins [9], and Zaldarriaga and Seljak [50] lay out much of the analysis required for forecasting the noise and errors for a temperature and polarisation map for a given CMB experiment. It is important to note that the CMB temperature and the polarisation maps are pixelized. If each pixel subtends the same area of sky then the expansion coefficients for the pixelized temperature map are

$$\begin{aligned} d_{(lm)}^T &= \int d\hat{\mathbf{n}} \left(\frac{T^{\text{map}}(\hat{\mathbf{n}}}{T_0} \right) Y_{(lm)}(\hat{\mathbf{n}}) \\ &\simeq \frac{1}{T_0} \sum_{j=1}^{N_{\text{pix}}} \frac{4\pi}{N_{\text{pix}}} T_j^{\text{map}} Y_{(lm)}(\hat{\mathbf{n}}_j) \ . \end{aligned} \tag{2.122}$$

Here, T^{map} is the temperature map and T_j^{map} is the temperature as measured by pixel j in the direction $\hat{\mathbf{n}}_j$ [51]. The $d_{(lm)}$s include the effects of both pixel noise and finite beam size. In reality $d_{(lm)} \simeq a_{(lm)}$ would be true if there were no pixelization noise. In reality $T_j^{\text{map}} = T_j + T_j^{\text{noise}}$ where T_j is the observed temperature because of the true CMB signal. It is assumed that each pixel has the same root mean square (rms) noise and it is assumed that there is no correlation between temperature noise on each pixel and the cosmological temperature signal measured by each pixel,

$$\left\langle T_i^{\text{noise}} T_j^{\text{noise}} \right\rangle = T_0^2 (\sigma_{\text{pix}}^T)^2 \delta_{ij}, \quad \left\langle T_i T_j^{\text{noise}} \right\rangle = 0 \ . \tag{2.123}$$

Then it is possible to take the correlation of the expansion coefficients,

$$\begin{aligned} \left\langle d_{(lm)}^T d_{(l'm')}^{T*} \right\rangle &= \left\langle a_{(lm)}^T a_{(l'm')}^{T*} \right\rangle + \left\langle a_{(lm)}^{T,\text{noise}} a_{(lm)}^{T,\text{noise}\,*} \right\rangle \\ &= |W_l^b|^2 C_l^T \delta_{ll'} \delta_{mm'} + \left\langle a_{(lm)}^{T,\text{noise}} a_{(l'm')}^{T,\text{noise}\,*} \right\rangle \ . \end{aligned} \tag{2.124}$$

The W_l^b term accounts for the beam smearing. The beam is usually given by a Gaussian window function $W_l^b \approx \exp(-l^2\sigma_b^2/2)$. Here $\sigma_b = \theta_{\rm FWHM}/8\ln 2$, where $\theta_{\rm FWHM}$ is full width of the beam at half maximum [10]. Now, the second term in (2.124) is found using the definition of $T_j^{\rm map}$ in terms of T_j and $T_{\rm noise}$, and using equation (2.122),

$$\left\langle a_{(lm)}^{T,\rm noise} a_{(l'm')}^{T,\rm noise\,*} \right\rangle = \frac{1}{T_0^2} \sum_{i=1}^{N_{\rm pix}} \sum_{j=1}^{N_{\rm pix}} \left(\frac{4\pi}{N_{\rm pix}} \right)^2 \left\langle T_i^{\rm noise} T_j^{\rm noise} \right\rangle Y_{(lm)}(\hat{\mathbf{n}}_i) Y^*_{(l'm')}(\hat{\mathbf{n}}_j) \ . \tag{2.125}$$

We then make a substitution of the ensemble average of the noise per pixel into the expression for the noise in harmonic space. This substitution of equation (2.123) is substituted into (2.125) gives

$$\left\langle a_{(lm)}^{T,\rm noise} a_{(l'm')}^{T,\rm noise\,*} \right\rangle = \frac{4\pi}{N_{\rm pix}} (\sigma_{\rm pix}^T)^2 \sum_{i=1}^{N_{\rm pix}} \frac{4\pi}{N_{\rm pix}} Y_{(lm)}(\hat{\mathbf{n}}_i) Y^*_{(l'm')}(\hat{\mathbf{n}}_i) = \frac{4\pi (\sigma_{\rm pix}^T)^2}{N_{\rm pix}} \delta_{ll'} \delta_{mm'} \ . \tag{2.126}$$

So finally the power spectrum,

$$\left\langle d_{(lm)}^T d_{(l'm')}^{T\,*} \right\rangle = \left(|W_l^b|^2 C_l^T + w_T^{-1} \right) \delta_{ll'} \delta_{mm'} \ , \tag{2.127}$$

is obtained. The w_T^{-1} factor is the noise power spectrum given in equation (2.126) [50].

This process must be repeated for polarisation. The correlations for the noise on the Stokes parameters are

$$\begin{aligned} \left\langle Q_i^{\rm noise} Q_j^{\rm noise} \right\rangle = \left\langle U_i^{\rm noise} U_j^{\rm noise} \right\rangle = T_0^2 (\sigma_{\rm pix}^P)^2 \delta_{ij} \\ \left\langle Q_i^{\rm noise} U_j^{\rm noise} \right\rangle = \left\langle Q_i^{\rm noise} T_j^{\rm noise} \right\rangle = \left\langle U_i^{\rm noise} T_j^{\rm noise} \right\rangle = 0 \ . \end{aligned} \tag{2.128}$$

Now, the noise polarisation tensor for a pixel i is denoted $\mathcal{P}_{ab}^{noise}(\hat{\mathbf{n}}_i)$. Using the Stokes parameter correlations and the tensor product it is found that

$$\begin{aligned} \left\langle \mathcal{P}_{ab}^{\rm noise}(\hat{\mathbf{n}}_i)\, \mathcal{P}_{cd}^{\rm noise}(\hat{\mathbf{n}}_j) \right\rangle = \frac{1}{4} T_0^2 (\sigma_{\rm pix}^P)^2 (g_{ac} g_{bd} - \epsilon_{ac} \epsilon_{bd}) \ , \\ \left\langle T_{ab}^{\rm noise}(\hat{\mathbf{n}}_i)\, \mathcal{P}_{cd}^{\rm noise}(\hat{\mathbf{n}}_j) \right\rangle = 0 \ . \end{aligned} \tag{2.129}$$

Now, it is possible to calculate the noise spectrum for the polarisation,

$$\begin{aligned} \left\langle a_{(lm)}^{X,\rm noise}\, a_{(l'm')}^{X',\rm noise} \right\rangle &= \left(\frac{4\pi}{N_{\rm pix} T_0} \right)^2 \sum_{i=1}^{N_{\rm pix}} \sum_{j=1}^{N_{\rm pix}} Y_{(lm)}^{X\,ab}(\hat{\mathbf{n}}_i) Y_{(l'm')}^{X'\,cd}(\hat{\mathbf{n}}_i) \left\langle \mathcal{P}_{ab}^{\rm noise}(\hat{\mathbf{n}}_i)\, \mathcal{P}_{cd}^{\rm noise})(\hat{\mathbf{n}}_j) \right\rangle \\ &= \frac{1}{4} \left(\frac{4\pi \sigma_{\rm pix}^P}{N_{\rm pix}} \right)^2 \sum_{i=1}^{N_{\rm pix}} 2 Y_{(lm)}^{X\,ab\,*}(\hat{\mathbf{n}}_i)\, Y_{(l'm')ab}^{X'}(\hat{\mathbf{n}}_i) \\ &= \frac{8\pi}{N_{\rm pix}} (\sigma_{\rm pix}^P)^2 \delta_{ll'} \delta_{mm'} \delta_{XX'} \ , \end{aligned} \tag{2.130}$$

where $X, X' \in \{E, B\}$. After a substitution for the expression for $\langle \mathcal{P}_{ab}^{\text{noise}}(\hat{\mathbf{n}}_i)\, \mathcal{P}_{cd}^{\text{noise}}(\hat{\mathbf{n}}_j)\rangle$ found in (2.129) is made the identity $M^{ab}N^{cd}\epsilon_{ac}\epsilon_{bd} = -M^{ab}N_{ab}$ is used to reach the second line in (2.129). Now, an expression for the power spectrum $\left\langle d^X_{(lm)} d^{X'*}_{(l'm')} \right\rangle$ can be written as

$$\begin{aligned} \left\langle d^X_{(lm)} d^{X'*}_{(l'm')} \right\rangle &= \left(|W_l^b|^2 C_l^{XX'} + w^{-1}_{XX'} \right) \delta_{ll'}\delta_{mm'} \\ &\equiv D_l^{XX'}\delta_{ll'}\delta_{mm'} \ . \end{aligned} \tag{2.131}$$

These are the ensemble averages of the pixelized temperature and polarisation maps including the pixelization noise [9]. Here, the $w^{-1}_{XX'}$ terms are defined as

$$w_T^{-1} = \frac{4\pi(\sigma^T_{\text{pix}})^2}{N_{\text{pix}}}, \quad w^{-1}_{EE} = w^{-1}_{BB} = \frac{8\pi(\sigma^P_{\text{pix}})^2}{N_{\text{pix}}} \ . \tag{2.132}$$

Now, X and X' have been redefined such that $X, X' \in \{E, B, T\}$. These can be rewritten as noting that $(\sigma_{\text{pix}})^2 = N_{\text{pix}}(\text{NET})^2/t_{\text{obs}}$ where t_{obs} is integration time for the experiment, and NET is the detector sensitivity in units of $\mu\text{Ks}^{1/2}$. So, w_T^{-1} and w_P^{-1} are

$$w_T^{-1} = \frac{4\pi(\text{NET})^2}{t_{\text{obs}}}, \quad w^{-1}_{EE} = w^{-1}_{BB} = \frac{8\pi(\text{NET})^2}{t_{\text{obs}}} \ . \tag{2.133}$$

Up to this point only the power C_l and D_l values that have been considered are found by taking the average of the ensemble of possible realizations of the random process that produces the CMB power spectrum. However, there is only one observable universe that can be measured and therefore only one realization. Therefore, the true ensemble average cannot be found directly from measurements of the CMB power spectrum. Instead it is necessary to construct estimators for C_l and D_l using the measured a_{lm}s and d_{lm}s respectively. The estimators are found by taking the mean over the $2l+1$ measured a_{lm} or d_{lm} values,

$$\widehat{C_l^{XX'}} = \frac{1}{2l+1}\sum_{m=-l}^{l} a^{X\,*}_{(lm)} a^{X'}_{(lm)}, \quad \widehat{D_l^{XX'}} = \frac{1}{2l+1}\sum_{m=-l}^{l} d^{X\,*}_{(lm)} d^{X'}_{(lm)} \ . \tag{2.134}$$

These two estimators are related to each other as follows [50]:

$$\widehat{C_l^{XX'}} = \sum_{m=-l}^{l} \left(\widehat{D_l^{XX'}} - w^{-1}_{XX'} \right) |W_l^b|^{-2} \ . \tag{2.135}$$

There are three different sets of $d_{(lm)}$ coefficients for six sets of the measured D_l moments. Therefore, there will be some covariance between the measured D_l moments. It is possible to construct a covariance matrix that describes the covariances between different D_l moments,

$$\begin{aligned} \Xi_{AA'} &\equiv \left\langle \widehat{C_l^A}\widehat{C_l^{A'}} \right\rangle - C_l^A C_l^{A'} \\ &= \left(\left\langle \widehat{D_l^A}\widehat{D_l^{A'}} \right\rangle - D_l^A D_l^{A'} \right) |W_l^b|^{-4} \ , \end{aligned} \tag{2.136}$$

where $A = XX'$. It is now necessary to find $\left\langle \widehat{D_l^A} \widehat{D_l^{A'}} \right\rangle$ in a more useful form. Begin by noting that for Gaussian random variables $\left\langle x_i^2 x_j^2 \right\rangle = \sigma_{ii}^2 \sigma_{jj}^2 - 2\sigma_{ij}^2$. Now, starting with the TT, EE and BB elements of the covariance matrix, the first term in the second line of equation (2.136) is

$$\left\langle \widehat{D_l^{XX}} \widehat{D_l^{X'X'}} \right\rangle = \sum_{mm'} \frac{\left\langle |d^X_{(lm)}|^2 |d^{X'}_{(lm)}|^2 \right\rangle}{(2l+1)^2} \ . \tag{2.137}$$

This can then expanded by treating the d_{lm} coefficients as Gaussian random variables,

$$\left\langle \widehat{D_l^{XX}} \widehat{D_l^{X'X'}} \right\rangle = \frac{1}{(2l+1)^2} \sum_{mm'} \left[\left\langle d^X_{(lm)} d^X_{(lm)} \right\rangle \left\langle d^{X'}_{(lm')} d^{X'}_{(lm')} \right\rangle + 2 \left\langle d^X_{(lm)} d^{X'}_{(lm')} \right\rangle^2 \right] \ . \tag{2.138}$$

Then the definition of D_l can be used to give

$$\begin{aligned} \left\langle \widehat{D_l^{XX}} \widehat{D_l^{X'X'}} \right\rangle &= \frac{1}{(2l+1)^2} \sum_{mm'} \left[D_l^{XX} D_l^{X'X'} + 2 (D_l^{XX'})^2 \delta_{mm'} \right] \\ &= D_l^{XX} D_l^{X'X'} + \frac{2}{2l+1} (D_l^{XX'})^2 \ . \end{aligned} \tag{2.139}$$

Now, the XX', XX' components must be found,

$$\left\langle \widehat{D_l^{XX'}} \widehat{D_l^{XX'}} \right\rangle = \frac{1}{(2l+1)^2} \sum_{mm'} \left\langle d^{X*}_{(lm)} d^{X'}_{(lm)} d^{X*}_{(lm')} d^{X'}_{(lm')} \right\rangle \ . \tag{2.140}$$

Using a similar procedure to before, this becomes

$$\begin{aligned} \left\langle \widehat{D_l^{XX'}} \widehat{D_l^{XX'}} \right\rangle &= \frac{1}{(2l+1)^2} \sum_{mm'} \left[D_l^{XX} D_l^{X'X'} + 2 (D_l^{XX'})^2 \right] \delta_{mm'} + (1 - \delta_{mm'}) (D^{XX'})^2 \\ &= \frac{1}{2l+1} \left[(D_l^{XX'})^2 + D_l^{XX} D_l^{X'X'} \right] + (D_l^{XX'})^2 \ . \end{aligned} \tag{2.141}$$

Now, the final set of terms are the $\left\langle \widehat{D_l^{XX}} \widehat{D_l^{XX'}} \right\rangle$ terms which are

$$\left\langle \widehat{D_l^{XX}} \widehat{D_l^{XX'}} \right\rangle = \left(\frac{2}{2l+1} + 1 \right) D_l^{XX} D_l^{XX'} \ . \tag{2.142}$$

From all these terms and equation (2.136) it is possible to construct the full 6×6 covariance matrix [50][52]. The covariance matrix is useful as it can be used to calculate the Fisher matrix [53]. The components of the Fisher matrix, $\mathcal{F}_{ij}$, for a given set of cosmological parameter x_i are

$$\mathcal{F}_{ij} = \sum_l \sum_{A,A'} \frac{\partial C_l^A}{\partial x_i} [\Xi^{-1}]_{AA'} \frac{\partial C_l^{A'}}{\partial x_j}, \tag{2.143}$$

where A is XX and XX' [54]. It is desireable to be able to include the effect of only mapping a fraction of the sky. If the noise is taken to not be correlated between different multipoles then the Fisher matrix is just multipled by the f_{sky}, which is the fraction of the sky that has

been surveyed [55]. This gives

$$\mathcal{F}_{ij} = f_{\text{sky}} \sum_{l} \sum_{A,A'} \frac{\partial C_l^A}{\partial x_i} \left[\Xi^{-1}\right]_{AA'} \frac{\partial C_l^{A'}}{\partial x_j} \tag{2.144}$$

The inverse of this matrix provides useful information about the uncertainties of the cosmological parameters,

$$[F]^{-1} = \begin{pmatrix} \sigma_i^2 & \sigma_{ij} \\ \sigma_{ij} & \sigma_j^2 \end{pmatrix} \tag{2.145}$$

where σ_i and σ_j are the uncertainties for the ith and jth parameters respectively. If the ith parameter was Ω_k the 1-σ uncertainty of this parameter would then be $\sigma_{\Omega_k} = \sqrt{[F^{-1}]_{ii}}$. Here the other parameters have been marginalized over. That is, this is the uncertainty if the other parameters are allowed to take any value [56]. Using the Fisher matrix it is possible to estimate the precision with which a CMB map will be able to recover particular cosmological parameters. Therefore, using the Fisher matrix, the covariance matrix, and the equations for the estimators for the power spectrum it is possible to forecast how well an experiment will measure the CMB power spectrum, and how precisely it will measure the cosmological parameters.

2.4.5 Data from the CMB

There have been a number of different experiments that have attempted to measure the birefringence rotation angle. However, it is very difficult to calibrate such an experiment. This is because the majority of CMB polarisation experiments test calibration assuming that the EB and TB cross correlation spectra are zero. However, as these are also the spectra that are used to measure the rotation angle this means that a different calibration method must be used. Inaccuracies in these calibration methods lead to problematic systematics in birefringence angle measurements. A discussion of some of the calibration methods used by CMB polarisation experiments is contained in [57]. These difficulties have lead to a range of measured values for a uniform birefringence angle as seen in table 2.1. Upcoming CMB experiments that may measure the CMB polarisation angle to a greater accuracy include CMB S4, LiteBIRD, BICEP array, and Simons Observatory.

It is also possible that the birefringence rotation angle is not uniform but anisotropic as seen in equation (2.43). A number of more recent works have attempted to measure this anisotropy. However, these experiments so far have found the anisotropy of the birefringence angle to be heavily constrained and consistent with zero [43][67][68].

Experiment	Frequency (Ghz)	l range	α (degrees)
WMAP7[58]	$41 + 61 + 94$	2 - 800	-1.1 ± 1.4 (± 1.5)
WMAP9[59]	53	2-800	-0.36 ± 1.24 (± 1.5)
BOOM03[58]	143	150 - 1000	-4.3 ± 4.1
QUaD[60]	100	200 - 2000	-1.89 ± 2.24 (± 0.5)
QUaD[60]	150	200 - 2000	$+0.83 \pm 0.94$ (± 0.5)
BICEP1[61] (DSC)	100+150	30 - 300	-2.77 ± 0.86 (± 1.3)
BICEP1 (grid)[61]	100+150	30 - 300	-1.71 ± 0.86 (± 1.3)
BICEP1 (design)[61]	100 + 150	30 - 300	-1.27 ± 0.86 (± 1.3)
POLARBEAR[62]	150	500 - 2100	-1.08 ± 0.2 (± 0.5)
BICEP2[63]	150	30 - 300	$\alpha \approx -1 \pm 0.2^a$
ACTPol[64]	146	500 - 2000	$\alpha = -0.2 \pm 0.5$
Planck[65]	Multiple	2 - 29 & 30 - 2500	0.0 ± 1.3 (± 1)
Planck + BKP[65]	Multiple	2 - 29 & 30 - 2500	0.32 ± 0.26 (± 1)
Planck [66]	Multiple, SMICA	map based	$\alpha < 0.72^\circ$

Table 2.1: This table contains the rotation angles from CMB polarisation with 1σ statistical and (systematic) uncertainty. In the final row the 95% C.L. constraint is presented.
[a] Systematic error is unpublished.
[57]

2.5 Using the CMB to detect anisotropic birefringence

2.5.1 Sources of anisotropic birefringence

In the case of anisotropic cosmological birefringence the cosmic polarization rotation angle α varies across the sky. This field of rotation angles is denoted $\alpha(\hat{\mathbf{n}})$. It is helpful to quantify this field in terms of its power spectrum, $C_L^{\alpha\alpha}$. It is then possible to make comparisons between observed spectrum and that predicted by theoretical models in order to test such models. There are two major scenarios in which an anisotropic cosmic birefringence effect could be produced.

The first is the case of anisotropic birefringence generated by a spatially varying pseudo scalar field ϕ as seen in equation (2.43). In the simplest scenario the pseudo scalar field is effectively massless during inflation leading to the scale invariant power spectrum for the cosmic polarization rotation field, $\alpha(\hat{\mathbf{n}})$ [44],

$$\frac{L(L+1)}{2\pi} C_L^{\alpha\alpha} = \left(\frac{H_I}{2\pi f_a}\right)^2 , \tag{2.146}$$

where H_I is the Hubble constant during inflation and f_a is the coupling strength between the photon and a. The second case is the case of birefringence generated by Faraday rotation in the presence of primordial magnetic fields;

$$\alpha(\hat{\mathbf{n}}) = \frac{3}{16\pi^2 e \nu^2} \int d\boldsymbol{l} \cdot \dot{\tau} \boldsymbol{b} \, . \tag{2.147}$$

Here, $\boldsymbol{b}$ is the comoving magnetic field, ν is the observed frequency, and $\dot{\tau}$ is the differential

Experiment	$A_{CB} \times 10^{-4}$ [rad^2]
WMAP	3.0 [77]
Planck (2018 release)	0.32 [78]
POLARBEAR	3.1 [43]
BICEP/Keck	0.33 [68]
SPTpol	0.1 [79]
ACT	0.1 [80]

Table 2.2: The 95% confidence limit (C.L.) upper bounds on A_{CB}, the amplitude of a scale invariant form of $C_L^{\alpha\alpha}$. Note that the result presented here, and in the source literature for WMAP is the 68% C.L. result.

optical depth. The scale invariant power spectrum in this case is [69]

$$\frac{L(L+1)}{2\pi}C_L^{\alpha\alpha} = 2.3 \times 10^{-5} \left(\frac{30\,\mathrm{GHz}}{\nu}\right)^4 \left(\frac{B}{1\,\mathrm{nG}}\right)^2 . \tag{2.148}$$

It is possible to write both of these more generally as [70]

$$\frac{L(L+1)}{2\pi}C_L^{\alpha\alpha} = A_{CB} , \tag{2.149}$$

where A_{CB} is a measured amplitude parameter. An anisotropic cosmological birefringence effect would distort the CMB polarization maps with a direction dependent rotation of the linear polarization angle of the photons propagating from the surface of last scatter. It is possible to search for these distortions in order to reconstruct $\alpha(\hat{\mathbf{n}})$.

2.5.2 Current constraints on anisotropic Birefringence from recent experiments

Data from range of satellite and ground based CMB experiments have been to used to place constraints on the amplitude, A_{CB}, for the anisotropic birefringence power spectrum, $C_L^{\alpha\alpha}$. These limits assume a scale invariant form for $C_L^{\alpha\alpha}$ (see equation (2.149).These experiments include the *Wilkinson Microwave Anisotropy Probe* (*WMAP*) [71], *Planck* [72], POLARBEAR [73], SPTpol [74], BICEP/Keck [75], and the Atacama Cosmology Telescope (ACT) [76]. These constraints are found by exploiting the distortions of the CMB polarization generated by the anisotropic birefringence field. Therefore, unlike in the case of uniform birefringence, constraints on anisotropic birefringence are not limited by the absolute calibration angle error.

The constraints for the aforementioned experiments are listed in Table 2.2. The best constraints, to date, come from the SPTpol, and ACT data. In the vast majority of these experiments a QE based technique is used to estimate the birefringence spectrum, $\widehat{C}_L^{\alpha\alpha}$. The details of QEs used to perform this estimation are presented in Section 2.5.3-2.5.4. In the case of the *Planck* analysis the power spectrum was estimated using a large-pixel approach. In this approach the sky was separated into small patches or "pixels". The uniform birefringence angle

was calculated for each of these "pixels". These values were then used produce a map of the direction dependent birefringence field $\alpha(\hat{\mathbf{n}})$. From this map $\widehat{C}_L^{\alpha\alpha}$ was inferred [67], [78]. In both the QE approach and the large-pixel approach likelihood analysis was then employed in order to calculate the upper bounds on A_{CB} [43], [68], [77]–[81].

2.5.3 The anisotropic birefringence QE in the flat sky limit

The majority of the CMB experiments which seek to either detect or place constraints on anisotropic birefringence have used a QE in order to reconstruct a map of $\alpha(\hat{\mathbf{n}})$. These QEs exploit the off diagonal correlations in the CMB covariance matrix, $\langle a_{lm} a^*_{l'm'} \rangle$, that are sourced by direction dependent distortions of the CMB maps [82].

The POLARBEAR [43], SPTpol [79], and BICEP/Keck [68] surveys all have a small enough sky-coverage that a flat-sky approximation can be used. Here, we will follow the approach found in [83] to summarize the derivation of a flat-sky QE. To begin constructing a QE it is necessary to understand how an anisotropic rotation of linear polarisation, $\alpha(\mathbf{L})$, affects the polarisation modes. In the flat sky limit the $E(\mathbf{l})$ and $B(\mathbf{l})$ modes are written as fields in l-space, where $\mathbf{l}$ is the multipole vector. The observed Stokes parameters are used to construct the $E(\mathbf{l})$ and $B(\mathbf{l})$ fields in a Fourier basis,

$$[\tilde{E} \pm i\tilde{B}](\mathbf{l}) = -\int d\hat{\mathbf{n}} [Q \pm iU](\hat{\mathbf{n}}) e^{\mp 2i\phi_{\mathbf{l}}} e^{-i\hat{\mathbf{n}}\cdot\mathbf{l}} \,, \tag{2.150}$$

where $Q(\hat{\mathbf{n}})$ and $U(\hat{\mathbf{n}})$ are the Stokes parameters at angular position $\hat{\mathbf{n}}$, and $\phi_{\mathbf{l}}$ is the angle of the multipole vector. This angle is measured from the axis which is defined with respect to the Q parameter. The exponential rotation term containing the angle of the multipole vector is necessary to transform the $\tilde{Q}(\mathbf{l})$ and $\tilde{U}(\mathbf{l})$ Stokes parameter into $\tilde{E}(\mathbf{l})$ and $\tilde{B}(\mathbf{l})$ the flat sky terms analogous to a^E_{lm} and a^B_{lm}. This rotation is often written in matrix form [84];

$$\begin{pmatrix} \tilde{E}(\mathbf{l}) \\ \tilde{B}(\mathbf{l}) \end{pmatrix} = \begin{pmatrix} \cos 2\phi_{\mathbf{l}} & \sin 2\phi_{\mathbf{l}} \\ -\sin 2\phi_{\mathbf{l}} & \cos 2\phi_{\mathbf{l}} \end{pmatrix} \begin{pmatrix} \tilde{Q}(\mathbf{l}) \\ \tilde{U}(\mathbf{l}) \end{pmatrix} \,. \tag{2.151}$$

In analogy to this rotation the effect of cosmological birefringence on the $Q(\hat{\mathbf{n}})$ and $U(\hat{\mathbf{n}})$ Stokes parameter is also introduced through an exponential rotation term [70],

$$[\breve{Q} \pm i\breve{U}](\hat{\mathbf{n}}) = e^{\mp 2i\alpha(\hat{\mathbf{n}})} [Q \pm iU](\hat{\mathbf{n}}) \,. \tag{2.152}$$

When this rotation is introduced (2.150) becomes

$$[\breve{E} \pm i\breve{B}](\mathbf{l}) = -\int d\hat{\mathbf{n}} e^{\mp 2i\alpha(\hat{\mathbf{n}})} [Q \pm iU](\hat{\mathbf{n}}) e^{\mp 2i\phi_{\mathbf{l}}} e^{-i\hat{\mathbf{n}}\cdot\mathbf{l}} \,. \tag{2.153}$$

As the α parameter is constrained to be small it is possible to Taylor expand this expression

in terms of α to first order, leading to

$$[\breve{E} \pm i\breve{B}](\mathbf{l}) = [\tilde{E} \pm i\tilde{B}](\mathbf{l}) + \int d\hat{\mathbf{n}} \frac{d^2\mathbf{L}}{(2\pi)^2} \pm 2i\alpha(\mathbf{L})[Q \pm iU](\hat{\mathbf{n}}) e^{\mp 2i\phi_{\mathbf{l}}} e^{-i\hat{\mathbf{n}}\cdot\mathbf{l}} e^{i\hat{\mathbf{n}}\cdot\mathbf{L}} \ . \quad (2.154)$$

Here, $\alpha(\hat{\mathbf{n}})$ has been rewritten using $\alpha(\hat{\mathbf{n}}) = \int \frac{d^2\mathbf{L}}{(2\pi)^2} \alpha(\mathbf{L}) e^{i\hat{\mathbf{n}}\cdot\mathbf{L}}$. Taking the Fourier transform of the final term in (2.154) and writing Q and U as a rotation of E and B gives

$$[\breve{E} \pm i\breve{B}](\mathbf{l}) = [\tilde{E} \pm i\tilde{B}](\mathbf{l}) + \int \frac{d^2\mathbf{L}}{(2\pi)^2} \pm 2i\alpha(\mathbf{L})[\tilde{E} \pm i\tilde{B}](\mathbf{l}-\mathbf{L}) e^{\pm 2i(\phi_{\mathbf{l}-\mathbf{L}} - \phi_{\mathbf{l}})} \ . \quad (2.155)$$

Euler's formula is employed to rewrite (2.155) as

$$\begin{aligned}[\breve{E} \pm i\breve{B}](\mathbf{l}) = [\tilde{E} \pm i\tilde{B}](\mathbf{l}) + \int \frac{d^2\mathbf{L}}{(2\pi)^2} 2\alpha(\mathbf{L})[&-\tilde{B}(\mathbf{l}-\mathbf{L}) \cos 2\phi_{\mathbf{l}-\mathbf{L},\mathbf{l}} - \tilde{E}(\mathbf{l}-\mathbf{L}) \sin 2\phi_{\mathbf{l}-\mathbf{L},\mathbf{l}} \\ &\pm i\tilde{E}(\mathbf{l}-\mathbf{L}) \cos 2\phi_{\mathbf{l}-\mathbf{L},\mathbf{l}} \mp i\tilde{B}(\mathbf{l}-\mathbf{L}) \sin 2\phi_{\mathbf{l}-\mathbf{L},\mathbf{l}}] \ , \end{aligned} \quad (2.156)$$

where $\phi_{\mathbf{l}-\mathbf{L},\mathbf{l}} = \phi_{\mathbf{l}-\mathbf{L}} - \phi_{\mathbf{l}}$. So the full rotated $\breve{E}(\mathbf{l})$ and $\breve{B}(\mathbf{l})$ fields are

$$\begin{aligned}\breve{E}(\mathbf{l}) &= \tilde{E}(\mathbf{l}) + E^{\alpha}(\mathbf{l}) \ , \\ \breve{B}(\mathbf{l}) &= \tilde{B}(\mathbf{l}) + B^{\alpha}(\mathbf{l}) \ , \end{aligned} \quad (2.157)$$

where the rotation introduces the corrections $E^{\alpha}(\mathbf{l})$ and $B^{\alpha}(\mathbf{l})$ which are given as

$$\begin{aligned}E^{\alpha}(\mathbf{l}) &= -\int \frac{d^2\mathbf{l}'}{(2\pi)^2} \left[\tilde{B}(\mathbf{l}') \cos 2\phi_{\mathbf{l}',\mathbf{l}} + \tilde{E}(\mathbf{l}') \sin 2\phi_{\mathbf{l}',\mathbf{l}}\right] 2\alpha(\mathbf{L}) \ , \\ B^{\alpha}(\mathbf{l}) &= \int \frac{d^2\mathbf{l}'}{(2\pi)^2} \left[\tilde{E}(\mathbf{l}') \cos 2\phi_{\mathbf{l}',\mathbf{l}} - \tilde{B}(\mathbf{l}') \sin 2\phi_{\mathbf{l}',\mathbf{l}}\right] 2\alpha(\mathbf{L}) \ , \end{aligned} \quad (2.158)$$

where the relabeling $\mathbf{l}' = \mathbf{l} - \mathbf{L}$ has been used.

To find the variance on α it is important to know the values of the ensemble averages of the rotated fields. For and unrotated field $\tilde{x}(\mathbf{l})$, where $\tilde{x}(\mathbf{l}) \in \{\tilde{E}(\mathbf{l}), \tilde{B}(\mathbf{l}), \tilde{T}(\mathbf{l})\}$,

$$\langle \tilde{x}(\mathbf{l}) \rangle = 0 \ , \qquad \langle \tilde{x}^*(\mathbf{l}) \tilde{x}'(\mathbf{l}') \rangle = (2\pi)^2 \delta(\mathbf{l} - \mathbf{l}') \tilde{C}_{\mathrm{l}}^{xx'} \ . \quad (2.159)$$

To look at how the ensemble averages of the rotated fields behave, for a fixed value of $\alpha(\mathbf{L})$ it is useful to look at the case of $\left\langle \breve{E}^*(\mathbf{l}_1) \breve{B}(\mathbf{l}_2) \right\rangle$, where

$$\left\langle \breve{E}^*(\mathbf{l}_1) \breve{B}(\mathbf{l}_2) \right\rangle = \left\langle \tilde{E}^*(\mathbf{l}_1) \tilde{B}(\mathbf{l}_2) \right\rangle + \left\langle E^{\alpha}(\mathbf{l}_1) \tilde{B}(\mathbf{l}_2) \right\rangle + \left\langle \tilde{E}^*(\mathbf{l}_1) B^{\alpha}(\mathbf{l}_2) \right\rangle + \langle E^{\alpha}(\mathbf{l}_1) B^{\alpha}(\mathbf{l}_2) \rangle \ . \quad (2.160)$$

Using the sifting property of the Dirac delta to negate sine containing terms, and using the

property that $\left\langle \tilde{E}^*(\mathbf{l}_1)\tilde{B}(\mathbf{l}_2)\right\rangle = 0$ this reduces to

$$\left\langle \breve{E}^*(\mathbf{l}_1)\breve{B}(\mathbf{l}_2)\right\rangle = \int \frac{d^2\mathbf{l}'_1}{(2\pi)^2}\left[\left\langle \tilde{E}(\mathbf{l}'_1)\tilde{E}(\mathbf{l}_2)\right\rangle \cos 2\phi_{\mathbf{l}'_1,\mathbf{l}_2} - \left\langle \tilde{B}(\mathbf{l}'_1)\tilde{B}(\mathbf{l}_2)\right\rangle \cos 2\phi_{\mathbf{l}'_1,\mathbf{l}_2}\right] , \tag{2.161}$$

which, after taking the integral, gives

$$\left\langle \breve{E}^*(\mathbf{l}_1)\breve{B}(\mathbf{l}_2)\right\rangle = 2\left[\tilde{C}^{EE}_{l_1} - \tilde{C}^{BB}_{l_2}\right]\cos 2\phi_{\mathbf{l}_1,\mathbf{l}_2} . \tag{2.162}$$

For brevity the term on the right hand side of the equation is denoted $f_{EB}(\mathbf{l}_1,\mathbf{l}_2)$. In general [85]

$$\langle \breve{x}^*(\mathbf{l})\breve{x}'(\mathbf{l}')\rangle = \langle \tilde{x}^*(\mathbf{l})\tilde{x}'(\mathbf{l}')\rangle + f_{xx'}(\mathbf{l},\mathbf{l}')\alpha(\mathbf{L}) , \tag{2.163}$$

where for the $E(\mathbf{l})$ and $B(\mathbf{l})$ fields

$$\begin{aligned} f_{EE}(\mathbf{l}_1,\mathbf{l}_2) &= 2\left[\tilde{C}^{EE}_{l_1} - \tilde{C}^{EE}_{l_2}\right]\sin 2\phi_{\mathbf{l}_1,\mathbf{l}_2} , \\ f_{BB}(\mathbf{l}_1,\mathbf{l}_2) &= \left[\tilde{C}^{BB}_{l_1} + \tilde{C}^{BB}_{l_2}\right]\sin 2\phi_{\mathbf{l}_1,\mathbf{l}_2} . \end{aligned} \tag{2.164}$$

It is now possible to invert (2.163) in order to construct the unbiased estimator for $\alpha(\mathbf{L})$. As seen in [86] this can be written as

$$\hat{\alpha}_{xx'}(\mathbf{L}) = A_{xx'}(L)\int \frac{d^2\mathbf{l}_1}{(2\pi)^2}\left[\breve{x}(\mathbf{l}_1)\breve{x}'(\mathbf{l}_2) - \langle \tilde{x}(\mathbf{l}_1)\tilde{x}'(\mathbf{l}_2)\rangle\right]F_{xx'}(\mathbf{l}_1,\mathbf{l}_2) , \tag{2.165}$$

where the normalisation term is defined as

$$A_{xx'}(L) = \left[\int \frac{d^2\mathbf{l}_1}{(2\pi)^2} f_{xx'}(\mathbf{l}_1,\mathbf{l}_2)F_{xx'}(\mathbf{l}_1,\mathbf{l}_2)\right]^{-1} , \tag{2.166}$$

and the $\mathbf{L}$ vector is defined as $\mathbf{L} = \mathbf{l}_2 - \mathbf{l}_1$. The normalization term, and the speccific form of the $F_{xx'}(\mathbf{l}_1,\mathbf{l}_2)$ term, defined as

$$F_{xx'}(\mathbf{l}_1,\mathbf{l}_2) = \frac{f_{xx'}(\mathbf{l}_1,\mathbf{l}_2)}{C^{xx}_{l_1}C^{x'x'}_{l_2}} , \tag{2.167}$$

are found by minimizing the variance of the estimator in (2.165). The C^{xx}_l terms are constructed from the observed maps. The variance on $C^{\alpha\alpha}_L$ is then

$$\langle \hat{\alpha}(\mathbf{L})\hat{\alpha}^*(\mathbf{L}')\rangle - \langle \hat{\alpha}(\mathbf{L})\rangle^2 = \Delta C^{\alpha\alpha}_L = (2\pi)^2\delta(\mathbf{L}-\mathbf{L}')\left[C^{\alpha\alpha}_L + A_{EB}(L)\right] , \tag{2.168}$$

giving the variance for anisotropic birefringence in the flat sky limit.

2.5.4 The anisotropic birefringence QE in the full sky formalism

For experiments with a larger sky coverage, such as WMAP [77], Planck [78] and ACT [80], the flat-sky approximation is not valid. In this case a full-sky QE is needed. Note, that for the *Planck* analysis in [67] and [78] a QE was not used to reconstruct $\alpha(\hat{\mathbf{n}})$. A full-sky QE can be found by following the approach outlined in in [39] and [38]. This approach is summarized here.

As in the flat sky case it is necessary to understand how anisotropic birefringence affects the E and B modes. First the $Q(\hat{\mathbf{n}})$ and $U(\hat{\mathbf{n}})$ Stokes parameters are rotated by the direction dependent rotation angle $\alpha(\hat{\mathbf{n}})$ as

$$\begin{pmatrix} Q_{\text{obs}}(\hat{\mathbf{n}}) \\ U_{\text{obs}}(\hat{\mathbf{n}}) \end{pmatrix} = \begin{pmatrix} \cos 2\alpha(\hat{\mathbf{n}}) & \sin 2\alpha(\hat{\mathbf{n}}) \\ -\sin 2\alpha(\hat{\mathbf{n}}) & \cos 2\alpha(\hat{\mathbf{n}}) \end{pmatrix} \begin{pmatrix} Q(\hat{\mathbf{n}}) \\ U(\hat{\mathbf{n}}) \end{pmatrix} . \tag{2.169}$$

As seen in equation (2.81) it is possible to write the Stokes parameters as a symmetric, trace-free polarisation tensor $P_{ab}(\hat{\mathbf{n}})$. Recall that the polarisation tensor has the form

$$P_{ab}(\hat{\mathbf{n}}) = \sum_{l=2}^{\infty} \sum_{m=-l}^{l} \left[E_{lm} Y^{E}_{(lm)ab}(\hat{\mathbf{n}}) + B_{lm} Y^{B}_{(lm)ab}(\hat{\mathbf{n}}) \right] , \tag{2.170}$$

where a minor change of notation has been introduced such that $E_{lm} \equiv a^{E}_{lm}$ and $B_{lm} \equiv a^{B}_{lm}$. As the effect of anisotropic birefringence on the polarisation tensor must be small [43], it is possible to write the effect as a perturbation;

$$P_{ab}(\hat{\mathbf{n}}) \to P_{ab}(\hat{\mathbf{n}}) + \delta P_{ab}(\hat{\mathbf{n}}) . \tag{2.171}$$

For simplicity it is assumed that at the surface of last scatter the polarisation tensor is made of purely E mode. The perturbation is then formed of pure E mode that have rotated by $\alpha(\hat{\mathbf{n}})$ into a B mode. This is expressed as [39]

$$\delta P_{ab}(\hat{\mathbf{n}}) = 2\alpha(\hat{\mathbf{n}}) P^{r}_{ab}(\hat{\mathbf{n}}) , \tag{2.172}$$

where $P^{r}_{ab}(\hat{\mathbf{n}})$ is the original, pure E mode containing polarisation tensor rotated 45° completely into a pure B mode. The $P^{r}_{ab}(\hat{\mathbf{n}})$ tensor is therefore expressed as

$$P^{r}_{ab}(\hat{\mathbf{n}}) = \sum_{l=2}^{\infty} \sum_{m=-l}^{l} E_{lm} Y^{B}_{(lm)ab} . \tag{2.173}$$

The anisotropic rotation can be expanded in spherical harmonics as it a direction dependent scalar field. Therefore,

$$\alpha(\hat{\mathbf{n}}) = \sum_{LM} \alpha_{LM} Y_{LM}(\hat{\mathbf{n}}) . \tag{2.174}$$

The α_{LM} coefficient is useful as it is possible to use it to construct the $C_L^{\alpha\alpha}$ power spectrum. However, it is important to relate the α_{LM} and the variance of the estimator of this coefficient to the observed polarisation modes. The orthonormality properties the spherical harmonics mean that it is possible to express the change in polarisation modes due to the rotation as

$$\begin{aligned}\delta B_{lm} &= \int d\hat{\mathbf{n}} \delta P_{ab}(\hat{\mathbf{n}}) Y^{B*,ab}_{(lm)}(\hat{\mathbf{n}}) \ , \\ \delta E_{lm} &= \int d\hat{\mathbf{n}} \delta P_{ab}(\hat{\mathbf{n}}) Y^{E*,ab}_{(lm)}(\hat{\mathbf{n}}) \ .\end{aligned} \tag{2.175}$$

Inserting the explicit expression for $\alpha(\hat{\mathbf{n}})$ and $\delta P_{ab}(\hat{\mathbf{n}})$ gives

$$\begin{aligned}\delta B_{lm} &= 2 \sum_{LM} \sum_{l_2 m_2} \alpha_{LM} E_{l_2 m_2} \int d\hat{\mathbf{n}} Y^{B*,ab}_{(lm)} Y_{(LM)} Y^{B}_{(l_2 m_2) ab} \ , \\ \delta E_{lm} &= 2 \sum_{LM} \sum_{l_2 m_2} \alpha_{LM} E_{l_2 m_2} \int d\hat{\mathbf{n}} Y^{E*,ab}_{(lm)} Y_{(LM)} Y^{B}_{(l_2 m_2) ab} \ .\end{aligned} \tag{2.176}$$

As seen in Section 2.4.1 the $Y^B_{(lm)ab}$ and $Y^E_{(lm)ab}$ are respectively expressed as curl-containing and curl free derivatives of the spherical harmonics. These derivatives can be more simply expressed in terms of spin weighted spherical harmonics. Expressing $Y^B_{(lm)ab}$ and $Y^E_{(lm)ab}$ in terms of spin weighted spherical harmonics its possible to write

$$\begin{aligned}Y^{B*,ab}_{(lm)} Y^{B}_{(l_2 m_2) ab} &= \frac{1}{2} \left[\left({}_{-2}Y^*_{(lm)} \times {}_{-2}Y_{(l_2 m_2)} \right) + \left({}_{+2}Y^*_{(lm)} \times {}_{+2}Y_{(l_1 m_2)} \right) \right] \ , \\ Y^{E*,ab}_{(lm)} Y^{B}_{(l_2 m_2) ab} &= \frac{i}{2} \left[\left({}_{+2}Y^*_{(lm)} \times {}_{+2}Y_{(l_2 m_2)} \right) - \left({}_{-2}Y^*_{(lm)} \times {}_{-2}Y_{(l_1 m_2)} \right) \right] \ .\end{aligned} \tag{2.177}$$

It is possible to use these expressions to rewrite the integrals in (2.176). Note, that it is possible to express the integral of three spin weighted spherical harmonic in terms of Wigner-3j symbols and that $Y_{(LM)}$ is a spin weighted spherical harmonic with a spin of 0 (that is $Y_{(LM)} = {}_0Y_{(LM)}$). Therefore, the integral in the expression for δB_{lm} is written as

$$\begin{aligned}\int d\hat{\mathbf{n}} Y^{B*,ab}_{(lm)} Y_{(LM)} Y^{B}_{(l_2 m_2) ab} &= \frac{1}{2} (-1)^m \sqrt{\frac{(2l+1)(2L+1)(2l_2+1)}{4\pi}} \\ &\times \left[\begin{pmatrix} l & L & l_2 \\ -2 & 0 & 2 \end{pmatrix} + \begin{pmatrix} l & L & l_2 \\ 2 & 0 & -2 \end{pmatrix} \right] \begin{pmatrix} l & L & l_2 \\ -m & M & m_2 \end{pmatrix} \ .\end{aligned} \tag{2.178}$$

A convenient notation is defined,

$$\begin{aligned}\xi^{LM}_{lml_2m_2} &\equiv (-1)^m \sqrt{\frac{(2l+1)(2L+1)(2l_2+1)}{4\pi}} \begin{pmatrix} l & L & l_2 \\ -m & M & m_2 \end{pmatrix} \ , \\ H^L_{ll_2} &\equiv \begin{pmatrix} l & L & l_2 \\ 2 & 0 & -2 \end{pmatrix} \ .\end{aligned} \tag{2.179}$$

A compact expression for the change in the polarisation B mode due to direction dependent

rotation is

$$\delta B_{lm} = 2 \sum_{LM} \sum_{l_2 m_2} \alpha_{LM} E_{l_2 m_2} \xi^{LM}_{l m l_2 m_2} H^L_{l l_2} \ , \tag{2.180}$$

where the nonzero terms in the sum are those where $l + L + l_2$ is even. Similarly the change in the E mode can be written

$$\delta E_{lm} = 2i \sum_{LM} \sum_{l_2 m_2} \alpha_{LM} E_{l_2 m_2} \xi^{LM}_{l m l_2 m_2} H^L_{l l_2} \ , \tag{2.181}$$

where the only surviving nonzero terms in the sum are those for which $l + L + l_2$ is odd.

As the effect of birefringence on the E and B modes is expressed $E_{lm} + E_{lm,0} + \delta E_{lm}$ and $B_{lm} = \delta B_{lm}$, where $E_{lm,0}$ is E_{lm} at the surface of last scattering, the primordial power spectrum for E_{lm} is expressed as

$$\left\langle E_{lm,0} E^*_{l'm',0} \right\rangle = C^{EE}_l \delta_{ll'} \delta_{mm'} \ . \tag{2.182}$$

Therefore, it is possible to write expressions for the full polarisation power spectra and the cross spectra, including the effects of anisotropic cosmological birefringence, in terms of the unrotated power spectra. For example, the full EB cross correlation can be written, to first order in α_{LM}, as

$$\begin{aligned} \langle B_{lm} E^*_{l'm'} \rangle &= 2 \sum_{LM} \alpha_{LM} C^{EE}_{l'} \xi^{LM}_{l m l' m'} H^L_{l l'} \\ &= \frac{1}{\sqrt{\pi}} \alpha_{00} C^{EE}_{l'} \delta_{ll'} \delta_{mm'} \\ &\quad + 2 \sum_{L \geq 1} \sum_{M=-L}^{L} \alpha_{LM} C^{EE}_{l'} \xi^{LM}_{l m l' m'} H^L_{l l'} \ , \end{aligned} \tag{2.183}$$

These off-diagonal correlations in this CMB covariance can be exploited to to reconstruct α_{LM} using a quadratic estimator. Now it is possible to define shorthand expression for m independent terms in the full power spectra. In general this term can be defined

$$D^{LM,A}_{ll'} \equiv 2 \alpha_{LM} Z^A_{ll'} H^L_{ll'} \ , \tag{2.184}$$

where $A \in \{BE, EB, TB, BT, TE, ET, EE\}$ for $l \neq l'$ and $A \in \{BE, TE, TB, EE\}$ for $l = l'$. In the case of the BE cross correlation it is easy to see from equation (2.183) that $Z^{BE}_{ll'} = C^{EE}_{l'}$. There are similar expressions for the other $Z^A_{ll'}$. Using $D^{LM,A}_{ll'}$, equation (2.183) can be neatly re-expressed as

$$\langle B_{lm} E^*_{l'm'} \rangle = \sum_{LM} D^{LM,BE}_{ll'} \xi^{LM}_{l m l' m'} \ . \tag{2.185}$$

More generally,

$$\langle X_{lm}(X^*_{l'm'})'\rangle = \sum_{LM} D^{LM,XX'}_{ll'}\xi^{LM}_{lml'm'} \ , \tag{2.186}$$

where $X \in \{T, E, B\}$. The next step is to find an estimator for $D^{LM,A}_{ll'}$. This begins by noting that if $D^{LM,XX',\,\mathrm{map}}_{ll'}$ is built from spherical harmonic coefficients obtained from a map then

$$D^{LM,XX',\,\mathrm{map}}_{ll'} = D^{LM,XX'}_{ll'} W^b_l W^b_{l'} \tag{2.187}$$

where W^b_l is the beam window function defined as $W^b_l = \exp(-l(l+1)\sigma_b^2/2)$ and $\sigma_b = \theta_{\mathrm{FWHM}}/8\ln 2$. As seen in [87] in the minimum variance estimator for $D^{LM,XX',\,\mathrm{map}}_{ll'}$ is obtained by multiplying both sides of the expression in (2.186) by $\xi^{L'M'}_{lml'm'}$ and taking the sum over m and m' to give

$$\widehat{D}^{LM,XX',\,\mathrm{map}}_{ll'} = \left[\sum_{mm'}(\xi^{LM}_{lml'm'})^2\right]^{-1} \sum_{mm'} X^{\mathrm{map}}_{lm} X^{\mathrm{map}}_{l'm'}\xi^{LM}_{lml'm'} \ . \tag{2.188}$$

Note that the X^{map}_{lm} are the harmonic space fields that correspond to the observed real space maps, and are therefore convolved with a Gaussian beam. To simplify the notation,

$$G^L_{ll'} \equiv \sum_{mm'}(\xi^{LM}_{lml'm'})^2 = \frac{(2l+1)(2l'+1)}{4\pi} \ . \tag{2.189}$$

The final term in this expression is shown to be true in the appendix of [38]. The estimator $\hat{D}^{LM,XX',\,\mathrm{map}}_{ll'}$ is a useful quantity as it is a measured quantity from which the value α_{LM} can be found. This is the case because $D^{LM,A}_{ll'}$ is directly related to α_{LM} as seen in (2.184). Therefore, it is straightforward to infer from equation (2.184) that the estimator for α_{LM} is related to $\hat{D}^{LM,XX',\,\mathrm{map}}_{ll'}$ as

$$(\hat{\alpha}_{LM})^A_{ll'} = \frac{\widehat{D}^{LM,A,\,\mathrm{map}}_{ll'}}{F^{L,A}_{ll'}} \ , \tag{2.190}$$

where

$$F^{L,A}_{ll'} \equiv 2Z^A_{ll'} H^L_{ll'} W^b_l W^b_{l'} \ . \tag{2.191}$$

Defining the estimator for α_{LM} in this way is useful as $(\hat{\alpha}_{LM})^A$ is proportional to $\hat{D}^{LM,A,\,\mathrm{map}}_{ll'}$ meaning that the covariance of $(\hat{\alpha}_{LM})^A$ is found entirely in terms of the covariance of the estimator $\widehat{D}^{LM,A,\,\mathrm{map}}_{ll'}$ scaled by factors of $F^{L,A}_{ll'}$. The covariance of $\hat{D}^{LM,A,\,\mathrm{map}}_{ll'}$ is defined as

$$\mathcal{C}^{ll'}_{AA'} \equiv G^L_{ll'}\left(\left\langle \widehat{D}^{LM,A,\,\mathrm{map}}_{ll'}\widehat{D}^{LM,A',\,\mathrm{map}}_{ll'}\right\rangle - \left\langle \widehat{D}^{LM,A,\,\mathrm{map}}_{ll'}\right\rangle\left\langle \widehat{D}^{LM,A',\,\mathrm{map}}_{ll'}\right\rangle\right) \ . \tag{2.192}$$

The total minimum variance estimator $\hat{\alpha}_{LM}$ is found by summing $(\hat{\alpha}_{LM})^A$ over A, and inverse variance weighting this sum by the total covariance. Therefore, the total estimator is

$$\hat{\alpha}_{LM} = \sigma^2_{\alpha_{LM}} \sum_{l'\geq l}\sum_{AA'} F^{L,A'}_{ll'}\widehat{D}^{LM,A,\,\mathrm{map}}_{ll'}\left[(\mathcal{C}^{ll'})^{-1}\right]_{AA'} \ , \tag{2.193}$$

and the noise for the estimator is

$$\sigma^2_{\alpha_{LM}} = \left(\sum_{l' \geq l} G^L_{ll'} \sum_{AA'} F^{L,A}_{ll'} F^{L,A'}_{ll'} \left[(\mathcal{C}^{ll'})^{-1} \right]_{AA'} \right)^{-1} . \tag{2.194}$$

This is the value of the noise on the anisotropic birefringence power spectrum if it is measured using information from the range of polarisation maps and cross spectra. It is often necessary to know the variance for the estimator when α_{LM} is found using single power spectrum or cross correlation spectrum. In the case of the EB cross correlation, the estimator is

$$\hat{\alpha}_{LM} = \sigma^2_{\alpha_{LM}} \sum_{l' \geq l} (1 + \delta_{ll'})^{-1} G^L_{ll'} \left(\frac{F^{L,BE}_{ll'} \widehat{D}^{LM,BE,\,\mathrm{map}}_{ll'}}{C^{BB,\,\mathrm{map}}_l C^{EE,\,\mathrm{map}}_{l'}} + \frac{F^{L,EB}_{ll'} \widehat{D}^{LM,EB,\,\mathrm{map}}_{ll'}}{C^{EE,\,\mathrm{map}}_l C^{BB,\,\mathrm{map}}_{l'}} \right) , \tag{2.195}$$

with a variance of

$$\sigma^2_{\alpha_{LM}} = \left[\sum_{l' \geq l} (1 + \delta_{ll'})^{-1} G^L_{ll'} \left(\frac{(F^{L,BE}_{ll'})^2}{C^{BB,\,\mathrm{map}}_l C^{EE,\,\mathrm{map}}_{l'}} + \frac{(F^{L,EB}_{ll'})^2}{C^{EE,\,\mathrm{map}}_l C^{BB,\,\mathrm{map}}_{l'}} \right) \right]^{-1} . \tag{2.196}$$

This QE is then used to estimate, $\hat{\alpha}_{LM}$ and, therefore, $\alpha(\hat{\mathbf{n}})$. From $\hat{\alpha}_{LM}$ the power spectrum $\widehat{C}^{\alpha\alpha}_L$ is found and a model dependent likelihood approach is used to constrain the amplitude of $\widehat{C}^{\alpha\alpha}_L$ [43], [81].

There are a range of different combinations of correlation that can be used in the QE. However, the EB correlations result in a comparatively lower variance than other choices of correlations in the majority of cases. Moreover, including other choices of correlations does not offer significant improvement over using EB alone [29].

2.6 Instrument systematics and the CMB B-modes

2.6.1 The importance of systematics diagnosis for *B*-mode detection

As the sensitivity of CMB polarization experiments continues to improve, with upcoming experiments such as LiteBIRD [88] and Simons Observatory [16] predicting unprecedentedly low levels of statistical instrument noise, a major concern in the search for primordial B-modes are systematic effects arising from imperfections in the instrument. With the low levels of expected instrument noise in future and contemporary experiments, systematic effects that generate distortions in the CMB maps are expected to have a relatively large impact on measurements of CMB polarization. Indeed, many systematic effects such as a differential detector gain can generate a spurious B-mode signal [89]. Therefore it will be important to diagnose and remove these systematics in order for robust claims of primordial B-mode detection to be made, or for strong constraints to be placed on the value of the tensor-to-scalar ratio, r.

It may be possible to use the CMB distortions generated by systematic effects in the instrument to diagnose the systematic effects using a QE, and potentially remove these distortions from the CMB maps [28]. In order to carry this out one must be able to correctly relate the distortions to their corresponding instrument systematics. There are two parts to this process; (i) characterizing a particular CMB distortion in terms of its corresponding instrument systematic and the instrument scan, and (ii) characterizing the effect of the distortion on the CMB maps, and the power spectra of these maps.

2.6.2 The instrument systematic and the scan

In order to assess the impact a systematic will have on the CMB maps, it is necessary to understand the relationship between a given systematic and the distortion it produces. This distortion in the CMB is sourced by a coupling between a particular imperfection in instrument design and the scan pattern of the instrument [89]. A comprehensive formalism describing this coupling is outlined in [90]; this expands on some of the work seen in [89]. The details that are relevant to this thesis are summarised below.

One begins by writing the signal detected in a given pixel as a function of orientation, $S^d(\psi, \hat{\mathbf{n}})$, in terms of the scan, $h(\psi, \hat{\mathbf{n}})$ and the signal in a pixel for a given crossing of that pixel, $S(\psi, \hat{\mathbf{n}})$,

$$S^d(\psi, \hat{\mathbf{n}}) = h(\psi, \hat{\mathbf{n}}) S(\psi, \hat{\mathbf{n}}) \ . \tag{2.197}$$

Here, $\hat{\mathbf{n}} = (\theta, \phi)$, and represents the on-sky latitude and longitude of each pixel respectively, and ψ represents the orientation of the focal plane of the detector with respect to north; the three angles together form the Euler angles for the pointing of the telescope [89]. An arbitrary scan may be described as

$$h(\psi, \hat{\mathbf{n}}) = \frac{2\pi}{N_{\text{hits}}(\hat{\mathbf{n}})} \sum_j \delta(\psi - \psi_j(\hat{\mathbf{n}})) \ , \tag{2.198}$$

where $N_{\text{hits}}(\hat{\mathbf{n}})$ is the number of crossings of a given pixel in the $\hat{\mathbf{n}}$ direction and j represents a discrete element in a set of angles of detector plane orientation for that pixel.

Both the detected signal and the scan may be decomposed as Fourier series into components of different spin, k. Written as a series of spins, the signal in the detectors is

$$S^d(\psi, \hat{\mathbf{n}}) = \sum_k {}_k\tilde{S}^d(\hat{\mathbf{n}}) e^{-ik\psi} \ . \tag{2.199}$$

Much like the real space scan field in (2.198), the Fourier space scan can be written explicitly as a sum over the detector orientations,

$$\tilde{h}_k(\hat{\mathbf{n}}) = \frac{1}{N_{\text{hits}}(\hat{\mathbf{n}})} \sum_j e^{ik\psi_j(\hat{\mathbf{n}})} \ . \tag{2.200}$$

The Fourier space detector signal, ${}_k\tilde{S}^d(\hat{\mathbf{n}})$, is then a convolution of the Fourier space scan, $\tilde{h}_k(\hat{\mathbf{n}})$, and Fourier space signal for each crossing, $\tilde{S}_k(\hat{\mathbf{n}})$ so that

$$ {}_k\tilde{S}^d(\hat{\mathbf{n}}) = \sum_{k'=-\infty}^{\infty} \tilde{h}_{k-k'}(\hat{\mathbf{n}})\tilde{S}_{k'}(\hat{\mathbf{n}}) \ . \tag{2.201} $$

The effect of given instrument systematic coupling to a given scan can then be translated into a detected on-sky signal. That is, this convolution allows the characterization of a systematic sourced CMB distortion in terms of the scan and an instrument effect.

This can be illustrated using the example of a differential detector gain present between two detector pairs. Consider the case where pair differencing is used to extract the polarization signal from the detected CMB signal. Note that the polarization forms the spin-2 portion of the detected signal. By calculating $\tilde{S}_k(\hat{\mathbf{n}})$ in the presence of a differential gain it is possible, using equation (2.201), to write down the resulting spin-2 portion of the detected signal in terms of the scan strategy and differential detector gain for the two detector pairs used in the pair differencing [90]. This gives

$$ \begin{aligned} {}_2\tilde{S}^d(\hat{\mathbf{n}}) &= \tilde{h}_0(\hat{\mathbf{n}})P(\hat{\mathbf{n}}) + \frac{1}{2}\tilde{h}_2(\hat{\mathbf{n}})(\delta g_1 - i\delta g_2)T(\hat{\mathbf{n}}) \\ &+ \frac{1}{4}\tilde{h}_0(\hat{\mathbf{n}})(g_1^A + g_1^B + g_2^A + g_2^B)P(\hat{\mathbf{n}}) + \frac{1}{4}\tilde{h}_4(\hat{\mathbf{n}})(g_1^A + g_2^B - g_2^A - g_2^B)P^*(\hat{\mathbf{n}}) \ . \end{aligned} \tag{2.202} $$

Here, $T(\hat{\mathbf{n}})$ and $P(\hat{\mathbf{n}})$ represent the temperature and polarization parts of the CMB signal. The gains of the detectors in detector pair i are denoted either g_i^A or g_i^B, with the A and B used to distinguish between the detectors in a given pair. The term δg_i represents the differential gain in detector pair i and is defined so that $\delta g_i = g_i^A - g_i^B$. The first term on the right hand side of (2.6.2) represents the polarization signal, unaffected by any distortion. The second term, $\frac{1}{2}\tilde{h}_2(\hat{\mathbf{n}})(\delta g_1 - i\delta g_2)I(\hat{\mathbf{n}})$, represents leakage from temperature to polarization. The remaining terms represent a distortion in the form of an overall amplification of the polarization, however they have a significantly smaller impact in comparison to the temperature to polarization leakage as the temperature signal is significantly larger in amplitude than the polarization signal.

2.6.3 Müller matrices and distortion field

The next step is to characterize how a particular distortion, or a complex set of distortions may impact CMB measurements at the map level, and by extension the measurement of the primordial B-mode signal. To do this a Müller matrix approach can be used. A Müller matrix formalism, used to calculate the impact of particular distortion on the CMB power spectra is described in [91].

Much of this section will follow the analysis found in [91]. The Müller matrix approach

describes the observed Stokes vector $\boldsymbol{s}_{\rm obs} = (T_{\rm obs}, Q_{\rm obs}, U_{\rm obs}, V_{\rm obs})^T$ as follows:

$$\boldsymbol{s}_{\rm obs} = \mathbf{M}\boldsymbol{s} \ , \tag{2.203}$$

where the Müller matrix is defined as

$$\mathbf{M} \equiv \begin{pmatrix} M_{TT} & M_{TQ} & M_{TU} & M_{TV} \\ M_{QT} & M_{QQ} & M_{QU} & M_{QV} \\ M_{UT} & M_{UQ} & M_{UU} & M_{UV} \\ M_{VT} & M_{VQ} & M_{VU} & M_{VV} \end{pmatrix} \ , \tag{2.204}$$

and $\mathbf{s}$ is the Stokes vector defined as $\mathbf{s} \equiv (T, Q, U, V)^T$. When no systematic errors are present $\mathbf{M}$ is merely the identity matrix. Systematics act as small perturbations to the identity matrix giving the different elements of the Müller matrix.

In the simulation the Müller matrix is applied to the Stokes vector formed from the simulated T, Q, and U maps after they have been rotated by $\alpha(\hat{\mathbf{n}})$ to give an observed Stokes vector according to (2.203). By applying different configurations of the systematics in the matrix then calculating the value of $C_L^{\alpha\alpha}$ from the observed maps it is possible to see which systematic effects will have the most profound effect on the measurements of cosmological birefringence.

An expression for the effect of instrument systematics on the cross correlation between the E and B fields is used as an example as to how particular distortions translate to the CMB poer spectra. It is prudent to rewrite the Müller matrix so that it acts on a complex Stokes vector $\boldsymbol{p} = (T, P, P^*, V)^T$. The elements of this Stokes vector have a defined spin, as do the elements of the Müller matrix when using this Stokes vector. Now, equation (2.203) is replaced with

$$\boldsymbol{p}_{\rm obs} = \begin{pmatrix} M_{TT} & M_{TP} & M_{TP^*} & M_{TV} \\ M_{PT} & M_{PP} & M_{PP^*} & M_{PV} \\ M_{P^*T} & M_{P^*P} & M_{P^*P^*} & M_{P^*V} \\ M_{VT} & M_{VP} & M_{VP^*} & M_{VV} \end{pmatrix} \boldsymbol{p} \ . \tag{2.205}$$

Here, $P(\boldsymbol{x})$ is defined as

$$P \equiv (Q + iU)(\hat{\mathbf{n}}) = \int \frac{d^2\boldsymbol{l}}{2\pi}[E(\boldsymbol{l}) + iB(\boldsymbol{l})]e^{2i\phi_{\boldsymbol{l}}}e^{i\boldsymbol{l}\cdot\hat{\mathbf{n}}} \ . \tag{2.206}$$

As calculating the observed Stokes field just involves convolving the true Stokes fields with the Müller matrix, it is possible to write the Fourier space expression [91],

$$\boldsymbol{p}_{obs}(\boldsymbol{l}) = 2\pi\mathbf{M}_{\rm eff}(-\boldsymbol{l})\boldsymbol{p}(\boldsymbol{l}) \ . \tag{2.207}$$

The E and B fields have the following expression in terms of the spin-2 polarization terms:

$$E(\boldsymbol{l}) = \frac{1}{2}\left[P(\boldsymbol{l})e^{-2i\phi_{\boldsymbol{l}}} + P^*(\boldsymbol{l})e^{2i\phi_{\boldsymbol{l}}}\right] , \tag{2.208}$$

$$B(\boldsymbol{l}) = \frac{1}{2i}\left[P(\boldsymbol{l})e^{-2i\phi_{\boldsymbol{l}}} - P^*(\boldsymbol{l})e^{2i\phi_{\boldsymbol{l}}}\right] . \tag{2.209}$$

The estimator for the band-crossspectra for E and B is

$$\hat{C}^{EB}_{b,\,\text{obs}} = \frac{1}{2f_{\text{sky}}\int_b ldl}\int_b d^2\boldsymbol{l} E_{\text{obs}}(\boldsymbol{l})B^*_{\text{obs}}(\boldsymbol{l}) . \tag{2.210}$$

From (2.208) and (2.209) it is easy to see that

$$\begin{aligned} E_{\text{obs}}(\boldsymbol{l})B^*_{\text{obs}}(\boldsymbol{l}) = \frac{1}{4i}\Big[&e^{-2i\phi_{\boldsymbol{l}}}P_{\text{obs}}(\boldsymbol{l})P_{\text{obs}}(\boldsymbol{l})e^{-2i\phi_{\boldsymbol{l}}} - e^{-2i\phi_{\boldsymbol{l}}}P_{\text{obs}}(\boldsymbol{l})P^*_{\text{obs}}(\boldsymbol{l})e^{2i\phi_{\boldsymbol{l}}} \\ &+ e^{2i\phi_{\boldsymbol{l}}}P^*_{\text{obs}}(\boldsymbol{l})P_{\text{obs}}(\boldsymbol{l})e^{-2i\phi_{\boldsymbol{l}}} - e^{2i\phi_{\boldsymbol{l}}}P^*_{\text{obs}}(\boldsymbol{l})P^*_{\text{obs}}(\boldsymbol{l})e^{2i\phi_{\boldsymbol{l}}}\Big] . \end{aligned} \tag{2.211}$$

It is possible to relate this to $\boldsymbol{p}_{\text{obs}}$. First the matrix $\Lambda(\phi_{\boldsymbol{l}})$ can be defined as $\Lambda(\phi_{\boldsymbol{l}}) \equiv \text{diag}(1, e^{-2i\phi_{\boldsymbol{l}}}, e^{2i\phi_{\boldsymbol{l}}})$. Then, consider the matrix $\Lambda(\phi_{\boldsymbol{l}})\boldsymbol{p}_{\text{obs}}(\boldsymbol{l})\boldsymbol{p}^\dagger_{\text{obs}}(\boldsymbol{l})\Lambda^\dagger(\phi_{\boldsymbol{l}})$ with the following form:

$$\begin{aligned} &\Lambda(\phi_{\boldsymbol{l}})\boldsymbol{p}_{\text{obs}}(\boldsymbol{l})\boldsymbol{p}^\dagger_{\text{obs}}(\boldsymbol{l})\Lambda^\dagger(\phi_{\boldsymbol{l}}) = \\ &\qquad\begin{pmatrix} T(\boldsymbol{l})T(\boldsymbol{l}) & T(\boldsymbol{l})P^*(\boldsymbol{l})e^{2i\phi_{\boldsymbol{l}}} & T(\boldsymbol{l})P(\boldsymbol{l})e^{-2i\phi_{\boldsymbol{l}}} \\ e^{-2i\phi_{\boldsymbol{l}}}P(\boldsymbol{l})T(\boldsymbol{l}) & e^{-2i\phi_{\boldsymbol{l}}}P(\boldsymbol{l})P^*(\boldsymbol{l})e^{2i\phi_{\boldsymbol{l}}} & e^{-2i\phi_{\boldsymbol{l}}}P(\boldsymbol{l})P(\boldsymbol{l})e^{-2i\phi_{\boldsymbol{l}}} \\ e^{2i\phi_{\boldsymbol{l}}}P^*(\boldsymbol{l})T(\boldsymbol{l}) & e^{2i\phi_{\boldsymbol{l}}}P^*(\boldsymbol{l})P^*(\boldsymbol{l})e^{2i\phi_{\boldsymbol{l}}} & e^{2i\phi_{\boldsymbol{l}}}P^*(\boldsymbol{l})P(\boldsymbol{l})e^{-2i\phi_{\boldsymbol{l}}} \end{pmatrix}_{\text{obs}} . \end{aligned} \tag{2.212}$$

It is clear from this explicit form that $E_{\text{obs}}(\boldsymbol{l})B^*_{\text{obs}}(\boldsymbol{l}))$ can be written as a sum over the elements in the matrix seen in (2.212),

$$E_{\text{obs}}(\boldsymbol{l})B^*_{\text{obs}}(\boldsymbol{l})) = \frac{1}{4i}\sum_{j,j'=2}^{3}(-1)^{j'+1}\left[\Lambda(\phi_{\boldsymbol{l}})\boldsymbol{p}_{\text{obs}}(\boldsymbol{l})\boldsymbol{p}^\dagger_{\text{obs}}(\boldsymbol{l})\Lambda^\dagger(\phi_{\boldsymbol{l}})\right]_{jj'} . \tag{2.213}$$

For convenience the matrix in (2.213) is relabeled so that

$$\mathbf{C}_{\text{obs}}(\boldsymbol{l}) \equiv \left[\Lambda(\phi_{\boldsymbol{l}})\boldsymbol{p}_{\text{obs}}(\boldsymbol{l})\boldsymbol{p}^\dagger_{\text{obs}}(\boldsymbol{l})\Lambda^\dagger(\phi_{\boldsymbol{l}})\right] . \tag{2.214}$$

Now it is possible to rewrite $\boldsymbol{p}_{\text{obs}}(\boldsymbol{l})$ in terms of the Müller matrix and $\boldsymbol{p}(\boldsymbol{l})$ using the convolution in equation (2.207). By also inserting the identity matrix between the Müller matrices and Stokes vectors one finds the following expression for $\mathbf{C}_{\text{obs}}(\boldsymbol{l})$:

$$\mathbf{C}_{\text{obs}}(\boldsymbol{l}) = 4\pi^2\left[\Lambda(\phi_{\boldsymbol{l}})\mathbf{M}_{\text{eff}}(-\boldsymbol{l})\Lambda^\dagger(\phi_{\boldsymbol{l}})\mathbf{C}(\boldsymbol{l})\Lambda(\phi_{\boldsymbol{l}})\mathbf{M}^\dagger_{\text{eff}}(-\boldsymbol{l})\Lambda^\dagger(\phi_{\boldsymbol{l}})\right] , \tag{2.215}$$

where $\mathbf{C}(\boldsymbol{l})$ has the same form as $\mathbf{C}_{\text{obs}}(\boldsymbol{l})$ but contains the true Stokes vector on the sky, $\boldsymbol{p}(\boldsymbol{l})$, instead of the observed Stokes vector, $\boldsymbol{p}_{\text{obs}}(\boldsymbol{l})$.

By inserting this into (2.210) and taking the ensemble average over realisations of T, Q, and U one finds an expression for the relationship between the EB cross-spectrum effected by the systematics and the true values of the power-spectra and cross-spectra. The form of the expression,

$$\left\langle \widehat{C}^{EB}_{b,\,\mathrm{obs}} \right\rangle = A \sum_{j,j'=2}^{3} (-1)^{j'+1} \int_b l dl d\phi_{\boldsymbol{l}} \left[\Lambda(\phi_{\boldsymbol{l}}) \mathbf{M}_{\mathrm{eff}}(-\boldsymbol{l}) \Lambda^{\dagger}(\phi_{\boldsymbol{l}}) \left\langle \mathbf{C}(\boldsymbol{l}) \right\rangle \Lambda(\phi_{\boldsymbol{l}}) \mathbf{M}^{\dagger}_{\mathrm{eff}}(-\boldsymbol{l}) \Lambda^{\dagger}(\phi_{\boldsymbol{l}}) \right]_{jj'} , \tag{2.216}$$

where the normalization factor, A, is given by

$$A = \frac{\pi^2}{2 i f_{\mathrm{sky}} \int_b l dl} \tag{2.217}$$

can be simplified further by taking the integral over the radial extent of the band, but before this is possible it is necessary to examine $\langle \mathbf{C}(\boldsymbol{l}) \rangle$. Note that this matrix is made up of the true power-spectra and cross-spectra. After taking the integral over the radial extent of the band -and noting that the Müller matrices do not vary over the radial extent of the band- this matrix is instead made up of band power-spectra and cross-spectra. This matrix is labeled $\mathbf{F}_l$ and has the form

$$\mathbf{F}_l = \begin{pmatrix} C_b^{TT} & C_b^{TE} - i C_b^{TB} & C_b^{TE} + i C_b^{TB} \\ C_b^{TE} + i C_b^{TB} & C_b^{EE} + C_b^{BB} - i C_b^{EB} + i C_b^{BE} & C_b^{EE} - C_b^{BB} + i C_b^{EB} + i C_b^{BE} \\ C_b^{TE} - i C_b^{TB} & C_b^{EE} - C_b^{BB} - i C_b^{EB} - i C_b^{BE} & C_b^{EE} + C_b^{BB} + i C_b^{EB} - i C_b^{BE} \end{pmatrix} . \tag{2.218}$$

After taking this integral the expression in (2.216) simplifies to

$$\left\langle \hat{C}^{EB}_{b,\,\mathrm{obs}} \right\rangle = \frac{\pi}{2i} \sum_{j,j'=2}^{3} (-1)^{j'+1} \int_b d\phi_{\boldsymbol{l}} \left[\Lambda(\phi_{\boldsymbol{l}}) \mathbf{M}_{\mathrm{eff}}(-\boldsymbol{l}) \Lambda^{\dagger}(\phi_{\boldsymbol{l}}) \mathbf{F}_l \Lambda(\phi_{\boldsymbol{l}}) \mathbf{M}^{\dagger}_{\mathrm{eff}}(-\boldsymbol{l}) \Lambda^{\dagger}(\phi_{\boldsymbol{l}}) \right]_{jj'} . \tag{2.219}$$

It is then possible to use any possible effective Müller matrix to extract a relatively simple expression for the observed cross-correlation given a known set of systematics parameters.

This formula can be used to capture the effect of distortions on the cross-spectra under for different simple scan strategy cases. In the case of the raster scan the instrument is always treated as being in the fiducial basis. A set of spacial Muller matrix elements which deviate from identity for the receiver can be defined as [91],

$$M_{PT} = \gamma_1 + i\gamma_2 \, , \tag{2.220}$$

$$M_{PP} = 1 + a + 2i\omega \, , \tag{2.221}$$

$$M_{PP^*} = f_1 + i f_2 \, . \tag{2.222}$$

Here, ω represents a rotation of the polarisation orientation, a represents an incorrect calibration of the polarisation amplitude, f_1 and f_2 represent a mixing of Q and U, and γ_1 and

γ_2 represent a leakage from intensity into polarisation. Inserting these into (2.219) gives a simple analytical formula for the observed $C^{EB}_{b,\,\mathrm{obs}}$ cross-spectrum,

$$C^{EB}_{b,\,\mathrm{obs}} = \left[(1+a)^2 - 4\omega^2\right] C^{EB}_b + 2\omega(1+a)(C^{EE}_b - C^{BB}_b)\ . \tag{2.223}$$

An interesting feature of this equation is that it indicates that intensity leakage has no effect on the measurement of $C^{EB}_{b,\,\mathrm{obs}}$. While this derivation follows a flat sky approach it is possible to carry out the derivation on using the full curved sky approach, however, the form of equation (2.223) does not change.

The expression in (2.223) is true only for distortions that do not vary across the sky. However, it is possible to consider anisotropic elements in the Müller matrices that is sky varying distortion fields. If (2.205) is expanded then the individual elements of $\boldsymbol{p}_{\mathrm{obs}}$ can be examined in real and harmonic space. As can be seen in [28], when one translates the results of this expansion to harmonic space the anisotropic distortions generate off diagonal correlations in the CMB covariance matrix, $\langle a_{lm} a^*_{l'm'} \rangle$. These off diagonal correlations are analogous to those generated by weak gravitational lensing [92], [93]. Therefore, as is discussed in [28], it may be possible to exploit these off diagonal correlations using a QE approach to reconstruct and remove the distortion fields in analogy to lensing reconstruction and internal delensing [86], [94], [95].

2.7 Conclusions

While electrodynamics appears to be well understood and well tested it is possible to modify Maxwell's laws so that a cosmological birefringence effect is predicted. It may be possible to observe such an effect and a number of CMB experiments have attempted to make such observations. However, better experiments with greater precision are required in order to constrain both a uniform and anisotropic birefringence signal further.

Experiments that will attempt to do so include Simons Observatory, and CMB S4, indeed forecasting for observations of the birefringence anisotropies for CMB S4 has already been carried out [70]. However, forecasting for a uniform birefringence effect must still be carried out for CMB S4. Moreover, forecasting for observations of both a uniform and an isotropic birefringence effect must still be carried out for Simons Observatory.

There has been a thorough theoretical investigation of the modifications that lead to the cosmological birefringence effect. However, it may still be necessary to further investigate other cosmological implications of the various models that predict cosmological birefringence in order to understand the physical implications of such models better. It may be possible that a number of such models may be ruled out by observations unrelated to birefringence. This would narrow the list of potential science targets for birefringence experiments, and possibly constrain the expected range of polarisation rotation angles. Further constraints on the cos-

mological birefringence effect - both uniform and anisotropic - will place further constraints on parity and possibly Lorentz violations, on models of axion inflation, and on the coupling between axion-like particles and the gauge field.

Quadratic estimators will play a large role in the constraint or potential detection of the birefringence effect. These tools are used as standard in CMB lensing research, and can be deployed whenever an effect induces non-zero correlations in the off-diagonal modes of the CMB covariance. It may also be possible to extend the use quadratic estimators to diagnose and remove distortions sourced by instrument systematics. This would compliment existing systematics cleaning techniques by quantifying the effectiveness of existing cleaning techniques and diagnosing and removing any residual distortions after traditional systematics mitigation has been carried out.

It is also worth noting that for the *Planck* experiment, a QE was not used to reconstruct the anisotropic birefringence field [67], [78]. Carrying out a QE analysis on the *Planck* data would provide an important compliment to the existing constraints as well as acting as an additional cross check of the existing constraints. Additionally, as the technique that has already been applied to the *Planck* data to search for anisotropic birefringence does not probe off diagonal correlations in the CMB covariance a QE will be required to detect any possible signatures of birefringence, other new physics, or unknown instrument systematics that may be encoded in these correlations.

Chapter 3

Uniform Birefringence Forecast

3.1 Introduction

In the coming years a number up upcoming CMB experiments will attempt to place constraints on the primordial CMB B-mode polarization signal. Two significant experiments that are under development are the Simons Observatory (SO), and CMB-S4. SO is expected to have first light in 2022 and begin its five year survey in 2023 [96], while CMB-S4 is still in the project development phase [37]. However, both promise to provide a measurement of the CMB polarization with unprecedented levels of precision and by measuring the primordial B-mode signal they promise to probe the tensor-to-scalar ratio r down to $r > 3 \times 10^{-3}$ in the case of SO [16] and down to $r > 1 \times 10^{-3}$ in the case of CMB-S4 [97].

However, while these experiments seek to detect B-modes sourced by primordial gravitational waves, this is not the only source of B-mode polarization. In Chapter 2 of this thesis we saw that modifications to electrodynamics could generate a rotation of linearly polarized photons as they propogate on cosmological scales in an effect called cosmological birefringence (CB). Such a rotation would induce mixing between the E- and B-modes resulting in B-mode power in addition to the primordial signal.

This modification to electrodynamics was discussed in detail in Chapter 2 and involves the inclusion of a Chern-Simons term in the electrodynamics Lagrangian [25], [27],

$$\mathcal{L}_{CS} = -\frac{\beta\phi}{2M} F_{\mu\nu}\tilde{F}^{\mu\nu} \ , \tag{3.1}$$

where $F_{\mu\nu}$ is the electromagnetic field strength tensor, $\tilde{F}^{\mu\nu}$ is the dual of the field strength tensor, β is a coupling constant, ϕ is a pseudo scalar, and M is a parameter with dimensions of mass that is dependent on the particular origin for this coupling between a pseudo scalar and the photon [27], [42], [44]. If this field does not vary spatially then this modification to Maxwell's laws will lead to a rotation of linearly polarized photons with rotation angle,

$$\alpha = \frac{\beta}{M} \int \frac{\partial\phi}{\partial\eta} d\eta \ , \tag{3.2}$$

where η is conformal time. This indicates that the rotation is dependent only on the initial

and final amplitude of the pseudo scalar so that

$$\alpha = \frac{\beta}{M}\delta\phi \ . \tag{3.3}$$

A more general approach is to consider a spatially varying pseudo scalar then this rotation angle is replaced by a direction dependent rotation field $\bar{\alpha}(\hat{\mathbf{n}})$ with

$$\bar{\alpha}(\hat{\mathbf{n}}) = \frac{\beta}{M}\int d\eta \left(\frac{\partial}{\partial\eta} + \hat{\mathbf{n}}\cdot\boldsymbol{\nabla}\right)\phi(\eta,\hat{\mathbf{n}}) \ . \tag{3.4}$$

This field can be thought of as a background uniform rotation field with direction dependent perturbations such that

$$\bar{\alpha}(\hat{\mathbf{n}}) = \alpha_0 + \alpha(\hat{\mathbf{n}}) \ . \tag{3.5}$$

Here, the background rotation α_0 is equivelant to the rotation angle for a spatially invariant field with the same dependence on ϕ. Throughout the rest of this chapter we denote the uniform CB angle α_0

As the possible models for the ϕ [27], [42] predict that it will vary on cosmological timescales we expect that α_0 would only have an observable rotational effect on polarized photons sourced at extremely high redshift, such as CMB photons. Indeed, it may be possible to use observations of the CMB power spectra to measure the uniform rotation angle by looking for mixing between the C_l^{EE}, and C_l^{BB} power-spectra, and non zero C_l^{EB} and C_l^{TB} cross-spectra due to this mixing. As SO and CMB-S4 are expected to make highly sensitive measurments of the CMB polarization and the corresponding CMB spectra they will be well placed to probe this rotation angle.

The focus of this chapter will be on forecasting the sensitivity that both SO and CMB-S4 will have to the uniform CB angle. This will amount to a forecast of the constraint on α_0 in the case of no detection of any rotation. Section 3.2 describes the Fisher forecast technique we employ, and the instrument setup assumed for SO and CMB-S4. In Section 3.3 we present the results of the forecast for both the SO Small Aperture Telescope (SAT) and the Large Aperture Telescope (LAT). Where the LAT is designed for better angular resolution, the SAT has a larger field of view, and is expected to be able to provide better control over noise from the atmosphere giving more precise measurments on larger angular scales [16]. Along with these forecasts we discuss which spectra are likely to give the best constraining power for both the LAT and SAT. Finally, in Section 3.3.4 we present the forecast for CMB-S4 along with an analysis of where the constraining power for S4 is likely to be the strongest.

3.2 The Fisher forecast for uniform cosmic rotation

3.2.1 Estimating the parameter sensitivity of CMB experiments

In order to successfully forecast the sensitivity of a particular experiment to CB effects we must take into account degeneracy between different cosmological parameters, and α_0. It is possible to use a technique called Fisher analysis to do this. Fisher analysis involves the construction of a Fisher matrix, which corresponds to the second order term in an expansion of the log of the likelihood for a given set of parameters in theory space [55]. From the Fisher matrix it is possible to directly calculate the estimate an experiment may have to a given parameter by marginalising over the other parameters. This is done by inverting the Fisher matrix to give [56]

$$[F]^{-1} = \begin{pmatrix} \sigma_i^2 & \sigma_{ij} \\ \sigma_{ij} & \sigma_j^2 \end{pmatrix} , \tag{3.6}$$

noting that the diagonal terms give the errors of each parameters marginalized over the others. In this example σ_i is the 1σ uncertainty on parameter i marginalized over parameter j [56].

For cosmological parameters the Fisher matrix can be constructed from a covariance matrix which contains the covariances between different power spectra and cross correlation spectra. Constructed in this way the Fisher matrix is [50]

$$\mathcal{F}_{ij} = f_{\text{sky}} \sum_l \sum_{A,A'} \frac{\partial C_l^A}{\partial x_i} \left[M^{-1}\right]_{AA'} \frac{\partial C_l^{A'}}{\partial x_j} . \tag{3.7}$$

Here, f_{sky} is used when taking into account the increased variance due to partial sky coverage, and here, $A \in [TT, EE, BB, TE, TB, EB]$. The parameters are x_i. In the case of uniform birefringence forecasts one parameter will be α_0 and the other parameters will be the set of six standard cosmological parameters. The covariance matrix $M_{AA'}$ is defined as [9]

$$M_{AA'} \equiv \left\langle \widehat{C_l^A} \widehat{C_l^{A'}} \right\rangle - C_l^A C_l^{A'} , \tag{3.8}$$

the $\widehat{C}_l^A$ terms are estimators and the C_l^A are the full ensemble averages $C_l^A = \left\langle a_{lm}^X (a_{lm}^{X'*})' \right\rangle$. The estimators are defined as [9]

$$\widehat{C}_l^{XX'} = \frac{1}{2l+1} \sum_{m=-l}^{l} a_{(lm)}^{X*} a_{(lm)}^{X'} , \tag{3.9}$$

where, $X, X' \in [T, E, B]$ so that $A = XX'$. For practical purposes in our forecast we calculate the form of the elements of the covariance matrix analytically, in terms of theory spectrum for the fiducial model, $\tilde{C}_l^{XX'}$ and noise spectrum for the relevant instrument, $N_l^{XX'}$.

For example, the on diagonal element for temperature M_{TTTT} is

$$M_{TTTT} = \frac{2}{2l+1}(\tilde{C}_l^{TT} + N_l^T)^2 \ . \tag{3.10}$$

For details of how these elements are calculated see Section 2.4.4 in Chapter 2 or see the covariance matrix calculation in [9].

For the Fisher forecast we use numerical derivatives, which, for the parameter x_i, have the form

$$\frac{\partial C_l^A(x_i)}{\partial x_i} \approx \frac{C_l^A(x_i + \delta x_i) - C_l^A(x_i - \delta x_i)}{2\delta x_i} \ , \tag{3.11}$$

where the power spectrum $C_l^A(x_i)$ is a function of the parameter x_i, and δx_i is a perturbative change to the parameter. For the standard cosmological parameters in our forecast we compute $C_l^A(x_i \pm \delta x_i)$ by injecting the perturbed parameter values $x_i \pm \delta x_i$ into the Boltzmann package CAMB [98] and computing the corresponding spectra.

As CB is non-standard cosmology there is no corresponding parameter in CAMB. Instead for the α_0 parameter we begin by noting that in our fiducial model $\alpha_0 = 0$. This means we will only need the spectra for rotation angles of $\pm\delta\alpha_0$. In order to find $C_l^A(\pm\delta\alpha_0)$ we compute the theory spectra for the fiducial model, $\tilde{C}_l^A$, using CAMB. From these, we calculate the CB rotated spectra, $C_l^A(\pm\delta\alpha_0)$, directly. The CMB spectra for rotation angles of $\pm\delta\alpha_0$ are [47], [49],

$$C_l^{EE}(\pm\delta\alpha_0) = \tilde{C}_l^{EE}\cos^2(\pm 2\delta\alpha_0) + \tilde{C}_l^{BB}\sin^2(\pm 2\delta\alpha_0) \ , \tag{3.12}$$

$$C_l^{BB}(\pm\delta\alpha_0) = \tilde{C}_l^{EE}\sin^2(\pm 2\delta\alpha_0) + \tilde{C}_l^{BB}\cos^2(\pm 2\delta\alpha_0) \ , \tag{3.13}$$

$$C_l^{TE}(\pm\delta\alpha_0) = \tilde{C}_l^{TE}\cos(\pm 2\delta\alpha_0) \ , \tag{3.14}$$

$$C_l^{TB}(\pm\delta\alpha_0) = \tilde{C}_l^{TE}\sin(\pm 2\delta\alpha_0) \ , \tag{3.15}$$

$$C_l^{EB}(\pm\delta\alpha_0) = \frac{1}{2}\left(\tilde{C}_l^{EE} - \tilde{C}_l^{BB}\right)\sin(\pm 4\delta\alpha_0) \ . \tag{3.16}$$

These derivatives combined with the covariance for the particular instrument model considered are used to produce the Fisher matrix and therefore the CB forecast.

3.2.2 Instrument setup and fiducial cosmology

The particular instrument noise and beam, fiducial cosmology, and choice of l mode range all form the key inputs in our forecast. The particular fiducial cosmological model we use, as presented in Table 3.1 are based on the *Planck* 2018 parameter results [99]. We attempt to emulate the forecasting setups of SO [16] and CMB-S4 [97] as closely as possible. We set our l ranges in accordance with the guidelines in the CMB-S4 science book [14], and SO parameter forecasts in [16].

For SO LAT and SAT we use the SO-V3 noise code to generate noise curves for the 93GHz

and 145GHz frequency channels for the threshold, baseline, and goal noise settings . The forecast is carried out for these channels as they are predicted to provide the strongest constraints on physical parameters [16]. We list the instrument sensitivities that correspond to these noise curves in Table 3.1. This code is designed not only to take into account the instrument sensitivity and beam but also atmospheric contributions to the noise. Note that while we include the threshold noise case in our forecast, at the time of writing of this thesis SO has ceased including the threshold case in their own forecasting, as it is anticipated that the instrument will far exceed this more pessimistic noise projection [16]. As with the SO forecast in [16] we use a different l range for the temperature and polarization spectra for the LAT.

The multipole range and sky coverage for the CMB-S4 forecasting requirements are similar to what is used for the SO LAT forecast [97]. For CMB-S4 no noise modeling code is provided. Instead we assume a simple noise spectrum consisting of the instrument sensitivity and the beam such that,

$$N_l^P = \sqrt{2} N_l^T = 2 w_T^{-2} |W_l^b|^{-2} \,, \tag{3.17}$$

where N_l^P is the polarization noise spectrum, N_l^T is the temperature noise spectrum, w_T^{-1} is the temperature sensitivity and W_l^b is the beam window function. Note that in this chapter we present the noise sensitivity, w^{-1}, in units of $[\mu\text{K arcmin}]$ as is common in the literature [16], [37], [88]. The values for the temperature sensitivity, beam, sky coverage, and multipole coverage are summarized in Table 3.1.

We include the effect of combining the *Planck* data with SO LAT and CMB-S4 by building an ad-hoc Planck instrument model. For this model we generate a Fisher matrix that can then be combined with the SO and S4 Fisher matrices. We used the noise and beam characteristics summarized in [100]. The *Planck* model includes noise and beam characteristics for each of the individual channels. The included channels are $\nu \in [100\text{GHz}, 143\text{GHz}, 217\text{GHz}, 353\text{GHz}, 545\text{GHz}, 857\text{GHz}]$. The effective temperature and polarization sensitivity, $w_{T/P}^{-1}$ and the average effective beam full width at half maximum (FWHM), $\theta_{\text{FWHM, avg.}}$, is given in Table 3.1. Also included in this table are the instrument characteristics and l ranges for SO LAT, SO SAT, and CMB-S4.

We validate our Fisher code and instrument models by comparing the forecast uncertainty, σ_{x_i}, for the fiducial model parameters, excluding α_0, to the existing SO and CMB-S4 forecasts. We find that results that our values for σ_{x_i} match the existing forecasts to within less than 10% for SO and CMB-S4. Any difference in the predictions are due to differences between the methods used to include *Planck* data in the forecasts. However, we do not expect these differences to have a significant impact on the validity of our forecasts as we find a negligible difference in σ_{α_0} between predictions made with *Planck* and predictions made without *Planck*.

	parameter	value
cosmological	H_0 $\left[\mathrm{km\,s^{-1}Mpc^{-1}}\right]$	69.0
	$\Omega_b h^2$	0.0222
	$\Omega_c h^2$	0.120
	τ	0.06
	n_s	0.966
	A_s	2.2×10^{-9}
	α	0.0
SO LAT instrument	l_{min}	30
	l^T_{max}	3000
	l^P_{max}	5000
	w_t^{-1} [μK arcmin]	7.54
	w_b^{-1} [μK arcmin]	6.26
	w_g^{-1} [μK arcmin]	4.25
	θ_{FWHM} [arcmin]	2.2
SO SAT instrument	l_{min}	30
	$l^{T/P}_{\mathrm{max}}$	400
	w_t^{-1} [μK arcmin]	3.72
	w_b^{-1} [μK arcmin]	2.81
	w_g^{-1} [μK arcmin]	1.89
	θ_{FWHM} [arcmin]	30
CMB-S4 instrument	l_{min}	30
	$l^{T/P}_{\mathrm{max}}$	5000
	w_T^{-1} [μK arcmin]	1
	θ_{FWHM} [arcmin]	3
Ad-hoc *Planck* instrument	l_{min} $f_{\mathrm{sky}} = 0.8$	1
	$l^{T/P}_{\mathrm{max}}$ $f_{\mathrm{sky}} = 0.8$	30
	l_{min} $f_{\mathrm{sky}} = 0.2$	30
	$l^{T/P}_{\mathrm{max}}$ $f_{\mathrm{sky}} = 0.2$	2500
	w_T^{-1} [μK arcmin]	19.7
	w_P^{-1} [μK arcmin]	27.1
	$\theta_{\mathrm{FWHM,\,avg.}}$ [arcmin]	6.46

Table 3.1: The fiducial cosmological model parameters for the Fisher forecast for CB for SO and CMB-S4. There parameters are based on the *Planck* 2018 results [99]. Also shown are the l ranges, white noise, and beam for CMB-S4, SO and *Planck*. The w_t^{-1}, w_b^{-1}, and w_g^{-1} are the temperature sensitivities for the threshold, baseline and goal cases respectively. For SO and CMB-S4 the polarization sensitivity is $w_P^{-1} = \sqrt{2}\, w_T^{-1}$. Note that for SO LAT a separate l_{max} value is used for temperature and polarization (indicated respectively with a T and P superscript).

3.3 Forecast results

3.3.1 The SO LAT forecast

For the SO LAT forecast we make predictions for 1σ α_0 constraints for three different values of sky coverage, including a 10% sky patch, a 20% sky patch and a 40% sky patch. The expected sky coverage of the LAT is 40%. Sky coverage will have an impact on the number

of noise modes included in the measurement of the parameter, and will increase the variance of the measurement due to the reduced number of modes included in the measurement. That is, the SO-V3 noise code calculates the noise as a function of integration time, noise effective temperature, $\sigma_{\rm NET}$, and sky area surveyed so that

$$N_l^T = \left(\frac{4\pi f_{\rm sky} \sigma_{\rm NET}^2}{t} + A_{\rm atm} \right) |W_l^b|^{-2} \ . \tag{3.18}$$

Here, $A_{\rm atm}$ is the atmospheric contribution to the noise and t is integration time. The amplitude of the noise power spectrum will increase as sky coverage increases proportional to $f_{\rm sky}$, and the overall variance will decrease by a factor of $f_{sky}^{-1/2}$. This leads to the behavior we see in the highest noise threshold, and baseline cases in Figure 3.1. For both of these settings the contribution of N_l^T to the variance is proportionally larger than the contribution of cosmic variance when compared with the goal case. In both the baseline and threshold cases N_l^T becomes the dominant contribution to the variance, and as N_l^T increases with $f_{\rm sky}$ so does the variance, once $f_{\rm sky} > 0.25$. In the goal case, the dominant contribution to the variance is cosmic-variance. As this is the case the overall variance is seen to decrease with increasing $f_{\rm sky}$.

We find an expected constraint of $\sigma_{\alpha_0} \sim 10^{-2}$ [degrees]. The strongest constraint that we forecast, from the most optimistic goal noise setting and largest sky coverage is $\sigma_{\alpha_0} = 6.06 \times 10^{-3}$ [degrees]. The sky coverage does not appear to have as significant an impact on the constraint as different levels of noise. This is positive, as any loss of sky coverage during the scan should not significantly impact the SO LAT constraint on α_0. This forecast is unchanged when the Planck Fisher data is not included, possibly indicating that it may not be necessary to included Planck in further forecasts for birefringence.

To further test the behavior of σ_{α_0} with different noise levels we carry out our forecast while varying the amplitude of the LAT noise curves. This is equivalent to varying the instrument sensitivity for the 93GHz and 145GHz channels. We use the same values of $f_{\rm sky}$ as in the previous forecasts. We see in figure 3.2 a more interesting relationship between the constraint and f_{sky} that what was initially seen in Figure 3.1. The constraint on α_0 is more sensitive to noise for smaller values of $f_{\rm sky}$. That is, the constraint appears to weaken more quickly with increasing instrument sensitivity when the sky coverage is smaller.

3.3.2 Where is the LAT's constraining power

In order to investigate which power spectrum provides the largest contribution to the constraint on α_0 from the LAT we calculate the signal-to-noise (S/N) ratio for the different possible CMB power spectrum and cross correlations. By calculating the S/N per l value we can see which modes are contributing the most to this constraint. The signal to noise for a given spectrum

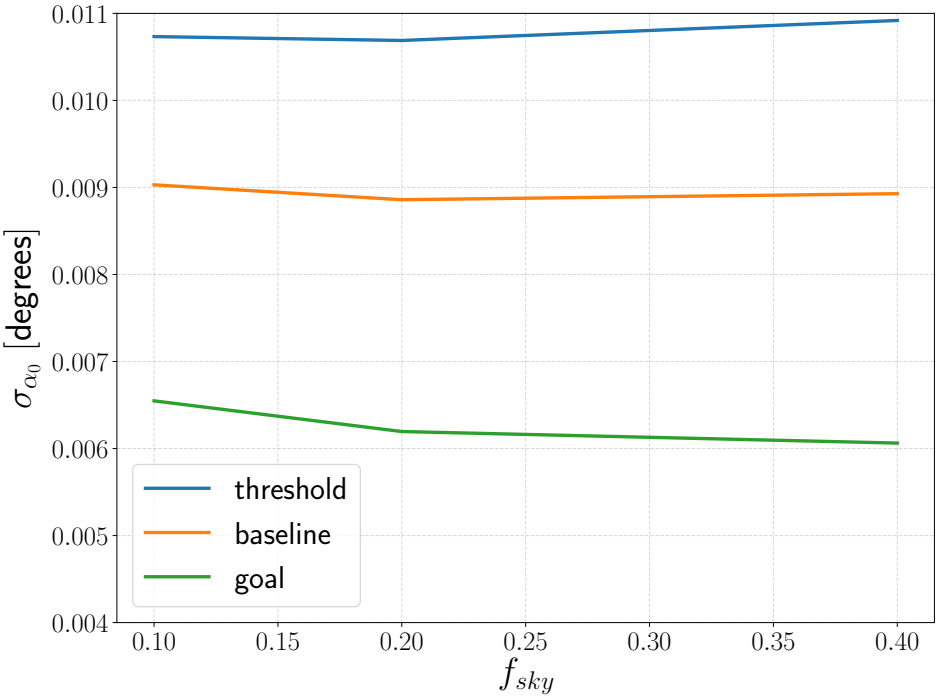

Figure 3.1: The forecast uncertainty on α_0, σ_{α_0} plotted for $f_{\rm sky} = 0.4$, 0.2, and 0.1. We show the uncertainty for three LAT sensitivity modes of the SO-V3 noise code including the most pessimistic threshold mode (blue), the baseline mode(orange), and the most optimistic goal mode (green).

is given as

$$\left(\frac{S}{N}\right)^2 = \sum_l \left(\frac{C_l^{XX',\rm rot} - C_l^{XX'}}{\Delta C_l^{XX',\rm rot}}\right)^2 . \tag{3.19}$$

Here $X \in \{T, E, B\}$, $C_l^{XX',\rm rot}$ indicates the spectrum after it has been affected by cosmological birefringence equivalent and is equivalent to $C_l^A(\alpha_0)$. We carry out this study assuming $\alpha_0 = 10^{-2}$ [degrees] for the rotated spectrum. This is the same order of magnitude as the constraint from LAT. Here, $C_l^{XX'}$ is a spectrum unaffected by the birefringence equivalent to $C_l^A(0)$. The $\Delta C_l^{XX',\rm rot}$ term indicates the standard deviation the CB rotated spectrum,

$$\begin{aligned}\Delta C_l^{XX',\rm rot} = \sqrt{\frac{1}{f_{\rm sky}(2l+1)}}\Big[&(C_l^{XX',\,\rm rot} + N_l^{XX'})^2 \\ &+ (C_l^{XX,\,\rm rot} + N_l^{XX})(C_l^{X'X',\,\rm rot} + N_l^{X'X'})\Big]^{\frac{1}{2}} .\end{aligned} \tag{3.20}$$

For the purpose of calculating the S/N ratio we set the l range to $30 \leq l \leq 5000$ for both the temperature and polarization spectrum, and fix the sky coverage to the expected value of $f_{\rm sky} = 0.4$ for the LAT. When calculating the standard deviation we use the baseline noise mode. The resulting S/N for α_0 from each spectrum is displayed in Table 3.2. It is easy to infer from these results that the best constraining power comes from C_l^{EB}, with the highest

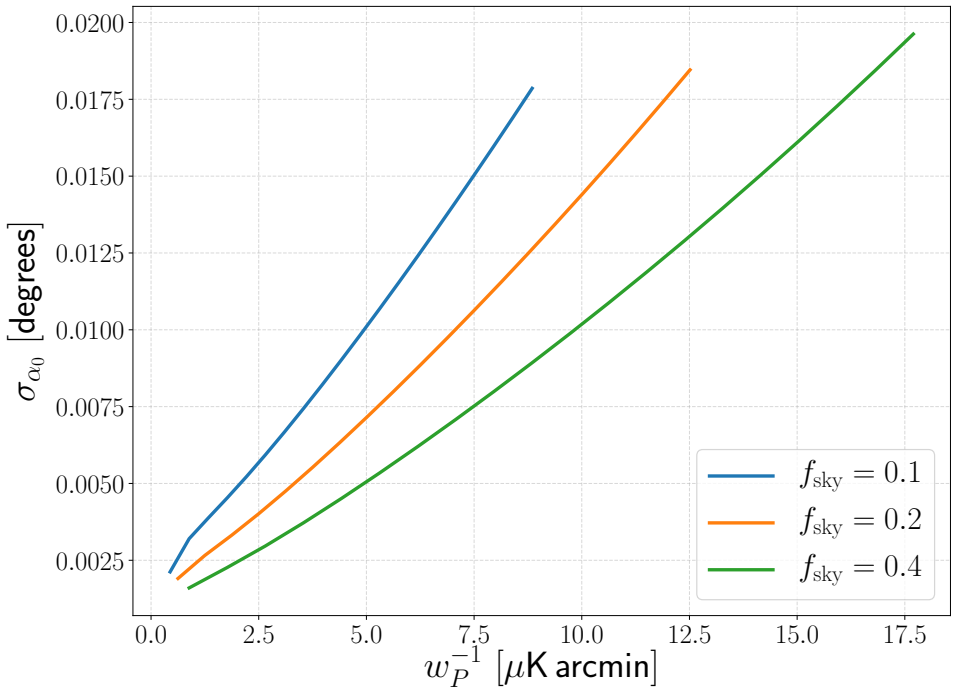

Figure 3.2: The uncertainty on α_0 as a function of polarization noise sensitivity, w_P^{-1}, for the SO LAT. We show curves for 40% (green), 20% (orange), and 10% (blue) sky coverage.

XX'	S/N
EE	8.88×10^{-5}
BB	1.0×10^{-3}
TE	8.88×10^{-5}
TB	0.35
EB	1.06

Table 3.2: The S/N ratios for α_0 as found using each CMB power spectrum or cross correlation expected to be measured using the LAT. Here, the noise mode is set to baseline and $f_{\rm sky} = 0.4$. We used a fixed multipole range of $30 \leq l \leq 5000$.

signal to noise. However, while the S/N of C_l^{TB} is $\sim 1/3$ of the C_l^{EB} S/N, it is still large enough that we expect it to make a significant contribution to the constraint on α_0. As the remaining spectrum have a significantly smaller S/N they are not expected to provide significant additional constraining power. For the best possible constraints on α_0 both C_l^{EB} and C_l^{TB} should be used.

We can go beyond calculating which spectrum provides the largest contribution to the constraint and also consider which specific l modes have the strongest constraining power. We do this by examining the S/N at each l, as shown in figure 3.3. We find that the best constraining power for the LAT should come from the C_l^{EB} cross correlation in a range of $30 \leq l \leq 2000$ with a significant reduction in constraining power with increasing l when $l \gtrsim 2000$.

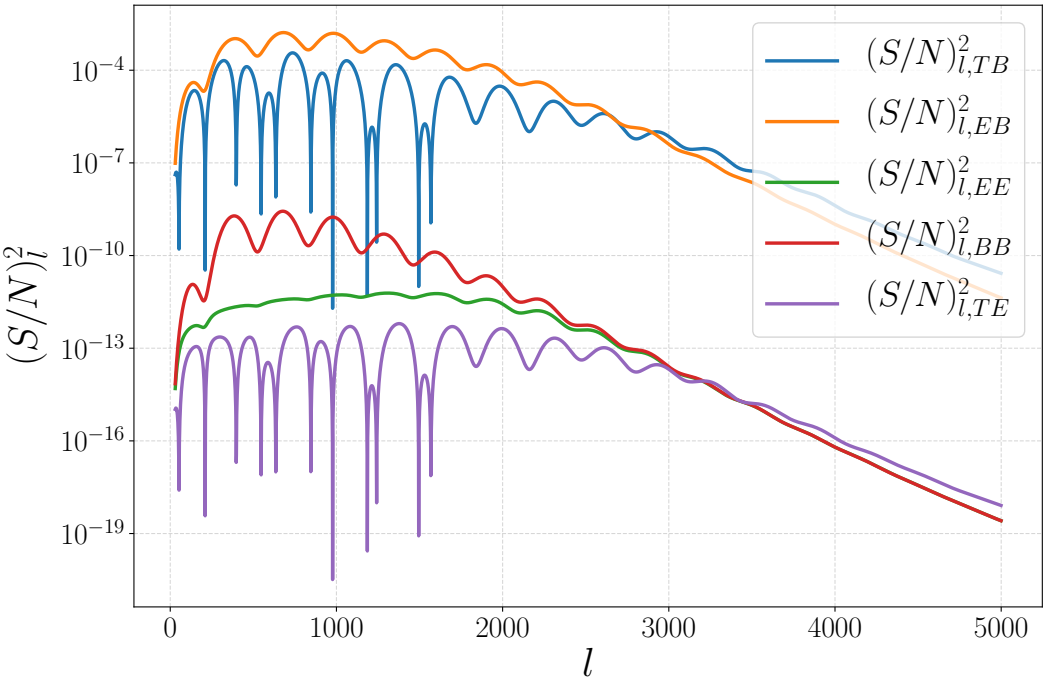

Figure 3.3: The square of the signal to noise ratio at each l for α_0 from SO LAT observations of the C_l^{TB} (blue), C_l^{EB} (orange), C_l^{EE} (green), C_l^{BB} (red), and C_l^{TE} (purple) spectra. The modes for which the square of S/N is largest provide the strongest contribution to the constraint on α_0. Here, $f_{\rm sky} = 0.4$, the noise mode is set to baseline and $30 \leq l \leq 5000$.

3.3.3 The SO SAT forecast

In order to assess which of the SAT or LAT will provide the strongest constraint we carry out a σ_{α_0} forecast for the SAT. We once again carry out our forecast for the 1σ constraints, for the 143GHz and 93GHz channels. The SAT temperature noise is not included in the V3 code as the it is not expected that the temperature spectrum will be used in scientific analysis of SAT data[16]. Therefore, we do not include the correlations with the temperature spectrum in our forecast. For the SAT forecast σ_{α_0} we use the threshold, baseline, and goal sensitivity modes. The V3 code allows the setting of an optimistic and pessimistic modes for the $1/f$ noise [101] for the SAT. The $1/f$ noise is expected to have a significant contribution on larger angular scales, most relevant to the SAT [16]. The $1/f$ noise generates an additional l dependent contribution to the overall polarization noise spectrum, which is modeled in the V3 code as [16]

$$N_l^{\frac{1}{f}} = N_w^P \left(\frac{l}{l_{\rm knee}}\right)^{\alpha_{\rm knee}} |W_l^b|^{-2} \,, \tag{3.21}$$

where N_w^P is w^{-2} re-scaled from units of $\left[\mu\mathrm{K}^2\,\mathrm{arcmin}^2\right]$ into $\left[\mu\mathrm{K}^2\,\mathrm{rad}^2\right]$. The $\alpha_{\rm knee}$ and $l_{\rm knee}$ are dimensionless parameters in the SO $1/f$ noise model [16]. For the 93GHz and 145GHz channels we study $\alpha_{\rm knee} = -2.5$ and $\alpha_{\rm knee} = -3$ respectively. Note that there is no

relationship between α_0 and α_{knee}, the symbolic similarity is coincidental. The pessimistic and optimistic $1/f$ noise setting varies the value of l_{knee} between $l_{\text{knee}} = 50$ for the pessimistic setting and $l_{\text{knee}} = 25$ for the optimistic setting.

The f_{sky} for this forecast is fixed to the expected coverage for the SAT of $f_{\text{sky}} = 0.1$. Our

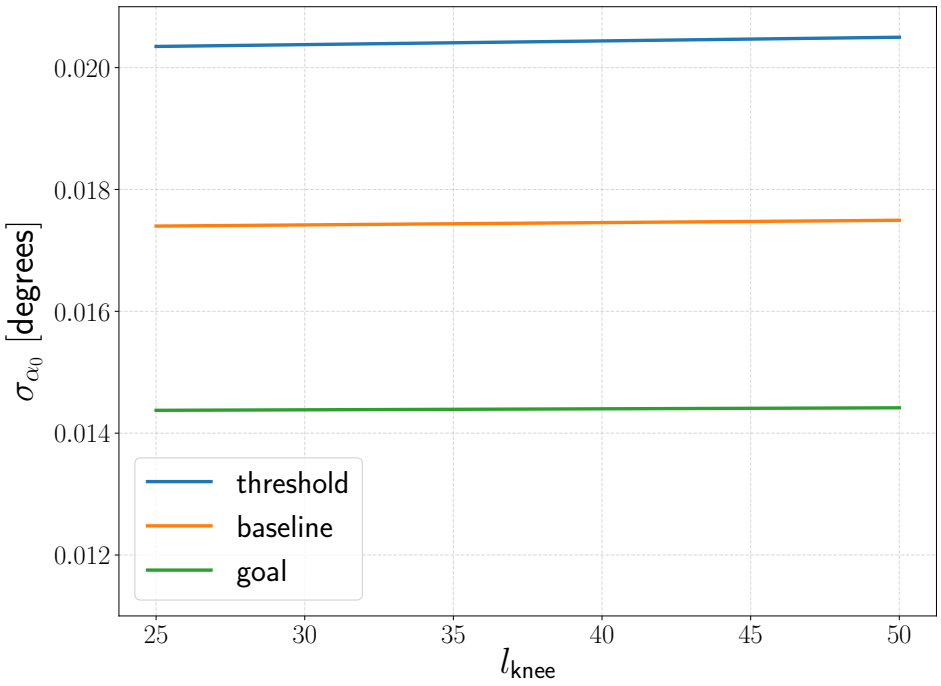

Figure 3.4: The forecast uncertainty on α_0, σ_{α_0} plotted for 0.1. We show the uncertainty for three SAT sensitivity modes of the SO-V3 noise code including the most pessimistic threshold mode (blue), the baseline mode(orange), and the most optimisitic goal mode (green). We consider both the optimistic, $l_{\text{knee}} = 25$, and the pessimistic, $l_{\text{knee}} = 50$, $1/f$ noise settings.

forecast, shown in Figure 3.4, suggests that variations in the $1/f$ noise profile may not have a significant impact on the performance of the SAT constraint. We see a weaker constraint from the SAT than from the LAT. We forecast constraints of $\sigma_{\alpha_0} \gtrsim 1.4 \times 10^{-2}$ for all three SO-V3 sensitivity settings. This is a worse expected σ_{α_0} than that for all three of the sensitivity settings of the LAT.

We calculate the S/N for each spectrum used in the SAT forecast. We fix the fiducial α_0 to the same value as in the LAT S/N study, $\alpha_0 = 10^{-2}$ [degrees], set the sensitivity to the baseline mode and assume a pessimistic $1/f$ noise mode. The l range and f_{sky} for this calculation are the same as is used in the forecast. As we did not carry out forecasts for the correlations with CMB temperature only the S/N for polarization spectra are included. The S/N values shown in Table 3.3 confirm that the constraining power for the SAT comes from the C_l^{EB} spectrum, as is was the case for the LAT. We find the total S/N from the combination of the polarization

XX'	S/N
EE	1.08×10^{-5}
BB	1.68×10^{-3}
EB	0.52

Table 3.3: The S/N ratios for α_0 as found using each CMB power spectrum or cross correlation expected to be measured with the SAT. Here the noise mode is set to baseline and $f_{\text{sky}} = 0.1$. We used a fixed multipole range of $30 \leq l \leq 400$.

spectra is less than $\mathcal{O}(1)$. This is not unexpected as the constraint from the baseline SAT mode is a factor of ~ 1.8 larger than than the fiducial rotation angle, $\alpha_0 = 10^{-2}$ [degrees].

Our SAT forecast, along with the study of S/N values for each instrument and each spectrum suggest that the best constraints will come from the LAT for SO. We expect that both the C_l^{EB} and C_l^{TB} spectra will make significant contributions to constraints on α_0. These forecasts are preliminary however, as the impact of foregrounds and systematics on SO have not been considered. The largest systematic impact on α_0 constraints is expected to come from the absolute polarization angle calibration error. This error will be dependent on the particular polarization angle calibration method utilized by SO [60], [102].

3.3.4 The CMB-S4 Forecast

We repeat our Fisher forecast for the 1σ CB angle, α_0, constraint for the CMB-S4 experiment. The details of the instrument and cosmological setup are described in Section 3.2.2. The CMB-S4 instrument is most naturally comparable to the LAT, rather than the SAT, as it is expected to be a high resolution instrument with a similar sky coverage and beam width. We perform our forecast for the same range of f_{sky} as was used for SO LAT. These are $f_{\text{sky}} \in [0.1, 0.2, 0.4]$. The uncertainty on α_0 is found to be $\sigma_{\alpha_0} = 1.8 \times 10^{-3}$ [degrees] for the expected 40% sky coverage and targeted sensitivity of $w_T^{-1} = 1$ [μK arcmin]. This order of magnitude improvement is not unexpected for the higher anticipated sensitivity of the CMB-S4 instrument.

We also investigate how the constraint will vary if the noise sensitivity does not meet the CMB-S4 mission requirements. In figure 3.5 we show the relationship between instrument sensitivity and forecast uncertainty in order to give an indication of the expected constraint for sensitivities equal to or greater than the CMB-S4 goal sensitivity. As in the case of the LAT, the constraint may be more sensitive to increased noise for smaller overall sky coverage.

3.3.5 The constraining power for CMB-S4

We once again investigate the S/N of α_0 for CMB-S4 for each of the CMB spectra used in the constraint. For the CMB-S4 experiment we find similar results to those for SO. We once again find that C_l^{EB} has the largest S/N, followed by a significant S/N for C_l^{TB}, with significantly

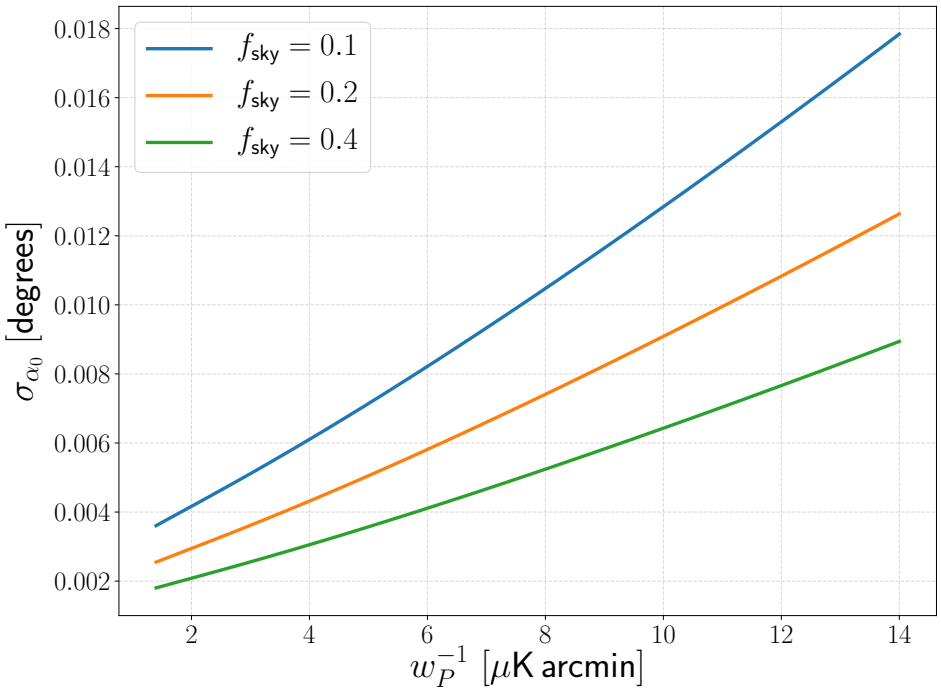

Figure 3.5: The uncertainty on α_0 as a function of polarization noise sensitivity, w_P^{-1}, for the CMB-S4. We show curves for 40% (green), 20% (orange), and 10% (blue) sky coverage. The smallest value for polarization sensitivity we show in this figure is $w_P^{-1} = \sqrt{2} w_T^{-1} = \sqrt{2}$ [μK arcmin], which is the expected sensitivity of of the CMB-S4 instrument [37].

smaller values for the remaining spectra. We show the S/N for each spectrum in Table 3.4. The fiducial birefringence angle used in this calculation is $\alpha_0 = 1.8 \times 10^{-3}$ [degrees] (i.e. the predicted error for α for CMB S4), the l range used is $30 \leq l \leq 5000$, and $f_{\text{sky}} = 0.4$ As we expect, the S/N for this value of α_0 is $\mathcal{O}(1)$. Our results suggest that the majority of the constraining power for CMB-S4 will come from C_l^{EB} with some additional contribution from C_l^{TB}.

XX'	S/N
EE	1.15×10^{-6}
BB	1.79×10^{-6}
TE	1.15×10^{-6}
TB	0.29
EB	0.95

Table 3.4: The S/N ratios for α_0 as found using each CMB power spectrum or cross correlation expected to be measured with the CMB-S4. The instrument temperature noise sensitivity is $w_T^{-1} = 1$ [μK arcmin] and $f_{\text{sky}} = 0.4$. We used a fixed multipole range of $30 \leq l \leq 5000$.

By comparing the S/N values for each spectrum at each value of l, shown in Figure 3.6,

we find that the constraining power for CMB-S4 should come from the range $30 \leq l \leq 3000$. For $l \lesssim 3000$ the S/N of C_l^{EB} decreases rapidly. As C_l^{EB} is expected to contribute the most to the constraint, the l range which we expect to provide the largest contribution is that where the C_l^{EB} S/N is largest.

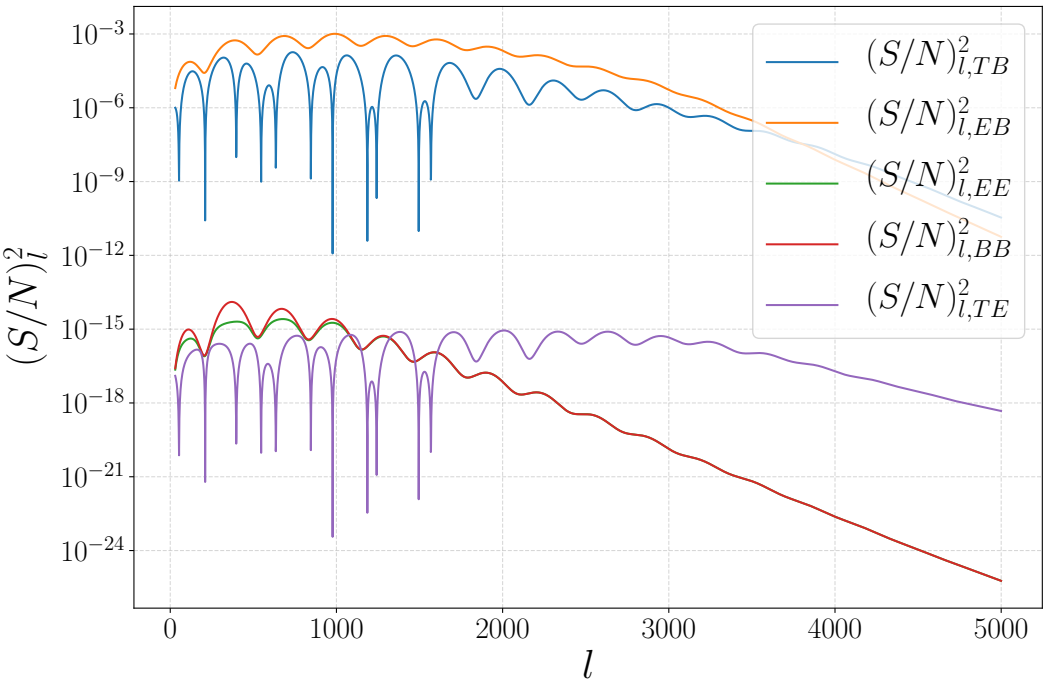

Figure 3.6: The square of the signal to noise ratio at each l for α_0 from CMB-S4 observations of the C_l^{TB} (blue), C_l^{EB} (orange), C_l^{EE} (green), C_l^{BB} (red), and C_l^{TE} (purple) spectra. The modes for which the square of S/N is largest provide the strongest contribution to the constraint on α_0. Here, $f_{\rm sky} = 0.4$, the temperature noise sensitivity is $w_T^{-1} = 1$ [μK arcmin] and $30 \leq l \leq 5000$.

As in the case of SO we have not considered the particular foreground effects and systematics that may have an impact on the α_0 constraints. We expect that α_0 constraints from CMB-S4 will be no less sensitive to absolute angle calibration error than any other CMB experiment [60], and that the exact level of uncertainty will be dependent on the calibration method [102]. As this source of uncertainty is expected to have the largest impact on CB constraints it will be important to factor it into constraints once the calibration method is known, or to use the new techniques discussed in [103]–[106] to mitigate this source of error.

3.4 Conclusions

The CB effect, which stems from a modification to electrodynamics, could be observed by CMB experiments. Several CMB experiments are well placed to attempt to measure this effect when they begin to take data. It has been forecast that CMB-S4 and SO will be able

to measure the uniform rotation effect with unprecedented precision. We have applied a Fisher forecasting method to ascertain the constraints that SO and CMB-S4 will be able to place on the uniform CB effect. For SO we forecast that the constraint on α_0 will be $\sigma_{\alpha_0} = 6.06 \times 10^{-3}$ [degrees]. For the more sensitive, future CMB-S4 experiment we forecast an even stronger constraint of $\sigma_{\alpha_0} = 1.8 \times 10^{-3}$. We have also analyzed the S/N of each spectrum involved in the constraint and found that the S/N for α_0 from C_l^{EB} was largest for both SO and CMB-S4, followed by a smaller but comparable S/N from C_l^{TB}. This suggests that the majority of the constraining power may come from C_l^{EB} with a significant contribution from C_l^{TB} for both experiments. For SO and CMB-S4 this constraining power is expected to be in the range $30 \leq l \leq 2000$ and $30 \leq l \leq 3000$ respectively.

It is important to note, however, that in our forecast we have assumed perfect absolute polarization angle calibration. It is expected that for both SO, and for CMB-S4 there will be a systematic error associated with the absolute angle calibration that will the limiting factor on the uniform birefringence constraint [16], [37], [60]. This associated error will vary depending on the angle calibration method that is chosen for each experiment. An interesting technique used to mitigate this absolute angle calibration error by using foregrounds to break the degeneracy between angle calibration error and uniform birefringence has been proposed and developed in [103]–[105]. In [106] this technique was been applied to experimental data in the form of the *Planck* 2018 data.

It will be important to constraint the uniform CB effect for future experiments. As the presence of a uniform polarization rotation across the sky will result in mixing of the C_l^{EE} and C_l^{BB} this effect could contaminate measurements of the primordial B-mode spectra. Such contamination must be removed before any claim of primordial B-mode detection is made. Beyond its role as a contaminant detection or constraint this effect is itself an important scientific goal. A uniform CB angle would indicate the presence of new and exciting beyond standard model physics, and may hint at a coupling between the photon field and a pseudoscalar field in the early universe such as the axion.

Moving beyond the uniform CB effect it is possible that the rotation has a direction dependent component. Such a component would generate additional correlations normally uncorrelated modes in the CMB. It may be possible to exploit these modes to reconstruct maps of this direction dependent rotation, and to constraint this anisotropic CB effect. The potential methods to constrain anisotropic CB, as well as the potential contamination that anisotropic CB might contribute to the B-mode power spectrum are investigated in detail in the next chapter of this thesis.

Chapter 4

Constraining cosmic polarization rotation and implications for primordial B-modes

4.1 Introduction

The temperature and polarization anisotropies in the Cosmic Microwave Background (CMB)[107] have been measured to high precision by the Wilkinson Microwave Anisotropy Probe (WMAP) and *Planck* satellite, placing very tight constraints on the cosmological parameters [99], [108], [109]. These observations have confirmed the standard ΛCDM cosmology, and are compatible with the predictions of inflation. The current observations (the temperature anisotropies, E-modes of polarization and B-modes sourced by weak lensing) primarily probe the scalar density perturbations. Most inflation models also predict the generation of tensor perturbations (gravitational waves). However, the predicted range of amplitudes, characterized typically by the ratio of power in tensor perturbations to power in scalar perturbations 'r', has no lower bound. These tensor perturbations source very specific B-mode of polarization patterns, with a fairly well known spectral shape, which has the most power on degree scales around $\ell \sim 80$. The ongoing (BICEP/Keck, Spider, PolarBear, ACT, SPT [62], [110]–[113]) and upcoming CMB (CMB) experiments (Simons Observatory (SO), *LiteBIRD*, CMB-S4 [16], [37], [88]) will measure the polarized CMB sky with an unprecendented precision and with exquisite control over systematics over the next decade; a robust detection of r being one of their primary science goals. These experiments are projected to improve the upper limits on r from the current limit of $r < 0.061$ [114] to $r \lesssim 10^{-3}$.

These programs of research assume that B-modes are only produced by inflationary gravitational waves. However, we know from previous chapters of this thesis that there may be other non-standard mechanisms which also generate B-modes. If these alternate sources of B-modes exist, then these could potentially act as contaminants to measurements of B-modes specifically induced by inflationary tensor perturbations and it is important to develop analysis techniques which allow us to distinguish between these different sources.

A well known example is that of B-mode generation due to weak gravitational lensing of the CMB[15]. Weak lensing results in the subtle remapping of the microwave polarization vectors, which in effect leaks some of the E-mode power into B-modes. To detect $r \sim 10^{-3}$ it is imperative to "de-lens" the polarized sky in order to separate the primordial B-modes from those generated due to weak lensing. Consequently, a significant effort has been invested to carry out robust "de-lensing" [40], [115]–[117].

However, we have previously discussed an alternative mechanism to this: B-modes generated due to cosmic polarization rotation (CPR) which could be sourced by so called Cosmological Birefringence [25], [27]. In the previous chapter of this thesis we focused on the uniform cosmological birefringence (CB) effect, its impact on the CMB and the constraints that Simons observatory and CMB-S4 may be able to place on its value. In this chapter however, we focus on the anisotropic CB effect, in which the CMB is rotated by a direction dependent field sourced by modifcations to the electromagnetic Lagrangian [25], [27] While we use this as our primary motivation to carry out this study, the constraints and methods discussed in this chapter are also applicable to other mechanism that results in a rotation of the CMB polarization.

4.1.1 Modified Electrodynamics

Parity violations are common place in the weak sector of the standard model, with many observational examples. However, the electromagnetic sector of the standard model as it is currently understood is not expected to contain parity violating interactions [47]. Despite this, the search to understand the dark sector and inflation has introduced a plethora of potential pseudo-scalar fields, such as the axion [118]. As was discussed in Chapter 2, such a pseudo-scalar is a Pseudo-Nambu-Goldstone Boson (PNGB) which can can couple to the gauge field through a Chern-Simons term [25], [27], [42], [119]

$$\mathcal{L}_{CS} = -\frac{\beta\phi}{2M} F_{\mu\nu}\tilde{F}^{\mu\nu} \ , \tag{4.1}$$

where β is a dimensionless coupling constant, M is the vacuum expectation value of the broken global symmetry, $F_{\mu\nu}$ is the electromagnetic field strength tensor and $\tilde{F}_{\mu\nu}$ is its dual.

In this case the parity violating physics introduced by the additional Chern-Simons term induces a difference between the effective refractive indexes for the right-handed and left-handed circular polarisation states of light. Linearly polarised light can be written as the superposition of the two circular polarisation states with a polarisation angle proportional to the difference in phase between the two states. The resulting change in phase during the propagation of light, due to difference in the effective refractive index for the different circular polarization states will cause a change in the linear polarisation angle [25]. This effect is known as cosmological birefringence and the resulting change in polarisation angle in direc-

tion $\hat{\mathbf{n}}$ is [44]

$$\bar{\alpha}(\hat{\mathbf{n}}) = \frac{\beta}{M} \int d\eta \left(\frac{\partial}{\partial \eta} + \hat{\mathbf{n}} \cdot \boldsymbol{\nabla} \right) \phi(\eta, \hat{\mathbf{n}}) \ , \tag{4.2}$$

where η conformal time and $\bar{\alpha}(\hat{\mathbf{n}}) = \alpha_0 + \alpha(\hat{\mathbf{n}})$. Here the integration is along the space-time path of the photon. Note, that this angle is direction dependent only if the gradient of the scalar field is also spatially varying. Otherwise the rotation angle is direction independent, $\bar{\alpha}(\hat{\mathbf{n}}) = \alpha_0$. The power spectrum for this spatially dependent field is expected to have a simple form,

$$C_L^{\alpha\alpha} = A_{CB} \frac{2\pi}{[L(L+1)]^\beta} \ , \tag{4.3}$$

where the constant A_{CB} is the amplitude of the power spectrum, a parameter which CMB experiments might seek to constrain. It is assumed that as long as the pseudo-scalar field that sources CB does not obtain a mass during the inflationary epoch then the power spectrum will be scale invariant, corresponding to $\beta = 1$ [44]. While some models predict oscillatory damping of the CB spectrum at high multipoles [120], [121], this scale invariant assumption is expected to remain valid in the spectral ranges probed by the experiments considered in this analysis. The true spectral shape of the CB spectrum remains unknown, so we have allowed for perturbation around scale invariance by including the additional free parameter β.

4.1.2 Birefringence and the CMB

The CMB polarisation anisotropies were generated in the Early Universe during the epoch of recombination via Thomson scattering. Approximately 10% of these CMB photons are linearly polarised. The high redshift origin of these polarised photons makes the CMB an ideal candidate for the detection of CB.

CB affects CMB polarization maps in a manner analogous to weak lensing modifications to the maps. Therefore CB not only modifies the angular power spectra (i.e. the diagonal of the harmonic space covariance matrix : $\langle a^X_{\ell m} a^Y_{\ell' m'} \rangle$) but also encodes information in the off-diagonal elements of the covariance matrix. The monopole component of the CB rotation angle causes mixing between the different angular power spectra at first order in α_0 - the uniform CB rotation angle. The anisotropies in the CB rotation angle also modify the different angular power spectra but leading order corrections appear only at second order (α^2). The anisotropies in the CB rotation angle are also encoded in the off-diagonals of the covariance matrix, and these are at first order (α) and these therefore can be reconstructed using the well known quadratic estimator (QE) technique [38], [39], [43], [83].

It is therefore possible to put constraints on CB affects in CMB polarization maps using two complementary methods. One can look for excess power in direct measurement of the polarization angular power spectra. The details of the modification to the polarization angular power due to CB are summarized in Section. 4.2.1. Alternately, one can use the QE technique, where $\alpha(\hat{n})$ is reconstructed, and the power spectrum of the reconstructed map is compared

to the null hypothesis of it being consistent with noise. Relevant details relating to the QE are discussed in Section. 4.2.2. It is important to note that constraining uniform birefringence is limited by the level of absolute polarisation angle calibration possible [57], however, such limitations do not apply when placing constraints on anisotropic birefringence. In this chapter we assume that any monopole birefringence effects have already been removed using self calibration [122] and focus on deriving constraints on anisotropic birefringence from upcoming CMB experiments using the two complementary methods discussed above. In Section. 4.3 we discuss the likelihoods we use, and the experimental configurations for BICEP/Keck, SO and *LiteBIRD* to derive constraints for each of these two methods.

Many CMB experiments have already placed constraints on both uniform and anisotropic CB [43], [57], [67], [68], [77], [123]. The current best constraint on the uniform CB rotation angle, α_0, comes from *Planck* whose 68% confidence limit is $\alpha_0 < 0.5^\circ$ [124]. The best constraint on anisotropic birefringence is a 95% confidence limit constraint on the amplitude of the CB power spectrum of $A_{CB} \leq 0.10 \times 10^{-4}$ rad^2, set by analysis on recent ACT, assuming a scale invariant power spectrum for CB (i.e. $\beta = 1$) [125]. In Section. 4.4 we present a forecast of the CB constraints from BICEP/Keck, SO and *LiteBIRD*. A qualitatively similar study was carried out in [126] and we find consistent results under similar settings. Further to the presentation of this forecast we compare the relative constraints one may be able to obtain using both the QE technique, and by looking for excess power in the polarization angular power spectra.

Due to the relationship between the CB and the coupling strength between the photon and the PNGB it is possible to forecast constraints for this coupling using constraints on CB. As the observable for CB, rotation of the CMB linear polarization angle, is the same as the observable for primordial magnetic fields (PMFs) it is possible to also use CB constraints to place constraints on the field strength of PMFs [127]–[129]. Forecasts for constraints on both physical phenomenon for BICEP/Keck, SO, and *LiteBIRD* are presented in Section. 4.4.

A measurement of the primordial B-modes, originating from tensor perturbations to the metric as predicted by most models of inflation, is one of the primary science goals of many observational programs. Since CB can induce excess B-mode power which can be potentially confused with these primordial B-modes it is important to understand the constraints on CB attainable via different experiments. This will be an important aspect of interpreting the B-mode measurements of the future. With this motivation, in Section 4.4 we compare the CB induced B-mode allowed by the forecasted upper bounds on CB for BICEP/Keck, SO small aperture telescope (SAT) and large aperture telescope (LAT), and *LiteBIRD*. An analogous theoretical study was performed in [120], where the was focus was on estimating induced B-modes sourced by CB spectra corresponding to different coupling strengths between a PNGB and CMB photons. We emphasize that here we estimate the B-mode power that cannot be ruled out, even after taking into account the best upper limits on CB that will be placed by

the corresponding experiments[1].

4.2 Constraining CB using CMB polarisation

The affects of anisotropic CB on the CMB polarisation are expected to be small and hence can be treated perturbatively. The CMB polarization is written in terms of the maps of the Stokes parameters $Q(\hat{\mathbf{n}})$ and $U(\hat{\mathbf{n}})$ on the sky. Defining the complex Stokes parameters,

$$ {}_{\pm}P(\hat{\mathbf{n}}) \equiv (Q \pm iU)(\hat{\mathbf{n}}) \,, \tag{4.4} $$

the rotation of the polarisation due to birefringence is given by: ${}_{\pm}P(\hat{\mathbf{n}}) = {}_{\pm}\tilde{P}(\hat{\mathbf{n}})e^{\mp i2\alpha(\hat{\mathbf{n}})}$. Note that tilde'd variables are used to denote the primordial (un-rotated) CMB fields. We reiterate that we focus only on anisotropic CB and assume that the monopole CB (or angle miscalibration) has already been corrected using self calibration. Treating this perturbatively and retaining terms to second order in α yield the following correction to the polarization vector,

$$ {}_{\pm}P(\hat{\mathbf{n}}) = {}_{\pm}\tilde{P}(\hat{\mathbf{n}}) \left[1 \mp i2\alpha(\hat{\mathbf{n}}) \pm 2\alpha^2(\hat{\mathbf{n}}) + \mathcal{O}(\alpha^3)\right] \,. \tag{4.5} $$

The E and B fields are an equivalent, but scalar (spin 0) representation of CMB polarization. In the following section we summarize how these CB corrections propagate to the harmonic space covariance of the scalar E and B fields.

4.2.1 The effect of CB on the B-mode power-spectrum

As previously mentioned, the dominant corrections to the CMB polarization angular power spectra, due to anisotropic CB rotation angle, appear at second order in α. These corrections result in mixing of power between different multipoles and also in mixing of power between the E and B mode of polarization.

The correction to the angular power spectrum of B-mode of polarization is given by [130],

$$ \delta C_{\ell}^{BB} = \frac{1}{\pi} \sum_{L} C_{L}^{\alpha\alpha} (2L+1) \sum_{l_2} (2l_2+1) \tilde{C}_{l_2}^{EE} (H_{ll_2}^{L})^2 + \mathcal{T}_B(B \to B) \,, \tag{4.6} $$

where only modes that satisfy the triangularity condition $l + L + l_2 =$ Even contribute to the sum and $H_{ll'}^{L} = \begin{pmatrix} l & L & l' \\ 2 & 0 & -2 \end{pmatrix}$ is a Wigner symbol. Similarly the correction to the angular power spectrum of the E-mode of polarization has the following form [130],

$$ \delta C_{\ell}^{EE} = \frac{1}{\pi} \sum_{L} C_{L}^{\alpha\alpha} (2L+1) \sum_{l_2} (2l_2+1) C_{l_2}^{EE} (H_{ll_2}^{L})^2 + \mathcal{T}_E(B \to E) \,, \tag{4.7} $$

[1] Here we implicitly assume that no significant detection of CB is made by the corresponding experiment.

where only modes that satisfy the triangularity condition $l + L + l_2 =$ Odd contribute to the sum. For brevity the explicit form for additional corrections $\mathcal{T}_B$ and $\mathcal{T}_E$ are not given here, since these are sub-dominant. Unlike in the case of monopole birefringence, the anisotropic birefringence does not generate C_l^{EB} when including corrections up to second order in α.

Since the power in the E-modes is significantly larger than in the B-modes, the dominant corrections result from mixing of E-mode power across multipoles and across polarization states. This is also the reason why the additional corrections ($\mathcal{T}_B$ & $\mathcal{T}_E$) sourced by B-mode power are sub-dominant. On evaluating the correction to the CMB polarization power spectrum (Eq. 4.7 & Eq. 4.6), with $C_L^{\alpha\alpha}$ consistent with the current constraints on anisotropic CB, it is seen that the corrections to the E-mode power spectrum are more than an order of magnitude below cosmic variance. This indicates that the E-mode power spectrum cannot place interesting constraints on CB. On the contrary corrections to the B-mode power spectrum are comparable to primordial B-mode power expected from the range of tensor to scalar ratio being targeted by current and upcoming CMB experiments. This indicates that the measured B-mode power spectrum can be used to place interesting constraints on CB.

4.2.2 The Quadratic Estimator

As noted previously, CB induces coupling between off-diagonal elements of the covariance matrix[2], at leading order in α, that can be measured from data and combined in an optimal manner, using the (QE) technique, to yield a map of α. This is entirely analogous to the more well known case of QE reconstruction of the weak lensing potential [131]. While the details of constructing these QE for CB can be found in [38], [39], here we summarize the QE details relevant to this chapter.

In practice, one carries out the CB reconstruction by extracting information from the each of the following covariance matrices: EB, EE, BB, TE & TB and finally combining the reconstruction from each estimator in an optimal way, duly accounting for the correlations between the different estimates. However, it is seen that the final result is dominated by the EB QE and the explicit form of this estimator is given by,

$$\widehat{\alpha}_{LM} = -2N_L \sum_{ll'} \frac{\tilde{C}_{l'}^{EE}}{C_l^{BB} C_{l'}^{EE}} \sum_{mm'} B_{lm} E^*_{l'm'} \xi^{LM}_{lml'm'} \ , \tag{4.8}$$

where $\tilde{C}_l$ represents the true primordial CMB power spectrum that is calculated using a Boltzmann code, such as CAMB, with an assumed fiducial cosmology, C_l denotes the observed power spectrum: $C_l = \tilde{C}_l + C_l^{\rm noise}$, E_{lm} and B_{lm} are beam deconvolved harmonic space fields,

[2] In the absence of CB the off-diagonal correlations are zero, except when considering analogous couplings induced by weak lensing of the CMB.

$\xi^{LM}_{lml'm'}$ represents the geometric kernel that is given by the following expression,

$$\xi^{LM}_{lml'm'} = (-1)^m \sqrt{\frac{(2l+1)(2L+1)(2l'+1)}{4\pi}} \begin{pmatrix} l & L & l' \\ -m & M & m' \end{pmatrix} H^L_{ll'} \,, \tag{4.9}$$

and N_L is the reconstruction noise power spectrum. N_L is the expected power spectrum of the reconstructed map in the absence of any CB and is given by the following expression,

$$N_L = \left[4 \sum_{ll'} \sqrt{\frac{(2l+1)(2l'+1)}{4\pi}} \frac{(\tilde{C}^{EE}_{l'} H^L_{ll'})^2}{C^{BB}_l C^{EE}_{l'}} \right]^{-1} \,. \tag{4.10}$$

The derivation of this quadratic estimator is summarized in detail in Chapter 2, though the final result is presented in a slightly different form.

It is important to note that, owing to parity conditions for the EB QE estimator, the sums in the estimator and the reconstruction noise only receive non-zero contribution when the condition $l + l' + L =$ Even is satisfied. To make forecasts using the QE technique, one only needs to evaluate N_L using Eq. 4.10, which requires the fiducial CMB power spectra, the noise and instrument beam for each experiment as an input.

4.3 Forecast methodology for A_{CB}

We employ a likelihood based approach to constrain the amplitude of the CB power spectrum, A_{CB}, using both the QE approach, and using direct observations of the B-mode power spectrum (BB). We forecast the upper bound on A_{CB} using both these QE and BB techniques for SO, *LiteBIRD*, and a simulated version of BICEP/Keck. As a robustness check we also derive A_{CB} limits using QE and BB techniques using actual BICEP/Keck band-power data and compare them against those quoted by BICEP/Keck [68].

For these analyses we work with a null hypothesis for primordial B-modes (i.e. $r = 0$). The maximum multipole is fixed to the same value for all experimental configurations. By so doing, the different multipole contributions to the likelihood are naturally determined by the noise in the respective measurements. The likelihood is given by $\mathcal{L} = \mathcal{N} e^{-\frac{1}{2}\chi^2}$ and the χ^2 has the following general form,

$$\chi^2(A_{CB}) = \quad \Delta d_l M^{-1}_{ll'} \Delta d'_l \,, \tag{4.11}$$

where $\Delta d_l = \left[C^{\rm obs}_l - C^{\rm model}_l(A_{CB}) \right]$ and $M_{ll'}$ is the covariance matrix evaluated at a fixed fiducial cosmology. Note that even for the model power spectra A_{CB} is the only parameter that is allowed to vary while other cosmological parameters are held fixed. The CB power spectrum is assumed to be a power law (see Eq.4.3) and we study the constraints by allowing the slope to vary by 15% around a scale invariant power spectrum.

In the following sub-sections we provide the specifics of the model spectra, observed spectra and covariance matrices used to define the BB and QE likelihoods.

4.3.1 The BB likelihood for A_{CB}

As discussed in Section 4.2.1 a non-vanishing CB effect will result in excess B-mode power, analogous to how weak lensing generates B-mode power by leaking some of the E-mode power. It is possible to put constraints on A_{CB} by searching for this excess power in the measured B-mode power spectrum. To do this we use the following definition of the model spectrum to evaluate the likelihood function [43],

$$C_\ell^{\rm model}(A_{CB}) = A_{CB} C_\ell^{\rm BB,CB} + A_{\rm lens} C_\ell^{\rm BB,lens} \,, \tag{4.12}$$

where $C_\ell^{\rm BB,CB}$ is the CB induced BB power spectrum which is evaluated by injecting the CB power spectrum, given in Eq. 4.3, into Eq. 4.6 for $A_{CB} = 1$ and a range of values of β. The covariance matrix, $M_{\ell\ell'}$, then has the following form,

$$M_{\ell\ell'} = \frac{2}{(2\ell+1) f_{\rm sky}} \left[A_{\rm lens} C_\ell^{BB,\rm lens} + C_\ell^{BB,\rm noise} W_\ell^{-2} \right]^2 \delta_{\ell\ell'} \,, \tag{4.13}$$

where, $C_\ell^{BB,\,\rm lens}$ is the B-mode power spectrum induced by lensing, $A_{\rm lens}$ generally characterizes the lensing power post de-lensing, $C_\ell^{BB,\rm noise}$ is the instrument noise power spectrum and W_ℓ is the beam window function. When using this method we also derive constraints for different amounts of de-lensing, which is done by simply using different values, $A_{\rm lens} \in \{1, 0.75, 0\}$[3], as this considerably changes the effective noise in the measurements of the BB power spectrum.

4.3.2 The QE likelihood for A_{CB}

In addition to inducing excess B-mode power, CB would also induce specific signatures in the off-diagonal elements of the covariance matrix and these can be used to reconstruct the CB rotation field, α, as discussed in Section 4.2.2. For the QE likelihood C_l^{obs} would be the power spectrum of the reconstructed α map which we denote by $C_L^{\alpha\alpha,\,\rm rec}$. The model spectrum is then given by [68],

$$C_L^{\rm model}(A_{CB}) = A_{CB} C_L^{\alpha\alpha,\,\rm ref} + N_L \,, \tag{4.14}$$

where $C_L^{\alpha\alpha,\,\rm ref}$ denotes a reference CB power spectrum and is assumed to have the same form as in. Eq. 4.3. N_L denotes the reconstruction noise power spectrum which can be evaluated

[3] $A_{lens} = 1$ means no de-lensing, while $A_{lens} = 0$ means perfect de-lensing.

using Eq. 4.10. Note that N_L can be evaluated given only the theoretical CMB spectra and the instrument noise power spectrum. The covariance matrix $M_{ll'}$ for the QE likelihood has the following form,

$$M_{LL'} = \frac{2}{(2L+1)f_{\rm sky}} N_L^2 \delta_{LL'} \ . \tag{4.15}$$

Unlike in the BB analysis where we derive constraint for different values of $A_{\rm lens}$, here we keep $A_{\rm lens} = 1$ fixed. We estimate the reconstruction noise by optimally combining the reconstruction noise for all the QE (EE, BB, EB, TE, TB) estimators. For all experimental configurations we find that this net reconstruction noise offers little improvement on A_{CB} constraints compared to those derived from using the reconstruction noise corresponding to the EB estimator alone.

4.3.3 Experimental configurations

The multipole ranges, sky coverage, noise and beam for the three experiments considered in this chapter are summarised in Table 4.1. Instead of artificially varying the $l_{\rm max}$ cutoff for each experiment, the maximum multipole of $l_{\rm max} = 3000$ was chosen so that the cutoff is instead where the signal becomes saturated by noise for each experiment.

Instrument	$\ell_{\rm min}$	$\ell_{\rm max}$	$f_{\rm sky}$	noise rms [μKarcmin]	$\theta_{\rm FWHM}$ [arcmin]
BICEP/Keck	30	3000	0.01	3.0	30
SO SAT 93GHz	30	3000	0.1	3.8	30
SO LAT 93GHz	30	3000	0.4	16.3	2.2
LiteBIRD	2	3000	0.7	2.5	30

Table 4.1: Instrument specifications used in construction of the respective likelihood functions. For BICEP/Keck, noise curves were fit to publicly available noise data. For SO the noise curves were produced using a publicly available SO noise forecast code. For both SO and BICEP/Keck the noise rms presented is the average value for these noise curves in the range $30 \leq \ell \leq 3000$. The noise curves for LiteBIRD were calculated directly from the beam and noise rms values.

The noise power spectrum used and the instrument beams for each analysis carried out in this chapter were chosen with the following prescriptions/reasons:

- BICEP/Keck actual band-power data: The publicly available 150GHz binned noise data was chosen [68] and the model spectra were identically binned using the prescription presented in [132].

- BICEP/Keck simulated forecast: The Gaussian noise model was fitted to the publicly avail-

able 150GHz channel binned noise[4][68]. We ensured that this fitted noise model closely resembles the BICEP noise. This procedure allows us to use an extended multipole range for making a forecast. The limit of $\ell_{\rm min} = 30$ for the simulated forecast was chosen to emulate the baseline QE analysis performed in [68].

- SO forecast: A publicly available noise curve code[5] was used to generate noise curves for the 93GHz channel. This channel was chosen as it gives the strongest constraint on A_{CB} [16]. Both the SAT and LAT noise curves were generated using the "baseline" mode of the noise code [6]. In addition to instrument noise, these noise curves include additional contributions from atmospheric noise. While for forecasts, we use these simulated noise curves, the rms noise quoted in Table 4.1 are estimated from fitting the amplitude of the Gaussian noise model to the simulated noise curved. The value of $\ell_{\rm min} = 30$ was chosen in order to be consistent with the ℓ range used for the SO forecasts presented in [16].

- *LiteBIRD* forecast: A noise curve was constructed using the average beam width and the rms noise values quoted in [88].

4.4 Results

4.4.1 Forecasted constraints on A_{CB}

We carry out the analysis described in section 4.3 for BICEP/Keck, SO, and *LiteBIRD*. The likelihood curves for A_{CB} are depicted in Fig. 4.1. We show the curves for $\beta = 1$ in order to draw easier comparisons with current constraints. Using these likelihood curves we calculated the 95% upper limit on A_{CB} and these are summarized in Table. 4.2. Below we discuss the salient features of the derived A_{CB} constraints for each of the experiments we study in this chapter, comparing the results of the QE and BB techniques for each experiment.

BICEP/Keck: The A_{CB} limits presented by BICEP/Keck are derived using the QE method using a maximum CMB multipole of $l_{\rm max} = 700$ [68]. In our BICEP/Keck simulated forecast, on using the inputs from Table 4.1 and evaluating the 95% upper limits on A_{CB} from the QE likelihood, we find that the resulting upper limit matches the limits found by BICEP/Keck, as seen in the top left panel of Fig. 4.1. Specifically note that in our setup we have $l_{\rm max} = 3000$ and the corresponding instrument beam and noise in the measurements naturally determine the weighting for the different modes. Using an identical setting we also evaluate the BB likelihood and find that the constraint on A_{CB} is only 1.4 ($A_{\rm lens} = 1$) times larger than the QE constraint. Naturally we find that the BB constraint could be improved if the B-mode map were to be de-lensed (by a factor of 1.5 in the case of perfect de-lensing). However

[4]The BICEP/Keck binned noise and band power data is available at `http://bicepkeck.org/bk15_2018_release.html`.

[5]The noise curves for the SO LAT and SAT telescopes can be found at `https://simonsobservatory.org/assets/supplements/20180822_SO_Noise_Public.tgz`.

[6]The "one over f" mode in the noise code was set to "optimistic"

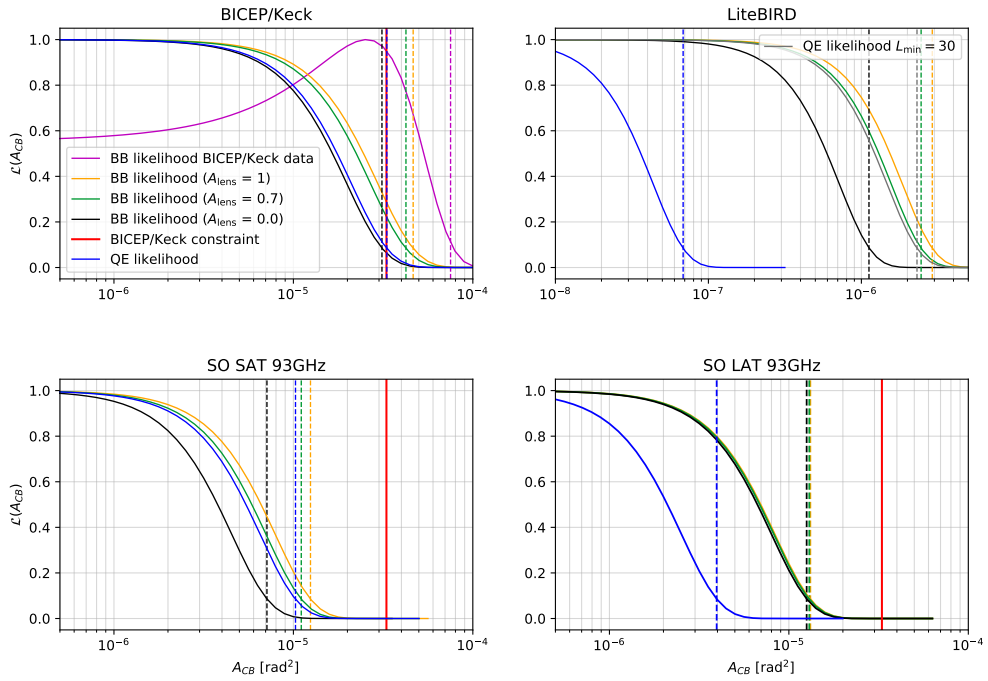

Figure 4.1: Forecasted likelihoods and 95% confidence limits for A_{CB} for the LAT and SAT SO 93GHz channels, BICEP/Keck, and *LiteBIRD*. The current experimental upper bound on A_{CB} of $A_{CB} < 0.33 \times 10^{-4}$ rad^{2}from [68] is indicated as the red vertical line. The forecasted constraint from the QE is shown in blue, whereas the forecast constraint from BB when no de-lensing is present is indicated in orange. The expected constraints from BB when $A_{\rm lens} = 0.7$ is indicated in green, and for perfect de-lensing ($A_{\rm lens} = 0$) is indicated in black. The constraint from the actual BICEP/Keck B-mode bandpower data is indicated in magenta. For the reference spectra used to calculate both the QE and BB likelihood curves shown $\beta = 1$. For the ground based experiments, BICEP/Keck and SO, the multipole range for the forecast is $30 \leq \ell \leq 3000$ and $30 \leq L \leq 3000$, whereas, for *LiteBIRD* $\ell_{\rm min} = 2$ and $L_{\rm min} = 1$. We also present the constraint for $L \geq 30$ in grey in order to provide a comparison with the other two experiments and indicate the effect that access to lower multipoles has on the QE constraint. The forecasted 95% confidence limits are noted with dashed vertical lines. The 95% upper limits are presented in table 4.2.

this finding contrasts the claim in [68], that constraints on A_{CB} using the BB technique are *significantly* worse than those derived using QE. In order to understand the origin of this contrasting conclusion, we also evaluate the BB likelihood using publicly available BICEP band power data[133] and find a relatively weaker constraint on $A_{CB} = 7.51 \times 10^{-5}$rad^2, a factor of 2.6 worse than the QE constraint. This weakening of the constraints can be understood as a consequence of using a truncated multipole range in the BB likelihood analysis[7]. Finally we also checked that using the $l_{\rm max} = 332$ when carrying out the simulated forecast results in a constraint that is consistent with that derived from the BICEP band power data. These

[7]BICEP used $l_{\rm max} = 332$ for the BB likelihood, however it uses an $l_{\rm max} = 700$ for evaluting their QE likelihood

tests and checks allow us to benchmark our forecasting tools with published constraints hence allowing us to now perform reliable forecasts for upcoming experiments.

Simons Observatory: As seen in both Figure 4.1 and Table 4.2, for the SO SAT the A_{CB} constraints derived from the BB likelihood are comparable to those derived from QE. These constraints are similar to the current best upper limits from ACT of $A_{CB} = 1.0 \times 10^{-5}\,\mathrm{rad}^2$, derived using the QE method [125]. However, for LAT, the QE analysis gives a significantly better constraint on A_{CB} than BB and is also 2.6 times better than the QE limits achievable from the SAT.

De-lensing has a significant impact on the BB constraints achievable using the SAT, with perfect de-lensing yielding an improvement on BB constraints from the SAT by a factor of 1.76. For the LAT perfect de-lensing can also improve BB limits, however, the QE constraints continue to be better, as seen in Table 4.2. In summary, the best constraints for SO come from the QE analysis on the LAT. Therefore, in analogy to weak lensing, carrying out QE analysis on the LAT to place the best possible constraint on CB, is likely the best strategy for putting limits on CB induced B-mode power. It is possible to apply the QE analysis on de-lensed B-mode skies but we have not explored this analysis strategy[8].

LiteBIRD: *LiteBIRD* is a space based experiment, and hence it significantly differs from both BICEP and SO/SAT, owing to its significantly larger sky coverage.

This immediately implies access to the largest angular scales on the sky, and this significantly enhances the constraints on A_{CB} from the QE likelihood, since the scale invariant CB power spectrum has more power at lower multipoles. Consequently we find that *LiteBIRD* will be able to place constraints on A_{CB} that are better than all other experiments considered in this chapter.

The white noise is expected to be smaller for *LiteBIRD* than that of BICEP/Keck and SO, as seen in Table 4.1. Owing to this the constraints on A_{CB} from the BB likelihood, even assuming no de-lensing, yields a constraint that is better than the best constraints achievable by any other experiment considered in this study. However, for *LiteBIRD*, the constraints on A_{CB} from the QE method yield constraints which are better by a factor of ~ 16 than those achievable from BB with perfect de-lensing.

To better appreciate the gains from being able to use the large angle modes, we also derive A_{CB} constraints that would be achievable by ignoring multipoles $L < 30$ in the QE likelihood analysis and the resultant constraints are presented in Table 4.2. We find that the A_{CB} constraints degrade by a factor of ~ 30 and become only marginally better than the QE constraints for SO LAT. We also carry out a similar exercise for the BB likelihood and find insignificant changes to the A_{CB} constraints.

[8] A careful treatment would require using revised noise estimates on the de-lensed B-mode maps.

	Instrument	A_{CB} [rad^2]	$B_{1\text{Mpc}}$ [nG]	$g_{\phi\gamma\gamma}$ [H_I^{-1}]
QE	BICEP/Keck	3.32×10^{-5}	30	7.24×10^{-2}
	SO LAT	3.96×10^{-6}	10.4	2.83×10^{-2}
	SO SAT	1.03×10^{-5}	16.8	4.03×10^{-2}
	LiteBIRD	6.84×10^{-8}	1.4	4.65×10^{-3}
($L > 30$)	*LiteBIRD*	2.31×10^{-6}	8.0	1.90×10^{-2}
	ACT	1.0×10^{-5}	16.6 (est.)	4.0×10^{-2}
BB	BICEP/Keck	4.65×10^{-5}	36	8.57×10^{-2}
$A_{\text{lens}} = 1$	BK data	7.51×10^{-5}	46	1.09×10^{-1}
	SO LAT	1.63×10^{-5}	19.1	4.56×10^{-2}
	SO SAT	1.25×10^{-5}	18.5	4.43×10^{-2}
	LiteBIRD	2.91×10^{-6}	9.0	2.14×10^{-2}
BB-DL	BICEP/Keck	4.24×10^{-5}	34	8.18×10^{-2}
$A_{\text{lens}} = 0.7$	SO LAT	1.30×10^{-5}	18.9	4.53×10^{-2}
	SO SAT	1.11×10^{-5}	17.5	4.18×10^{-2}
	LiteBIRD	2.46×10^{-6}	8.2	1.97×10^{-2}
BB-NL	BICEP/Keck	3.12×10^{-5}	29	7.01×10^{-2}
$A_{\text{lens}} = 0$	SO LAT	1.26×10^{-5}	18.6	4.45×10^{-2}
	SO SAT	7.12×10^{-6}	14.0	3.35×10^{-2}
	LiteBIRD	1.12×10^{-6}	5.6	1.33×10^{-2}

Table 4.2: Forecasted 95% upper bounds on A_{CB}, which is converted into a limit on PMF field strength, with a reference frequency of $\nu = 150$ GHz, or a PNGB-photon coupling, for both QE and BB calculated with $\beta = 1$. For BB this is carried out for $A_{\text{lens}} = 1$, $A_{\text{lens}} = 0.7$ (BB-DL) and $A_{\text{lens}} = 0.0$ (BB-NL). These constraints are calculated for BICEP/Keck, SO, and *LiteBIRD*. The constraint from the analysis of the BICEP/Keck B-mode data is also presented (BK data). The values for ACT presented here are from [125] except the constraint on $B_{1\text{Mpc}}$, which is estimated from the ACT constraint on A_{CB}.

4.4.2 Constraints on Physical Phenomena

While the focus till now has been on constraining CB, the origin and motivation for this chapter, the forecasted constraints can be used to place constraints on a more broad range of phenomena which result in CPR.

One possible cause of CPR could be Faraday rotation induced by PMFs [69], [127], [129]. The PMF amplitude is related to the CB power spectrum via the following relation [43], [68]:

$$B_{1\text{Mpc}} = 2.1 \times 10^4\,\text{nG} \left(\frac{\nu}{30\text{GHz}}\right)^2 \sqrt{\frac{L(L+1)C_L^{\alpha\alpha}}{2\pi}}\,. \tag{4.16}$$

Here, ν is the observed photon frequency. Assuming a scale invariant form for the CB power spectrum results in the following relation between the PMF strength and A_{CB},

$$B_{1\text{Mpc}} = 2.1 \times 10^4\,\text{nG} \left(\frac{\nu}{30\text{GHz}}\right)^2 \sqrt{A_{CB}}\,. \tag{4.17}$$

Note that the above equation is independent of multipole and can be used to translate A_{CB} constraints to those on the amplitude of the PMF. We invert Eq. 4.17 at $\nu = 150$ GHz to derive the upper limits on the primordial magnetic field strength for the different experiments

and these are tabulated in Table 4.2. Not surprisingly the constraint we forecast on the PMF strength, B_{1Mpc}, using the QE method matched the limits presented by BICEP/Keck[68].

We find from the forecasts for the QE method that LiteBIRD could improve upon the existing BICEP/Keck limits by a factor of ~ 21. While there is no quoted constraint on PMF amplitude from ACT, we translate A_{CB} constraints from ACT in [125] using the same prescription as above and the resultant PMF constraint is given in Table 4.2. Comparing this estimate to the QE forecast for *LiteBIRD* suggests that *LiteBIRD* may also be able to improve on any potential constraints ACT might place on $B_{1\text{Mpc}}$ by nearly a factor of ~ 12. We find that the *LiteBIRD* experiment is expected to give a PMF constraint that is a factor of ~ 8 better than the PMF constraint expected from SO LAT, and a factor of ~ 12 better than the PMF constraint expected from SO SAT.

The primary motivation for this chapter, cosmological birefringence, is usually attributed to the coupling of a PNGB to the gauge field. There are a variety of exciting and physically well motivated physical candidates for the PNGB including the dark matter axion, therefore constraining the strength of the coupling between the PNGB and the photon is of great interest. One can convert to an axion photon coupling, $g_{\phi\gamma\gamma} = \beta/2M$ and the relationship between $g_{\phi\gamma\gamma}$ and the CB power spectrum is [44], [68],

$$g_{\phi\gamma\gamma} = \frac{4\pi}{H_I}\sqrt{\frac{L(L+1)C_L^{\alpha\alpha}}{2\pi}}\ , \tag{4.18}$$

or, according to (4.3) assuming the PNGB does not obtain a mass during inflation,

$$g_{\phi\gamma\gamma} = \frac{4\pi}{H_I}\sqrt{A_{CB}}\ . \tag{4.19}$$

Here, H_I is the Hubble parameter during inflation. We have also used the forecasted constraints on A_{CB} to place possible upper bounds on $g_{\phi\gamma\gamma}$ for Simons Observatory, and *LiteBIRD* and these are presented in Table 4.2. As a test case, we compute an upper bound on $g_{\phi\gamma\gamma}$ using the QE method for BICEP/Keck and find that it matches the existing QE bound found in [68].

The best constraint on $g_{\phi\gamma\gamma}$ is expected to come, once again, from *LiteBIRD*. Morever, the *LiteBIRD* experiment could significantly improve upon existing bounds by nearly a factor of ~ 16 over the BICEP/Keck bound [68] and nearly a factor of ~ 9 over the ACT bound [125]. *LiteBIRD* may give a constraint on $g_{\phi\gamma\gamma}$ that is a factor of ~ 6 better than the forecasted constraint from SO LAT and a factor of ~ 9 better than the forecasted constraint from SO SAT .

4.4.3 Effect of birefringence on primordial B-modes

As seen in Eq. (4.6) additional B-mode power is induced by CB. We argued and demonstrated how this can be used to place constraints on CB from the measurements of C_l^{BB}. We now turn our attention to understanding the potential implications of the CB constraint study on measurement of primordial B-modes, since this is a primary science goal for the experiments considered in this chapter. Under the assumption that CB exists, we characterize the contamination by evaluating the induced B-mode power spectrum from the best 95% upper limits placed on A_{CB} for all experiments. That is, we take the best 95% confidence limits on A_{CB} for each experiment, use them as the amplitude for CB spectra and compute the B-mode induced by each of these spectra. To gain some insight on the dependence on the slope of the CB spectra, we extend our analysis by estimating the QE likelihood constraints on A_{CB}, for CB spectra which deviate from the scale invariant form, specifically assuming $\beta = [0.85, 1.15]$. Note that when deriving constraints on $A_{\rm CB}$ for these non-scale invariant spectra, we re-normalize C_L^{α} to match the scale invariant spectra amplitude at the pivot multipole $L_0 = 1$. While we do not provide these constraints here, we use these to evaluate the corresponding induced B-mode spectra, which are depicted in Fig. 4.2.

Since the shape of the B-mode spectra induced by CB differs from that induced by tensors, we compare the amplitudes at $\ell \sim 80$. For all the ground based experiments, the CB induced B-mode power spectra can constitute of order 1 to a few ten percent of the total primordial B-mode for $r \in [10^{-2}, 10^{-3}]$ as can be seen in Fig. 4.2. Further we note that the shallower CB spectrum ($\beta = -0.85$) results in a induced B-mode spectrum with a smaller amplitude while a steeper CB spectrum ($\beta = -1.15$) results in a B-mode spectrum with a larger amplitude. This, as we now argue, is quite counter intuitive. With pivoting at $L_0 = 1$ and $A_{\rm CB} = 1$, it is clear that the C_ℓ^{BB} induced by a shallower CB spectrum will have an overall higher amplitude than one induced by a steeper CB spectrum, owing to greater amplitude of the shallower spectrum than the steeper spectrum at most multipoles (except at L_0). Since QE analyses are highly sensitive to low multipoles, on reducing access to the large angle modes, the $A_{\rm CB}$ constraints on a steeper CB spectrum are more weakened than they are for a shallower CB spectrum. This weakening of constraints results in the induced C_ℓ^{BB} from a steeper CB spectrum having a higher amplitude than that induced from the shallower CB spectrum, when evaluated for the best $A_{\rm CB}$ limits derived from the QE likelihood, resulting in the corresponding ordering of the induced B-mode spectrum - explaining the counter intuitive trend.

For *LiteBIRD* the story is significantly different, owing to enhanced sensitivity and access to low multipoles, the A_{CB} constraints are more stringent. Therefore the CB induced B-mode spectra have a very low amplitude and cannot act as major contaminants to measurements of primordial B-modes with the corresponding target amplitudes. Here it is interesting to note that the steeper CB spectrum induces a smaller B-mode spectrum than the shallower CB spectrum, as one may have expected. In this case, since the $A_{\rm CB}$ constraints are driven

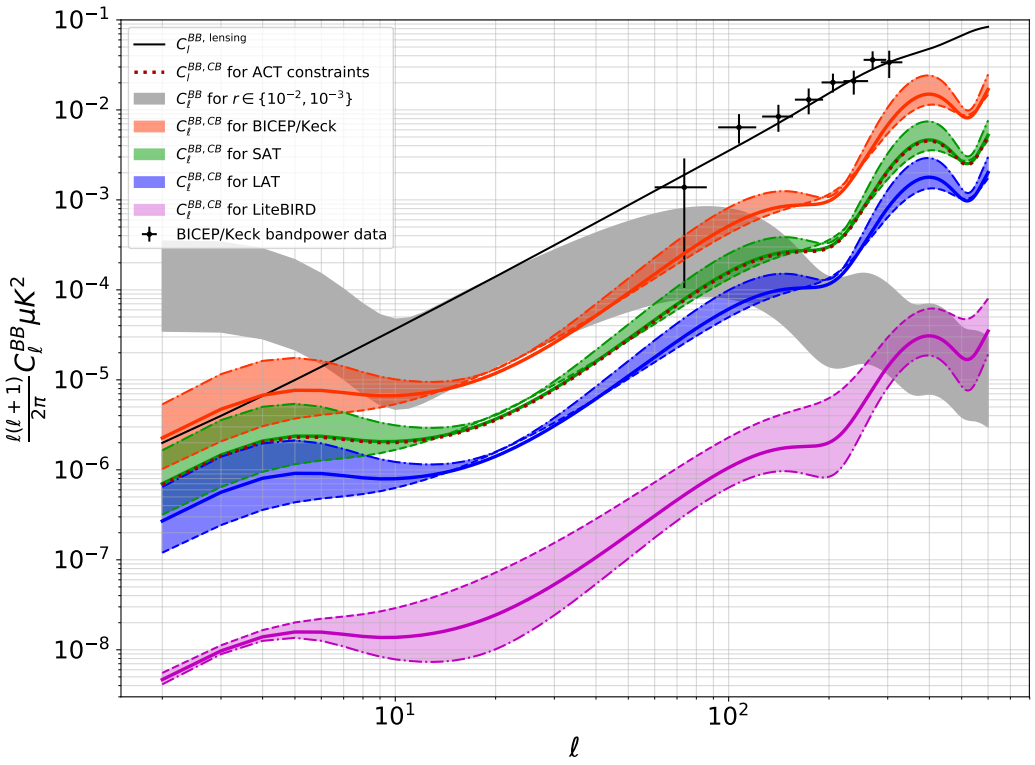

Figure 4.2: Maximum CB induced B-modes spectra, for varying CB spectral slopes: $C_L^{\alpha\alpha} \propto (L(L+1))^{-0.85}$ (dashed lines), scale-invariant $C_L^{\alpha\alpha} \propto (L(L+1))^{-1}$ case (solid lines) and $C_L^{\alpha\alpha} \propto (L(L+1))^{-1.15}$ (dot-dashed lines), with best A_{CB} upper limits derived using the QE likelihood. The $C_\ell^{BB,CB}$ are compared to the primordial $\tilde{C}_\ell^{BB}$ when the tensor to scalar ratio r is in the range $\sim 10^{-2} - 10^{-3}$. The CB induced $C_l^{BB,CB}$ allowed by the most recent ACT constraint is shown as a dotted maroon line.

dominantly low multipoles, there is relatively smaller variation in the $A_{\rm CB}$ limits and the B-mode spectra induced by CB spectra of different slopes follow the expected trend.

4.5 Conclusions

Future prospects for the detection and constraint of CB by the upcoming *LiteBIRD* and SO experiments, and current constraints on CB from the contemporary BICEP/Keck experiment have been discussed. The constraints these experiments should be able to place on CB, or more generally CPR, using both a QE and BB approach have been compared. It was found that the QE approach yields the strongest constraints. However, it was also found that in the SO SAT and BICEP/Keck forecast that the QE approach will yield only a marginal improvement over the constraint found using the BB method. In such cases, the computational expense and relative complexity of the QE method may make the use of the BB approach a much more favourable option for placing constraints on anisotropic CB. As long as the CB signal is found

to be consistent with zero using BB, no QE investigation is needed. However, if in these cases a non-zero CB signal is found using the BB method, a QE method must be used to verify this signal is in fact sourced by CB.

The much weaker constraint from the BICEP/Keck band-power B-mode data compared to the strength of the constraint in the forecast BICEP/Keck case, along with the degradation in quality of the forecast constraint when the multipole range is limited, suggests that limits in multipole range may have lead to the lower quality BICEP/Keck constraint from BB analysis mentioned in [68]. The strongest constraint is expected to come from the *LiteBIRD* experiment using a QE approach. The *LiteBIRD* is expected to offer roughly an order of magnitude improvement over the other experiments included in this analysis when using a QE approach. This improvement will be due to the improved sky coverage a low multipole access of the instrument.

The constraints on CPR were also used to predict constraints on the possible physical sources of CPR, both primordial magnetic fields and cosmological birefringence. More specifically, we calculated upper bounds on both the field strength for primordial magnetic fields, and for the PNGB-photon coupling. Stronger constraints on A_{CB} will yield stronger constraints on both the PNGB-photon coupling and PMF field strength, and it was found that *LiteBIRD* is expected to be able to place the strongest constraint on both of these physical parameters. It is expected that the strong constraints are due to the large expected sky coverage of the *LiteBIRD* instrument. In a later chapter of this thesis we will discuss the application of a QE approach to reconstruct the CB map and power spectrum using data from *Planck*, another full-sky satellite experiment.

In previous searches for primordial CMB B-mode the cosmological birefringence effect has been seen as largely irrelevant. The perspective has been that, while it is may be an interesting prospect to detect such an exotic physical effect, CB has little or no bearing on more mainstream CMB cosmology. However, as CMB experiments continue to probe primordial B-modes with more and more sensitivity, and as de-lensing techniques become more efficient CB may become a significant potential contaminant to B-mode science that needs to be excluded. In this chapter we have shown that the presence of an anisotropic CB effect with a power spectrum of an amplitude allowed by current upper bounds will indeed induce a large enough B-mode signal to act as a contaminant in future surveys seeking to constrain the tensor to scalar ratio in the range $r \sim 10^{-2}$ to $r \sim 10^{-3}$. Therefore, it will be necessary to truly ensure that such a contaminant is indeed not present. For future experiments such as SO it will be important to perform a QE based analysis to ensure that any detected B-mode signal is not from a CB contaminant. If a significant CB is detected, its influence on primordial B-mode studies can be removed by first de-rotating the polarization sky to remove the effects of CB, using techniques that bear strong resemblance to the de-lensing analysis [38], [39]. A detected CB signal would be an exciting prospect and a signal of new exciting physics. However, such a detection would warrant the removal of additional induced B-mode power

in order to recover the true primordial B-mode signal.

The QE techniques discussed in this chapter may have an application beyond the reconstruction and constraint of the CB signal. It may be possible to apply these QE techniques to diagnose systematic effects sourced by imperfections in CMB instruments and to apply techniques analogous to delensing to remove these systematics at the map level [28]. In the next chapter we will apply this approach to a realistic set of time ordered simulations to demonstrate its viability for systematics removal and unbiased B-mode recovery.

Chapter 5

Blind Map Level Systematics Cleaning: A Quadratic Estimator Approach

5.1 Introduction

The Cosmic Microwave Background (CMB) intensity and polarization are key observables for cosmology. The frontiers of cosmology have been pushed back by progressively more sensitive measurement of the CMB delivered by Cosmic Background Explorer (*COBE*) [134], the Wilkinson Microwave Anisotropy Probe (*WMAP*) [135], and *Planck* [136]. Future surveys, including satellite and ground-based, will measure the CMB sky with unprecedented sensitivities, with the primordial B-mode polarization spectrum as one of the primary targets. With these ever increasing sensitivities, precision control over systematics and their removal will become increasingly important.

Robust measurement of the primordial B-mode signals will require overcoming a number of analysis challenges, including foreground removal, removal of the weak-lensing B-mode signal and potential contamination from instrument systematic effects, as well as B-mode contamination from the cosmological birefringence (CB) effect mentioned in the previous chapters. Recent studies have shown that the upcoming experiments in principle have sufficient sensitivity and frequency coverage for robust recovery of B-mode signal corresponding to $r \sim 10^{-3}$ [16], [137]. Similarly other studies have examined how well B-mode skies may be de-lensed [e.g. 95], and in the previous chapter we discussed how well upcomming experiments will be able to recover and constrain the CB effect. Much of the previous chapter focused on the application of a Quadratic Estimator (QE) approach to the recovery of CB. In this chapter we extend this approach, focusing our attention on systematics from instruments.

Common approaches to the removal of instrument systematics require complex modeling and prior knowledge of the instrument itself. An appealing aspect of a QE approach is that it in principle allows a largely agnostic approach to dealing with instrument systematics. That is, the effect of systematics on the CMB data can be modeled as a set distortions to the CMB data. Reconstructing these distortions using a QE does not require prior knowledge or modeling of the instrument sourcing the distortions. QE cleaning and reconstruction is therefore a

promising complimentary approach to traditional systematic modeling techniques.

Previous works have suggested the use of QE as a method to quantify the level of systematics in CMB maps [e.g 28], formulating QE for a variety of instrumental systematics. These included gain fluctuations, differential systematics, and instrumental polarisation rotation, to list a few among a much longer list of possible instrument systematics. QEs are most commonly employed in reconstruction of the lensing potential map [e.g. 138] but have also been used to constrain cosmological birefringence [43], [68], [77]. QE studies frequently draw from understanding gained from lensing reconstruction. We improve upon previous studies of QEs as applied to systematic effects by considering an estimator in the full sky regime, accounting for realistic scan patterns, and testing whether certain aspects of the conventional wisdom from lensing studies apply. We consider two scenarios throughout this chapter: (i) a no lensing, noise, and beam free scenario which we refer to as the "ideal case", and (ii) a scenario we refer to as the "more realistic, non-ideal case" that includes the effect of lensing on the CMB spectra, a gaussian white noise of $w_{TT}^{-1} = 2.7\mu$K arcmin and a full width at half maximum of $\theta_{\rm FWHM} = 30'$. This is motivated by the effective noise and beam expected for the *LiteBIRD* experiment [88].

The QE approach would, in principle, leave us to deal with many systematics. In practice, to understand the most relevant ones it is useful to use rough estimates of the expected contamination sources and then deal with those that are most prominent. A potentially large source of CMB contamination is a temperature to polarization (T to P) leakage caused by a differential gain systematic. Since the CMB temperature anisotropy signal is 3-4 orders of magnitude larger than primordial B-mode signal, even a small leakage can induce large B-mode power. Therefore, this systematic may be a large hindrance for primordial B-mode studies. In this chapter we will refine aspects of analysis presented in [28], with our detailed scrutiny limited to focusing on this systematic.

We reiterate that, while all tasks necessary for controlling and understanding this instrument systematic will be performed, it is essential that these efforts be complemented with refined analysis methods that allow mitigation of the such systematics in the observed maps. At the very least, these methods will serve as important null tests, which will need to be performed to claim a robust primordial B-mode signal.

This paper is organized as follows: We begin with a review of different map level instrument systematics in Section 5.2, indicating the levels of contamination that may be induced by different types of distortion fields. We then discuss the details of the respective QE in Section 5.3. The iterative cleaning process which we employ in this chapter is presented in Section 5.4. Here we also introduce a semi-analytical forecasting procedure that allows us to predict the expected cleaning of B-mode maps. In Section 5.5 we present details of the simulation where the differential gain systematic is injected and discuss why realistic scan strategy is needed to give credible results. The results from QE analysis on simulated data are presented in Section 5.6. We do this for the ideal case to show the limits of the QE method

and for the more realistic, non-ideal case. We further quantify the results in Section 5.7 where we discuss the impact on cleaning on the inferred tensor to scalar ratio r using a likelihood based approach.

5.2 Distortions of the CMB

In an ideal setting the true CMB polarisation signal would be isolated and easily measured without introducing any distortions. However, in practice the measurement are subject to a number of measurement artefacts which need to be controlled and corrected post measurement via some modelling. These contaminants can be typically characterised by their spin dependence and, as such, readily written in to a set of distortion fields.

Both [28] and [139] use a Müller matrix approach [91] to describe the various systematic and cosmological signals that could affect measurements of the CMB polarization using a series of distortion fields. These distortions can be written as a coupling between different spin combinations of the instrument and observable fields,

$$\begin{aligned} {}_{\pm}\delta X(\hat{\mathbf{n}}) =& [a \pm i2\omega](\hat{\mathbf{n}})_{\pm}\tilde{X}(\hat{\mathbf{n}}) + {}_{\pm}f(\hat{\mathbf{n}})_{\mp}\tilde{X}(\hat{\mathbf{n}}) + {}_{\pm}\gamma(\hat{\mathbf{n}})\tilde{T}(\hat{\mathbf{n}}) \; + \; \sigma_{+\mathbf{1}}\mathbf{p}(\hat{\mathbf{n}}) \cdot \nabla\tilde{X}(\hat{\mathbf{n}}; \sigma_{\text{fwhm}}) \\ &+ \sigma_{\pm} d(\hat{\mathbf{n}})_{\pm}\eth\tilde{T}(\hat{\mathbf{n}}; \sigma_{\text{fwhm}}) + \sigma^2 q(\hat{\mathbf{n}})_{\pm}\eth^2\tilde{T}(\hat{\mathbf{n}}; \sigma_{\text{fwhm}}) + ... \end{aligned} \tag{5.1}$$

where ${}_{\pm}\tilde{X}(\hat{\mathbf{n}}) = (\tilde{Q} \pm i\tilde{U})(\hat{\mathbf{n}})$ is the spin ± 2, uncontaminated cosmological polarisation signal, $\tilde{T}$ represents the cosmological temperature signal, and ${}_{\pm}\delta X(\hat{\mathbf{n}})$ denotes the total induced distortion, where ${}_{\pm}\eth$ denote the spin raising/lowering operators respectively. The $a(\hat{\mathbf{n}})$ and $\omega(\hat{\mathbf{n}})$ terms are scalar fields describing an amplitude scaling and a polarisation plane rotation respectively, and ${}_{\pm}f(\hat{\mathbf{n}})$ is a spin ± 4 field which couples the conjugate polarisation fields. The ${}_{\pm}\gamma(\hat{\mathbf{n}})$ field is spin ± 2 field and couples the temperature to polarisation directly.The ${}_{\pm\mathbf{1}}\mathbf{p}$ term is a spin ± 1 deflection field that describes direction changes of the photons, the bold face indicating the vector nature of this quantity. Here, ${}_{\pm}d(\hat{\mathbf{n}})$ is a spin ± 1 field and $q(\hat{\mathbf{n}})$ is a scalar field that couple the first and second derivatives of the temperature field to the polarisation respectively. Since ${}_{\pm}X(\hat{\mathbf{n}})$ is a spin ± 2 field the distortions to this must also be spin ± 2.

Equation 5.1 has been constructed such that the top line corresponds to mixing between polarisation and temperature in a known direction on the sky. The bottom line presents terms which involve mixing in a local region of the sky with some directional dependence such that they leak the derivative of the CMB fields, such as a pointing error or lensing. The length scale σ_{fwhm} corresponds to the width of a Gaussian beam that is smoothing the CMB fields. The terms in the second line are sourced by a simple first order Taylor expansion of the CMB fields around $\hat{\mathbf{n}}$.

There are no known processes that cause T to P conversion along the line of sight. There-

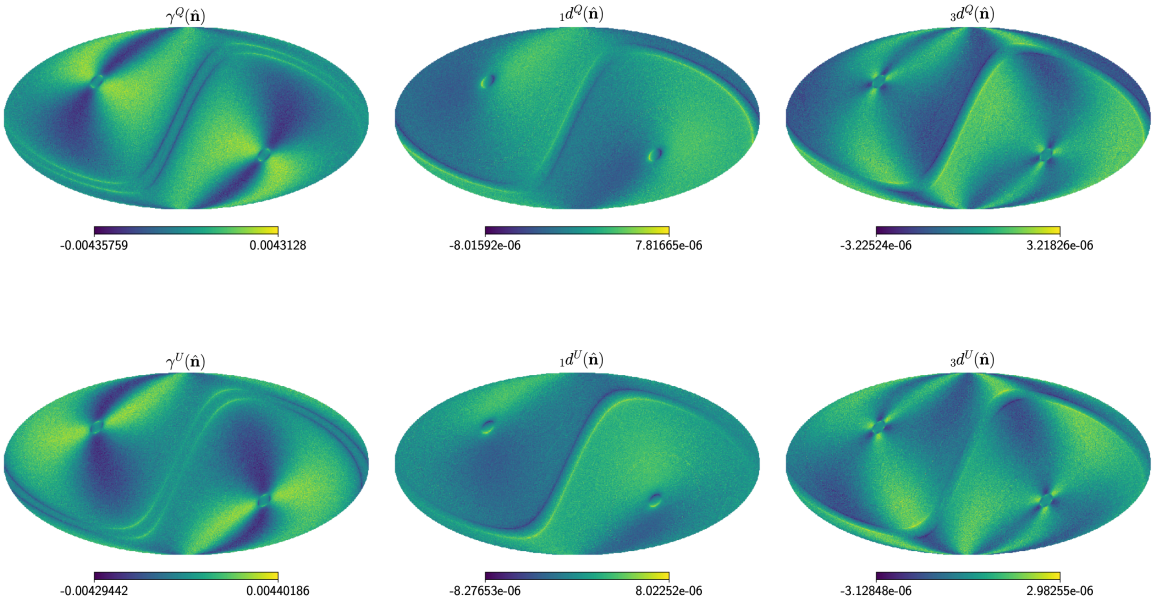

Figure 5.1: The left column shows maps of the spin-2 $(\gamma^Q + i\gamma^U)(\hat{\mathbf{n}})$ distortion field sourced by a 1% differential gain systematic which causes a T leakage into the polarisation. The second and third columns show the spin-1 $({}_1d_1 + i_1d_2)(\hat{\mathbf{n}})$ and spin-3 $({}_3d_1 + i_3d_2)(\hat{\mathbf{n}})$ distortion fields sourced by a $0.1'$ differential pointing systematic which causes a leakage of the derivative of the temperature into the polarisation. These levels of gain and pointing are typical of those found in recent CMB experiments [e.g. 62], [140].

fore, each of the $\tilde{T}(\hat{\mathbf{n}})$ containing terms can be attributed to some systematic. Some example distortion fields are depicted in Figure 5.1. Here it is important to note that the form of these distortion fields depends on the scanning strategy and therefore a realistic scan should be employed when assessing the importance of different systematics. We will revisit this detail in Section 5.5.5.

Note that we only consider CMB fields and their distortions in this chapter. In particular, we do not include foreground fields; We expect that foregrounds would be removed using standard techniques [141], [142], and we leave any complications arising from interactions between the two methods for future work.

In this paper we will focus on the T to P leakage mediated by the field ${}_\pm\gamma(\hat{\mathbf{n}})$, which is sourced by differential gain variations in the detector [62], [140] coupled with the instrument scan. Earlier work noted that the ${}_\pm\gamma(\hat{\mathbf{n}})$ field poses the largest potential obstruction to the robust primordial B-mode recovery [28]. Specific details on inclusion of these systematics in the simulated CMB maps will be presented in Section 5.5.

5.2.1 Additional distortion terms

There exist other systematics that contribute at leading order to the distortions described in Equation (5.1). These have been ignored in previous literature [28]. For completeness, here we briefly discuss these 'new' terms; these are encoded in the following expression,

$$\begin{aligned} {}_{\pm}\delta X^{\rm New}(\hat{\mathbf{n}}) = \sigma\, {}_{-1}\mathbf{p}(\hat{\mathbf{n}})\cdot\nabla_{\pm}\tilde{X}(\hat{\mathbf{n}};\sigma) + \sigma\, {}_{3}\mathbf{p}(\hat{\mathbf{n}})\cdot\nabla_{\mp}\tilde{X}(\hat{\mathbf{n}};\sigma) + \sigma\, {}_{5}\mathbf{p}(\hat{\mathbf{n}})\cdot\nabla_{\mp}\tilde{X}(\hat{\mathbf{n}};\sigma) \\ + \sigma\, {}_{3}\mathbf{d}(\hat{\mathbf{n}})_{\mp}\eth\,\tilde{T}(\hat{\mathbf{n}};\sigma) + \sigma^2\, {}_{4}\mathbf{q}(\hat{\mathbf{n}})_{\mp}\eth^2\tilde{T}(\hat{\mathbf{n}};\sigma). \end{aligned} \tag{5.2}$$

where symbols in bold-face are vector quantities.

In particular, note that a differential pointing systematic, which would contribute to the terms containing the ${}_{\pm}d(\hat{\mathbf{n}})$ and ${}_{1}\mathbf{p}(\hat{\mathbf{n}})$ field in Equation (5.1), also contributes to a number of terms in Equation (5.2). This includes additional coupling of the conjugate of the derivative of the temperature field with the polarisation through the spin-3 ${}_{3}\mathbf{d}(\hat{\mathbf{n}})$ field. From Figure 5.1, it is clear that this contributes a systematic at a level comparable to the spin-1 contribution, ${}_{1}\mathbf{p}(\hat{\mathbf{n}})$, and as such may not be neglected. In addition the differential pointing will also contribute to the terms containing the fields ${}_{-1}\mathbf{p}(\hat{\mathbf{n}})$, ${}_{5}\mathbf{p}(\hat{\mathbf{n}})$, and ${}_{3}\mathbf{p}(\hat{\mathbf{n}})$ which induce polarisation mixing as detailed in [90].

The bias sourced by these additional systematics could in principle hinder a robust claim of primordial B-mode detection. Neglecting these terms can potentially lead to distortion fields sourced by some systematics remaining undiagnosed, but we leave more detailed explorations of these new systematics to future work.

5.3 Quadratic estimators

For a statistically isotropic (SI) CMB sky, the off-diagonal correlation of the harmonic space covariance matrix $\langle X_{lm}X'_{l'm'}\rangle \propto \delta_{ll'}\delta_{mm'}$, for $X, X' \in [T, E, B]$. However, secondary anisotropies and measurement artifacts such as the distortion fields described in Section 5.2 can induce off-diagonal correlations. Therefore, by measuring and combining optimally combining these off-diagonal correlations it is possible to draw inferences on the fields that induce deviations from SI. This is commonly referred to as the quadratic estimator (QE) technique and it has been very successfully used to measure the subtle signatures of weak lensing in the CMB and deduce the lensing deflection angle map [93], [95], [143], to test deviations from the standard cosmological assumption of isotropy [144] and also to seek signatures of non-standard physics [29], [68], [125]. Some aspects of QE can be discussed quite generally without specific details about the systematics that source the distortions fields, and we refer the reader to [28] for such a discussion. In this chapter we focus out attention to the QE required to reconstruct the spin-2 γ fields which mediates the T to P leakage, the details of which we discuss next.

5.3.1 Quadratic estimator for the spin-2 γ field

We improve on the work presented in [28], by first deriving the full sky QE (i.e without making the flat sky approximation) and then presenting its efficient real space form. We begin by writing the map level model for the observed, distorted CMB sky which is given by the following expression,

$$ {}_{\pm}X(\hat{\mathbf{n}}) = {}_{\pm}\tilde{X}(\hat{\mathbf{n}}) \star B(\hat{\mathbf{n}}) + {}_{\pm}\gamma(\hat{\mathbf{n}})[\tilde{T}(\hat{\mathbf{n}}) \star B(\hat{\mathbf{n}})] + N(\hat{\mathbf{n}}) \,, \tag{5.3} $$

where, $\star$ represents a convolution operation, B denotes the beam, ${}_{\pm}\gamma(\hat{\mathbf{n}})$ represents the T to P leakage fields, and finally $N(\hat{\mathbf{n}})$ represents the measurement noise. Given that ${}_{\pm}X$ and ${}_{\pm}\gamma$ are spin two fields, they can be decomposed in the spin weighted spherical harmonic basis as follows,

$$ {}_{\pm}X(\hat{\mathbf{n}}) \equiv \sum_{lm} {}_{\pm}X_{l_1m_1} \, {}_{\pm2}Y_{l_1m_1}(\hat{\mathbf{n}}) = Q(\hat{\mathbf{n}}) \pm iU(\hat{\mathbf{n}}) \,, \tag{5.4a} $$

$$ {}_{\pm}\gamma(\hat{\mathbf{n}}) \equiv \sum_{LM} {}_{\pm}\gamma_{LM} \, {}_{\pm2}Y_{LM}(\hat{\mathbf{n}}) = \gamma^{Q}(\hat{\mathbf{n}}) \pm i\gamma^{U}(\hat{\mathbf{n}}) \,, \tag{5.4b} $$

where the spherical harmonic coefficients can be expressed in terms of the scalar E and pseudo scalar B as follows,

$$ E_{l_1m_1} = -\frac{1}{2}\left({}_{+}X_{l_1m_1} + {}_{-}X_{l_1m_1}\right) \quad ; \quad B_{l_1m_1} = -\frac{1}{2i}\left({}_{+}X_{l_1m_1} - {}_{-}X_{l_1m_1}\right) \,, \tag{5.5a} $$

$$ \gamma^{E}_{LM} = -\frac{1}{2}\left({}_{+}\gamma_{LM} + {}_{-}\gamma_{LM}\right) \quad ; \quad \gamma^{B}_{LM} = -\frac{1}{2i}\left({}_{+}\gamma_{LM} - {}_{-}\gamma_{LM}\right) \,. \tag{5.5b} $$

Given these definition the harmonic space coefficients of expansion of the contaminant spin-2 field is given by,

$$ \begin{aligned} {}_{\pm}\delta X_{l_1m_1} &= \sum_{LM}\sum_{l_2m_2} {}_{\pm}\gamma_{LM} \, \tilde{T}_{l_2m_2} \int d\hat{\mathbf{n}} \, {}_{\pm2}Y_{LM}(\hat{\mathbf{n}}) Y_{l_2m_2}(\hat{\mathbf{n}}) {}_{\pm2}Y^{*}_{l_1m_1}(\hat{\mathbf{n}}) \,, \\ &= \sum_{LM}\sum_{l_2m_2} {}_{\pm}\gamma_{LM} \, \tilde{T}_{l_2m_2} \, {}_{\pm}I^{Ll_2l_1}_{Mm_2m_1} \,, \end{aligned} \tag{5.6} $$

where that both ${}_{\pm}\delta X_{l_1m_1}$ and $\tilde{T}_{l_2m_2}$ fields are beam convolved. We note that the integral ${}_{\pm}I^{Ll_2l_1}_{Mm_2m_1}$ has the property: ${}_{+}I^{Ll_2l_1}_{Mm_2m_1} = (-1)^{\ell} {}_{-}I^{Ll_2l_1}_{Mm_2m_1}$ where $\ell \equiv L + l_1 + l_2$. Motivated by this property we define the even and odd parity projection operators as: $P_{e/o} = \frac{(1\pm(-1)^{\ell})}{2}$, which as we will see allows to condense a lot of the algebra that follows. Given all the definitions, Equation (5.6) can be re-expressed in the following form,

$$ \delta E_{l_1m_1} = -\frac{1}{2}\sum_{LM}\sum_{l_2m_2}\left({}_{+}\gamma_{LM}\tilde{T}_{l_2m_2} \, {}_{+}I^{Ll_2l_1}_{Mm_2m_1} + {}_{-}\gamma_{LM}\tilde{T}_{l_2m_2} \, {}_{-}I^{Ll_2l_1}_{Mm_2m_1}\right) \,, \tag{5.7a} $$

$$ \delta B_{l_1m_1} = \frac{i}{2}\sum_{LM}\sum_{l_2m_2}\left({}_{+}\gamma_{LM}\tilde{T}_{l_2m_2} \, {}_{+}I^{Ll_2l_1}_{Mm_2m_1} - {}_{-}\gamma_{LM}\tilde{T}_{l_2m_2} \, {}_{-}I^{Ll_2l_1}_{Mm_2m_1}\right) \,. \tag{5.7b} $$

The above equations can be further reduced to be expressed in terms of the γ^E_{LM} and γ^B_{LM}, which after some simple algebra can be expressed in the following form,

$$\delta E_{l_1 m_1} = \sum_{LM} \sum_{l_2 m_2} \left[\gamma^E_{LM} \tilde{T}_{l_2 m_2} + I^{Ll_2 l_1}_{M m_2 m_1} P_e + i \gamma^B_{LM} \tilde{T}_{l_2 m_2} + I^{Ll_2 l_1}_{M m_2 m_1} P_o \right] , \tag{5.8a}$$

$$\delta B_{l_1 m_1} = \sum_{LM} \sum_{l_2 m_2} \left[\gamma^B_{LM} \tilde{T}_{l_2 m_2} + I^{Ll_2 l_1}_{M m_2 m_1} P_e - i \gamma^E_{LM} \tilde{T}_{l_2 m_2} + I^{Ll_2 l_1}_{M m_2 m_1} P_o \right] . \tag{5.8b}$$

The polarization contamination in the measured E or B fields generated by the γ^B_{LM} and γ^E_{LM} fields can be treated separately by choosing a specific parity. For example, $\delta B_{l_1 m_1}$ for the $\ell =$ even parity is given by,

$$\delta B_{l_1 m_1} = \sum_{LM} \sum_{l_2 m_2} \gamma^B_{LM} \tilde{T}_{l_2 m_2} + I^{Ll_2 l_1}_{M m_2 m_1} P_e , \tag{5.9}$$

from which we will derive an estimator that will allow us to reconstruct γ^B_{LM}. Choosing the odd parity mode for δB will allow us to derive a QE that will allow us to reconstruct γ^E_{LM}. Note that QE derivations for other mode combinations follow a near identical procedure. To illustrate the key points we now carry forward the derivation of the QE for γ^B_{LM} starting from Equation (5.9).

The cross correlation between the observed temperature anisotropy map with the observed B-mode maps, under an ensemble average is given by the following expression,

$$\left\langle B^{\rm obs}_{l_1 m_1} (T^{\rm obs}_{l'_1 m'_1})^* \right\rangle = \sum_{LM} \gamma^B_{LM} \tilde{C}^{TT}_{l'_1} + I^{Ll'_1 l_1}_{M m'_1 m_1} P_e . \tag{5.10}$$

where we have implicitly assumed that the correlation between the true temperature and the true B-mode map is zero owing to parity arguments[1]. Throughout this chapter $\tilde{C}^{TT}_l$ represents the beam convolved power spectrum of the primordial CMB temperature signal. We now introduce another identity (see Appendix A for details) associated with the integral I,

$$\sum_{m_1 m_2} \pm I^{Ll_2 l_1}_{M m_2 m_1} \pm I^{L' l_2 l_1}_{M' m_2 m_1} = \frac{(H^L_{l_2 l_1})^2}{2L+1} \delta_{LL'} \delta_{MM'} , \tag{5.11}$$

where $H^L_{l_2 l}$ is defined in terms of Wigner-3j symbol as, $H^L_{l_2 l_1} \equiv \sqrt{\frac{(2L+1)(2l_2+1)(2l_1+1)}{4\pi}} \begin{pmatrix} L & l_2 & l_1 \\ -2 & 0 & 2 \end{pmatrix}$. Using this identity, the estimator for the correlation in equation (5.10) can be shown to reduce to the following form,

$$\sum_{m_1 m'_1} B^{\rm obs}_{l_1 m_1} (T^{\rm obs}_{l'_1 m'_1})^* + I^{Ll'_1 l_1}_{M' m'_1 m_1} = \widehat{\gamma}^B_{LM} \tilde{C}^{TT}_{l'_1} P_e \frac{(H^L_{l'_1 l_1})^2}{2L+1} . \tag{5.12}$$

Note that the ensemble average from (5.10) is no longer included here. In reality, we only

[1]For this particular TB QE it is important to note that this estimator does not suffer from any mean field bias and therefore we will not address this detail further.

have access to a single realization of the observed polarization fields when estimating γ^B_{LM} and γ^E_{LM}. This is also why it is necessary to replace the γ^B_{LM} symbol in (5.10) with the symbol for the estimate $\widehat{\gamma}^B_{LM}$ in (5.12). We can easily invert equation (5.12) to construct an estimator for γ^B_{LM} given by,

$$(\widehat{\gamma}^B_{LM})_{l_1 l'_1} = \frac{\sum_{m_1 m'_1} B^{\rm obs}_{l_1 m_1} (T^{\rm obs}_{l'_1 m'_1})^* + I^{L l'_1 l_1}_{M' m'_1 m_1}}{F^L_{l'_1 l_1}} \,, \tag{5.13}$$

where $F^L_{l'_1 l_1} \equiv \tilde{C}^{TT}_{l'_1} P_e \frac{(H^L_{l'_1 l_1})^2}{2L+1}$. This however is only an estimator for γ^B_{LM} from a single multipole pair (l, l'). It is now possible devise a minimum variance estimator (MVE) by carrying out the inverse variance weighted sum of the estimator across all possible multipole pairs. For this purpose we begin by evaluating the variance of the estimator for a given multipole pair and this is given by the following expression,

$$\begin{aligned} \mathcal{C}^L_{l_1 l'_1} \equiv \left\langle \widehat{\gamma}^B_{LM} (\widehat{\gamma}^B_{L_2 M_2})^* \right\rangle &= \sum_{m_1 m'_1} \sum_{m_2 m'_2} \frac{B^{\rm obs}_{l_1 m_1} (T^{\rm obs}_{l'_1 m'_1})^* (B^{\rm obs}_{l_2 m_2})^* T^{\rm obs}_{l'_2 m'_2} + I^{L l'_1 l_1}_{M' m'_1 m_1} + I^{L_2 l'_2 l_2}_{M'_2 m'_2 m_2}}{F^L_{l'_1 l_1} F^{L_2}_{l'_2 l_2}} \,, \\ &= \frac{(2L+1)}{(H^L_{l'_1 l_1})^2} \frac{\widehat{C}^{BB}_{l_1} \widehat{C}^{TT}_{l'_1}}{\tilde{C}^{TT}_{l'_1} \tilde{C}^{TT}_{l'_1} (P_e)^2} \,. \end{aligned}$$

The $\widehat{C}^{TT}_{l_1}$ and $\widehat{C}^{BB}_{l_1}$ terms are the power spectra estimated from the observed temperature and B-mode polarization fields respectively

Performing an inverse variance weighted sum of the estimator in (5.13) over $l_1 l'_1$ yields the MVE QE,

$$\widehat{\gamma}^B_{LM} = N^{\gamma^B}_L \sum_{l_1 m_1} \sum_{l'_1 m'_1} \frac{B^{\rm obs}_{l_1 m_1} (T^{\rm obs}_{l'_1 m'_1})^* \tilde{C}^{TT}_{l'_1} + I^{L l'_1 l_1}_{M m'_1 m_1} P_e}{\widehat{C}^{BB}_{l_1} \widehat{C}^{TT}_{l'_1}} \,, \tag{5.14}$$

where $N^{\gamma^B}_L$ is a normalization, which is also the reconstruction noise (i.e. the power spectrum of the noise in the reconstructed γ^B_{LM} map) which is given by inverse of the variances of all the modes added in parallel, specifically,

$$N^{\gamma^B}_L = \left[\sum_{l_1 l'_1} \frac{(H^L_{l'_1 l_1})^2}{(2L+1)} \frac{(\tilde{C}^{TT}_{l'_1} P_e)^2}{\widehat{C}^{BB}_{l_1} \widehat{C}^{TT}_{l'_1}} \right]^{-1} \,. \tag{5.15}$$

Note that in Equation (5.14) and Equation (5.15) only the even parity modes (i.e. $L + l_1 + l'_1 \rightarrow$ Even) contribute, which only corresponds to only half the elements in the harmonic space covariance matrix. One can show that the other half of the TB harmonic space covariance matrix encodes information on the E-modes of the spin-2 γ field. Following the same procedure as described above, considering the $\ell =$ Odd modes, it can be shown that the estimator

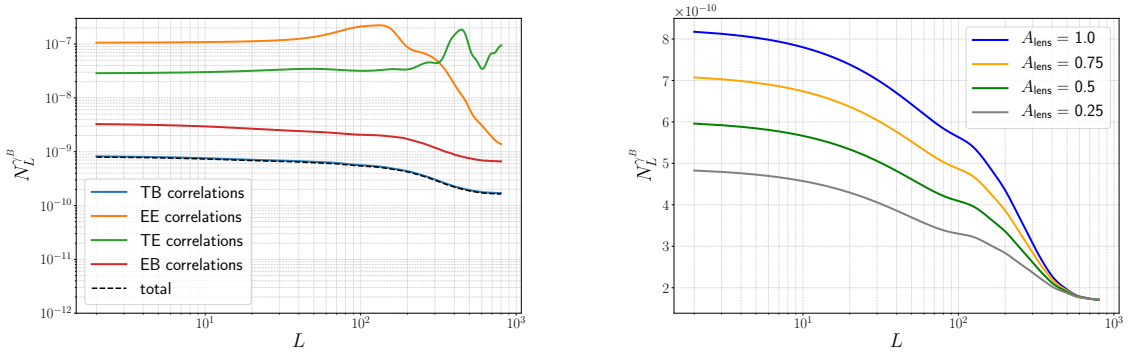

Figure 5.2: The left panel shows the reconstruction noise estimated for the respective QE assuming $A_{\rm lens} = 1$. The reconstruction noise for the combination of all the estimators is indicated with a black dashed line. The right panel shows the how the TB reconstruction noise varies as a function of $A_{\rm lens}$. Both plots assume instrument noise and beam characteristics compatible with the *LiteBIRD* instrument. Here we display only $N_L^{\gamma^B}$, as $N_L^{\gamma^E}$ shows the same trends.

for γ^E_{LM} is given by the following expression,

$$\widehat{\gamma}^E_{LM} = -iN_L^{\gamma^E} \sum_{l_1 m_1} \sum_{l_1' m_1'} \frac{B^{\rm obs}_{l_1 m_1} (T^{\rm obs}_{l_1' m_1'})^* \tilde{C}^{TT}_{l_1'} + I^{L l_1' l_1}_{M m_1' m_1} P_o}{\widehat{C}^{BB}_{l_1} \widehat{C}^{TT}_{l_1'}} \,, \tag{5.16}$$

with the reconstruction noise, analogously given by the following expression,

$$N_L^{\gamma^E} = \left[\sum_{l_1 l_1'} \frac{(H^L_{l_1' l_1})^2}{(2L+1)} \frac{(\tilde{C}^{TT}_{l_1'} P_o)^2}{\widehat{C}^{BB}_{l_1} \widehat{C}^{TT}_{l_1'}} \right]^{-1} \,. \tag{5.17}$$

While the forms of the reconstruction noise for $\widehat{\gamma}^B_{LM}$ and $\widehat{\gamma}^E_{LM}$ are nearly the same, they differ in the parity of modes that contribute to the sum and therefore their numerical values are not identical values. These are curved sky equivalents of the flat sky estimators presented in Equation (10) of [28].

5.3.2 The reconstruction noise

When reconstructing the distortion fields, in our case γ^E_{LM} and γ^B_{LM}, the reconstruction noise determines which harmonic modes of these fields can be recovered. Multipoles that are dominated by reconstruction noise cannot be properly reconstructed. Therefore, it is important to perform the reconstruction with as little noise as possible. While the reconstruction noise can be generally reduced by decreasing the measurement noise and increasing the angular resolution of the measurements, we will be interested in minimizing the reconstruction noise for a fixed instrument configuration.

The reconstructions can be performed using QE constructed from a variety of cross cor-

relations: EE, TE, TB & EB and by optimally combining all of them. The reconstruction noise resulting from combining all the estimators naturally is the best. However this requires significant more effort which may not be warranted. This can be assessed by estimating the reconstruction noise for each of the estimators and performing a relative comparison.

We perform this test in three different settings: (i) in the cosmic variance limited ideal case, (ii) in the more realistic, non-ideal case with a noise sensitivity of $w_{TT}^{-1} = 2.7\mu$K arcmin and a full-width at half-maximum of $\theta_{\rm FWHM} = 30'$, and (iii) assuming the CMBpol configuration with $w_{TT}^{-1} = 1.4\mu$K arcmin and $\theta_{\rm FWHM} = 4'$. The results from this exercise, for the $w_{TT}^{-1} = 2.7\mu$K arcmin, and $\theta_{\rm FWHM} = 30'$ case study, are summarized in Figure 5.2. In all three cases we find the reconstruction noise associated with the TB QE is the lowest and closely matches the estimated reconstruction noise expected from optimally combining all the different QE. Motivated by this observation we derive all our results using only the TB estimator.

These findings differ from the conclusions drawn in [28] where it is stated that for the CMBpol configurations the EB QE yields the lowest reconstruction noise. This highlights the importance of using detailed case studies for specific distortion fields in order to test the conventional wisdom when applying quadratic estimators. The highest sensitivity choice of correlations for any given distortion field depends on the details of the estimator and it is therefore important to check which choice of correlations yields the most desirable reconstruction noise for each distortion field separately.

Impact of de-lensing on reconstruction noise

The B-modes generated by weak lensing of the CMB act as a competing signal for measurement of primordial B-mode signal sourced by tensor perturbations. Therefore many upcoming analysis strategies necessarily include a de-lensing procedure, thereby reducing the additional variance introduced by the lensing signal and consequently improving the measurements or upper bounds on r. CMB B-mode power induced by lensing also contributes to the reconstruction noise for the TB correlations. The blind systematic cleaning being proposed in this chapter can also potentially[2] benefit from the reduced impact of lensing on the observed B-mode spectrum. Note that we do not carry out the de-lensing procedure, but model it simply by scaling the lensing power spectrum with an amplitude $A_{\rm lens}$.

In the cosmic variance limited case the reconstruction noise scales very simply with different amounts of delensing such that $N_L^\gamma = A_{\rm lens} N_L^\gamma|_{A_{\rm lens}=1}$. This simple relationship breaks down in a realistic scenario where the dominant contribution to the B-mode variance at high l comes from the instrument noise. This results in de-lensing having little impact on the reconstruction noise for high L modes. In the more realistic, non-ideal case this translates to modes greater than $L \sim 600$, as is seen in Figure 5.2. De-lensing can still reduce the B-mode

[2] In principle there might be an additional coupling between the lensing and distortion fields which may bias the lensing reconstruction. We leave the exploration of this subtlety to future work.

variance for modes where the instrument noise is not the dominant contribution, and this will be encoded as a reduction in reconstruction noise for lower multipoles.

It is possible to further minimise the impact of the reconstruction noise by carrying out iterative cleaning of the CMB maps and by constructing the optimal filter for $\widehat{\gamma}^{E}_{LM}$ and $\widehat{\gamma}^{B}_{LM}$ and we will return to discussing this in Section 5.4.

5.3.3 Efficient real space estimators

These harmonic space estimators derived above involve large sums over multipoles (scaling roughly as $\sim (l_{\rm max})^4$. and also requires evaluation of the Wigner symbols, therefore they are not very computationally efficient. These estimators appear as convolutions in harmonic space and one therefore expects to be able to express them as direct products of some real space fields. This procedure exists and is routinely implemented for the weak lensing estimators [92]. Here we derive an analogous real space operator for reconstructing the spin-2 γ field. By using the explicit integral form of ${}_{\pm}I^{Ll_1'l_1}_{Mm_1'm_1}$ we can rewrite Equation (5.14) and Equation (5.16), which after some algebra can be expressed in the following form,

$$\widehat{\gamma}^{B}_{LM} = \frac{N^{\gamma^B}_{L}}{2}\int d\hat{\mathbf{n}}\big[\,({}_{+2}A_{B^*}(\hat{\mathbf{n}}))^*\,A^{TT}_{T^*}(\hat{\mathbf{n}})\,{}_{+2}Y_{LM}(\hat{\mathbf{n}}) + ({}_{-2}A_{B^*}(\hat{\mathbf{n}}))^*\,A^{TT}_{T^*}(\hat{\mathbf{n}})\,{}_{-2}Y_{LM}(\hat{\mathbf{n}})\big]\,, \quad (5.18)$$

$$\widehat{\gamma}^{E}_{LM} = \frac{-iN^{\gamma^E}_{L}}{2}\int d\hat{\mathbf{n}}\big[\,({}_{+2}A_{B^*}(\hat{\mathbf{n}}))^*\,A^{TT}_{T^*}(\hat{\mathbf{n}})\,{}_{+2}Y_{LM}(\hat{\mathbf{n}}) - ({}_{-2}A_{B^*}(\hat{\mathbf{n}}))^*\,A^{TT}_{T^*}(\hat{\mathbf{n}})\,{}_{-2}Y_{LM}(\hat{\mathbf{n}})\big]\,. \quad (5.19)$$

where $*$ indicates the complex conjugate and the real space fields are defined as follows,

$${}_{\pm2}A_{B^*}(\hat{\mathbf{n}}) = \sum_{l_1m_1}\frac{1}{\widehat{C}^{BB}_{l_1}}(B^{\rm obs}_{l_1m_1})^*\,{}_{\pm2}Y_{l_1m_1}(\hat{\mathbf{n}})\,, \quad (5.20)$$

$$A^{TT}_{T^*}(\hat{\mathbf{n}}) = \sum_{l_1m_1}\frac{\tilde{C}^{TT}_{l_1}}{\widehat{C}^{TT}_{l_1}}(T^{\rm obs\,\prime}_{l_1m_1})^*Y_{l_1m_1}(\hat{\mathbf{n}})\,, \quad (5.21)$$

where $X, Y \in [T, E, B]$. Since these real space fields can be computed independently and merely involve a few spin harmonic transforms, as opposed to explicit multipole sums and evaluations of Wigner symbols, these are significantly more numerically efficient.

5.4 Iterative cleaning

The QE technique detailed in the previous section provides an excellent tool for diagnosis and reconstruction of potential contaminants, which we demonstrate in Section 5.6. However, in this section we shift our attention to discussing how the reconstructed distortion fields can be used to optimally de-contaminate the observed CMB maps. A cleaned CMB map has a lower reconstruction noise, which in effect allows for uncovering the components of the distortions fields that were noise dominated in the original map. These additional components of the reconstructed distortion fields can then be fed back to the cleaning algorithm. This translates to the cleaning of additional contaminated modes. We will refer to this procedure as iterative cleaning; this procedure allows for a more detailed recovery of the distortion fields. We now discuss how the reconstructed distortion fields can be optimally combined with the contaminated maps to yield de-contaminated maps.

5.4.1 Optimally de-contaminating the CMB maps

The residual contamination in the de-contaminated B-mode map is given by,

$$B^{\rm res}_{lm} = \delta B_{lm} - \delta\widehat{B}_{lm} \ . \tag{5.22}$$

where δB denotes the true contamination and $\delta\widehat{B}$ is the estimated map of contamination. $\delta\widehat{B}$ sourced by the B-mode component of the γ field can be estimated using the following expression,

$$\delta\widehat{B}_{l_1m_1} = \sum_{LM}\sum_{l_2m_2} \widehat{\gamma}^B_{LM}\tilde{T}_{l_2m_2+}I^{Ll_2l_1}_{Mm_2m_1}f^L_{l_2} \ , \tag{5.23}$$

which is the same as Equation (5.8b), except that the distortion field is replaced by the estimated distortion field using the QE as described in Section 6.2 and we have introduced the weights $f^L_{l_2}$ which need to be determined. We define an optimal cleaning algorithm as one that minimizes the power spectrum of the residual contamination after each iteration of cleaning. Given Equation (5.23), the angular power spectrum of the residual contamination map is given by the following expression,

$$C^{BB,\,\rm res}_{l_1} = \sum_{Ll_2}\frac{(H^L_{l_2l})^2}{(2l_2+1)}\left[\tilde{C}^{\gamma^B\gamma^B}_L\tilde{C}^{TT}_{l_2} - 2\tilde{C}^{\gamma^B\gamma^B}_L\tilde{C}^{TT}_{l_2}f^L_{l_2} + \widehat{C}^{\gamma^B\gamma^B}_L\widehat{C}^{TT}_{l_2}(f^L_{l_2})^2\right] \ , \tag{5.24}$$

and the optimal $\delta\widehat{B}$ can be estimated by solving for the weights $f^L_{l_2}$ that minimize Equation 5.24. Taking the derivative with respect to $f^L_{l_2}$ to calculate the minimum of the residual, $C^{BB,\,\rm res}_l$, results in a filter of the form,

$$f^L_{l_2} = \frac{\tilde{C}^{\gamma^B\gamma^B}_L\tilde{C}^{TT}_{l_2}}{C^{\widehat{\gamma}^B\widehat{\gamma}^B}_L\widehat{C}^{TT}_{l_2}} \ . \tag{5.25}$$

It is useful to think of this filter as being composed of two separable parts $f^L_{l_2} = f^{\gamma^B}_L f^T_{l_2}$, where

$$f^{\gamma^B}_L = \frac{\tilde{C}^{\gamma^B\gamma^B}_L}{\widehat{C}^{\gamma^B\gamma^B}_L} \;\; ; \;\; f^T_{l_2} = \frac{\tilde{C}^{TT}_{l_2}}{\widehat{C}^{TT}_{l_2}} \, , \tag{5.26}$$

which can be understood as being the corresponding Wiener filters for γ^B_{LM} and T_{lm} fields, on noting that $\hat{C}_l = \tilde{C}_l + N_l$. A similar calculation can be carried through for estimating the contamination sourced by the E-mode component of the γ field. This parallels closely the algorithm followed in de-lensing of the CMB sky [95].

Given the Wiener filtered maps $\widehat{\gamma}^{E,\mathrm{WF}}$, $\widehat{\gamma}^{B,\mathrm{WF}}$ and T^{WF}, the decontaminated polarization maps are given by the following estimator,

$${}_{\pm}X^{\mathrm{clean},\,i}(\hat{\mathbf{n}}) = {}_{\pm}X^{i}(\hat{\mathbf{n}}) - {}_{\pm}\widehat{\gamma}^{\mathrm{WF},\,i}(\hat{\mathbf{n}}) T^{\mathrm{WF},\,i}(\hat{\mathbf{n}}) \, , \tag{5.27}$$

where we have again used the intergral form of ${}_{\pm}I$ to express the multipole sum in Equation 5.23 in its equivalent and efficient real space form. Note that throughout this derivation we work with the beam convolved fields.

The index 'i' in the above equation indicates the cleaning iteration. For each iteration of the cleaning beyond the zeroth, the cleaned polarization fields from the previous iteration become the new observed fields to be passed to the QE as well as the cleaning estimator. As expected, the temperature field remains unaltered through this cleaning process. Note that since the reconstructed γ fields and the corresponding reconstruction noise estimates are continuously updated, the Wiener filters must be freshly estimated at each iteration. This cleaning process is repeated until the reconstruction noise and the B-mode power spectrum converges to their respective floors. We reiterate that in this case study we focus on the details of the iterative cleaning algorithm for the T to P leakage distortion sourced by differential gain, however, this can be generalized to the full range of distortions described in Section 5.2.

Gaussian Filters

While it is important that the filters lead to the smallest residual contamination after each iteration of the cleaning, it is also important that the filter prevents the cleaning process from introducing excess bias. While we have shown that the Wiener filters are the optimal filters that minimize $C^{BB,\,\mathrm{res}}_l$, in our numerical experiments working with idealized low noise simulations we find that Wiener filters tend to overestimate the contamination for modes where the reconstruction noise is high, thereby making the iterative procedure have an undesirable non-convergent behaviour. We understand this to be a special feature of a T to P leakage systematic in which $T >> B$ and therefore even a small error in the reconstructed γ maps can lead to a large errors in the de-contaminated the B-mode maps in particular. To prevent

this we propose a Gaussian filtering scheme,

$$f_L^\gamma = A \exp\left(- \left[\frac{\widehat{C}_L^{\gamma\gamma}}{\widehat{C}_L^{\gamma\gamma} - N_L^\gamma} \right]^2 \right) , \tag{5.28}$$

where the normalization A is set such that $\max(f_l^\gamma) = 1$. In our numerical simulations we perform, we find this to be a convergent scheme in all cases (unlike Wiener filtering), as it is more aggressive in suppressing modes that are contaminated by noise, thereby preventing excess bias from being introduced into the cleaning.

5.4.2 Forecasting the reconstruction noise and C_l^{BB} floors

Due to the imperfect reconstruction of the γ fields, it is in practice not possible to perfectly decontaminate the polarization maps using this procedure. To answer this question we have devised a forecasting procedure that enables us to predict the reconstruction noise and C_l^{BB} floors that the iterative cleaning procedure should in principle achieve.

Making these forecasts involves evaluating the following algorithm. We begin by making an estimate of the reconstruction noise under the assumption that polarization map can be perfectly cleaned. After this initialization we iterate over the following steps until convergence:

- Use the estimated reconstruction noise to simulate Weiner filtered γ maps, using the true systematic maps as input.
- Use the filtered γ maps to perform cleaning on a simulation of contaminated polarization maps using the same procedure prescribed in Section 5.4.1.
- Use the mock cleaned maps to make revised estimates of the reconstruction noise.

The B-mode calculated from the mock cleaned maps, and the estimates of the reconstruction noise were found to converge after five iterations of the above process. This procedure provides a forecast for both the reconstruction noise floor as well as the cleaned power spectrum characterizing the polarization maps. We can compare these estimates to the reconstruction noise and the polarization power spectra derived from employing the iterative cleaning procedure to assess if the blind cleaning is performing as expected.

Note that this procedure uses information from the true CMB and systematics maps and as such is only useful for testing the analysis pipeline. For an actual experiment, where we can assume no prior knowledge of the contaminants, we will not have the liberty of carrying out such validation tests. For actual data analysis we would carry out iterations until the reconstruction noise converges, as we will demonstrate in Section 5.6.

5.5 Simulating Temperature to Polarization Leakage

5.5.1 Systematic - Differential Gain

In upcoming experiments, both satellite- and ground-based, control of T to P leakage will be essential. The relative amplitudes of the signals means that even temperature leakage at the percent level could be a significant contaminant to the B-mode signal. This section will describe the simulation of T to P leakage and the scan strategy we consider for our differential gain case study, following the approach of [89], [90]; see those works for a more exhaustive discussion. We reiterate that the quadratic estimator approach is applicable to a wide range of distortions, we are just choosing this systematic for our detailed case study as it generates the γ distortion field that was found to be most important in [28].

The signal observed by a single detector contains both the temperature and modulated polarisation signals and may be written as

$$d^X = (1 + \delta g^X)\tilde{T}(\hat{\mathbf{n}}) + \tilde{Q}(\hat{\mathbf{n}})\cos(2\psi) + \tilde{U}(\hat{\mathbf{n}})\sin(2\psi) \ , \tag{5.29}$$

where X denotes which detector is being considered, and ψ is the crossing angle (the orientation of the focal plane on the sky). We have represented a possible constant gain or calibration factor by δg^X, but for our case study we only apply this factor to the temperature signal. A calibration or gain difference can also cause other effects, such as an amplifcation of the polarisation signal, but we focus on this as it is the most significant problem and is the one that can manifest as a γ type distortion.

We consider a pair-differencing experiment, consisting of co-located detector pairs that are oriented 90 degrees apart. whose observed signals are differenced. Ideally the temperature signal would be completely removed by this procedure, however, any mismatch in the detector gain δg^X between the two detectors will result in leakage of the temperature signal into the polarisation map. We write the differenced signal for a detector pair i as

$$\begin{aligned} d_i =& \frac{1}{2}\left(d_i^A - d_i^B\right) \\ =& \frac{1}{2}\Big[(\delta g_i^A - \delta g_i^B)\tilde{T}(\hat{\mathbf{n}}) + 2\tilde{Q}(\hat{\mathbf{n}})\cos(2\psi) + 2\tilde{U}(\hat{\mathbf{n}})\sin(2\psi)\Big] \ , \end{aligned}$$

where A and B denote each detector in the co-located pair. The temperature leakage will occur if $\delta g_i = \delta g_i^A - \delta g_i^B \neq 0$, and is given by

$$\delta d_i^g = \frac{\delta g_i}{2}\,\tilde{T}(\hat{\mathbf{n}}) \ , \tag{5.30}$$

which is a spin-0 quantity. This will combine with the spin-2 part of the scan strategy to create a spurious spin-2 signal that contaminates the polarisation measurement. We may describe a

given scanning strategy by a real space field (again, see [89], [90] for more details)

$$\tilde{h}_k = \frac{1}{N_{\rm hits}(\theta,\phi)} \sum_j e^{ik\psi_j(\theta,\phi)} \ , \tag{5.31}$$

where ψ_j is the jth crossing angle of a given pixel, and $N_{\rm hits}$ is the total number of measurements in that pixel. The survey mask is described by $\tilde{h}_0$, while $\tilde{h}_2$ and $\tilde{h}_4$ naturally appear in simple map-making, and various k values contribute to different systematic effects (see e.g. [89], [90], [145]. In the differential gain case considered here, the systematic couples to $\tilde{h}_2$ [89], [90], so the spurious signal due to a detector pair i is

$${}_2(\delta d_i^g) = \frac{1}{2}\tilde{h}_2(\hat{\mathbf{n}})(\delta g_i)\,\tilde{T}(\hat{\mathbf{n}}) \ . \tag{5.32}$$

In particular for our simulations, we will use a focal plane with two such pairs of detectors, oriented at 45 degrees to one another to allow simultaneous measurement of both $\tilde{Q}$ and $\tilde{U}$ signals. The combined systematic contribution from the two detector pairs is given by

$${}_2(\delta d^g) = \frac{1}{2}\tilde{h}_2(\hat{\mathbf{n}})(\delta g_1 - i\delta g_2)\,\tilde{T}(\hat{\mathbf{n}}) \tag{5.33}$$

where the factor of i in the second detector term is due to the rotated orientation of 45 degrees.

For simplicity we choose a setup where each pair of the detectors experiences the same differential gain, $\delta g_1 = \delta g_2 = 10^{-2}$, which corresponds to a 1% differential gain. This simplification will not affect the generality of the QE results presented, but one may expect slightly different levels of gain mismatch for different focal plane setups. [3]

By comparing equation (5.1) to (5.33), we can see that the differential gain be related to the γ distortion as

$$(\gamma^Q \pm i\gamma^U)(\hat{\mathbf{n}})\tilde{T}(\hat{\mathbf{n}}) = \frac{1}{2}\tilde{h}_{\pm 2}(\hat{\mathbf{n}})(\delta g_1 \mp i\delta g_2)\,\tilde{T}(\hat{\mathbf{n}}) \ . \tag{5.34}$$

5.5.2 Differential gain r-bias

We examine the expected biases on r that correspond to a range of levels of differential gain. We define the bias sourced by the systematic, δ_r, as the difference between the mean of the posterior of the contaminated and uncontaminated spectra. In Figure 5.3 we show the bias on r, δ_r, for differential gains in the range $\delta g = 10^{-5} \to 10^{-2}$, in the presence of a noise sensitivity of $w_{TT}^{-1} = 2.7\mu$K arcmin and a full-width at half-maximum of $\theta_{\rm FWHM} = 30'$. We calculate the biases for a fiducial tensor-to-scalar ratio of $r = 10^{-3}$. For $\delta g \lesssim 7 \times 10^{-4}$ the bias is smaller than the 1σ statistical variance on r and cleaning would not be necessary. For

[3] There are other methods for handling differential systematics [36], [146], however here we study the QE approach in detail rather than performing a comparison of methods. One alternative method being investigated is rotating half wave plates, in which case it is not clear whether detector differencing should be used [147], [148]. We note that the important systematics in a HWP setup are likely to be different, and it is unclear to what extent our distortion field setup will capture the important systematics. We leave the investigation of the utility of QE in such a situation to future work.

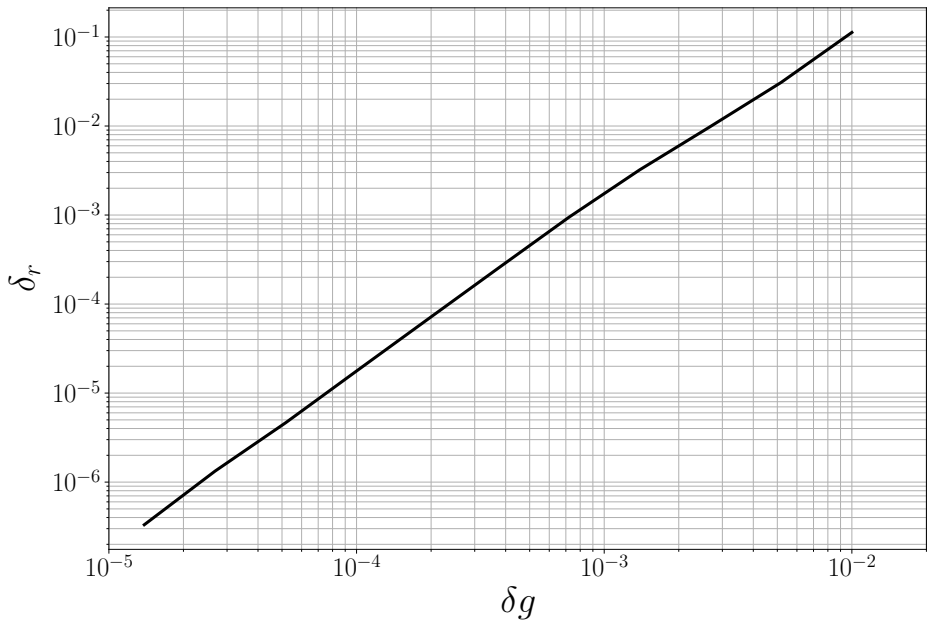

Figure 5.3: The bias on a fiducial tensor-to-scalar ratio of $r = 10^{-3}$ for levels of differential gain of $\delta g = 10^{-6} \rightarrow 10^{-2}$ in the presence of a white noise level of $w_{TT}^{-1} = 2.7\mu$K arcmin and a full-width at half-maximum of $\theta_{\rm FWHM} = 30'$. For values of $\delta g \sim 1.4 \times 10^{-5}$ the bias is $\delta_r = 0$ to machine precision.

values greater than this the bias becomes significant, increasing to ~ 100 times the fiducial r value for $\delta g \sim 10^{-2}$. In this range the bias will have a significant impact on the robustness of attempts to measure r. While the QE cleaning process we present here is able to remove the bias for a range of levels of differential gain, we present results for $\delta g = 10^{-3}$ in order to demonstrate that it is possible to remove even very large levels of contamination sourced by differential detector gain. Note that this larger level of differential detector gain is typical for a number of contemporary ground-based CMB experiments [e.g. 62], [140], for which we also expect the QE approach to be valuable.

5.5.3 Scan Strategy

We choose to adopt the Experimental Probe of Inflationary Cosmology (*EPIC*) satellite scan strategy [145]. This will be representative of other future CMB satellite surveys. The design of the EPIC scan strategy optimises crossing angle coverage and is defined by its boresight angle (50°), precession angle (45°), spin period (1 min), and precession period (3 hrs) (for further details see [89] and [149]). This scan is represented as a list of hits, i.e. datapoints, where each hit is specified by its location on the sky (RA and Dec) and parallactic angle (ψ). We expect the QE technique to be equally useful for ground based CMB surveys however, because of the role of the scan strategy in the simulations, we have used a satellite survey for two reasons. Firstly, because no ground-based survey covers the whole sky, and we wanted

to avoid complications due to partial sky coverage. Secondly, because ground based surveys differ more between experiments and cannot be simply described by a few parameters as satellite scans can, since they depend on complicated constraints and detailed scheduling choices.[4]

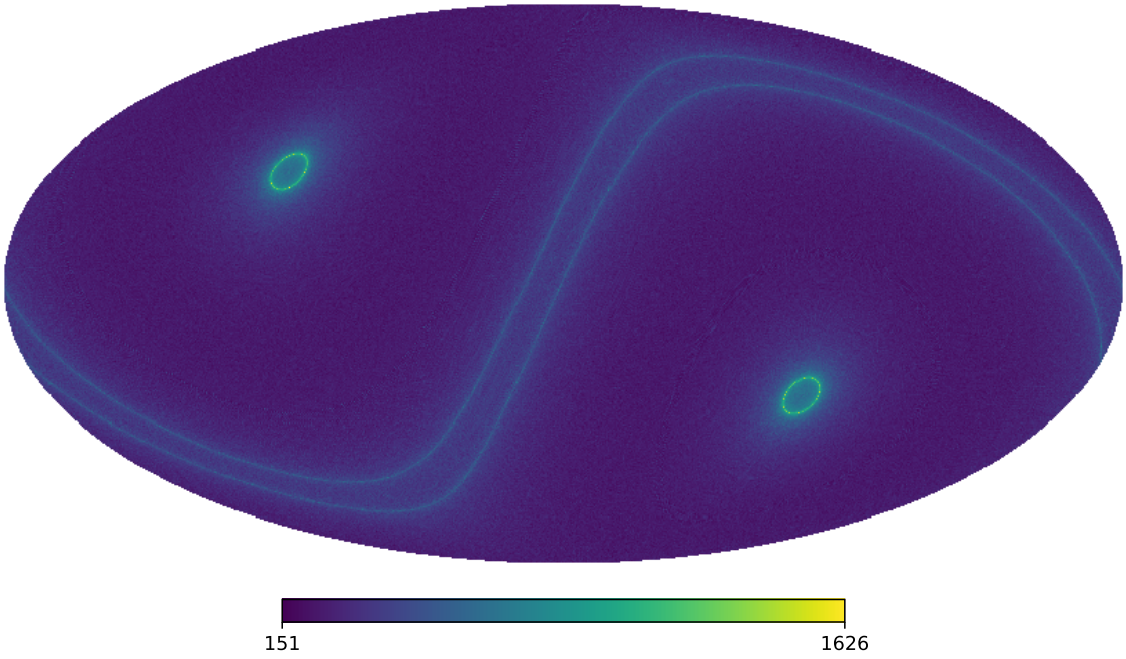

Figure 5.4: The hit map of the *EPIC* scan strategy. This survey has been designed to maximise crossing angle coverage, and the hit map is well filled across the full sky with many observations at different orientations. Note that the ecliptic poles have been prioritised to aid the understanding of foregrounds.

The scan strategy of *EPIC* provides a relatively uniform distribution of hits and crossing angles which should reduce scan coupled differential systematics fairly well. The ecliptic poles are observed more frequently to aid in foreground analysis, which results in some structure appearing in the survey fields as seen in Figure 5.4. The $\tilde{h}_{\pm 2}$ field (equation (5.31)) encodes the spin-2 part of the scan that turns the gain systematic into a spurious spin-2 signal. This field is shown in Figure 5.5 for the *EPIC* scan strategy. The $\tilde{h}_2$ is dominated by its large scale features, and this will result in a low l dominated systematic.

5.5.4 Simulation

We use a modified version of the code used in [89]. The input to the time ordered data (TOD) simulation code consists of maps of the CMB $\tilde{T}$, $\tilde{Q}$ and $\tilde{U}$ fields which are generated using the SYNFAST routine of the HEALPIX package [151]. The input CMB power spectra were created in CAMB using a six parameter ΛCDM cosmological model, specified in Table 5.1

[4] Although see [150] for some simple approaches to approximate ground-based scan strategies that capture the features relevant for studies such as this one.

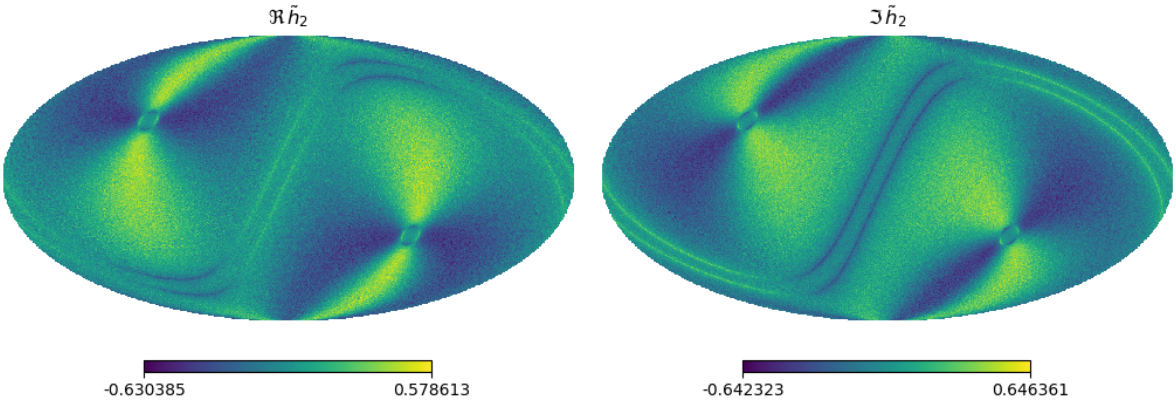

Figure 5.5: The real (left panel) and imaginary (right panel) parts of the $\tilde{h}_2$ field (defined in equation 5.31), which encodes the spin-2 part of the scan that turns the gain systematic into a spurious spin-2 signal. The $\tilde{h}_2$ field is dominated by its large scale features, which will result in a low l dominated systematic.

[152]. For the simulations including noise, we include a Gaussian beam post process. A white noise is applied to the data at map level, where a noise is added to each pixel of the level $w_{TT}^{-1} = 2.7\mu$K arcmin [88].

	Simulation Inputs
Cosmology	H_0 = 67.4
	$\Omega_b h^2 = 0.022$
	$\Omega_c h^2 = 0.120$
	$\tau = 0.06$
	$n_s = 0.97$
	$10^9 A_s = 2.2$
	$r = 0.001$
Map-making	$N_{\rm side} = 2048$
	$\ell_{\rm max} = 3000$
	$\lvert\delta g_1\rvert = 0.01$
	$\lvert\delta g_2\rvert = 0.01$

Table 5.1: The fiducial cosmological parameters and the map-making inputs for the TOD simulations. The simulated maps are smoothed by a Gaussian beam and noise is added per pixel.

The simulation computes values for each of the four detectors for each hit as described in equation (5.29), using HEALPIX interpolation to observe the input sky maps at the appropriate location, and using the corresponding parallactic angle ψ for that hit, generated from the *EPIC* scan strategy. As described in section 5.5, the ψ values are offset by 90° for the two detectors within a pair, and by 45° between the two pairs of detectors. The differential gain systematic is added for each pair of detectors by increasing the signal by a factor $(1 - \delta g_i)$ in the second detector d_i^B in each pair, where we use $|\delta g_1| = |\delta g_2| = 0.01$ for the simulations in this chapter [153]. This level of systematic is indicative of the differential gain seen in recent CMB surveys [e.g. 62], [140], and corresponds to an r bias of $\sim 30\sigma$.

Maps are made from the time streams according to a simple binning map making tech-

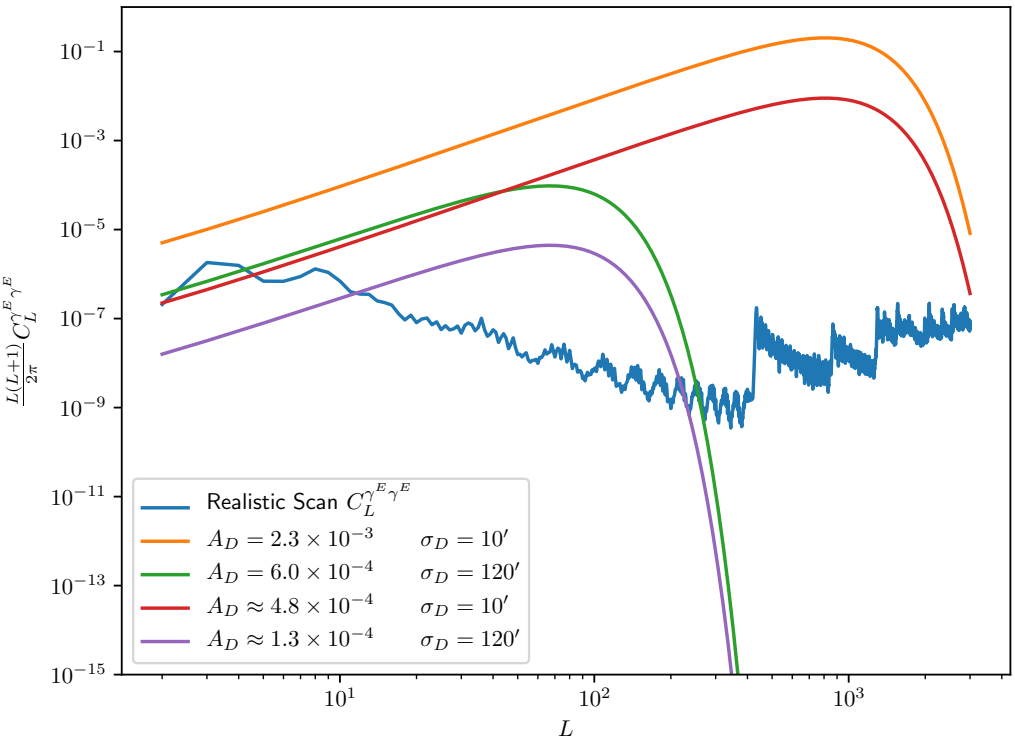

Figure 5.6: The E-mode spectrum of the ${}_{\pm}\gamma(\hat{\mathbf{n}})$ distortion fields, the orange and green lines show the spectra plotted for the $A_D^{\rm Max}$ amplitudes of [28] for coherences scales of $10'$ and $120'$ respectively, the red and purple lines show the spectra plotted for the $A_D^{\rm Min}$ amplitudes of [28] for the CMBPol satellite estimate corresponding to r=0.005 for coherences scales of $10'$ and $120'$ respectively. The blue line shows the realistic spectrum calculated from the a combination of the systematic and the *EPIC* scan strategy that we adopt for our simulations. It is clear here that the approximation used for the distortion power spectra does not describe the realistic case well at higher multipoles. It overestimates the power at high multipoles in comparison to the realistic case for small coherence scales. Additionally the sharp drop off in power after the peak is not consistent with the realistic spectra as is evident for all sets of curves showing the approximation.

nique,

$$\begin{pmatrix} Q \\ U \end{pmatrix} = \begin{pmatrix} \langle \cos^2(2\psi_i) \rangle & \langle \cos(2\psi_i) \sin(2\psi_i) \rangle \\ \langle \sin(2\psi_i) \cos(2\psi_i) \rangle & \langle \sin^2(2\psi_i) \rangle \end{pmatrix}^{-1} \begin{pmatrix} \langle d_i \cos(2\psi_i) \rangle \\ \langle d_i \sin(2\psi_i) \rangle \end{pmatrix} , \tag{5.35}$$

where the angle brackets $\langle\rangle$ denote an average over the measurements in a pixel, and the d_j here correspond to the detector measurements (i.e. the sum of the timestreams from the two differenced pairs) each with its an associated angle ψ_j.

5.5.5 Realistic Systematic Spectra

In previous studies [e.g. 28], [139] the distortion fields of equation 5.1 have been assumed to be statistically isotropic and Gaussian, and defined by power spectra of the form

$$C_l^{DD} = A_D^2 e^{-l(l+1)\sigma_D^2/8\ln 2}\,, \tag{5.36}$$

where A_D represents the root mean squared of the distortion field, and σ_D represents a coherence scale beyond which the distortion power spectrum becomes white noise. We show a comparison between this spectrum and the realistic spectrum from our simulations in figure 5.6. There are significant differences apparent between the approximation of equation 5.36 for the power spectra describing the distortion fields used in previous literature, and the realistic distortion field that is derived from the more realistic simulation used in our study.

Although the spectrum generated from equation 5.36 results in most of the power being at low multipoles similar to the realistic spectra, it does not capture the high l nature of the realistic distortion fields. The realistic distortion fields have an initial much sharper drop off, before levelling out, compared to the more gradual drop off of the approximation. In figure 5.6 we show that the two extreme coherence scales used in [28] both suffer from the same issue that they accrue too much power at high l compared to the realistic spectra, hence the results found will be biased by this. In our analysis in Section 5.6 we reconstruct the distortion power spectrum up to $L = 800$ and, as can be seen in figure 5.6, the shapes of the realistic and approximate spectra differ significantly for this range of multipoles. This shows the advantage of carrying out detailed case studies on individual distortions.

We note that the smallest $A_D^{\rm min} \approx 1.3 \times 10^{-4}$ for $\sigma_D = 120'$ quoted from [28] corresponds to a gain mismatch of 6.4×10^{-4} (0.064%). This is significantly smaller than a realistic gain mismatch of 0.01 (1%), in the analysis in [28] it was found that the QE technique would still be effective for this small value of the systematic.

5.6 Reconstructing and removing the temperature to polarization leakage

Here we discuss the results of employing the statistical analysis methods developed in Section 6.2 and Section 5.4 to contaminated CMB maps simulated as in Section 5.5. Note that we include lensing effects only at the power spectrum level, implying that the off-diagonal elements sourced by weak lensing are not included in our simulations. This is not expected to influence our inference of the reconstruction and removal of the T to P leakage systematic, owing to different spins associated with the two effects[5].

[5]Note that this is not generally true for other instrument systematics. As an example a differential pointing systematic directly couples to the weak lensing effect and in a analogous study the weak lensing induced correlations cannot be ignored.

Parameter	Ideal	Non-ideal
$l_{\rm max}$	1400	1400
$L_{\rm max}$	800	800
$N_{\rm side}$	1024	1024
w_{TT}^{-1}	0	2.7 μK arcmin
θ_{FWHM}	0	$30'$
r	10^{-3}	10^{-3}
$A_{\rm lens}$	0	1

Table 5.2: This table summarizes the QE parameter settings used in all our analyses and also the simulation settings for the two different sets of simulations used in results presented in this section.

In all our analyses we iterate over the following steps until convergence:

- Reconstruct map of systematics given some input $[T, Q, U]$ maps using the QE algorithm. In the first iteration the inputs correspond to the observed maps, while for the subsequent iterations these correspond to the contamination cleaned maps.

- Clean the input maps using the reconstructed γ maps following the optimal cleaning procedure discussed in Section 5.4.1.

Here we reemphasize that the cleaning analysis is agnostic to details of the particular systematic, as evident by the fact that the cleaning procedure only works with the observed maps as inputs. All QE evaluations required in the blind cleaning process are carried out assuming the parameter settings summarized in Table 5.2. We make forecasts for the reconstruction noise and the C_l^{BB} spectrum that one expects to recover from the iteratively cleaned maps, following procedures outlined in Section 5.4.2. We use these forecasted power spectra as benchmarks for our blind cleaning analysis.

We present the results of this analysis on two different set of simulations, the ideal case and the more realistic, non-ideal case, in sections 5.6.1 and 5.6.2 respectively. A discussion with particular emphasis on the measurement of tensor to scalar ratio r is presented in Section 5.7.

5.6.1 The cosmic variance limits of the blind cleaning algorithm

Here we discuss the results derived from analyses on simulations which are ideal in the sense that they include no measurement noise & beam smoothing and also do not include any lensing induced B-modes. These simulations allow us to probe the limitations of the blind cleaning algorithm in this extreme setting, in process highlighting how well this procedure could in principle work.

The reconstructed γ maps at some example iterations of the analysis are depicted in Fig. 5.7. Here we note that the systematics reconstructed from the original observed maps are quite noisy as inferred by comparing the top and middle panels of Fig. 5.7. This observation

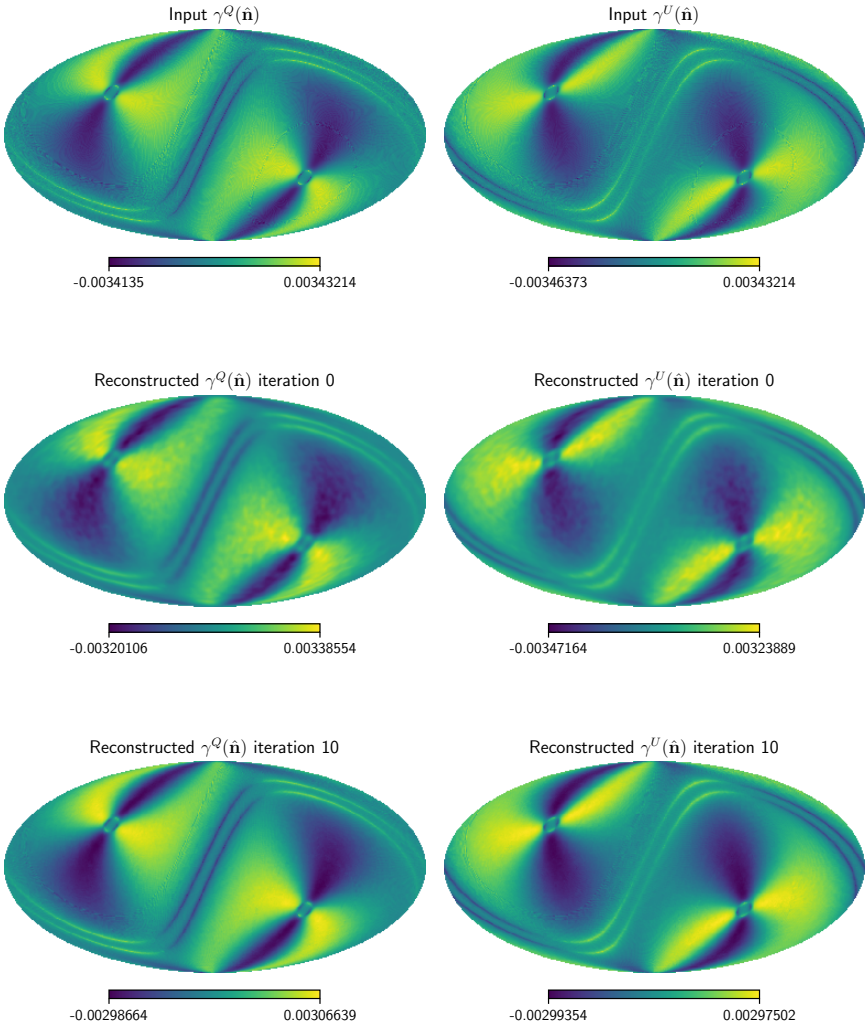

Figure 5.7: This figure depicts the $\gamma^Q(\hat{\mathbf{n}})$ and $\gamma^U(\hat{\mathbf{n}})$ systematic maps that mediate the T to P leakage. The top panels depicts the true systematic maps used to simulate the contaminated CMB maps. The middle panels shows the QE reconstruction of the γ maps from the observed CMB maps for the 0th iteration. The bottom panels depict the reconstructed γ maps after 10 iterations of cleaning and reconstructing of the systematic maps.

is better quantified in Fig. 5.8, where by inspecting the reconstruction noise for the 0^{th} iteration and comparing it to the true γ power spectrum, it is clear that only $L \lesssim 30$ multipoles of the γ map can be reliably recovered. The reconstruction noise being high is due to the excess B-mode power sourced by the systematics in the observed CMB maps as seen in Fig 5.9.

We now use these reconstructed γ maps together with the observed temperature anisotropy map to remove part of the contamination, sourced by modes in the γ maps that have been reliably recovered. This procedure involves using the high SNR modes of the temperature and γ maps, the formal details of which are discussed in Section 5.4.1. In the case of these idealized simulations, we find that the conventional Wiener filtering scheme causes the iterative scheme

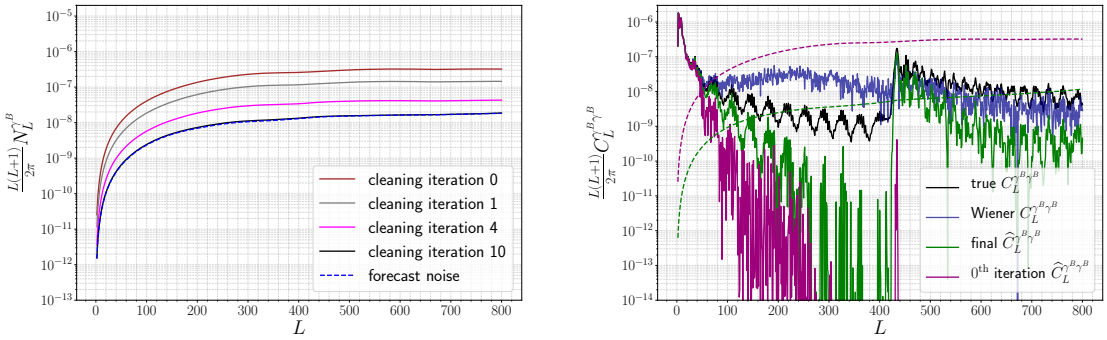

Figure 5.8: The left panel shows the evolution of the reconstruction noise for different iterations of the algorithm. Note that the reconstruction noise reduces with iterations and approaches that predicted using the forecasting procedure. The right panel shows the power spectra of the true and reconstructed and filtered γ maps. The corresponding reconstruction noise curves are plotted for reference. Note that the Wiener filtered, $\hat{C}_L^{\gamma^B\gamma^B,\mathrm{WF}}$, spectrum is most reliably recovered for modes where $C_L^{\gamma^B\gamma^B}$ is much greater than $N_L^{\gamma^B\gamma^B}$. Similar results found for γ^E, not show here for brevity.

to diverge after few initial iterations. We suspect this behaviour arises from the fact that the Wiener filter does not sufficiently suppress modes that have a noisy recovery, which combined with the fact that $T >> B$, leads to a faulty cleaning of the polarization maps, in effect adding more power to the B-mode map as opposed to subtracting it. This eventually leads to run away behaviour. We deal with this issue by employing the Gaussian filtering scheme instead (see Section 5.4.1 for details) which mitigates this issue by imposing a stronger suppression of the noisy modes, leading to more stable and convergent results. The right panel of Fig. 5.8 depicts the power spectrum of the γ^B maps after the Gaussian and Weiner filters are applied to them, where notably the Weiner filtered maps retain a lot of power from the unreliably recovered modes, as opposed to the Gaussian filtered map where these noisy modes are more heavily suppressed.

After the first cleaning (i.e. cleaning iteration 0), the B-mode power spectrum reduces compared to the spectrum estimated from the observed B-mode map as seen in Fig 5.9. This results in the reconstruction noise of the QE to reduce as can be understood by comparing the curves corresponding to "iteration 0" and "iteration 1" in Fig. 5.8. This reduction in the reconstruction noise, facilitates the recovery of modes in the γ map that were dominated by the reconstruction noise in the previous iteration. These newly recovered modes of the systematic map are then fed to the cleaning algorithm to further remove the contamination from the polarization maps. This whole process is repeated until we observe no further improvements in either the reconstruction noise and/or the C_ℓ^{BB} spectrum.

On repeating this procedure we see that the contamination in the CMB polarization maps is progressively removed as indicated by the systematic reduction in the amplitude of C_l^{BB} amplitude in Fig. 5.9. Note that initial iterations show relatively big reductions in power, with

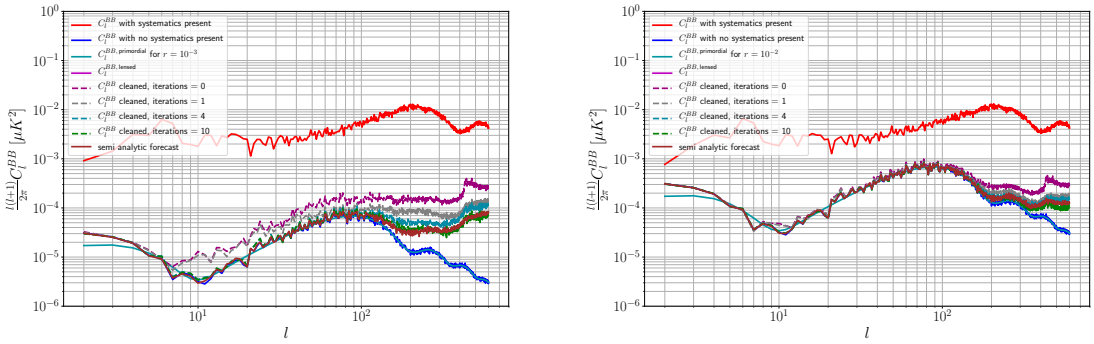

Figure 5.9: This figure depicts the B-mode power spectrum corresponding to the systematic ridden maps, the true cosmological primordial signal and the evolution of the estimated power spectrum across different iterations of the cleaning algorithm. The left and right panels show the cleaning for $r = 10^{-3}$ and $r = 10^{-2}$ respectively. Also shown is the prediction for the B-mode power spectrum expected post cleaning evaluated using the forecasting procedure.

subsequent iterations resulting in more subtle improvements and the final few iterations show no appreciable updates to the spectrum. The performance of the cleaning process improves if the amplitude of the uncontaminated B-mode spectrum increases. For the ideal case this translates to improved performance for larger values of r. We note that even in this perfect setting of no instrument and lensing noise, the recovered B-mode spectrum is not perfectly cleaned. This can be interpreted as an intrinsic limitation to how well the cleaning can in principle perform. Nonetheless, the proposed blind cleaning procedure enables robust removal of contamination power that is roughly two orders of magnitude larger than the injected signal, and yields an unbiased recovery of the true signal at most multipoles. This systematic reduction in the B-mode power is only possible due to the simultaneously reduction in the reconstruction noise (sourced by reduction in C_ℓ^{BB}) as seen in Fig. 5.8, which results in robust recovery of the higher multipole of the γ maps (which in turn facilitates more cleaning of the polarization maps). To contrast the effect of iterative cleaning note that while the "iteration 0" only allowed for recovery of the modes $L \lesssim 30$, the reconstruction noise associated with the final iteration of cleaning allows robust recovery of modes up to $L \simeq 800$ as can be seen in right panel of Fig. 5.8. This stark improvement in the recovery of high L modes of the γ maps can be better appreciated by simultaneously comparing the recovered total γ maps shown in the bottom panels of Fig. 5.7 to those depicted in the panels above. Note that the total systematic maps is recovered by adding together the filtered maps of systematics estimated at each iteration[6]. The input maps have a higher amplitude than those reconstructed which is primarily a consequence of our maps being filtered and the reconstruction being terminated at $L_{\text{max}} = 800$.

Here, it is also important to appreciate the non-monotonic nature of the true $C_L^{\gamma\gamma}$ which

[6]The γ maps recovered at each iteration do not include the modes that were in effect subtracted from the polarization data in the previous iteration.

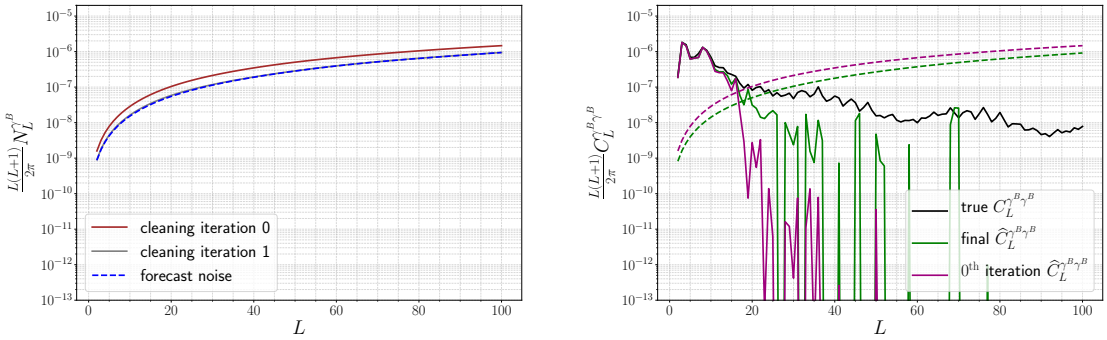

Figure 5.10: The left panel shows the reconstruction noise $N_L^{\gamma^B}$ for one iteration of the reconstruction and cleaning process. After a single iteration the cleaning reconstruction noise converges with the forecasted reconstruction noise. The right panel shows $\widehat{C}_L^{\gamma^B\gamma^B}$ for the reconstructed and filtered γ maps before cleaning and after ten iterations of cleaning (green) and the true $C_L^{\gamma^B\gamma^B}$ is also shown for comparison. Corresponding reconstruction noise shown for reference.

features a prominent jump in power at $L \sim 400$. This is a consequence of using realistic scan maps in our simulations. There is a corresponding feature in the cleaned B-mode spectra in Figure 5.9. This feature is present because not all modes below $L \lesssim 800$ are reconstructed, as some intermediate modes which are dominated by reconstruction noise are suppressed. We reiterate that this would not have been observed in studies using the approximate spectra, [28], [139], generated using equation (5.36) because of the difference in shape between the realistic and approximate spectra. It is necessary to carry out detailed case studies systematics in order to observe these important details. Unlike in weak lensing studies, for instrument systematics it is not possible to make a generic forecasts as was done in [28].

Finally, we note that the spectrum converges to the prediction from our forecasting procedure. This is true both for C_l^{BB} as well as $N_L^{\gamma\gamma}$ as seen in Fig. 5.9 and Fig. 5.8 respectively. It is important to note this near consistency for two reasons, (i) it serves as a validation of our blind cleaning algorithm (ii) the actual analysis is performed using the Gaussian filter, while our forecasting procedure continues to use Wiener filters, and the near equivalence of the two solutions suggests that the Gaussian filtering is close to optimal.

5.6.2 Employing blind systematic cleaning for a non-ideal experiment

Here we discuss results simulations that incorporate weak lensing induced B-modes as well as the measurement noise and beam smoothing in the previously described more realistic, non-ideal case. The assumed measurement noise and beam are summarized in Table 5.2 and correspond to the foreground cleaned Q/U maps that will result from linearly combining the multi-frequency measurements. Unlike in the previous section where these were ignored, here we treat the lensing B-modes as an important cosmological signal that we recover by

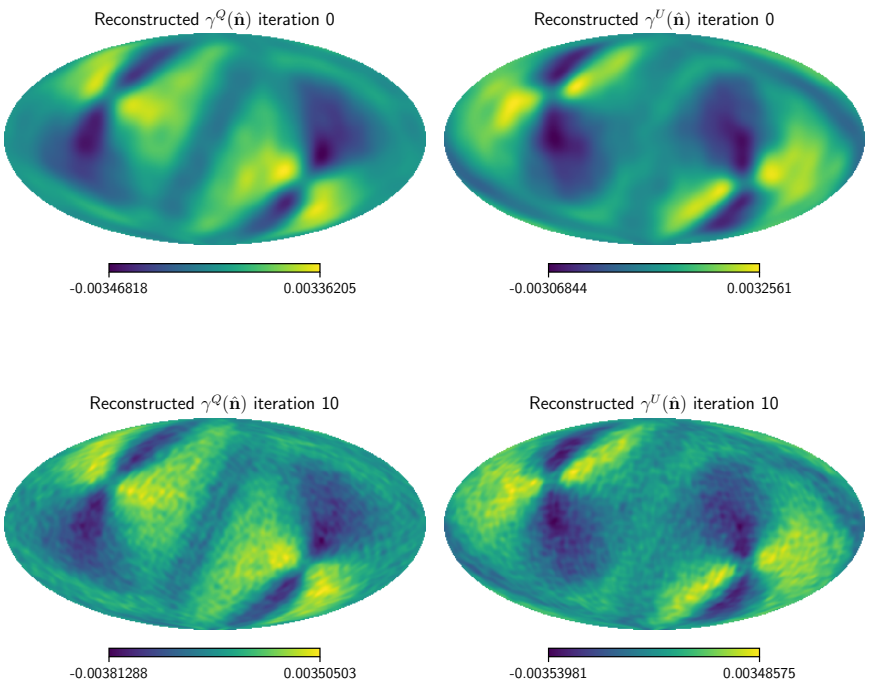

Figure 5.11: The top panels show the reconstructed filtered γ maps recovered from simulated observations, while the bottom panels show those recovered after a few iterations of cleaning. Note that even in the presence of instrument and lensing noise the iterative procedure helps with extracting bits of information on the systematics.

carrying out the iterative de-contamination procedure.

We carry out an analysis, identical to that described in the previous section, on these more realistic simulations. The simulations used here primarily differ from those used in the previous section by inclusion of the relatively high noise in the observed maps due to inclusion of lensing and measurement noise. We note that for these relatively high noise simulations, the Wiener filtering schemes is stable and convergent, and the results are very similar to those found when using the Gaussian filtering. We however continue to present results derived from employing the Gaussian filtering scheme through the rest of the paper. The relatively high noise results in a higher QE reconstruction noise floor, which consequently limits the reliable reconstruction of the γ maps to only the large angle modes $L \lesssim 20$, even after ten iterations of cleaning as seen in Fig. 5.10. This is even reflected in the total reconstructed γ maps as seen in Fig. 5.11. However note that the carrying out a number of iterative cleaning procedures does help in recovering some additional features in the reconstructed γ maps, the sharpening of the features in the equatorial plane in the bottom left panel of Fig. 5.11 is particularly noticeable. As we will see in Section 5.7 these subtle improvements in recovery of the systematic maps will play a crucial role in more robust removal of contaminations from the observed maps.

We now shift our attention to the evolution of C_l^{BB} across the cleaning iterations. Carrying

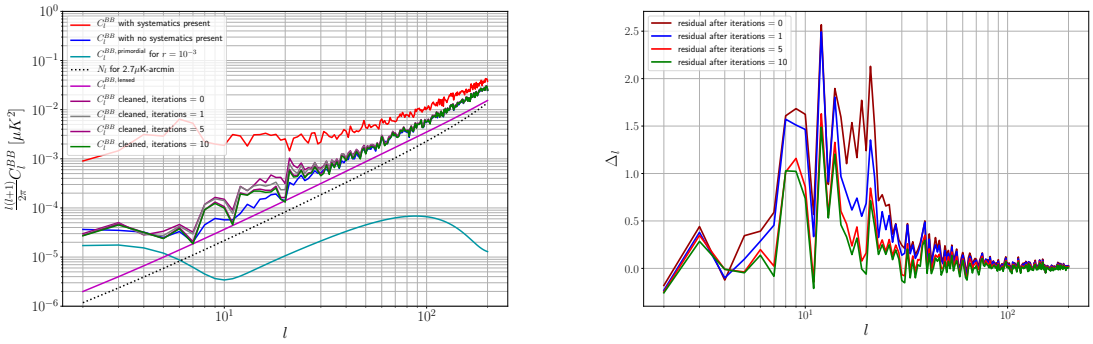

Figure 5.12: The left panel shows cleaned B-mode power spectra for 1 and 10 iterations of cleaning. The right panel shows the evolution of the relative difference $\Delta_l = (C_l^{BB,\,\mathrm{clean}} - C_l^{BB,\,\mathrm{true}})/C_l^{BB,\,\mathrm{true}}$ with iterations.

out higher iterations of cleaning does make small improvements to the convergence. These subtle but important improvements are highlighted in the right panel of Fig. 5.12, where the relative differences between the spectra derived from the cleaned maps at different iterations and true spectrum are depicted. In Section 5.7 we will highlight the importance of these subtle corrections in the context of measurement of tensor to scalar ratio r.

5.7 Recovering the tensor-to-scalar ratio

In the previous section we demonstrated that blind systematic cleaning method proposed here can yield nearly un-biased recovery of the true CMB B-mode power spectrum. Upcoming experiments aim to recover $r \in [10^{-2}, 10^{-3}]$ [16], [88]. Here we demonstrate that the blind cleaning technique can yield nearly un-biased recovery of r.

To demonstrate this we carry out a likelihood analysis for which we assume this specific form of the log-likelihood [81], [154], which accounts for the non-Gaussian nature of the power spectrum at low multipoles,

$$-2\ln\mathcal{L}(r) = \sum_l (2l+1)\left[\frac{\widehat{C}_l^{BB}}{r\,C_l^{BB,\,GW} + C_l^{BB,\,\mathrm{lens}} + N_l^{BB}} + \ln\left(r\,C_l^{BB,\,GW} + A_{\mathrm{lens}} C_l^{BB,\,\mathrm{lens}} + N_l^{BB}\right) - \frac{2l-1}{2l+1}\ln\left(\widehat{C}_l^{BB}\right)\right] + \text{const.}\,, \tag{5.37}$$

where $\widehat{C}_l^{BB}$ denotes the power spectrum estimated from the simulated data, corrected for the instrument beam, $C_l^{BB,\,GW}$ is the B-mode signal generated by primordial gravitational waves evaluated for $r = 1$, $C_l^{BB,\,\mathrm{lens}}$ denotes the lensing induced B-mode spectrum and N_l^{BB} is the instrument noise power spectrum. We evaluate this likelihood analysis on power spectra derived from the cleaned maps at a number of different iterations and compare the estimated

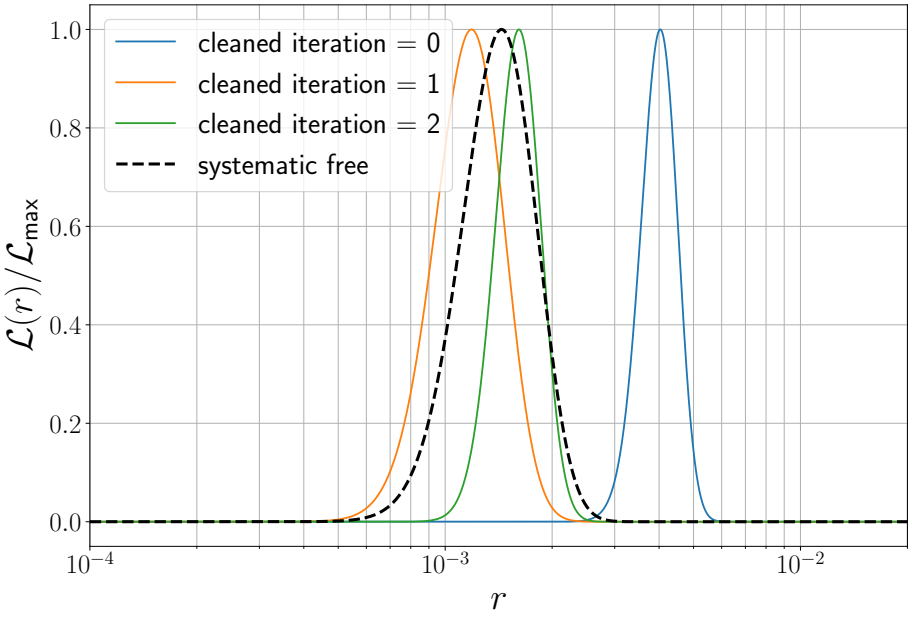

Figure 5.13: The evolution of the r-posterior across different cleaning iterations using the Wiener filter. The bias on r reduces with each iteration and is remarkably consistent with the posterior derived from the systematic free simulation. There is a bias on the profile likelihood for the iteratively cleaned spectra as we do not marginalize over the reconstructed T to P leakage.

posteriors on r to those derived from an analysis on a contamination free simulation.

We begin by noting that the r inferred from the contaminated B-mode simulations returns a highly biased measurement of $r \sim 10^{-1}$, off-set by two orders of from the true value. However, on repeatedly applying the iterative cleaning algorithm to it using either the Wiener or the Gaussian filter, the bias in the measurement of r reduces. The reduction in r-bias is largest in the non-ideal setup when using Wiener filtering. As seen in Fig. 5.13, after 2 iterations we find that the measured value of r is consistent with the true value to better than 1σ. This corresponds to a near perfect removal of a bias of order ~ 100. Beyond the 2nd iteration of cleaning there is no further change to the likelihood. Note that this cleaning also reduces the uncertainty on r by a similar order of magnitude. With lower values of $A_{\rm lens}$, corresponding to delensed maps, r is still consistent with the true value. However, more iterations are required to achieve convergence after delensing, as the reconstruction noise floor is lowered. Delensing does not significantly improve the level of cleaning that it is possible to achieve with the more realistic, non-ideal case. A joint study of delensing and systematics cleaning could become more relevant in the case of higher sensitivity experiments such as PICO [155].

	iteration	r	r_-	r_+
Contaminated	-	113	111	115
Cleaned	0	4.03	3.58	4.53
	1	1.19	0.972	1.5
	2	1.61	1.41	1.88
	3	1.61	1.41	1.88
True	-	1.44	1.16	1.86

Table 5.3: This table presents the central value of r, and 68% CI upper and lower bounds in units of 10^{-3}. These results assume no de-lensing i.e. $A_{\text{lens}} = 1$.

5.8 Conclusions

Systematic effects originating in the instrument pose a major challenge for upcoming CMB experiments seeking to measure the primordial CMB B-mode of polarization. Many of the existing techniques for mitigating these effects rely on complex instrument modeling and detailed knowledge of the instrument design. We have presented a detailed case study, implementing a QE approach to carry out cleaning of the CMB B-mode without detailed prior knowledge of the instrument. We have shown that this QE technique can successfully remove a T to P leakage sourced by a differential detector gain systematic, resulting in a near optimum recovery of the primordial B-mode and the reduction of the bias on the tensor-to-scalar ratio by ~ 2 orders of magnitude. Our robust implementation builds on the previous work by carrying out systematic recovery and map correction on a full TOD simulation including the effects of a realistic satellite scan strategy, and by the use of newly-derived efficient full-sky estimators. In our recovery and map correction we use a novel Gaussian filter which we find to be an effective alternative in cases where the Wiener filter caused the map correction to fail.

Our case study involved two scenarios. The first scenario, with no noise, beam or lensing, was used to illustrate the absolute limit to the cleaning process in an ideal world when there are no complications. The second scenario provides a more realistic, non-ideal example of the cleaning for a contemporary CMB experiment by using realistic levels of noise and beam comparable to those expected for the *LiteBIRD* instrument [88]. It was necessary to test the iterative cleaning scheme used in our map correction. We carried out this testing using a semi-analytical forecast for the ideal and realistic cleaning. Our cleaning was successful as it was found to be consistent with the forecast

We used our case study to test the conventional wisdom applied in previous studies of this approach [28] and from CMB weak lensing research. We find that in specific cases this wisdom does not hold. For example, previous studies suggest that using EB will result in the best reconstruction of T to P leakage. However, we find that the TB correlations provide the best reconstruction. In some cases using the Wiener filter, the optimum filter that is used in delensing, resulted in divergence when cleaning. The aforementioned Gaussian filter was found to avoid this divergence. These examples, where the conventional wisdom does not

apply in the case of systematics cleaning, show the importance of carrying out this case study.

A number of complications exist which will need addressing for this method to be viable that we leave to future work to consider. These complications include the inclusion of foregrounds, and the presence of multiple different systematics. It may be possible to reconstruct and remove these systematics simultaneously. Moreover, is may be possible break the degeneracy between some cosmological signals and systematics using a QE approach in combination with prior knowledge of the scan strategy.

Despite the additional complications that need to be considered, this detailed study of the QE reconstruction and the improvements made to the iterative cleaning process are an important step towards implementing QEs to reconstruct and remove systematic effects from upcoming CMB surveys. We suggest that this QE technique should be used to compliment traditional systematic correction techniques to diagnose and remove residual contamination in the data not corrected by other methods.

Many different contributions to the B-mode signal must be considered by any modern CMB experiment before a measurement of primordial B-modes is claimed. Up till now in this thesis we have considered only forecasts for constraints on these B-mode sources, and theoretical studies of ways to detect and constrain them. However, in the next chapter we go beyond the theoretical and apply the QE technique to attempt to reconstruct, and constrain the CB effect using the *Planck* 2018 polarization data. We believe this study may produce CB constraints that improve upon those found by applying non QE reconstruction techniques to *Planck*, and may be competitive with QE constraints that come from more recent CMB experiments such as BICEP2/Keck and ACTpol.

Chapter 6

Quadratic Estimator Constraints on Cosmological Birefringence from Planck 2018 Data

6.1 Introduction

In the previous chapter of this thesis we discussed systematic effects that could contaminate the primordial CMB B-mode signal, and in Chapter 4 we discussed the potential B-mode contamination that cosmological birefringence (CB) may source. However, now we will shift emphasis from the contamination of primordial to B-modes to the corresponding cosmological sources themselves. The CB effect, and in general cosmic polarization rotation (CPR), may represent an exciting observable for extensions to the theory of electromagnetism, and for the presence of primordial magnetic fields (PMFs).

The theory of electromagnetism is extremely well understood, and has undergone rigorous lab-based and astrophysical tests. It has long been known that it is a parity symmetric theory. However, it is important to test such symmetries in order to see if they are broken under extreme conditions, such as on cosmological scales. Parity symmetry has been shown to be broken in the weak sector, and it is possible to show that it could be broken in the electromagnetic sector through a simple extension to the standard model with a Chern-Simons term [25]. This is discussed at length in Chapter 2. However, here we offer a brief review of the concepts that are relevant to this chapter.

The Chern-Simons term is an additional contribution to the Lagrangian for electromagnetism of the form [27], [47]

$$\mathcal{L}_{CS} = -\frac{g_{\phi\gamma\gamma}}{2}\phi F_{\mu\nu}\tilde{F}^{\mu\nu} \ , \tag{6.1}$$

where ϕ is a pseudo-Nambu-Goldstone-boson (PNGB) field, $g_{\phi\gamma\gamma}$ is the coupling strength between the PNGB and the photon, $F_{\mu\nu}$ is the electromagnetic field strength tensor, and $\tilde{F}^{\mu\nu}$ is its dual. The Maxwell's equations are modified as a result of the inclusion of the this term

in the Lagrangian. Such modifications would lead to a rotation of the linear polarization angle of photons in direction $\hat{\mathbf{n}}$ from the observer. This rotation, sourced by parity violating modifications to electrodynamics, is known as CB [25]. The rotation angle is dependent on the coupling strength and the fluctuations of the PNGB between the source of the observed polarized photons and the observer [44],

$$\bar{\alpha}(\hat{\mathbf{n}}) = g_{\phi\gamma\gamma} \int d\eta \left(\frac{\partial}{\partial \eta} + \hat{\mathbf{n}} \cdot \boldsymbol{\nabla} \right) \phi(\eta, \hat{\mathbf{n}}) \ . \tag{6.2}$$

We can write this rotation in terms of direction dependent, $\alpha(\hat{\mathbf{n}})$, and monopole, α_0, components, so that $\bar{\alpha}(\hat{\mathbf{n}}) = \alpha_0 + \alpha(\hat{\mathbf{n}})$.

This extension to the standard model is motivated by a number of models where the PNGB in the Chern-Simons term is an axion or an axion-like particle [42], [118]. For a PNGB that is massless during the epoch of inflation the direction dependent map of the rotation angle along the line of sight, $\hat{\mathbf{n}}$, is expected to have a scale invariant power spectrum of the form [44], [156]

$$C_L^{\alpha\alpha} = A_{CB} \frac{2\pi}{L(L+1)} \tag{6.3}$$

where A_{CB} is the amplitude of the power spectrum and is related to the coupling strength and the Hubble constant during inflation, H_I, as [44], [156],

$$A_{CB} = \left(\frac{H_I g_{\phi\gamma\gamma}}{4\pi} \right)^2 \ . \tag{6.4}$$

Another physical phenomenon that may source the direction dependent rotation field, $\alpha(\hat{\mathbf{n}})$ is the presence of the aforementioned PMFs [69], [83], [129]. These primordial magnetic fields can induce Faraday rotation of polarized photons as they propagate from sources in the early universe. The rotation angle of photons propagating along the line of sight $\hat{\mathbf{n}}$ on the sky is [43], [157], [158]

$$\alpha(\hat{\mathbf{n}}) = \frac{3c^2}{16\pi^2 e} \nu^{-2} \int \dot{\tau}\, \mathbf{B} \cdot d\mathbf{l} \ . \tag{6.5}$$

Here, ν is the photon frequency, $\dot{\tau}$ is the differential optical depth, $\mathbf{B}$ is the magnetic field strength, and $d\mathbf{l}$ is the infinitesimal length element along the trajectory of the photon. Both the magnetic field strength and length element are in comoving coordinates. This effect would also result in a scale invariant power spectrum of the same form as (6.3). In this case the amplitude would be [43]

$$A_{CB} = \left[\frac{B_{\text{1Mpc}}}{(2.1 \times 10^2 \,\text{nG})(\nu/30\text{GHz})^2} \right]^2 \ , \tag{6.6}$$

where B_{1Mpc} is the magnetic field strength smoothed over 1Mpc.

In the case of both axion-photon coupling and PMFs, if one is able to place a constraint on A_{CB} from reconstruction of the $C_L^{\alpha\alpha}$ power spectrum from observations, then it is possible

to use this constraint to place an upper bound on these physical phenomenon by rewriting equations (6.4) and (6.6) to give [44], [156]

$$g_{\phi\gamma\gamma} = \frac{4\pi}{H_I}\sqrt{A_{CB}}\ , \tag{6.7}$$

for the axion photon coupling strength and

$$B_{1\text{Mpc}} = 2.1 \times 10^2\,\text{nG}\left(\frac{\nu}{30\,\text{GHz}}\right)^2\sqrt{A_{CB}}\ , \tag{6.8}$$

for the primordial magnetic field strength. The frequency dependence of the term in (6.8) would allow the separation of the PMF effect from the rotation generated by a pseudo-scalar coupling to the photon field. However, this frequency dependence also renders it difficult to place PMF constraints using component separated maps which use combinations of CMB map measurements taken from multiple frequency channels [159].

It is possible to place a constraint on A_{CB} by reconstructing $C_L^{\alpha\alpha}$ by using observations of the CMB polarization. A rotation of the linear polarization angle of photons will generate distortions in the CMB polarization maps of the $Q(\hat{\mathbf{n}})$ and $U(\hat{\mathbf{n}})$ Stokes parameters. When written in the spin weighted complex form, ${}_{\pm}P(\hat{\mathbf{n}}) = (Q \pm iU)(\hat{\mathbf{n}})$, the distortion of the Stokes parameters by this rotation can be written as

$${}_{\pm}P(\hat{\mathbf{n}}) = {}_{\pm}\tilde{P}(\hat{\mathbf{n}})e^{\mp 2i\alpha(\hat{\mathbf{n}})};\,. \tag{6.9}$$

Here, the tilde denotes the unrotated Stokes parameters. A distortion of the CMB polarization of this form will generate non-zero off-diagonal correlations in the CMB covariance matrix, $\langle a_{lm}a^*_{l'm'}\rangle$.

It is possible to use a quadratic estimator (QE) approach to leverage these off-diagonal correlations to reconstruct the $\alpha(\hat{\mathbf{n}})$ map and the $C_L^{\alpha\alpha}$ power spectrum, using existing observations of the CMB polarization[1]. While this has been done for a number of contemporary ground based experiments such as POLARBEAR [43], BICEP/Keck [68] and ACT [125], a QE approach to reconstruct $\alpha(\hat{\mathbf{n}})$ has not been applied to the *Planck* polarization data [136]. As the expected shape of $C_L^{\alpha\alpha}$ suggests there may be more power in larger scale modes it may be advantageous to use data from a full-sky satellite experiment in order to reconstruct $\alpha(\hat{\mathbf{n}})$. The results in Chapter 4 suggest that full-sky experiments, with access to larger scale scales, may be able to place stronger constraints on the amplitude of $C_L^{\alpha\alpha}$ than partial-sky experiments with comparable sensitivity.

While the *Planck* data has been used to reconstruct $\alpha(\hat{\mathbf{n}})$ and constrain A_{CB} in both [67] for the 2015 release data and [78] for the 2018 release data, neither work employed a QE approach. Instead an alternative approach, described in [67], was employed in both studies. This approach involves using the CMB polarization spectra to measure uniform CB in small

[1] In Section 2.5.4 of Chapter 2 we discuss the generation of off-diagonal correlations by CB, and summarize the derivation of the corresponding QE.

patches of the sky, and then combining these patches to form a map of $\alpha(\hat{\mathbf{n}})$. The constraint achieved using the 2015 release data was $A_{CB} \leq 2.74 \times 10^{-5}$ $\left[\text{rad}^2\right]$ within 95% C.L. [67]. A consistent, but stronger 95% C.L. constraint was found using the 2018 release data to $A_{CB} \leq 2.59 \times 10^{-5}$ $\left[\text{rad}^2\right]$. However, by applying a QE approach it may be possible to improve upon the existing constraints from *Planck*. Additionally, a QE approach will not be subject to absolute angle calibration error [102]. This error primarily effects studies of uniform CB. However, as studies of anisotropic CB which use the technique described in [67], [78] involve taking measurements of uniform CB on small patches of the sky they may also be vulnerable to this calibration error for the measurements in each patch. Recent attempts have been made to circumvent absolute calibration error in the uniform CB study presented in [106], leading to exciting new hints of a CB signal present in the *Planck* data. Therefore, it is prudent to carry out further investigate into anisotropic CB using *Planck*, applying the QE approach with the 2018 release data for the first time. This is the primary focus of this work.

In Section 6.2 of this chapter we focus on the analysis pipeline for our study, including the efficient QE, the map processing techniques, and the likelihood for A_{CB}. We follow this, in Section 6.3, with the results of tests we use to validate our QE pipeline and likelihood code. Finally, in Section 6.4 we present the results of our QE analysis of the *Planck* 2018 SMICA maps [159]. These results include new stronger *Planck* constraints on A_{CB} and the axion-photon coupling strength $g_{\phi\gamma\gamma}$.

6.2 Analysis Techniques

6.2.1 The quadratic estimator

A direction dependent distortion of the CMB polarization, like the one shown in equation (6.9), will result in non-zero off-diagonal modes in the CMB covariance matrix in harmonic space. Normally, the CMB covariance is only non-zero on the diagonal. Quadratic estimators (QEs) use the information encoded in the off-diagonals in order to reconstruct the distortion field. The full-sky QE for the rotation field sourced by CB was first derived in [38] and [39]. Here, we will summarize the important practical details pertaining to the reconstruction of CB using QEs. We will also introduce the efficient form of the QE for CB, in analogy to the efficient lensing estimators introduced in [160]. We primarily employ an estimator that makes use of the $\langle E_{lm} B^*_{l'm'} \rangle$ cross correlations, as these are expected to give the smallest reconstruction noise [70], [83].

The quadratic estimator for the reconstructed harmonic space CB field, $\widehat{\alpha}_{LM}$, as derived in [38] and [39] and discussed in detail in Chapter 2 has the form [29]

$$\widehat{\alpha}_{LM} = -2N_L^{\alpha\alpha} \sum_{ll'} \frac{\tilde{C}_{l'}^{EE}}{C_l^{BB,\,\text{map}} C_{l'}^{EE,\,\text{map}}} \sum_{mm'} B_{lm} E^*_{l'm'} \xi^{LM}_{lml'm'}\, p_\ell^e \,, \tag{6.10}$$

where $N_L^{\alpha\alpha}$ is the reconstruction noise and has the form

$$N_L^{\alpha\alpha} = \left[4 \sum_{ll'} \sqrt{\frac{(2l+1)(2l'+1)}{4\pi}} \frac{\left(\tilde{C}_{l'}^{EE} H_{ll'}^{L} \, p_\ell^e\right)^2}{C_l^{BB,\,\mathrm{map}} C_{l'}^{EE,\,\mathrm{map}}} \right]^{-1} . \tag{6.11}$$

Here, the parity-even operator, $p_\ell^e \equiv (1 + (-1)^\ell)/2$, enforces the condition $\ell \equiv l + l' + L =$ Even. The $\tilde{C}_l^{EE}$ terms are theory power spectra. It is assumed that the $\tilde{C}_l^{EE}$ spectrum is well measured by existing CMB experiments. In this work, for all theory spectra we use the *Planck* best fit ΛCDM spectra from the baseline *Planck* likelihood [161]. The $C_l^{XX,\,\mathrm{map}}$ spectra are spectra calculated directly from the data maps themselves.

The geometric kernel term $\xi_{lml'm'}^{LM}$ encodes the geometric behavior of the spin-weighted spherical harmonics and is written, in terms of Wigner-3j symbols, as

$$\xi_{lml'm'}^{LM} = (-1)^m \sqrt{\frac{(2l+1)(2L+1)(2l'+1)}{4\pi}} \begin{pmatrix} l & L & l' \\ -m & M & m' \end{pmatrix} H_{ll'}^{L} , \tag{6.12}$$

where,

$$H_{ll'}^{L} = \begin{pmatrix} l & L & l' \\ 2 & 0 & -2 \end{pmatrix} . \tag{6.13}$$

In this form the estimator is a convolution in harmonic space. However, it is more efficient to rewrite it as a product of real-space fields. To do this we first rewrite the geometric kernel explicitly in terms of the spherical harmonics so that

$$2\xi_{lml'm'}^{LM} p_\ell^e = \int d\hat{\mathbf{n}} \left[{}_{+2}Y_{lm}^*(\hat{\mathbf{n}}) Y_{LM}(\hat{\mathbf{n}}) {}_{+2}Y_{l'm'}(\hat{\mathbf{n}}) + {}_{-2}Y_{lm}^*(\hat{\mathbf{n}}) Y_{LM}(\hat{\mathbf{n}}) {}_{-2}Y_{l'm'}(\hat{\mathbf{n}}) \right] . \tag{6.14}$$

Substituting equation (6.14) into the estimator in (6.10) gives the expression

$$\begin{aligned} \widehat{\alpha}_{LM} = - N_L^{\alpha\alpha} \int d\hat{\mathbf{n}} \Bigg[& \sum_{lm} \frac{1}{C_l^{BB,\,\mathrm{map}}} B_{lm+2} Y_{lm}^*(\hat{\mathbf{n}}) \sum_{l'm'} \frac{\tilde{C}_{l'}^{EE}}{C_{l'}^{EE,\,\mathrm{map}}} E_{l'm'+2}^* Y_{l'm'}(\hat{\mathbf{n}}) \\ & + \sum_{lm} \frac{1}{C_l^{BB,\,\mathrm{map}}} {}_{-2}Y_{lm}^*(\hat{\mathbf{n}}) \sum_{l'm'} \frac{\tilde{C}_{l'}^{EE}}{C_{l'}^{EE,\,\mathrm{map}}} E_{l'm'} {}_{-2}Y_{l'm'}(\hat{\mathbf{n}}) \Bigg] Y_{LM}(\hat{\mathbf{n}}) . \end{aligned}$$

This is easily written as the spherical harmonic transform of a product of real-space fields,

$$\widehat{\alpha}_{LM} = -N_L^{\alpha\alpha} \int d\hat{\mathbf{n}} \left[\left({}_{+2}A_{B^*}(\hat{\mathbf{n}})\right)^* {}_{+2}A_{E^*E^*}(\hat{\mathbf{n}}) + \left({}_{-2}A_{B^*}(\hat{\mathbf{n}})\right)^* {}_{-2}A_{E^*E^*}(\hat{\mathbf{n}}) \right] Y_{LM} , \tag{6.15}$$

where the real-space fields are defined as

$$ {}_{\pm2}A_{B^*}(\hat{\mathbf{n}}) = \sum_{lm} \frac{1}{C_l^{BB,\,\mathrm{map}}} B^*_{lm\pm2}Y_{lm}(\hat{\mathbf{n}}) \ , \tag{6.16} $$

$$ {}_{\pm2}A_{E^*E^*}(\hat{\mathbf{n}}) = \sum_{lm} \frac{\tilde{C}_l^{EE}}{C_l^{EE,\,\mathrm{map}}} E^*_{lm\pm2}Y_{lm}(\hat{\mathbf{n}}) \ . \tag{6.17} $$

In this form the quadratic estimators are significantly more computationally efficient than in (6.10), where multidimensional sums over large ranges of modes must be carried out. This efficient form of the estimator was used in the full sky WMAP anisotropic birefringence analysis [77].

6.2.2 The analysis pipeline

In this work we use the same analysis pipeline for our tests, and our data analysis. This is to ensure that the data analysis we carry out is consistent with our validation test, and our validation tests are carried out in conditions as close to the real data analysis as possible. The summary of the steps taken in the pipeline is as follows:

1. *Beam Deconvolution*: The maps that we analyze first undergo beam deconvolution, by transforming the maps to harmonic space maps and multiplying by the inverse of the beam window function. This is done as the QE code we use assumes beam deconvolved maps.

2. *Masking*: A mask is applied to the beam deconvolved maps to remove high intensity polarization sources and the galactic plane.

3. *Passing data maps and theory spectra*: The masked, beam deconvolved maps are passed to the QE code. We also pass theory spectra described in Section 6.2 to the code.

4. *Process the returned maps*: The QE code returns estimated harmonic and real-space fields. Before we calculate the CB power spectrum remove the monopole as we are only interested in the anisotropic CB effect in this chapter.

5. *Calculate the CB power spectrum*: The CB power spectrum is estimated from the processed $\widehat{\alpha}(\hat{\mathbf{n}})$ map and the QE pipeline is complete.

Note that when estimating the CB power spectrum we define the noise biased spectrum estimated directly from the processed maps as

$$ C_L^{\widehat{\alpha}\widehat{\alpha}} = \frac{1}{f_{\mathrm{sky}}(2L+1)} \sum_M |\widehat{\alpha}_{LM}|^2 \ . \tag{6.18} $$

We use $\widehat{C}_L^{\alpha\alpha}$ to indicate the spectrum with the noise bias $N_L^{\alpha\alpha}$ subtracted and to distinguish it from the noise-biased $C_L^{\widehat{\alpha}\widehat{\alpha}}$ spectrum so that $C_L^{\widehat{\alpha}\widehat{\alpha}}$ is equivalent to $\widehat{C}_L^{\alpha\alpha} + N_L^{\alpha\alpha}$. Note that $N_L^{\alpha\alpha}$

as calculated using equation (6.11) only accounts for the isotropic noise bias. Anisotropic noise that biases the off-diagonals of the CMB covariance are not accounted for using (6.11). In addition to providing information about the power of the $\widehat{\alpha}(\hat{\mathbf{n}})$ map on different scales the estimated power spectra can be used in model dependent likelihood analysis in order to constrain the amplitude of the scale invariant spectrum introduced in equation (6.3).

6.2.3 Model dependent analysis

We carry out likelihood analysis for the estimated spectra in order to estimate/constrain A_{CB}, the amplitude of the model dependent CB power spectrum. This is a model dependent analysis since how we choose to model the CB spectrum, that is what spectral shape we choose, will directly impact the constraint we place on the amplitude of the spectrum using the likelihood approach. In this analysis we vary the amplitude of a reference spectrum, C_L^{ref}. We choose a CB model with a scale invariant power spectrum as shown in equation (6.3). The scale independent spectrum is commonly chosen in the literature [43], [68], [77], [125] when placing model dependent constraints on anisotropic CB. We use the likelihood described in [81], adapting it for use with the CB spectrum,

$$-2\ln\mathcal{L}(A_{CB}) = \sum_L (2L+1)\left[\frac{C_L^{\widehat{\alpha}\widehat{\alpha}}}{A_{CB}C_L^{\text{ref}}+C_L^{\text{fid}}} + \ln\left(A_{CB}C_L^{\text{ref}}+C_L^{\text{fid}}\right) - \frac{2L-1}{2L+1}C_L^{\widehat{\alpha}\widehat{\alpha}}\right] . \tag{6.19}$$

Here, C_L^{fid} is the fiducial model spectrum. We also assume a fiducial model where no CB is present and the fiducial spectrum consists entirely of reconstruction noise.

This form of the likelihood assumes use on the full sky. For a realistic CMB sky where a mask is applied this is adapted according to the procedure seen in [162]. In this case we write the likelihood as

$$-2\ln\mathcal{L}(A_{CB}) = \sum_{LL'} C_L^{\text{fid}}\, g(x_L)\, M^{-1}_{LL'}\, g(x_{L'})\, C_{L'}^{\text{fid}} , \tag{6.20}$$

where $M^{-1}_{LL'}$ is the inverse covariance matrix, the function $g(x_L)$ is defined as

$$g(x_L) = \text{sign}(x-1)\sqrt{2(x_L+\ln x_L - 1)} , \tag{6.21}$$

and x_L is constructed from the data, model and reference spectra and takes the form

$$x_L = \frac{C_L^{\widehat{\alpha}\widehat{\alpha}}}{A_{CB}C_L^{\text{ref}}+C_L^{\text{fid}}} . \tag{6.22}$$

By defining the likelihood explicitly in terms of the covariance matrix, it is possible to account for the extra variance introduced by only including data from a fraction of the sky, f_{sky}. In our likelihood we consider low L modes. As the majority of the power in our model is on large angular scales the low L modes are particularly important for the likelihood constraint.

These modes are expected to have a non-Gaussian distribution [154]. The form of the likelihood presented in [81] includes additional corrections to take into account this non-Gaussian distribution of the low L modes.

6.3 Simulation tests

In order to validate our pipeline we carry out a series of blind tests of the QE using $\alpha(\hat{\mathbf{n}})$ maps that are drawn from two fiducial $C_L^{\alpha\alpha}$ spectra, each with a different A_{CB}. One of these maps is for the null scenario where no CB is present, that is $A_{CB} = 0$. These $\alpha(\hat{\mathbf{n}})$ maps are used to rotate a set of simulated CMB polarization maps. We then pass these to the analysis pipeline, blind to the injected A_{CB}. We do this in order to test whether we are able to recover $\alpha(\hat{\mathbf{n}})$ map, power spectrum and A_{CB} from an unseen data map, with no foreknowledge of what the signal should look like. This emulates the process of reconstructing the CB signal from actual data, where one does not know what the true signal is.

After the conclusion of the analysis the injected A_{CB}, and corresponding $C_L^{\alpha\alpha}$ spectra and $\alpha(\hat{\mathbf{n}})$ maps are revealed. These are then compared to reconstructed spectrum and map, and the mean A_{CB} resulting from likelihood analysis. The simulated CMB maps emulate the *Planck* 143GHz channel noise and beam, as this has a simple noise and beam profile when compared with component separated *Planck* maps such as the SMICA map [159]. Note that only the CMB maps are rotated by the injected CB signal, and not the noise components of those maps, which are applied after the rotation. For the QE analysis we used $l_{\text{max}} = 1024$, both with and without masking in order to test for possible bias introduced by masking. The masks we study are summarized as follows:

- The *Planck* common confidence masks. Separate polarization and intensity masks are included. The sky coverage after these non apodized masks are applied is $\sim 78\%$.
- The combined *Planck* galactic plane mask and common confidence mask with $\sim 76\%$ sky coverage.
- The combined *Planck* non galactic plane mask and common confidence mask with $\sim 68\%$ sky coverage.
- The combined *Planck* galactic plane mask and common confidence mask with $\sim 59\%$ sky coverage.

It is important to be able to reconstruct the $\alpha(\hat{\mathbf{n}})$ map using the QE. We compare the injected map, with $A_{CB} = 5 \times 10^{-5}$, to the masked and full sky reconstructed maps in Figure 6.1. We compare the Wiener filtered [41] maps to better distinguish features of the reconstructed $\hat{\alpha}(\hat{\mathbf{n}})$ maps from reconstruction noise. The Wiener filter dampens modes which are dominated by reconstruction noise but preserves modes with a strong signal-to-noise ratio.

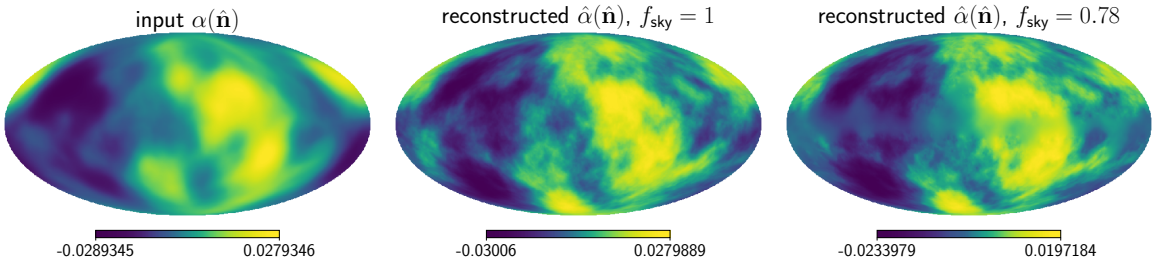

Figure 6.1: The Wiener filtered $\alpha(\hat{\mathbf{n}})$ map drawn from an input $C_L^{\alpha\alpha}$ spectrum with $A_{CB} = 5 \times 10^{-5}$ $\left[\text{rad}^2\right]$. This is compared to the Wiener filtered $\hat{\alpha}(\hat{\mathbf{n}})$ map reconstructed with no mask, and the Wiener filtered $\hat{\alpha}(\hat{\mathbf{n}})$ map reconstructed with the common confidence mask with $f_{\rm sky} = 0.78$.

We find that the QE can successfully reconstruct larger scale features for angular scales associated with modes where the reconstruction noise does not dominate over the reconstructed signal.

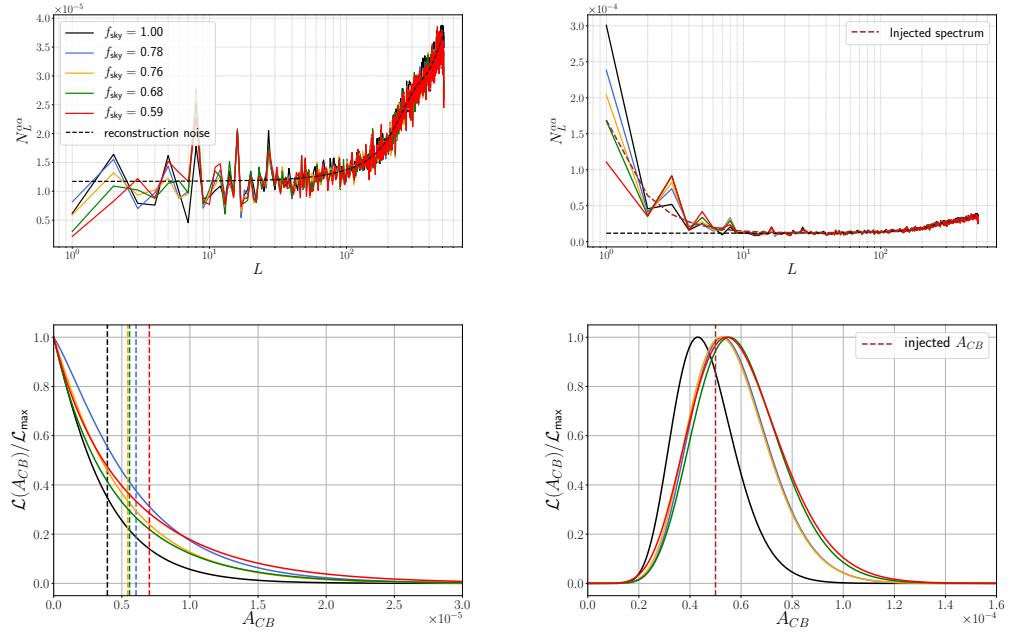

Figure 6.2: The power spectra and likelihoods for two different sets of CMB polarization maps rotated by a simulated $\alpha(\hat{\mathbf{n}})$ map that corresponds to an injected A_{CB} value. This value was selected blindly, and was only seen after the analysis pipeline had concluded. Also included in the upper right panel is the theory $C_L^{\alpha\alpha}$, from which the $\alpha(\hat{\mathbf{n}})$ map is drawn, combined with the reconstruction noise $N_L^{\alpha\alpha}$ in order to be compared to the reconstructed $\widehat{C}_L^{\alpha\alpha} + N_L^{\alpha\alpha}$ spectra. The injected amplitudes are $A_{CB} = 0.0$ (left panels), $A_{CB} = 5 \times 10^{-5}$ (right panels). In the lower panels, on the left we show the 1σ or 68% C.L. upper bounds as vertical dashed lines, and on the right we show the injected A_{CB} as a brown, vertical dashed line.

Our likelihood analysis is carried out as described in Section 6.2.3. When calculating

the covariance for this test we assume a fiducial model with no CB present, with a diagonal covariance matrix consisting only of the fiducial variance, σ_L^2, where

$$\sigma_L = \sqrt{\frac{2}{f_{\rm sky}(2L+1)}} N_L^{\alpha\alpha} \ . \tag{6.23}$$

The injected values are $A_{CB} = 0.0$, $A_{CB} = 5 \times 10^{-5}$. We see from our likelihood and power spectra, shown in Figure 6.2, that in both cases the measured value of A_{CB} is consistent with the injected value corresponding well within 1σ, and the reconstructed and injected spectra match to within 1σ variance limits. We list the recovered A_{CB} values and errors on those values for the full sky, and masked analyses in Table 6.1. We find that in comparison with the full sky case, the masked cases lead to a small bias. However, it is small enough that the masked and full-sky cases are consistent with each other for both of the injected A_{CB} values. The introduction of a mask also leads to an increased variance and widening of the likelihood, which is expected with reduction of sky coverage. In the null case ($A_{CB} = 0.0$) this resulted in an error that was ~ 1.5 times larger when using the common mask than for the full-sky case.

	$A_{CB} = 0$		$A_{CB} = 5.0$		
$f_{\rm sky}$	A_{CB}	$+\sigma_{A_{CB}}$	A_{CB}	$-\sigma_{A_{CB}}$	$+\sigma_{A_{CB}}$
1.0	0.0	0.39	4.27	0.94	1.43
0.78	0.0	0.60	5.25	1.23	1.81
0.76	0.0	0.54	5.25	1.27	1.80
0.68	0.0	0.56	5.50	1.33	1.98
0.59	0.0	0.70	5.50	1.46	2.09

Table 6.1: The mean recovered A_{CB} values and 1σ errors, given in units of $\times 10^{-5}$ $\left[\text{rad}^2\right]$, for two blindly injected CB signals. We show these for a range of different masks, and for reconstruction carried out on the full-sky maps.

We have used a variety of masks to ensure that our constraints are stable with choice of mask. We find that our recovered A_{CB} values for both sets of injected signals do not vary significantly with different choices of mask. The lack of significant bias from different choices of mask is important as we will use a range of masks in our SMICA data analysis. We do this in order to ensure minimal bias from foregrounds or foreground residuals in our constraints. If we do not see significant variation in our constraints with changes in our mask and sky coverage then we can infer that foregrounds are not significantly biasing our results.

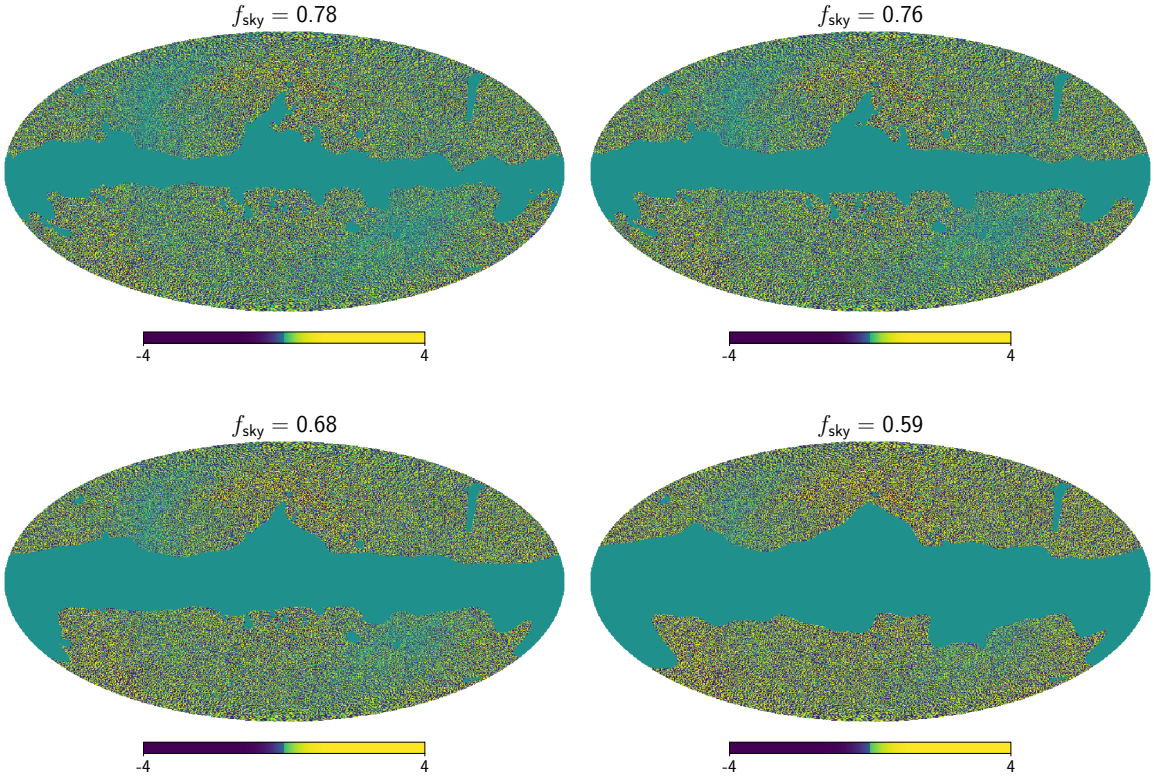

Figure 6.3: The $\hat{\alpha}(\hat{\mathbf{n}})$ map constructed from $\hat{\alpha}_{LM}$ with the monopole removed. The maps are reconstructed for $l_{\rm max} = 1440$. We apply the *Planck* common confidence mask with $f_{\rm sky} = 0.78$, and for the combination of the galactic plane and the *Planck* common confidence mask for $f_{\rm sky} = 0.76$, $f_{\rm sky} = 0.68$, and $f_{\rm sky} = 0.59$.

6.4 SMICA analysis

6.4.1 The CB power spectrum reconstruction

For the initial data analysis we applied the QE to the SMICA polarization maps. The SMICA maps are generated from the linear combination of data from different frequency channels while utilising a multipole dependent weighting of this data in order to achieve foreground cleaned maps. The SMICA map files include intensity and polarization beams, which have an effective beam of $\theta_{\rm FWHM} = 5'$ and $\theta_{\rm FWHM} = 10'$ respectively.

In a similar way to our blind simulation tests, in order to avoid results that depend on either $l_{\rm max}$ or the mask, we carry out our analysis for a range of masks and $l_{\rm max}$ cutoffs. We carry out the analysis for the masks explored in Section 6.3 and for $l_{\rm max} \in \{512, 768, 1024, 1440\}$. We consider this range of $l_{\rm max}$ values as we do not see significant improvement in constraints beyond $l_{\rm max} = 1440$. We seek stable results for different choices of masks. This is to ensure that our constraints are not impacted by bias from foregrounds or foreground residuals.

While it appears from these figures that the reconstructed spectra may have a non-zero amplitude, A_{CB}, it is necessary to carry out likelihood analysis to confirm whether or not the

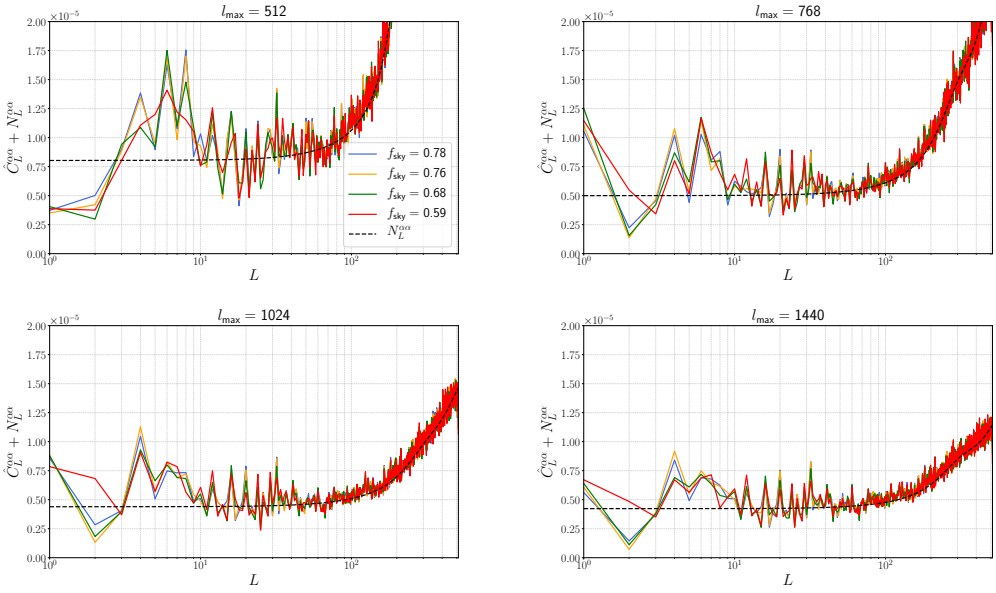

Figure 6.4: The $\widehat{C}_L^{\alpha\alpha} + N_L^{\alpha\alpha}$, reconstructed using the SMICA maps, for the common mask with $f_{\rm sky} = 0.78$ (blue), and the combined common mask and galactic plane mask with $f_{\rm sky} = 0.76$ (orange), $f_{\rm sky} = 0.68$ (green) and $f_{\rm sky} = 0.59$ (red). Also shown as a dashed black line is the reconstruction noise, $N_L^{\alpha\alpha}$. We show the spectrum without the reconstruction noise bias subtracted in order to compare the reconstructed spectra to the reconstruction noise. There is an insignificant difference between the reconstruction noises for different masks at each value of $l_{\rm max}$. Therefore, we only show the reconstruction noise for the $f_{\rm sky} = 0.78$ mask. Here, the spectra shown were reconstructed for four different $l_{\rm max}$ values as displayed above each figure panel. Of the four choices of $l_{\rm max}$ the smallest reconstruction noise is found for $l_{\rm max} = 1440$.

amplitude of $\widehat{C}_L^{\alpha\alpha}$ is truly consistent with zero.

6.4.2 SMICA model dependent analysis

We carry out a likelihood analysis for the amplitude of $C_L^{\alpha\alpha}$ in order to establish what the most probably A_{CB} value is for the reconstructed $\widehat{C}_L^{\alpha\alpha}$, and to establish a constraint if A_{CB} is found to be consistent with zero. For this analysis we fit for the scale invariant spectrum seen in equation 6.3. As such, we apply the likelihood discussed in Section 6.2.3, for the full reconstructed spectra ($1 \leq L \leq 512$), using the reference spectrum $C_L^{\rm ref} = 2\pi/L(L+1)$. In our fiducial model we assume no CB, therefore, the fiducial model spectrum consists of the reconstruction noise power spectrum $N_L^{\alpha\alpha}$ only. The covariance is assumed to consist of the diagonal variance elements σ_L^2 only, where σ_L takes the form seen in equation (6.23).

Our data spectra are the reconstructed $C_L^{\widehat{\alpha}\widehat{\alpha}}$ spectra discussed in Section 6.4.1, where we carry out analysis for the same range of $l_{\rm max}$ values and for the same set of masks. In Figure 6.5 we see that, while the mean A_{CB} is not centered at zero, A_{CB} is consistent with zero within the 2σ bound. The strongest constraint, $A_{CB} \leq 1.97 \times 10^{-5}$ $\left[\text{rad}^2\right]$ within 95% C.L., comes from

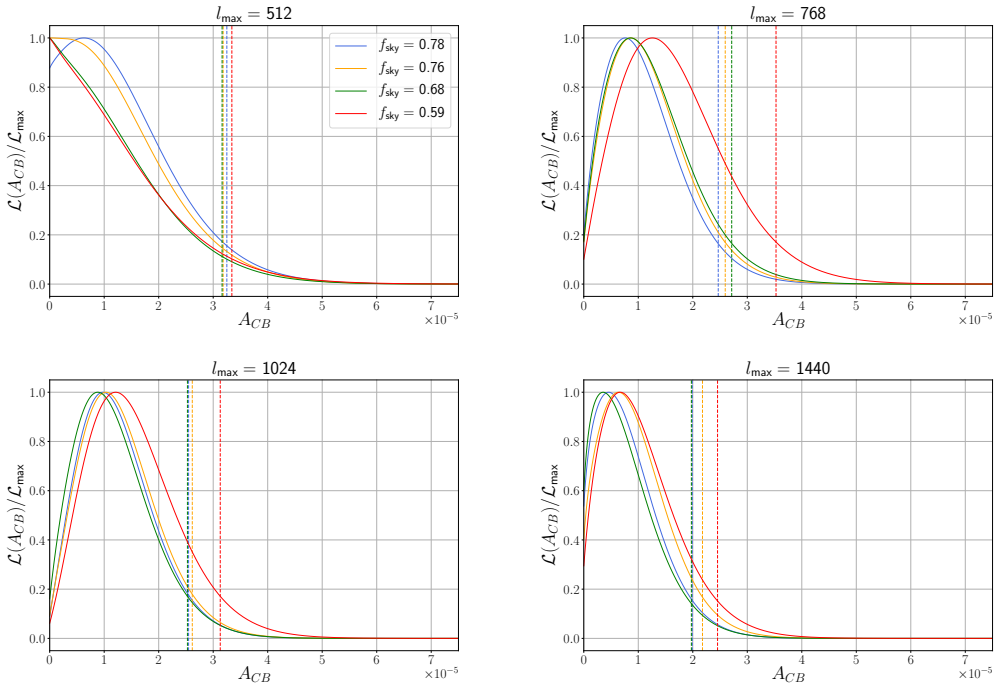

Figure 6.5: The likelihood and 95% C.L. for A_{CB} from the SMICA maps for the common confidence mask $f_{\rm sky} = 0.78$ (blue), and the combined galactic plane and common confidence mask with $f_{\rm sky} = 0.76$ (orange), $f_{\rm sky} = 0.68$ (green) and $f_{\rm sky} = 0.59$ (red). The 95% C.L. is displayed as a dashed line. The data spectra for these likelihoods are the reconstructed $\widehat{C}_L^{\alpha\alpha}$ spectra for four different $l_{\rm max}$ values. These are displayed above their corresponding likelihoods. These likelihoods are carried out with $1 \leq L \leq 512$.

the power spectrum reconstructed using $l_{\rm max} = 1440$, using the combined galactic plane and common confidence mask, with an associated sky coverage of $f_{\rm sky} = 0.68$. This constraint translates to a constraint on the axion-photon coupling strength of $g_{\phi\gamma\gamma} \leq 5.58 \times 10^{-2}$ $\left[H_I^{-1}\right]$. If this constraint had come from analysis of 150GHz channel maps then it would translate to an equivalent PMF strength of $B_{\rm 1Mpc} \leq 23.3$ [nG]. However, as we have used combined channel, component separated maps it is not possible to directly translate our results to a PMF constraint. The full list of constraints and mean A_{CB} values are presented in Table 6.2 along with a full list of constraints on the axion-photon coupling strength.

6.5 Conclusions

The *Planck* polarization maps are the best full-sky satellite measurements of the CMB polarization to date. This provides a great opportunity to study the CB effect, which is expected to have high power on the largest angular scales, encoded in polarization modes that are most easily accessible with full-sky observations. We have, for the first time, applied a QE to *Planck* data in order to reconstruct the CB map and power spectrum, and have used these spectra to place a constraint on A_{CB}, the amplitude of a scale invariant CB power spectrum.

	f_{sky}	A_{CB}	95% C.L.	$g_{\phi\gamma\gamma}$
$l_{\text{max}} = 512$	0.78	0.63	3.25	7.16×10^{-2}
	0.76	0.04	3.18	7.09×10^{-2}
	0.68	0.00	3.16	7.07×10^{-2}
	0.59	0.00	3.34	7.27×10^{-2}
$l_{\text{max}} = 768$	0.78	0.76	2.47	6.24×10^{-2}
	0.76	0.87	2.60	6.40×10^{-2}
	0.68	0.85	2.71	6.55×10^{-2}
	0.59	1.26	3.53	7.46×10^{-2}
$l_{\text{max}} = 1024$	0.78	0.98	2.55	6.34×10^{-2}
	0.76	1.02	2.62	6.43×10^{-2}
	0.68	0.89	2.53	6.31×10^{-2}
	0.59	1.20	3.13	7.03×10^{-2}
$l_{\text{max}} = 1440$	0.78	0.46	1.99	5.61×10^{-2}
	0.76	0.63	2.18	5.86×10^{-2}
	0.68	0.35	1.97	5.58×10^{-2}
	0.59	0.66	2.45	6.23×10^{-2}

Table 6.2: The mean A_{CB} values and the 95% C.L. constraints in units of $\times 10^{-5}$ $\left[\text{rad}^2\right]$. The list of means and constraints is for power spectra reconstructed using four different listed l_{max} values, using the *Planck* common confidence mask with $f_{\text{sky}} = 0.78$, and the combined *Planck* galactic plane and common confidence masks with $f_{\text{sky}} = 0.76$, $f_{\text{sky}} = 0.68$ and $f_{\text{sky}} = 0.59$. Also shown, are the constraints on the axion-photon coupling strength $g_{\phi\gamma\gamma}$ in units of $\left[H_I^{-1}\right]$.

We have first validated our code with a set of blind tests that included a null test. We find that we are able to reconstruct the injected maps, and power spectra with both full-sky, and masked maps. The QE code we employ is able to recover the details of the injected $\alpha(\hat{\mathbf{n}})$ map for angular scales that are not dominated by reconstruction noise. By employing a Hamimeche and Lewis likelihood [81] we were able to recover the amplitude of the power spectrum for the injected CB maps for both full-sky and masked polarization maps. We find that choice of mask does not significantly bias the results of this test.

We then applied our successfully validated QE estimator code to both the *Planck* SMICA CMB polarization maps. For these maps we applied a variety of masks to the polarization maps and found that the combined common confidence mask and galactic plane mask with $f_{\text{sky}} = 0.68$ performed the best. The power spectra that were reconstructed for both SMICA and are consistent with zero within 1σ bounds for the majority of modes, however, for some modes this increased to 2σ.

Using a likelihood approach we have placed a model dependent constraint on A_{CB} using the CB power spectrum reconstructed for the SMICA maps. We find the strongest 95% C.L. constraint to be $A_{CB} \leq 1.97 \times 10^{-5}$ $\left[\text{rad}^2\right]$. This is comparable to constraints from recent CMB experiments such as BICEP/Keck [68] and ACT [125], and offers a factor of ~ 1.4 improvement over the existing constraint from the *Planck* 2015 polarization data [67] and a factor ~ 1.3 improvement over the existing constraint from the *Planck* 2018 polarization data [78]. This constraint translates to constraints on physical phenomenon such as a constraint

on the axion-photon coupling of $g_{\phi\gamma\gamma} \leq 5.58 \times 10^{-2}$ $\left[H_I^{-1}\right]$.

In future work it will be necessary to apply the QE estimator to a range of data channels in order to test whether features in the reconstructed CB spectra have frequency dependence, and in order to place constraints on PMFs. It will also be necessary to apply the QE estimator that employs $\langle T_{lm} B^*_{l'm'} \rangle$ correlations as this may provide a constraint on A_{CB} that is competitive to that from the $\langle E_{lm} B^*_{l'm'} \rangle$ correlations. Utilizing both sets of correlations in the CB estimator may reduce the variance of the reconstructed spectrum and map, leading to stronger A_{CB} constraints. In order to better debias the CB spectrum, and to better model the variance of this spectrum, future study should include the use of fiducial Markov-Chain Monte-Carlo simulations of the data maps, passed through the same map construction and analysis pipeline. If these simulations are able to include potential foreground, and systematic effects then will be possible to remove not only the isotropic bias, but also bias in the off-diagonal correlations.

Moving beyond the existing set of CMB surveys future satellite CMB experiments such as *LiteBIRD* [88] and ground based experiments such as the Simons Observatory [16] will probe an even larger parameter space than *Planck*. As these experiments seek to place constraints on primordial B-modes they will need to constrain the CB effect to ensure that it does not bias the measurements of these B-modes. This is an exciting prospect as stronger constraints on A_{CB} would result in stronger constraints on the axion-photon coupling strength, and a detection of a non-zero CB signal would indicate new and exotic physics.

Chapter 7

Conclusions

7.1 Summary and discussion of thesis results

7.1.1 Overview

The search for primordial B-modes is an important one, with many upcoming experiments setting their sights on becoming the first to detect this hard sought after signal that may provide the first constraints on the energy levels of inflation and a clearer understanding of the nature of this important early universe epoch. Examples of these experiments include Simons Observatory (SO) [16], *LiteBIRD* [88] and the proposed CMB-S4 [37]. The precision of such experiments is expected to be unprecedented and, in the next decade, they may be able to probe the B-mode signal to levels with an equivalent tensor-to-scalar ratio of $r \sim 10^{-3}$ [16], [88].

However, a number of challenges to the detection of primordial B-modes exist in the form of systematics, and cosmological signals that source spurious signals, contaminating the B-mode and adding confusion to the search for the primordial signal. Such contamination must be characterized and removed before a valid detection of of primordial B-modes can be claimed. Further to this, the cosmological sources of contamination are themselves an important signature of exotic physics. For example, detection of cosmic polarization rotation (CPR), or cosmological birefringence (CB) would hint at extensions to the electromagnetic sector of the standard model or the presence of primordial magnetic fields (PMFs) in the early universe.

The detection and characterization of additional mechanisms of B-mode production, both cosmological and instrument based, has been the primary focus of this thesis. We have considered the different approaches by which the CB effect may be detected and constrained, as well as the levels of constraints on CB for both uniform and anisotropic CB. Additionally, we have studied the potential levels of B-mode contamination for upcoming experiments if a CB signal is present that is consistent with these constraints. One method of detection of CB is by quadratic estimators (QEs) which are often employed in weak gravitational lensing studies [15], [40], [115], [116]. In this thesis we have considered an extension of the application of QEs, deploying them to diagnose and remove systematic effects that may interfere with

primordial B-mode detection and bias r. Beyond both the theoretical studies into CB constrains and systematics cleaning we have also taken an observational approach by applying a QE to *Planck* 2018 data, providing real constraints on the CB effect from experimental CMB data. In this chapter we provide a general summary the key results from each of the previous scientific chapters. We will follow this with a discussion of the potential future avenues of research that go beyond the work presented in this thesis.

7.1.2 Chapter 3 - Uniform birefringence forecast

In Chapter 3 the focus was on the uniform CB effect. The main body of work that was included was a forecast of the constraints on uniform CB that are expected for SO and CMB-S4. This was supplemented with a study of the constraining power of each measured CMB spectra, with the aim of determining which spectra should be used to give the strongest constraint on CB, as well as which l modes provide the best constraining power.

The fisher forecast for SO and S4 resulted in projected 1σ constraints of $\alpha_0 \leq 6.06 \times 10^{-3}$ [degrees] and $\alpha_0 \leq 1.8 \times 10^{-3}$ [degrees] respectively. Of the SO instruments, we expect that the large aperture telescope (LAT) will perform the better than the SAT. We also expect that the strongest constraint will from the C_l^{EB} cross spectrum. The modes that we expect to contribute most to the constraining power for SO LAT and CMB-S4 are in the range $2 \leq l \lesssim 2000$ and $2 \leq l \lesssim 3000$ respectively.

Crucially the constraints that were forecast in this chapter were made assuming perfect polarization angle calibration. It is expected that the limiting factor for the uniform CB constraint will be the precision to which the absolute polarization angle can be calibrated [60]. It may be possible to mitigate some of this error by applying technique described in [103]–[106] to simultaneously determine the absolute polarization angle calibration error and the CB angle.

7.1.3 Chapter 4 - Constraining cosmic polarization rotation and implications for primordial B-modes

The primary focus of Chapter 4 was a comparison between two different methods of constraining anisotropic CB. The methods were a QE approach, and a method that involved directly examining the observed B-mode power spectrum and comparing it to the expected spectrum induced by a CB effect; we denote the latter approach the BB approach. An additional focus was on the contamination that could be present for anisotropic CB with amplitudes lower than the forecast constraint for SO, BICEP/Keck and *LiteBIRD*.

One of the most interesting results of this study is the large difference in constraining power that *LiteBIRD* had in comparison to the other experiments considered with similar levels of sensitivity, such as the SO small aperture telescope (SAT) instrument. Despite the expected

noise rms of SO SAT being only a factor of ~ 1.5 larger than that projected for *LiteBIRD*, the best constraint that is forecast for *LiteBIRD* is a factor of ~ 100 better than that forecast for SO SAT. This may be due to the larger sky coverage of *LiteBIRD*. As CB is expected to have a scale invariant spectrum with large power at low L, then we would expect that CB would be best constrained by larger angular modes.

Another interesting result was the relative performance of the BB approach when compared to using a QE for BICEP/Keck and SO SAT. For these experiments we forecast only a marginal improvement when using a QE as opposed to the BB approach. It may be sufficient to place constraints using a BB approach for these experimental configurations, avoiding the relatively complex, and computationally expensive QE approach.

We found that the possible contaminant for a CB effect with amplitudes consistent with the constraints for SO SAT, SO LAT and BICEP/Keck may be significant. The B-modes that can be sourced by CB allowed by the upper bounds that we forecast are of the same order of magnitude as primordial B-modes consistent with a tensor to scalar ratio in the range $r \sim 10^{-3} \rightarrow r \sim 10^{-2}$.

7.1.4 Chapter 5 - Blind Map Level Systematics Cleaning: A Quadratic Estimator Approach

In the case study we described in Chapter 5 we showed that, for a realistic set of time ordered data (TOD) simulations, it is possible to apply a QE approach to diagnose and remove systematic effects. Our focus in this chapter was on the diagnosis and removal of a temperature to polarization (T-to-P) leakage sourced by a differential detector gain using a QE approach. Applying QEs to clean systematics was first discussed in [28]. We were able to improve upon this work through the use of realistic time ordered simulations and by carrying out a detailed study into the iterative cleaning process required to remove the reconstructed T-to-P leakage.

Using the QE approach are successfully able to diagnose the contamination, recovering maps of the T-to-P distortion that was generated by a simulated 1% differential detector gain differential gain. We found that, by applying the iterative cleaning process to remove the diagnosed contamination, we are able to reduce the bias on r by a factor of ~ 100 and recover r to within less than 1σ of the value injected into the simulations. We also introduced a novel new Gaussian filter which improves the stability of cleaning for very low noise simulations.

We suggest that this QE method could be used to compliment existing systematic mitigation techniques. A QE diagnosis could be carried out after these methods are applied in order to confirm no residual contamination remains. Additionally, iterative cleaning could be used in order to remove any residual contamination that may still be present in the CMB maps.

7.1.5 Chapter 6 - Quadratic Estimator Constraints on Cosmological Birefringence from Planck 2018 Data

Planck iss the foremost full-sky satellite CMB experiment. As such the public release of the *Planck* 2018 data provides a great opportunity to study and place constraints on CB from from real observations. In Chapter 6 we applied a QE to the *Planck* 2018 data to reconstruct the CB map and power spectrum, and to place constraints on the amplitude of the CB power spectrum, A_{CB}. We specifically focused on the foreground removed SMICA processed maps.

We were able to validate our QE pipeline using a blind analysis where two sets of maps were passed to the pipeline, each set with an unknown injected CB signal. The recovered A_{CB} values, maps, and corresponding power spectra were compared to the blindly selected injected values. We successfully recovered the injected A_{CB} value for both sets of maps. One set was a null case with no injected signal, and the other had an injected signal with $A_{CB} = 5 \times 10^{-5} \ \left[\text{rad}^2\right]$.

By carrying out a QE analysis on the *Planck* data we were able to place a constraint of $A_{CB} \leq 1.97 \times 10^{-5} \ \left[\text{rad}^2\right]$, within 95% C.L., on the amplitude of the CB power spectrum. This is a factor of ~ 1.3 improvement over the best existing constraints from the *Planck* 2018 data [78]. This can be linked to constraints on actual physical phenomenon in the form of the coupling between the photon and the axion, $g_{\phi\gamma\gamma} \leq 5.58 \times 10^{-2} \ \left[H_I^{-1}\right]$. We found that our results were consistent with no CB signal to within less than 2σ.

7.2 Future work

In this thesis we have studied sources of non-inflationary B-mode CMB polarization. These studies have included both cosmological sources in the form of uniform and anisotropic CB and instrument based systematic sources. We have carried out analysis on real data and made theoretical forecasts using simulations. We have studied techniques to remove some sources of B-mode contamination, and considered others as important science goals. The range of different studies in this work opens up a wide avenue for future research.

With upcoming experiments such as SO, *LiteBIRD* and the later CMB-S4 it will be possible to use CMB power and cross spectra to improve constraints the uniform CB effect. It will be important to reduce impact of the absolute polarization angle calibration error, as this will have the largest impact on future constraints on uniform CB [60]. Promising techniques to reduce this error have been introduced in [103], [104], and [105], and applied to the *Planck* 2018 data in [106]. If these techniques can be applied to SO, *LiteBIRD* and S4 then it will be possible to place strong constraints on, or even make a detection of the uniform CB effect.

Beyond the uniform CB effect, future experiments will be able to place stronger constraints on the anisotropic CB effect. It will be important for any future experiments to constrain the

CB effect in order to claim a robust detection of primordial B-mode due to the potential of CB sourced contamination. Any detection of B-modes, not sourced by lensing, will need to be accompanied by the application of a QE for CB in order to confirm that CB is not the source of this signal.

A future experiments are expected to have small enough statistical noise that the dominant source of error will come from instrument systematics it will be vital to diagnose and remove these in the search for primordial B-modes. Existing approaches could be supplemented by the QE approach we have discussed in this thesis. However, there is more work to be done to understand certain aspects of this approach. It will be necessary to study the impact of foregrounds on the effectiveness of this technique. In addition, estimators for a range of systematics would be need to be developed to render this an effective tool. Work must be done to understand the interaction between these estimators and off-diagonal correlations in the CMB covariance generated by weak lensing. Moreover, use of partial sky maps can also generate off diagonal correlations. Work must be done to understand how this will impact the use of this technique. If these challenges can be overcome then this approach may become a promising tool to compliment existing techniques.

While our analysis of the *Planck* data has produced a strong constraint on the amplitude of the CB power spectrum, a deeper analysis of the *Planck* data is possible. In our analysis we restricted ourselves to using variance and model spectra determined by the reconstruction noise of our spectra. A more thorough approach would involve the use of Markov-Chain Monte-Carlo simulations in order to establish a fiducial model spectrum and to estimate the variance on our measurements. Further work, using simulations, would allow for proper debiasing of the reconstructed CB spectrum and produce a more robust constraint on CB.

Future detection of either the primordial B-mode signal or a signal from cosmological effects such as CB is an exciting prospect. In the former case such a detection would allow better understanding of inflation, including a constraint on inflationary models and the energy scale at which inflation occurs. In the latter case this would provide an exciting observational signature of beyond standard model physics. Both cases would result in a significant alteration to our understanding of the fundamental physics of our universe, its evolution, and its origins.

Appendices

Appendix A

Geometric identity

The QEs, as derived in Section 6.2, rely on geometric couplings between the modes of spin-2 and spin-0 fields. Here, we present details of the important geometric terms used in the QE derivations, and derive the identity found in equation (5.11). We begin with the integral of the spherical harmonic terms. In general this term can be written in terms of the Wigner-3j symbols,

$$\int d\hat{\mathbf{n}}\ {}_{s_1}Y_{l_1m_1}(\hat{\mathbf{n}})_{s_2}Y_{l_2m_2}(\hat{\mathbf{n}})_{s_3}Y_{l_3m_3}(\hat{\mathbf{n}}) = \sqrt{\frac{(2l_1+1)(2l_2+1)(2l_3+1)}{4\pi}} \times \begin{pmatrix} l_1 & l_2 & l_3 \\ m_1 & m_2 & m_3 \end{pmatrix} \begin{pmatrix} l_1 & l_2 & l_3 \\ -s_1 & -s_2 & -s_3 \end{pmatrix}. \tag{A.1}$$

Using this identity we see that the geometric term, ${}_{\pm}I^{Ll_2l}_{Mm_2m}$, that was introduced in equation (5.6) is explicitly written as

$$\begin{aligned} {}_{\pm}I^{Ll_2l_1}_{Mm_2m_1} &= \int d\hat{n}\ {}_{\pm2}Y_{LM}(\hat{\mathbf{n}})Y_{l_2m_2}(\hat{\mathbf{n}})_{\pm2}Y^*_{l_1m_1}(\hat{\mathbf{n}}) \\ &= (-1)^{m_1}\sqrt{\frac{(2L+1)(2l_2+1)(2l_1+1)}{4\pi}} \begin{pmatrix} L & l_2 & l_1 \\ M & m_2 & -m_1 \end{pmatrix} \begin{pmatrix} L & l_2 & l_1 \\ \mp2 & 0 & \pm2 \end{pmatrix}. \end{aligned} \tag{A.2}$$

We can use the coupling parity, $\ell \equiv L + l_2 + l_1$, and the $H^L_{l_2l_1}$ term,

$$H^L_{l_2l_1} \equiv \sqrt{\frac{(2L+1)(2l_2+1)(2l_1+1)}{4\pi}} \begin{pmatrix} L & l_2 & l_1 \\ -2 & 0 & 2 \end{pmatrix}, \tag{A.3}$$

to simplify equation (A.2) giving

$$\pm I^{Ll_2l_1}_{Mm_2m_1} = (-1)^{m_1}(\pm 1)^{\ell}\, H^L_{l_2l_1} \begin{pmatrix} L & l_2 & l_1 \\ M & m_2 & -m_1 \end{pmatrix} . \tag{A.4}$$

The identity in equation (5.11) can then be derived starting with

$$\sum_{m_2m_1} \pm I^{Ll_2l_1}_{Mm_2m_1} \pm I^{L'l_2l_1}_{M'm_2m_1} = \sum_{m_2m_1} (\pm 1)^{\ell+\ell'}\, H^L_{l_2l_1}\, H^{L'}_{l_2l_1} \begin{pmatrix} L & l_2 & l_1 \\ M & m_2 & -m_1 \end{pmatrix} \begin{pmatrix} L' & l_2 & l_1 \\ M' & m_2 & -m_1 \end{pmatrix} . \tag{A.5}$$

Carrying out the sum on the right hand side and applying the property of the Wigner-3j symbols,

$$\sum_{m_1m_2} (2L+1) \begin{pmatrix} l_1 & l_2 & L \\ m_1 & m_2 & M \end{pmatrix} \begin{pmatrix} l_1 & l_2 & L' \\ m_1 & m_2 & M' \end{pmatrix} = \delta_{LL'}\delta_{MM'} , \tag{A.6}$$

simplifies the right hand side of (A.5), giving the identity in (5.11),

$$\sum_{m_2m_1} \pm I^{Ll_2l_1}_{Mm_2m_1} \pm I^{L'l_2l_1}_{M'm_2m_1} = \frac{\left(H^L_{l_2l_1}\right)^2}{2L+1} \delta_{LL'}\delta_{MM'} . \tag{A.7}$$

References

[1] A. Einstein, "Die grundlage der allgemeinen relativitã€tstheorie," *Annalen der Physik*, vol. 354, no. 7, pp. 769–822, 1916. DOI: https://doi.org/10.1002/andp.19163540702. eprint: https://onlinelibrary.wiley.com/doi/pdf/10.1002/andp.19163540702. [Online]. Available: https://onlinelibrary.wiley.com/doi/abs/10.1002/andp.19163540702.

[2] A. Einstein, "Die Feldgleichungen der Gravitation," *Sitzungsberichte der Königlich Preußischen Akademie der Wissenschaften (Berlin*, pp. 844–847, Jan. 1915.

[3] A. Friedmann, "Über die Krümmung des Raumes," *Zeitschrift fur Physik*, vol. 10, pp. 377–386, Jan. 1922. DOI: 10.1007/BF01332580.

[4] G. Lemaître, "Expansion of the universe, A homogeneous universe of constant mass and increasing radius accounting for the radial velocity of extra-galactic nebulae," *MNRAS*, vol. 91, pp. 483–490, Mar. 1931. DOI: 10.1093/mnras/91.5.483.

[5] S. Dodelson, *Modern cosmology*. Elsevier, 2003.

[6] J. Chluba, G. M. Vasil, and L. J. Dursi, "Recombinations to the Rydberg states of hydrogen and their effect during the cosmological recombination epoch," *Monthly Notices of the Royal Astronomical Society*, vol. 407, no. 1, pp. 599–612, Aug. 2010, ISSN: 0035-8711. DOI: 10.1111/j.1365-2966.2010.16940.x. eprint: https://academic.oup.com/mnras/article-pdf/407/1/599/3088827/mnras0407-0599.pdf. [Online]. Available: https://doi.org/10.1111/j.1365-2966.2010.16940.x.

[7] T. Avgoustidis, E. Copeland, A. Moss, and C. Skordis, *Lecture notes on modern cosmology*, Feb. 2017.

[8] C. L. Bennett, A. J. Banday, K. M. Górski, G. Hinshaw, P. Jackson, P. Keegstra, A. Kogut, G. F. Smoot, D. T. Wilkinson, and E. L. Wright, "Four-year *COBE* DMR cosmic microwave background observations: Maps and basic results," *The Astrophysical Journal*, vol. 464, no. 1, pp. L1–L4, Jun. 1996. DOI: 10.1086/310075. [Online]. Available: https://doi.org/10.1086/310075.

[9] M. Kamionkowski, A. Kosowsky, and A. Stebbins, "Statistics of cosmic microwave background polarization," *Physical Review D*, vol. 55, no. 12, pp. 7368–7388, Jun. 1997, ISSN: 0556-2821. DOI: 10.1103/PhysRevD.55.7368. [Online]. Available: https://link.aps.org/doi/10.1103/PhysRevD.55.7368.

[10] R. Durrer, *The Cosmic Microwave Background*. New York: Cambridge University Press, 2008, ISBN: 9780521847049.

[11] A. Challinor, "Cosmic microwave background anisotropies," in *The Physics of the Early Universe*, E. Papantonopoulos, Ed. Berlin, Heidelberg: Springer Berlin Heidelberg, 2005, pp. 71–103, ISBN: 978-3-540-31535-3. DOI: 10.1007/978-3-540-31535-3_3. [Online]. Available: https://doi.org/10.1007/978-3-540-31535-3_3.

[12] A. Kosowsky, M. Milosavljevic, and R. Jimenez, "Efficient cosmological parameter estimation from microwave background anisotropies," *Phys. Rev. D*, vol. 66, p. 063 007, 6 Sep. 2002. DOI: 10.1103/PhysRevD.66.063007. [Online]. Available: https://link.aps.org/doi/10.1103/PhysRevD.66.063007.

[13] The Planck Collaboration, Aghanim, N., *et al.*, "Planck 2018 results - vi. cosmological parameters," *A&A*, vol. 641, A6, 2020. DOI: 10.1051/0004-6361/201833910. [Online]. Available: https://doi.org/10.1051/0004-6361/201833910.

[14] K. N. Abazajian *et al.*, *Cmb-s4 science book, first edition*, 2016. arXiv: 1610.02743 [astro-ph.CO].

[15] A. Lewis and A. Challinor, "Weak gravitational lensing of the cmb," *Physics Reports*, vol. 429, no. 1, pp. 1–65, 2006, ISSN: 0370-1573. DOI: https://doi.org/10.1016/j.physrep.2006.03.002. [Online]. Available: https://www.sciencedirect.com/science/article/pii/S0370157306000810.

[16] The Simons Observatory Collaboration, Peter Ade, *et al.*, "The simons observatory: Science goals and forecasts," *Journal of Cosmology and Astroparticle Physics*, vol. 2019, no. 02, pp. 056–056, Feb. 2019. DOI: 10.1088/1475-7516/2019/02/056. [Online]. Available: https://doi.org/10.1088.

[17] A. Starobinsky, "A new type of isotropic cosmological models without singularity," *Physics Letters B*, vol. 91, no. 1, pp. 99–102, 1980, ISSN: 0370-2693. DOI: https://doi.org/10.1016/0370-2693(80)90670-X. [Online]. Available: https://www.sciencedirect.com/science/article/pii/037026938090670X.

[18] A. H. Guth, "Inflationary universe: A possible solution to the horizon and flatness problems," *Phys. Rev. D*, vol. 23, pp. 347–356, 2 Jan. 1981. DOI: 10.1103/PhysRevD.23.347. [Online]. Available: https://link.aps.org/doi/10.1103/PhysRevD.23.347.

[19] A. Linde, "A new inflationary universe scenario: A possible solution of the horizon, flatness, homogeneity, isotropy and primordial monopole problems," *Physics Letters B*, vol. 108, no. 6, pp. 389–393, 1982, ISSN: 0370-2693. DOI: https://doi.org/10.1016/0370-2693(82)91219-9. [Online]. Available: https://www.sciencedirect.com/science/article/pii/0370269382912199.

[20] A. Kosowsky, "Cosmic Microwave Background Polarization," *Annals of Physics*, vol. 246, no. 1, pp. 49–85, Feb. 1996, ISSN: 0003-4916. DOI: 10.1006/APHY.1996.0020. [Online]. Available: http://www.sciencedirect.com/science/article/pii/S0003491696900202?via%3Dihub.

[21] C. Feng, B. Keating, H. P. Paar, and O. Zahn, "Reconstruction of gravitational lensing using wmap 7-year data," *Phys. Rev. D*, vol. 85, p. 043 513, 4 Feb. 2012. DOI: 10.1103/PhysRevD.85.043513. [Online]. Available: https://link.aps.org/doi/10.1103/PhysRevD.85.043513.

[22] The Planck Collaboration, Ade, P. A. R., *et al.*, "Planck intermediate results - xli. a map of lensing-induced b-modes," *A&A*, vol. 596, A102, 2016. DOI: 10.1051/0004-6361/201527932. [Online]. Available: https://doi.org/10.1051/0004-6361/201527932.

[23] BICEP2/Keck collaboration, P. A. R. Ade, *et al.*, "Bicep2/KECK ARRAY VIII: MEASUREMENT OF GRAVITATIONAL LENSING FROM LARGE-SCALEB-MODE POLARIZATION," *The Astrophysical Journal*, vol. 833, no. 2, p. 228, Dec. 2016. DOI: 10.3847/1538-4357/833/2/228. [Online]. Available: https://doi.org/10.3847/1538-4357/833/2/228.

[24] The ACT Collaboration, Sherwin, B. D., *et al.*, "Two-season atacama cosmology telescope polarimeter lensing power spectrum," *Phys. Rev. D*, vol. 95, p. 123 529, 12 Jun. 2017. DOI: 10.1103/PhysRevD.95.123529. [Online]. Available: https://link.aps.org/doi/10.1103/PhysRevD.95.123529.

[25] S. M. Carroll, G. B. Field, and R. Jackiw, "Limits on a lorentz- and parity-violating modification of electrodynamics," *Physical Review D*, vol. 41, no. 4, pp. 1231–1240, 1990, ISSN: 05562821. DOI: 10.1103/PhysRevD.41.1231.

[26] C. Scóccola, D. Harari, and S. Mollerach, "B polarization of the cmb from faraday rotation," *Phys. Rev. D*, vol. 70, p. 063 003, 6 Sep. 2004. DOI: 10.1103/PhysRevD.70.063003. [Online]. Available: https://link.aps.org/doi/10.1103/PhysRevD.70.063003.

[27] S. M. Carroll, "Quintessence and the Rest of the World: Suppressing Long-Range Interactions," *Physical Review Letters*, vol. 81, no. 15, pp. 3067–3070, 1998, ISSN: 0031-9007. DOI: 10.1103/PhysRevLett.81.3067. [Online]. Available: https://link.aps.org/doi/10.1103/PhysRevLett.81.3067.

[28] A. P. S. Yadav, M. Su, and M. Zaldarriaga, "Primordial B-mode diagnostics and self-calibrating the CMB polarization," *Phys. Rev. D*, vol. 81, no. 063512, 2010. DOI: 10.1103/PhysRevD.81.063512. [Online]. Available: https://journals.aps.org/prd/pdf/10.1103/PhysRevD.81.063512.

[29] J. Williams, A. Rotti, and R. Battye, "Constraining cosmic polarization rotation and implications for primordial b-modes," *Journal of Cosmology and Astroparticle Physics*, vol. 2020, no. 09, pp. 006–006, Sep. 2020. DOI: 10.1088/1475-7516/2020/09/006. [Online]. Available: https://doi.org/10.1088/1475-7516/2020/09/006.

[30] J. Williams, N. McCallum, A. Rotti, D. B. Thomas, R. Battye, and M. L. Brown, "Blind map level systematics cleaning: A quadratic estimator approach," *Journal of Cosmology and Astroparticle Physics*, vol. 2021, no. 07, p. 016, Jul. 2021. DOI: 10.1088/1475-7516/2021/07/016. [Online]. Available: https://doi.org/10.1088/1475-7516/2021/07/016.

[31] J. Clerk and Maxwell, "A Dynamical Theory of the Electromagnetic Field," *Phil. Trans. R. Soc. Lond.*, vol. 155, no. 1, pp. 459–512, 1865. [Online]. Available: http://rstl.royalsocietypublishing.org/.

[32] E. Dimastrogiovanni, M. Fasiello, and T. Fujita, "Primordial gravitational waves from axion-gauge fields dynamics," *Journal of Cosmology and Astroparticle Physics*, 2017, ISSN: 14757516. DOI: 10.1088/1475-7516/2017/01/019.

[33] M. M. Anber and L. Sorbo, "Naturally inflating on steep potentials through electromagnetic dissipation," *Physical Review D*, vol. 81, no. 4, p. 043 534, 2010, ISSN: 15507998. DOI: 10.1103/PhysRevD.81.043534.

[34] N. Barnaby, E. Pajer, and M. Peloso, "Gauge field production in axion inflation: Consequences for monodromy, non-Gaussianity in the CMB, and gravitational waves at

interferometers," *Physical Review D*, vol. 85, no. 2, p. 023 525, 2012, ISSN: 15507998. DOI: 10.1103/PhysRevD.85.023525.

[35] R. R. Caldwell and C. Devulder, "Axion Gauge Field Inflation and Gravitational Leptogenesis: A Lower Bound on B Modes from the Matter-Antimatter Asymmetry of the Universe," *arXiv:1706.03765v2*, 2017.

[36] N. J. Miller, M. Shimon, and B. G. Keating, "CMB polarization systematics due to beam asymmetry: Impact on cosmological birefringence," *Physical Review D*, vol. 79, no. 10, p. 103 002, 2009, ISSN: 15507998. DOI: 10.1103/PhysRevD.79.103002. [Online]. Available: https://journals.aps.org/prd/pdf/10.1103/PhysRevD.79.103002.

[37] CMB-S4 Collaboration, Abazajian, K., *et al.*, "CMB-S4 Science Case, Reference Design, and Project Plan," Jul. 2019. arXiv: 1907.04473. [Online]. Available: http://arxiv.org/abs/1907.04473.

[38] V. Gluscevic, M. Kamionkowski, and A. Cooray, "Derotation of the cosmic microwave background polarization: Full-sky formalism," *Phys. Rev. D - Part. Fields, Gravit. Cosmol.*, vol. 80, p. 023 510, 2009, ISSN: 15507998. DOI: 10.1103/PhysRevD.80.023510. arXiv: 0905.1687. [Online]. Available: https://journals.aps.org/prd/pdf/10.1103/PhysRevD.80.023510.

[39] M. Kamionkowski, "How to derotate the cosmic microwave background polarization," *Phys. Rev. Lett.*, vol. 102, p. 111 302, 2009, ISSN: 00319007. DOI: 10.1103/PhysRevLett.102.111302. arXiv: 0810.1286. [Online]. Available: https://journals.aps.org/prl/pdf/10.1103/PhysRevLett.102.111302.

[40] R. Pearson, B. Sherwin, and A. Lewis, "Cmb lensing reconstruction using cut sky polarization maps and pure b modes," *Phys. Rev. D*, vol. 90, p. 023 539, 2 Jul. 2014. DOI: 10.1103/PhysRevD.90.023539. [Online]. Available: https://link.aps.org/doi/10.1103/PhysRevD.90.023539.

[41] M. Mirmelstein, J. Carron, and A. Lewis, "Optimal filtering for cmb lensing reconstruction," *Phys. Rev. D*, vol. 100, p. 123 509, 12 Dec. 2019. DOI: 10.1103/PhysRevD.100.123509. [Online]. Available: https://link.aps.org/doi/10.1103/PhysRevD.100.123509.

[42] D. Leon, J. Kaufman, B. Keating, and M. Mewes, "The cosmic microwave background and pseudo-Nambu–Goldstone bosons: Searching for Lorentz violations in the cosmos," *Mod. Phys. Lett. A*, vol. 32, no. 02, p. 1 730 002, 2017, ISSN: 0217-

7323. DOI: 10.1142/S0217732317300026. [Online]. Available: http://www.worldscientific.com/doi/abs/10.1142/S0217732317300026.

[43] The POLARBEAR Collaboration, Ade, P A R, *et al.*, "POLARBEAR constraints on cosmic birefringence and primordial magnetic fields," *Physical Review D*, vol. 92, no. 12, p. 123 509, Dec. 2015. DOI: 10.1103/PhysRevD.92.123509. [Online]. Available: https://link.aps.org/doi/10.1103/PhysRevD.92.123509.

[44] R. R. Caldwell, V. Gluscevic, and M. Kamionkowski, "Cross-correlation of cosmological birefringence with CMB temperature," *Physical Review D*, vol. 84, no. 4, pp. 1–9, 2011, ISSN: 15507998. DOI: 10.1103/PhysRevD.84.043504.

[45] G. Raffelt and L. Stodolsky, "Mixing of the photon with low-mass particles," *Phys. Rev. D*, vol. 37, no. 5, p. 1237, 1988. [Online]. Available: https://journals.aps.org/prd/pdf/10.1103/PhysRevD.37.1237.

[46] A. Mirizzi, G. G. Raffelt, and P. D. Serpico, "Photon-Axion Conversion in Intergalactic Magnetic Fields and Cosmological Consequences," in *Axions*, 2008, pp. 115–134. DOI: 10.1007/978-3-540-73518-2. [Online]. Available: https://link.springer.com/content/pdf/10.1007%2F978-3-540-73518-2_7.pdf.

[47] A. Lue, L. Wang, and M. Kamionkowski, "Cosmological Signature of New Parity-Violating Interactions," *Phys. Rev. Lett.*, vol. 23, no. 8, p. 1506, 1999. [Online]. Available: https://journals.aps.org/prl/pdf/10.1103/PhysRevLett.83.1506.

[48] G.-B. Zhao, Y. Wang, J.-Q. Xia, M. Li, and X. Zhang, "An efficient probe of the cosmological CPT violation," *JCAP*, vol. 07, no. 032, 2015. DOI: 10.1088/1475-7516/2015/07/032. [Online]. Available: http://iopscience.iop.org/article/10.1088/1475-7516/2015/07/032/pdf.

[49] A. Gruppuso, G. Maggio, D. Molinari, and P. Natoli, "A note on the birefringence angle estimation in CMB data analysis," *JCAP*, vol. 05, no. 020, 2016, ISSN: 1475-7516. DOI: 10.1088/1475-7516/2016/05/020. [Online]. Available: http://adsabs.harvard.edu/cgi-bin/nph-data_query?bibcode=2016arXiv160405202G&link_type=ABSTRACT%5Cnpapers://ee00755c-a478-4d4e-a50b-ef01ee7b9957/Paper/p33065.

[50] M. Zaldarriaga and U. Seljak, "All-sky analysis of polarization in the microwave background," *Physical Review D*, vol. 55, no. 4, pp. 1830–1840, 1997, ISSN: 0556-2821. DOI: 10.1103/PhysRevD.55.1830. [Online]. Available: https://journals.aps.org/prd/pdf/10.1103/PhysRevD.55.1830%20https://link.aps.org/doi/10.1103/PhysRevD.55.1830.

[51] L. Knox, "Determination of inflationary observables by cosmic microwave background anisotropy experiments," *Physical Review D*, vol. 52, no. 8, p. 4307, 1995. [Online]. Available: https://journals.aps.org/prd/pdf/10.1103/PhysRevD.52.4307.

[52] U. Seljak, "Measuring Polarization in the Cosmic Microwave Background," *The Astrophysical Journal*, vol. 482, no. 1, pp. 6–16, 1997, ISSN: 0004-637X. DOI: 10.1086/304123. [Online]. Available: http://iopscience.iop.org/article/10.1086/304123/pdf%20http://stacks.iop.org/0004-637X/482/i=1/a=6.

[53] R. A. Fisher, "The Logic of Inductive Inference," *Journal of the Royal Statistical Society*, vol. 98, no. 1, p. 39, 1935, ISSN: 09528385. DOI: 10.2307/2342435. [Online]. Available: http://www.jstor.org/stable/10.2307/2342435?origin=crossref.

[54] V. Gluscevic and M. Kamionkowski, "Testing parity-violating mechanisms with cosmic microwave background experiments," *Physical Review D*, vol. 81, no. 8, p. 123 529, 2010. DOI: 10.1103/PhysRevD.81.123529. [Online]. Available: https://journals.aps.org/prd/pdf/10.1103/PhysRevD.81.123529.

[55] M. Farhang, J. R. Bond, and J. Chluba, "Semi-blind eigen analyses of recombination histories using cosmic microwave background data," *The Astrophysical Journal*, vol. 752, no. 2, p. 88, 2012, ISSN: 15384357. DOI: 10.1088/0004-637X/752/2/88. [Online]. Available: http://iopscience.iop.org/article/10.1088/0004-637X/752/2/88/pdf.

[56] D. Coe, "FISHER MATRICES AND CONFIDENCE ELLIPSES: A QUICK-START GUIDE AND SOFTWARE," *arXiv:0906.4123v1*, 2006. [Online]. Available: https://arxiv.org/pdf/0906.4123.pdf.

[57] J. P. Kaufman, B. G. Keating, and B. R. Johnson, "Precision tests of parity violation over cosmological distances," *Monthly Notices of the Royal Astronomical Society*, vol. 455, no. 2, pp. 1981–1988, Jan. 2016, ISSN: 0035-8711. DOI: 10.1093/mnras/stv2348. [Online]. Available: http://adsabs.harvard.edu/cgi-bin/nph-data_query?bibcode=2016MNRAS.455.1981K&link_type=ABSTRACT%5Cnpapers://ee00755c-a478-4d4e-a50b-ef01ee7b9957/Paper/p39397%20https://academic.oup.com/mnras/article-lookup/doi/10.1093/mnras/stv2348.

[58] WMAP Collaboration, Komatsu, E., *et al.*, "Seven-Year Wilkinson Microwave Anisotropy Probe (WMAP) Observations: Cosmological Interpretation," *The Astro-*

physical Journal Supplement Series, vol. 192, no. 2, p. 18, 2010, ISSN: 0067-0049. DOI: 10.1088/0067-0049/192/2/18. [Online]. Available: http://arxiv.org/abs/1001.4538%0Ahttp://dx.doi.org/10.1088/0067-0049/192/2/18.

[59] WMAP Collaboration, Hinshaw, G, *et al.*, "Nine-year Wilkinson Microwave Anisotropy Probe (WMAP) Observations: Cosmological Parameter Results," *The Astrophysical Journal Supplement Series*, vol. 208, no. 2, p. 19, 2013. [Online]. Available: http://stacks.iop.org/0067-0049/208/i=2/a=19.

[60] QUaD Collaboration, Wu, E. Y. S., *et al.*, "Parity violation constraints using cosmic microwave background polarization spectra from 2006 and 2007 observations by the quad polarimeter," *Phys. Rev. Lett.*, vol. 102, p. 161 302, 16 Apr. 2009. DOI: 10.1103/PhysRevLett.102.161302. [Online]. Available: https://link.aps.org/doi/10.1103/PhysRevLett.102.161302.

[61] BICEP Collaboration, Kaufman, J P, *et al.*, "Self-calibration of BICEP1 three-year data and constraints on astrophysical polarization rotation," *Physical Review D*, vol. 89, no. 6, p. 62 006, Mar. 2014. DOI: 10.1103/PhysRevD.89.062006. [Online]. Available: https://link.aps.org/doi/10.1103/PhysRevD.89.062006.

[62] The POLARBEAR Collaboration, Ade, P. A. R., *et al.*, "A Measurement of the Cosmic Microwave Background B-mode Polarization Power Spectrum at Sub-degree Scales with POLARBEAR," *Astrophysical Journal*, vol. 794, no. 2, 171, p. 171, Oct. 2014. DOI: 10.1088/0004-637X/794/2/171. arXiv: 1403.2369 [astro-ph.CO]. [Online]. Available: https://ui.adsabs.harvard.edu/abs/2014ApJ...794..171P.

[63] BICEP Collaboration, Ade, P A R, *et al.*, "Detection of B-Mode Polarization at Degree Angular Scales by BICEP2," *Physical Review Letters*, vol. 112, no. 24, p. 241 101, Jun. 2014. DOI: 10.1103/PhysRevLett.112.241101. [Online]. Available: https://link.aps.org/doi/10.1103/PhysRevLett.112.241101.

[64] The ACT Collaboration, Sigurd N, *et al.*, "The Atacama Cosmology Telescope: CMB polarization at 200<ℓ<9000," *JCAP*, vol. 10, no. 007, 2014. [Online]. Available: http://stacks.iop.org/1475-7516/2014/i=10/a=007.

[65] A. Gruppuso, M. Gerbino, P. Natoli, L. Pagano, N. Mandolesi, and D. Molinari, "Constraints on cosmological birefringence from Planck and Bicep2/Keck data," *JCAP*, vol. 06, no. 001, 2015, ISSN: 1475-7516. DOI: 10.1088/1475-7516/2016/06/001. [Online]. Available: http://adsabs.harvard.edu/cgi-bin/nph-data_

query?bibcode=2015arXiv150904157G&link_type=ABSTRACT%5Cnpapers://ee00755c-a478-4d4e-a50b-ef01ee7b9957/Paper/p21213.

[66] C. R. Contaldi, "IMAGING PARITY-VIOLATING MODES IN THE CMB," *The Astronomical Journal*, vol. 153, no. 1, p. 41, Dec. 2016. DOI: 10.3847/1538-3881/153/1/41. [Online]. Available: https://doi.org/10.3847/1538-3881/153/1/41.

[67] D. Contreras, P. Boubel, and D. Scott, "Constraints on direction-dependent cosmic birefringence from Planck polarization data," *Journal of Cosmology and Astroparticle Physics*, vol. 12, no. 046, 2017. [Online]. Available: https://doi.org/10.1088/1475-7516/2017/12/046%20http://arxiv.org/abs/1705.06387.

[68] BICEP/Keck Collaboration, Ade, P. A. R., *et al.*, "BICEP2 / Keck Array IX: New Bounds on Anisotropies of CMB Polarization Rotation and Implications for Axion-Like Particles and Primordial Magnetic Fields," *Phys. Rev. D*, vol. 96, no. 10, p. 102 003, 2017, ISSN: 24700029. DOI: 10.1103/PhysRevD.96.102003. arXiv: 1705.02523. [Online]. Available: http://arxiv.org/abs/1705.02523.

[69] S. De, L. Pogosian, and T. Vachaspati, "CMB Faraday rotation as seen through the Milky Way," *Phys. Rev. D - Part. Fields, Gravit. Cosmol.*, vol. 88, no. 6, 2013, ISSN: 15507998. DOI: 10.1103/PhysRevD.88.063527. arXiv: 1305.7225. [Online]. Available: https://journals.aps.org/prd/pdf/10.1103/PhysRevD.88.063527.

[70] T. Namikawa, "Testing parity-violating physics from cosmic rotation power reconstruction," *Phys. Rev. D*, vol. 95, no. 4, p. 043 523, 2017, ISSN: 24700029. DOI: 10.1103/PhysRevD.95.043523. [Online]. Available: https://journals.aps.org/prd/pdf/10.1103/PhysRevD.95.043523.

[71] C. L. Bennett, M. Bay, M. Halpern, G. Hinshaw, C. Jackson, N. Jarosik, A. Kogut, M. Limon, S. S. Meyer, L. Page, D. N. Spergel, G. S. Tucker, D. T. Wilkinson, E. Wollack, and E. L. Wright, "TheMicrowave anisotropy ProbeMission," vol. 583, no. 1, pp. 1–23, Jan. 2003. DOI: 10.1086/345346. [Online]. Available: https://doi.org/10.1086/345346.

[72] The Planck Collaboration, Ade, P. A. R., *et al.*, "Planck 2013 results. i. overview of products and scientific results," *A&A*, vol. 571, A1, 2014. DOI: 10.1051/0004-6361/201321529. [Online]. Available: https://doi.org/10.1051/0004-6361/201321529.

[73] The POLARBEAR Collaboration, Arnold K., *et al.*, "The POLARBEAR CMB polarization experiment," in *Millimeter, Submillimeter, and Far-Infrared Detectors and Instrumentation for Astronomy V*, W. S. Holland and J. Zmuidzinas, Eds., International Society for Optics and Photonics, vol. 7741, SPIE, 2010, pp. 404–414. DOI: 10.1117/12.858314. [Online]. Available: https://doi.org/10.1117/12.858314.

[74] SPT Collaboration, Austermann J. E., *et al.*, "SPTpol: an instrument for CMB polarization measurements with the South Pole Telescope," in *Millimeter, Submillimeter, and Far-Infrared Detectors and Instrumentation for Astronomy VI*, W. S. Holland, Ed., International Society for Optics and Photonics, vol. 8452, SPIE, 2012, pp. 393–410. DOI: 10.1117/12.927286. [Online]. Available: https://doi.org/10.1117/12.927286.

[75] BICEP Collaboration, Ade P. A. R., *et al.*, "BICEP2. II. EXPERIMENT AND THREE-YEAR DATA SET," *The Astrophysical Journal*, vol. 792, no. 1, p. 62, Aug. 2014. DOI: 10.1088/0004-637x/792/1/62. [Online]. Available: https://doi.org/10.1088/0004-637x/792/1/62.

[76] A. Kosowsky, "The atacama cosmology telescope," *New Astronomy Reviews*, vol. 47, no. 11, pp. 939–943, 2003, Proceedings of the Workshop on The Cosmic Microwave Background Radiation and its Polarization, ISSN: 1387-6473. DOI: https://doi.org/10.1016/j.newar.2003.09.003. [Online]. Available: https://www.sciencedirect.com/science/article/pii/S1387647303002148.

[77] V. Gluscevic, D. Hanson, M. Kamionkowski, and C. M. Hirata, "First cmb constraints on direction-dependent cosmological birefringence from wmap-7," *Phys. Rev. D*, vol. 86, p. 103 529, 10 Nov. 2012. DOI: 10.1103/PhysRevD.86.103529. [Online]. Available: https://link.aps.org/doi/10.1103/PhysRevD.86.103529.

[78] A. Gruppuso, D. Molinari, P. Natoli, and L. Pagano, "Planck 2018 constraints on anisotropic birefringence and its cross-correlation with CMB anisotropy," *Journal of Cosmology and Astroparticle Physics*, vol. 2020, no. 11, pp. 066–066, Nov. 2020. DOI: 10.1088/1475-7516/2020/11/066. [Online]. Available: https://doi.org/10.1088/1475-7516/2020/11/066.

[79] SPT Collaboration, Bianchini, F., *et al.*, "Searching for anisotropic cosmic birefringence with polarization data from sptpol," *Phys. Rev. D*, vol. 102, p. 083 504, 8 Oct. 2020. DOI: 10.1103/PhysRevD.102.083504. [Online]. Available: https://link.aps.org/doi/10.1103/PhysRevD.102.083504.

[80] The ACT Collaboration, Namikawa, Toshiya, *et al.*, "Atacama cosmology telescope: Constraints on cosmic birefringence," *Phys. Rev. D*, vol. 101, p. 083 527, 8 Apr. 2020. DOI: 10.1103/PhysRevD.101.083527. [Online]. Available: https://link.aps.org/doi/10.1103/PhysRevD.101.083527.

[81] S. Hamimeche and A. Lewis, "Likelihood analysis of cmb temperature and polarization power spectra," *Phys. Rev. D*, vol. 77, p. 103 013, 10 May 2008. DOI: 10.1103/PhysRevD.77.103013. [Online]. Available: https://link.aps.org/doi/10.1103/PhysRevD.77.103013.

[82] W. Hu, "Angular trispectrum of the cosmic microwave background," *Phys. Rev. D*, vol. 64, p. 083 005, 8 Sep. 2001. DOI: 10.1103/PhysRevD.64.083005. [Online]. Available: https://link.aps.org/doi/10.1103/PhysRevD.64.083005.

[83] A. P. S. Yadav, M. Shimon, and B. G. Keating, "Revealing cosmic rotation," *Phys. Rev. D - Part. Fields, Gravit. Cosmol.*, vol. 86, no. 8, 2012, ISSN: 15507998. DOI: 10.1103/PhysRevD.86.083002. arXiv: 1207.6640. [Online]. Available: https://journals.aps.org/prd/pdf/10.1103/PhysRevD.86.083002.

[84] M. Kamionkowski and E. D. Kovetz, "The Quest for B Modes from Inflationary Gravitational Waves," *Annu. Rev. Astron. Astrophys*, vol. 54, pp. 227–69, 2016. DOI: 10.1146/annurev-astro-081915-023433. [Online]. Available: https://www.annualreviews.org/doi/pdf/10.1146/annurev-astro-081915-023433.

[85] A. P. Yadav, R. Biswas, M. Su, and M. Zaldarriaga, "Constraining a spatially dependent rotation of the cosmic microwave background polarization," *Phys. Rev. D - Part. Fields, Gravit. Cosmol.*, vol. 79, no. 12, 2009, ISSN: 15507998. DOI: 10.1103/PhysRevD.79.123009. arXiv: 0902.4466. [Online]. Available: https://journals.aps.org/prd/pdf/10.1103/PhysRevD.79.123009.

[86] W. Hu and T. Okamoto, "Mass Reconstruction with Cosmic Microwave Background Polarization," *Astrophys. J.*, vol. 574, no. 2, pp. 566–574, 2002, ISSN: 0004-637X. DOI: 10.1086/341110. arXiv: 0111606 [astro-ph]. [Online]. Available: http://iopscience.iop.org/article/10.1086/341110/pdf.

[87] A. R. Pullen and M. Kamionkowski, "Cosmic microwave background statistics for a direction-dependent primordial power spectrum," *Phys. Rev. D - Part. Fields, Gravit. Cosmol.*, vol. 76, p. 103 529, 2007, ISSN: 15507998. DOI: 10.1103/PhysRevD.76.103529. arXiv: 0709.1144. [Online]. Available: https://journals.aps.org/prd/pdf/10.1103/PhysRevD.76.103529.

[88] LiteBIRD Collaboration, Hazumi, M., *et al.*, "Litebird: A satellite for the studies of b-mode polarization and inflation from cosmic background radiation detection," *Journal of Low Temperature Physics*, vol. 194, no. 5, pp. 443–452, Mar. 2019, ISSN: 1573-7357. DOI: 10.1007/s10909-019-02150-5. [Online]. Available: https://doi.org/10.1007/s10909-019-02150-5.

[89] C. G. R. Wallis, M. L. Brown, R. A. Battye, and J. Delabrouille, "Optimal scan strategies for future CMB satellite experiments," *Monthly Notices of the Royal Astronomical Society*, vol. 466, no. 1, pp. 425–442, Oct. 2016, ISSN: 0035-8711. DOI: 10.1093/mnras/stw2577. eprint: https://academic.oup.com/mnras/article-pdf/466/1/425/10864929/stw2577.pdf. [Online]. Available: https://doi.org/10.1093/mnras/stw2577.

[90] N. McCallum, D. B. Thomas, M. L. Brown, and N. Tessore, "Spin characterization of systematics in CMB surveys - a comprehensive formalism," *Monthly Notices of the Royal Astronomical Society*, vol. 501, no. 1, pp. 802–832, Nov. 2020, ISSN: 0035-8711. DOI: 10.1093/mnras/staa3609. eprint: https://academic.oup.com/mnras/article-pdf/501/1/802/35077383/staa3609.pdf. [Online]. Available: https://doi.org/10.1093/mnras/staa3609.

[91] D. O'Dea, A. Challinor, and B. R. Johnson, "Systematic errors in cosmic microwave background polarization measurements," *Mon. Not. R. Astron. Soc.*, vol. 376, no. 4, pp. 1767–1783, Oct. 2007, ISSN: 00358711. DOI: 10.1111/j.1365-2966.2007.11558.x. arXiv: 0610361 [astro-ph]. [Online]. Available: http://arxiv.org/abs/astro-ph/0610361%20http://dx.doi.org/10.1111/j.1365-2966.2007.11558.x.

[92] W. Hu, "Weak lensing of the CMB: A harmonic approach," *Phys. Rev. D*, vol. 62, no. 4, p. 043 007, Jul. 2000, ISSN: 0556-2821. DOI: 10.1103/PhysRevD.62.043007. [Online]. Available: https://link.aps.org/doi/10.1103/PhysRevD.62.043007.

[93] A. Lewis and A. Challinor, "Weak gravitational lensing of the CMB," *Phys. Rep.*, vol. 429, no. 1, pp. 1–65, Jun. 2006, ISSN: 0370-1573. DOI: 10.1016/J.PHYSREP.2006.03.002. [Online]. Available: https://www.sciencedirect.com/science/article/pii/S0370157306000810.

[94] U. Seljak and C. M. Hirata, "Gravitational lensing as a contaminant of the gravity wave signal in the cmb," *Phys. Rev. D*, vol. 69, p. 043 005, 4 Feb. 2004. DOI: 10.

1103/PhysRevD.69.043005. [Online]. Available: https://link.aps.org/doi/10.1103/PhysRevD.69.043005.

[95] B. D. Sherwin and M. Schmittfull, "Delensing the cmb with the cosmic infrared background," *Phys. Rev. D*, vol. 92, p. 043 005, 4 Aug. 2015. DOI: 10.1103/PhysRevD.92.043005. [Online]. Available: https://link.aps.org/doi/10.1103/PhysRevD.92.043005.

[96] The Simons Observatory Collaboration, Maximilian H. Abitbol, *et al.*, *The simons observatory: Astro2020 decadal project whitepaper*, 2019. arXiv: 1907.08284 [astro-ph.IM].

[97] CMB-S4 Collaboration, Kevork Abazajian, *et al.*, *Cmb-s4: Forecasting constraints on primordial gravitational waves*, 2020. arXiv: 2008.12619 [astro-ph.CO].

[98] A. Lewis and A. Challinor, *CAMB: Code for Anisotropies in the Microwave Background*, Feb. 2011. ascl: 1102.026.

[99] The Planck Collaboration, N. Aghanim, *et al.*, "Planck 2018 results. vi. cosmological parameters," 2018. arXiv: 1807.06209 [astro-ph.CO].

[100] The Planck Collaboration, Adam, R., *et al.*, "Planck 2015 results - viii. high frequency instrument data processing: Calibration and maps," *A&A*, vol. 594, A8, 2016. DOI: 10.1051/0004-6361/201525820. [Online]. Available: https://doi.org/10.1051/0004-6361/201525820.

[101] Maino, D., Burigana, C., Maltoni, M., Wandelt, B. D., Górski, K. M., Malaspina, M., Bersanelli, M., Mandolesi, N., Banday, A. J., and Hivon, E., "The planck-lfi instrument: Analysis of the $1/f$ noise and implications for the scanning strategy," *Astron. Astrophys. Suppl. Ser.*, vol. 140, no. 3, pp. 383–391, 1999. DOI: 10.1051/aas:1999429. [Online]. Available: https://doi.org/10.1051/aas:1999429.

[102] B. G. Keating, M. Shimon, and A. P. S. Yadav, "SELF-CALIBRATION OF COSMIC MICROWAVE BACKGROUND POLARIZATION EXPERIMENTS," *The Astrophysical Journal*, vol. 762, no. 2, p. L23, Dec. 2012. DOI: 10.1088/2041-8205/762/2/l23. [Online]. Available: https://doi.org/10.1088/2041-8205/762/2/l23.

[103] Y. Minami, H. Ochi, K. Ichiki, N. Katayama, E. Komatsu, and T. Matsumura, *Simultaneous determination of the cosmic birefringence and miscalibrated polarization angles from CMB experiments*, 083E02, Aug. 2019. DOI: 10.1093/ptep/ptz079. eprint: https://academic.oup.com/ptep/article-pdf/2019/8/083E02/

29117835/ptz079.pdf. [Online]. Available: https://doi.org/10.1093/ptep/ptz079.

[104] Y. Minami, "Determination of miscalibrated polarization angles from observed cosmic microwave background and foreground EB power spectra: Application to partial-sky observation," *Progress of Theoretical and Experimental Physics*, vol. 2020, no. 6, Jun. 2020, 063E01, ISSN: 2050-3911. DOI: 10.1093/ptep/ptaa057. eprint: https://academic.oup.com/ptep/article-pdf/2020/6/063E01/33368027/ptaa057.pdf. [Online]. Available: https://doi.org/10.1093/ptep/ptaa057.

[105] Y. Minami and E. Komatsu, "Simultaneous determination of the cosmic birefringence and miscalibrated polarization angles II: Including cross-frequency spectra," *Progress of Theoretical and Experimental Physics*, vol. 2020, no. 10, Oct. 2020, 103E02, ISSN: 2050-3911. DOI: 10.1093/ptep/ptaa130. eprint: https://academic.oup.com/ptep/article-pdf/2020/10/103E02/34002973/ptaa130.pdf. [Online]. Available: https://doi.org/10.1093/ptep/ptaa130.

[106] ——, "New extraction of the cosmic birefringence from the planck 2018 polarization data," *Phys. Rev. Lett.*, vol. 125, p. 221 301, 22 Nov. 2020. DOI: 10.1103/PhysRevLett.125.221301. [Online]. Available: https://link.aps.org/doi/10.1103/PhysRevLett.125.221301.

[107] A. A. Penzias and R. W. Wilson, "A Measurement of Excess Antenna Temperature at 4080 Mc/s.," *Astrophysical Journal*, vol. 142, pp. 419–421, Jul. 1965. DOI: 10.1086/148307. [Online]. Available: https://ui.adsabs.harvard.edu/abs/1965ApJ...142..419P.

[108] WMAP Collaboration, G. Hinshaw, *et al.*, "Nine-year wilkinson microwave anisotropy probe (wmap) observations: Cosmological parameter results," *The Astrophysical Journal Supplement Series*, vol. 208, no. 2, p. 19, Sep. 2013. DOI: 10.1088/0067-0049/208/2/19. [Online]. Available: https://doi.org/10.1088%2F0067-0049%2F208%2F2%2F19.

[109] The Planck Collaboration, Ade, P. A. R., *et al.*, "Planck 2015 results - xiii. cosmological parameters," *A&A*, vol. 594, "A13", 2016. DOI: "10.1051/0004-6361/201525830". [Online]. Available: https://doi.org/10.1051/0004-6361/201525830.

[110] BICEP/Keck Collaboration, Ade, P. A. R., *et al.*, "Joint analysis of bicep2/keck array and planck data," *Phys. Rev. Lett.*, vol. 114, p. 101 301, 10 Mar. 2015. DOI: 10.1103/

PhysRevLett.114.101301. [Online]. Available: https://link.aps.org/doi/10.1103/PhysRevLett.114.101301.

[111] The SPIDER Collaboration, Gualtieri, R, *et al.*, "SPIDER: CMB Polarimetry from the Edge of Space," *J. Low Temp. Phys.*, vol. 193, no. 5, pp. 1112–1121, 2018, ISSN: 1573-7357. DOI: 10.1007/s10909-018-2078-x. [Online]. Available: https://doi.org/10.1007/s10909-018-2078-x.

[112] The ACT Collaboration, Jonathan L Sievers, *et al.*, "The atacama cosmology telescope: Cosmological parameters from three seasons of data," *Journal of Cosmology and Astroparticle Physics*, vol. 2013, no. 10, pp. 060–060, Oct. 2013. DOI: 10.1088/1475-7516/2013/10/060. [Online]. Available: https://doi.org/10.1088%2F1475-7516%2F2013%2F10%2F060.

[113] T. K. K. Schaffer *et al.*, "The FIRST PUBLIC RELEASE OF SOUTH POLE TELESCOPE DATA: MAPS OF a 95 deg2field FROM 2008 OBSERVATIONS," *The Astrophysical Journal*, vol. 743, no. 1, p. 90, Nov. 2011. DOI: 10.1088/0004-637x/743/1/90. [Online]. Available: https://doi.org/10.1088%2F0004-637x%2F743%2F1%2F90.

[114] The Planck Collaboration, Y. Akrami, *et al.*, *Planck 2018 results. x. constraints on inflation*, 2018. arXiv: 1807.06211 [astro-ph.CO].

[115] W. Hu, "Weak lensing of the cmb: A harmonic approach," *Phys. Rev. D*, vol. 62, p. 043 007, 4 Jul. 2000. DOI: 10.1103/PhysRevD.62.043007. [Online]. Available: https://link.aps.org/doi/10.1103/PhysRevD.62.043007.

[116] B. D. Sherwin and M. Schmittfull, "Delensing the cmb with the cosmic infrared background," *Phys. Rev. D*, vol. 92, p. 043 005, 4 Aug. 2015. DOI: 10.1103/PhysRevD.92.043005. [Online]. Available: https://link.aps.org/doi/10.1103/PhysRevD.92.043005.

[117] J. Carron, A. Lewis, and A. Challinor, "Internal delensing of planck CMB temperature and polarization," *Journal of Cosmology and Astroparticle Physics*, vol. 2017, no. 05, pp. 035–035, May 2017. DOI: 10.1088/1475-7516/2017/05/035. [Online]. Available: https://doi.org/10.1088%2F1475-7516%2F2017%2F05%2F035.

[118] D. J. E. Marsh and M. P. Kamionkowski, "Axion cosmology," *Phys. Rep.*, vol. 643, pp. 1–79, 2016. DOI: 10.1016/j.physrep.2016.06.005. [Online]. Available: https://ac.els-cdn.com/S0370157316301557/1-s2.0-S0370157316301557-main.pdf?%7B%5C_%7Dtid=aa371c58-598b-

4405-9cb4-bd97dbc3072c%7B%5C&%7Dacdnat=1530026674%7B%5C_%7D933cdf476096b18b4492a6f842b67a8d.

[119] J. A. Frieman, C. T. Hill, A. Stebbins, and I. Waga, "Cosmology with ultralight pseudo nambu-goldstone bosons," *Phys. Rev. Lett.*, vol. 75, pp. 2077–2080, 11 Sep. 1995. DOI: 10.1103/PhysRevLett.75.2077. [Online]. Available: https://link.aps.org/doi/10.1103/PhysRevLett.75.2077.

[120] W. Zhao and M. Li, "Fluctuations of cosmological birefringence and the effect on cmb *b*-mode polarization," *Phys. Rev. D*, vol. 89, p. 103 518, 10 May 2014. DOI: 10.1103/PhysRevD.89.103518. [Online]. Available: https://link.aps.org/doi/10.1103/PhysRevD.89.103518.

[121] L. M. Capparelli, R. R. Caldwell, and A. Melchiorri, "Cosmic birefringence test of the hubble tension," *Phys. Rev. D*, vol. 101, p. 123 529, 12 Jun. 2020. DOI: 10.1103/PhysRevD.101.123529. [Online]. Available: https://link.aps.org/doi/10.1103/PhysRevD.101.123529.

[122] B. G. Keating, M. Shimon, and A. P. S. Yadav, "SELF-CALIBRATION OF COSMIC MICROWAVE BACKGROUND POLARIZATION EXPERIMENTS," *The Astrophysical Journal*, vol. 762, no. 2, p. L23, Dec. 2012. DOI: 10.1088/2041-8205/762/2/l23. [Online]. Available: https://doi.org/10.1088%2F2041-8205%2F762%2F2%2Fl23.

[123] G.-C. Liu and K.-W. Ng, "Axion dark matter induced cosmic microwave background b modes," *Physics of the Dark Universe*, vol. 16, pp. 22–25, 2017, ISSN: 2212-6864. DOI: https://doi.org/10.1016/j.dark.2017.02.004. [Online]. Available: http://www.sciencedirect.com/science/article/pii/S2212686417300171.

[124] Aghanim, N. *et al.*, "Planck intermediate results - xlix. parity-violation constraints from polarization data," *A&A*, vol. 596, A110, 2016. DOI: 10.1051/0004-6361/201629018. [Online]. Available: https://doi.org/10.1051/0004-6361/201629018.

[125] T. Namikawa *et al.*, "The Atacama Cosmology Telescope: Constraints on Cosmic Birefringence," Jan. 2020. arXiv: 2001.10465. [Online]. Available: http://arxiv.org/abs/2001.10465.

[126] L. Pogosian, M. Shimon, M. Mewes, and B. Keating, "Future cmb constraints on cosmic birefringence and implications for fundamental physics," *Physical Review D*, vol. 100, no. 2, Jul. 2019, ISSN: 2470-0029. DOI: 10.1103/physrevd.100.023507. [Online]. Available: http://dx.doi.org/10.1103/PhysRevD.100.023507.

[127] A. Yadav, L. Pogosian, and T. Vachaspati, "Probing primordial magnetism with off-diagonal correlators of cmb polarization," *Phys. Rev. D*, vol. 86, p. 123 009, 12 Dec. 2012. DOI: 10.1103/PhysRevD.86.123009. [Online]. Available: https://link.aps.org/doi/10.1103/PhysRevD.86.123009.

[128] S. De, L. Pogosian, and T. Vachaspati, "Cmb faraday rotation as seen through the milky way," *Phys. Rev. D*, vol. 88, p. 063 527, 6 Sep. 2013. DOI: 10.1103/PhysRevD.88.063527. [Online]. Available: https://link.aps.org/doi/10.1103/PhysRevD.88.063527.

[129] L. Pogosian, "Searching for primordial magnetism with multifrequency cosmic microwave background experiments," *Monthly Notices of the Royal Astronomical Society*, vol. 438, no. 3, pp. 2508–2512, Jan. 2014, ISSN: 0035-8711. DOI: 10.1093/mnras/stt2378. eprint: http://oup.prod.sis.lan/mnras/article-pdf/438/3/2508/18470442/stt2378.pdf. [Online]. Available: https://doi.org/10.1093/mnras/stt2378.

[130] S.-Y. Li, J.-Q. Xia, M. Li, H. Li, and X. Zhang, "Primordial gravitational waves measurements and anisotropies of cmb polarization rotation," *Physics Letters B*, vol. 751, pp. 579–585, 2015, ISSN: 0370-2693. DOI: https://doi.org/10.1016/j.physletb.2015.10.089. [Online]. Available: http://www.sciencedirect.com/science/article/pii/S0370269315008680.

[131] T. Okamoto and W. Hu, "Cosmic microwave background lensing reconstruction on the full sky," *Phys. Rev. D*, vol. 67, p. 083 002, 8 Apr. 2003. DOI: 10.1103/PhysRevD.67.083002. [Online]. Available: https://link.aps.org/doi/10.1103/PhysRevD.67.083002.

[132] E. Hivon, K. M. Gorski, C. B. Netterfield, B. P. Crill, S. Prunet, and F. Hansen, "MASTER of the cosmic microwave background anisotropy power spectrum: A fast method for statistical analysis of large and complex cosmic microwave background data sets," *The Astrophysical Journal*, vol. 567, no. 1, pp. 2–17, Mar. 2002. DOI: 10.1086/338126. [Online]. Available: https://doi.org/10.1086%2F338126.

[133] BICAP/Keck Collaboration, Ade, P. A. R., *et al.*, "Constraints on primordial gravitational waves using $planck$, wmap, and new bicep2/$keck$ observations through the 2015 season," *Phys. Rev. Lett.*, vol. 121, p. 221 301, 22 Nov. 2018. DOI: 10.1103/PhysRevLett.121.221301. [Online]. Available: https://link.aps.org/doi/10.1103/PhysRevLett.121.221301.

[134] C. L. Bennett, A. J. Banday, K. M. Gorski, G. Hinshaw, P. Jackson, P. Keegstra, A. Kogut, G. F. Smoot, D. T. Wilkinson, and E. L. Wright, "Four-Year COBE DMR Cosmic Microwave Background Observations: Maps and Basic Results," *ApJL*, vol. 464, p. L1, Jun. 1996. DOI: 10.1086/310075. arXiv: astro-ph/9601067 [astro-ph].

[135] WMAP Collaboration, Bennett, C. L., *et al.*, "Nine-year Wilkinson Microwave Anisotropy Probe (WMAP) Observations: Final Maps and Results," *ApJS*, vol. 208, no. 2, 20, p. 20, Oct. 2013. DOI: 10.1088/0067-0049/208/2/20. arXiv: 1212.5225 [astro-ph.CO].

[136] The Planck Collaboration, Aghanim, N., *et al.*, "Planck 2018 results - i. overview and the cosmological legacy of planck," *A&A*, vol. 641, A1, 2020. DOI: 10.1051/0004-6361/201833880. [Online]. Available: https://doi.org/10.1051/0004-6361/201833880.

[137] M. Remazeilles, A. Rotti, and J. Chluba, "Peeling off foregrounds with the constrained moment ILC method to unveil primordial CMB B-modes," *arXiv e-prints*, arXiv:2006.08628, arXiv:2006.08628, Jun. 2020. arXiv: 2006.08628 [astro-ph.CO].

[138] The Planck Collaboration, Aghanim, N., *et al.*, "Planck 2018 results - viii. gravitational lensing," *A&A*, vol. 641, A8, 2020. DOI: 10.1051/0004-6361/201833886. [Online]. Available: https://doi.org/10.1051/0004-6361/201833886.

[139] W. Hu, M. M. Hedman, and M. Zaldarriaga, "Benchmark parameters for CMB polarization experiments," *Phys. Rev. D*, vol. 67, no. 4, 043004, p. 043 004, Feb. 2003. DOI: 10.1103/PhysRevD.67.043004. arXiv: astro-ph/0210096 [astro-ph].

[140] P. A. R. Ade *et al.*, "Bicep2 III: Instrumental Systematics," *ApJ*, vol. 814, no. 2, 110, p. 110, Dec. 2015. DOI: 10.1088/0004-637X/814/2/110. arXiv: 1502.00608 [astro-ph.IM].

[141] J. Delabrouille and J.-F. Cardoso, "Diffuse source separation in cmb observations," in *Data Analysis in Cosmology*, V. J. Martinez, E. Saar, E. M. Gonzales, and M. J. Pons-Borderia, Eds. Berlin, Heidelberg: Springer Berlin Heidelberg, 2009, pp. 159–205, ISBN: 978-3-540-44767-2. DOI: 10.1007/978-3-540-44767-2_6. [Online]. Available: https://doi.org/10.1007/978-3-540-44767-2_6.

[142] K. Ichiki, "CMB foreground: A concise review," *Progress of Theoretical and Experimental Physics*, vol. 2014, no. 6, Jun. 2014, 06B109, ISSN: 2050-3911. DOI: 10.1093/ptep/ptu065. eprint: https://academic.oup.com/ptep/article-

pdf/2014/6/06B109/4447714/ptu065.pdf. [Online]. Available: https://doi.org/10.1093/ptep/ptu065.

[143] J. Carron, A. Lewis, and A. Challinor, "Internal delensing of Planck CMB temperature and polarization," *J. Cosmol. Astropart. Phys.*, vol. 2017, no. 5, p. 035, May 2017, ISSN: 14757516. DOI: 10.1088/1475-7516/2017/05/035. arXiv: 1701.01712. [Online]. Available: https://iopscience.iop.org/article/10.1088/1475-7516/2017/05/035%20https://iopscience.iop.org/article/10.1088/1475-7516/2017/05/035/meta.

[144] The Planck Collaboration, Ade, P. A. R., *et al.*, "Planck 2015 results - xvi. isotropy and statistics of the cmb," *A&A*, vol. 594, A16, 2016. DOI: 10.1051/0004-6361/201526681. [Online]. Available: https://doi.org/10.1051/0004-6361/201526681.

[145] J. Bock *et al.*, "Study of the Experimental Probe of Inflationary Cosmology (EPIC)-Intemediate Mission for NASA's Einstein Inflation Probe," *arXiv e-prints*, arXiv:0906.1188, arXiv:0906.1188, Jun. 2009. arXiv: 0906.1188 [astro-ph.CO].

[146] P. A. R. Ade *et al.*, "Bicep2 III: Instrumental Systematics," *ApJ*, vol. 814, no. 2, 110, p. 110, Dec. 2015. DOI: 10.1088/0004-637X/814/2/110. arXiv: 1502.00608 [astro-ph.IM].

[147] A. Kusaka, T. Essinger-Hileman, J. W. Appel, P. Gallardo, K. D. Irwin, N. Jarosik, M. R. Nolta, L. A. Page, L. P. Parker, S. Raghunathan, J. L. Sievers, S. M. Simon, S. T. Staggs, and K. Visnjic, "Modulation of cosmic microwave background polarization with a warm rapidly rotating half-wave plate on the atacama b-mode search instrument," *Review of Scientific Instruments*, vol. 85, no. 2, p. 024 501, 2014. DOI: 10.1063/1.4862058. eprint: https://doi.org/10.1063/1.4862058. [Online]. Available: https://doi.org/10.1063/1.4862058.

[148] A. Kusaka, J. Appel, T. Essinger-Hileman, J. A. Beall, L. E. Campusano, H.-M. Cho, S. K. Choi, K. Crowley, J. W. Fowler, P. Gallardo, *et al.*, "Results from the atacama b-mode search (abs) experiment," *Journal of Cosmology and Astroparticle Physics*, vol. 2018, no. 09, p. 005, 2018.

[149] J. Bock, A. Cooray, S. Hanany, B. Keating, A. Lee, T. Matsumura, M. Milligan, N. Ponthieu, T. Renbarger, and H. Tran, "The Experimental Probe of Inflationary Cosmology (EPIC): A Mission Concept Study for NASA's Einstein Inflation Probe," *arXiv e-prints*, arXiv:0805.4207, arXiv:0805.4207, May 2008. arXiv: 0805.4207 [astro-ph].

[150] D. B. Thomas, N. McCallum, and M. L. Brown, *Sky rotation in ground-based cosmic microwave background experiments*, 2021. arXiv: 2102.02284 [astro-ph.IM].

[151] K. M. Górski, E. Hivon, A. J. Banday, B. D. Wand elt, F. K. Hansen, M. Reinecke, and M. Bartelmann, "HEALPix: A Framework for High-Resolution Discretization and Fast Analysis of Data Distributed on the Sphere," *ApJ*, vol. 622, no. 2, pp. 759–771, Apr. 2005. DOI: 10.1086/427976. arXiv: astro-ph/0409513 [astro-ph].

[152] A. Lewis, A. Challinor, and A. Lasenby, "Efficient computation of CMB anisotropies in closed FRW models," *ApJ*, vol. 538, pp. 473–476, 2000. DOI: 10.1086/309179. arXiv: astro-ph/9911177 [astro-ph].

[153] D. B. Thomas, N. McCallum, and M. L. Brown, "Controlling systematics in ground-based CMB surveys with partial boresight rotation," *MNRAS*, vol. 491, no. 2, pp. 1960–1969, Jan. 2020. DOI: 10.1093/mnras/stz2607. arXiv: 1905.12647 [astro-ph.CO].

[154] N. Katayama and E. Komatsu, "Simple foreground cleaning algorithm for detecting primordial b-mode polarization of the cosmic microwave background," *The Astrophysical Journal*, vol. 737, no. 2, p. 78, Aug. 2011. DOI: 10.1088/0004-637x/737/2/78. [Online]. Available: https://doi.org/10.1088%2F0004-637x%2F737%2F2%2F78.

[155] S. Hanany *et al.*, "Pico: Probe of inflation and cosmic origins," 2019. arXiv: 1908.07495 [astro-ph.IM].

[156] M. Pospelov, A. Ritz, and C. Skordis, "Pseudoscalar perturbations and polarization of the cosmic microwave background," *Phys. Rev. Lett.*, vol. 103, p. 051 302, 5 Jul. 2009. DOI: 10.1103/PhysRevLett.103.051302. [Online]. Available: https://link.aps.org/doi/10.1103/PhysRevLett.103.051302.

[157] A. Kosowsky and A. Loeb, "Faraday Rotation of Microwave Background Polarization by a Primordial Magnetic Field," *Astrophysical Journal*, vol. 469, p. 1, Sep. 1996. DOI: 10.1086/177751. arXiv: astro-ph/9601055 [astro-ph]. [Online]. Available: https://ui.adsabs.harvard.edu/abs/1996ApJ...469....1K.

[158] D. D. Harari, "Imprints of a primordial magnetic field upon the cosmic microwave background anisotropy and polarization," *Int. J. Theor. Phys.*, vol. 36, no. 11, pp. 2513–2523, 1997, ISSN: 1572-9575. DOI: 10.1007/BF02768940. [Online]. Available: https://doi.org/10.1007/BF02768940.

[159] The Planck Collaboration, Akrami, Y., *et al.*, "Planck 2018 results - iv. diffuse component separation," *A&A*, vol. 641, A4, 2020. DOI: 10.1051/0004-6361/201833881. [Online]. Available: https://doi.org/10.1051/0004-6361/201833881.

[160] T. Okamoto and W. Hu, "Cosmic microwave background lensing reconstruction on the full sky," *Phys. Rev. D*, vol. 67, no. 8, Jan. 2003, ISSN: 15502368. DOI: 10.1103/PhysRevD.67.083002. arXiv: 0301031 [astro-ph]. [Online]. Available: http://arxiv.org/abs/astro-ph/0301031%20http://dx.doi.org/10.1103/PhysRevD.67.083002.

[161] The Planck Collaboration, Aghanim, N., *et al.*, "Planck 2018 results - v. cmb power spectra and likelihoods," *A&A*, vol. 641, A5, 2020. DOI: 10.1051/0004-6361/201936386. [Online]. Available: https://doi.org/10.1051/0004-6361/201936386.

[162] M. Gerbino, M. Lattanzi, M. Migliaccio, L. Pagano, L. Salvati, L. Colombo, A. Gruppuso, P. Natoli, and G. Polenta, "Likelihood methods for cmb experiments," *Frontiers in Physics*, vol. 8, p. 15, 2020, ISSN: 2296-424X. DOI: 10.3389/fphy.2020.00015. [Online]. Available: https://www.frontiersin.org/article/10.3389/fphy.2020.00015.